TITLE OF THESIS

HOT DEFORMATION AND FLOW SOFTENING IN β- ZIRCONIUM ALLOYS

Bernard HERITIER
PhD Thesis
Dept- of MET. ENG.

HIGH TEMPERATURE DEFORMATION AND FLOW SOFTENING IN BETA ZIRCONIUM ALLOYS

by

Bernard HERITIER

A Thesis Submitted to the
Faculty of Graduate Studies and Research
in Partial Fulfilment of the Requirements for the Degree of
Doctor of Philosophy

Department of Mining and Metallurgical Engineering
McGill University
Montreal, Canada

June 1976

ABSTRACT

The flow properties of the β-phase Zr-Mo and Zr-Nb alloys were investigated by means of compression testing in a nominally pure argon atmosphere. The stress strain curves determined for the Zr-Mo alloys were unusual in that they exhibited a continuous decrease in flow stress with strain, after little or no work-hardening. A further unusual feature of the tests was that the flow stress in interrupted tests increased with delay time in all the alloys. By contrast, crystal bar Zr exhibited neither flow softening nor very large interruption hardening, but deformed in a conventional manner. The results obtained from X-ray investigations, as well as from interrupted tests and from tests carried out in a more purified atmosphere, indicated that the occurrence of both interruption hardening and flow softening was associated with the presence of an oxygen-stabilized α-layer on the outer surface of the sample. Growth of the hard α-layer during annealing produces strengthening while its decrease in volume during deformation produces softening. A model, based on the assumption that the hard α-phase shares the load applied to the sample, was developed and its predictions agree satisfactorily with the experimental observations.

The stress sensitivity of the strain rate in these alloys decreases from 4.0 to 3.4 as the molybdenum concentration is increased from 0 to 6%, for both the yield and the steady-state regimes of flow. The alloy flow stress increases with molybdenum concentration C approximately as $C^{0.7}$, although it is apparent that the molybdenum atoms are indirect strengtheners, and do not act as individual obstacles to flow.

The flow curves obtained on Zr-Nb alloys containing 10, 15 and 20% Nb also exhibited flow softening, and the magnitude of this effect decreased as the temperature was increased. All three alloys also exhibited anneal hardening, i.e. an increase in flow stress at 825°C with annealing time at 1000°C. Neither the flow softening, nor the anneal hardening could be associated with environmental effects, as in the Zr-Mo alloys, nor could they be attributed to texture changes or to the occurrence of dynamic recrystallization. These effects, as well as the results obtained from X-ray and microprobe investigations, and from grain size measurements are discussed and it is concluded that the anneal hardening is due to the combined effect of grain growth and the formation of solute clusters during annealing. By analogy, flow softening is attributed to the destruction of the solute clusters by straining.

Finally, stress-strain curves were determined in the Zr-2.5% Nb alloy. The flow curves do not exhibit either flow softening or anneal hardening, as do the high Nb alloys. The flow stresses were found to be highly strain rate dependent, as well as temperature dependent; with stress sensitivities of about 5.5 for yielding and 4.5 for steady-state flow.

RÉSUMÉ

La déformation plastique des alliages Zr-Nb et Zr-Mo en phase β a été étudiée au moyen d'essais de compression sous atmosphère d'argon. Les courbes effort/déformation des alliages Zr-Mo présentent une décroissance de la contrainte lors de la déformation, après une courte période de consolidation; propriété inexplicable par la restauration dynamique seule. Des essais de compression interrompue ont été effectués. La contrainte lors de la reprise de la déformation croît avec le temps d'interruption, en conflit avec le comportement usuel. Le zirconium non allié, au contraire, ne présente ni adoucissement par déformation, ni durcissement très marqué lors d'interruptions. L'analyse par rayons X, ainsi que les résultats de tests effectués sous atmosphère de haute pureté ont montré que les effets d'adoucissement par déformation et de durcissement lors d'essais de compression interrompue sont associés à l'existence, près de la surface de l'échantillon, d'une couche de phase α, stabilisée par l'oxygène. La croissance de cette phase avec le temps d'interruption est la cause du durcissement observé tandis que sa décroissance en volume lors de la déformation fait apparaître le phénomène d'adoucissement. Un modèle basé sur l'hypothèse d'une répartition de la charge appliquée sur les phases β et α est présenté, et s'avère capable d'expliquer d'une manière satisfaisante les résultats expérimentaux.

La sensibilité de la contrainte à la vitesse de déformation décroît de 4.0 à 3.4 lorsque la teneur pondérale en molybdène s'élève de 0 à 6%, pour l'écoulement à la limite élastique aussi bien qu'en régime permanent. Les contraintes varient également avec la teneur en molybdène élevée à la puissance 0.7, bien qu'il soit apparent que les atomes de molybdène ne

constituent pas directement des obstacles au mouvement des dislocations.

La déformation plastique des alliages contenant 10, 15 et 20% Nb présente également un phénomène d'adoucissement par déformation, qui décroît lorsque la température croît. De plus, la contrainte d'écoulement à 825°C apparaît anormalement affectée par le temps de recuit préalable à 1000°C. Aucun de ces deux effets ne semble pouvoir être attribué à un phénomène d'oxydation de surface, comme dans le cas des alliages Zr-Mo, ni à des mécanismes d'adoucissement connus tels que la recristallisation dynamique ou la variation de texture au cours de la déformation. Le comportement mécanique, les résultats d'analyses par rayons X et par microsonde, ainsi que les résultats de mesures de taille de grains sont examinés. Il est conclu que le durcissement au cours du recuit est probablement causé par l'effet combiné de la croissance du grain et de la formation d'amas de soluté (semblables aux zones GP1). D'une manière analogue, l'adoucissement par déformation pourrait avoir pour origine la destruction de ces amas par les dislocations.

Dans un dernier temps, les courbes contrainte/déformation de l'alliage Zr-2.5% Nb ont été obtenues. Celles-ci ne présentent pas d'adoucissement par déformation, ni ne paraissent sensibles au temps de recuit à 1000°C. Les contraintes cependent varient fortement avec la vitesse de déformation et modérément avec la température. La sensibilité de la contrainte à la vitesse de déformation décroît de 5.0 à la limite élastique à 4.5 pour le régime permanent.

ACKNOWLEDGEMENTS

The author wishes to express his gratitude to Dr. J.J. Jonas, director of this research, for his help and constant encouragement during the course of this work, as well as to Dr. M.J. Luton for many stimulating discussions and for reviewing the manuscript.

The author would like to acknowledge the many useful suggestions he received from Dr. W.T. Thompson with regard to thermodynamics and some delicate problems, and extends his particular thanks to several scientists at the Chalk River Nuclear Laboratories: to Dr. C.E. Ells and R.A. Holt for their enlightening comments and Dr. D.O. Northwood for assistance with electron microscopy.

The author is grateful to his fellow graduate students for their interest and support along the various stages of this work.

Finally, the author is indebted to the Department of Metallurgical Engineering at the Ecole Polytechnique for the use of their texture goniometer, to Atomic Energy of Canada Limited for the supply of materials, and to the National Research Council of Canada for the award of a postgraduate scholarship.

TABLE OF CONTENTS

LIST OF FIGURES

LIST OF TABLES

CHAPTER 1

INTRODUCTION

The steady increase in energy demand, due to both population growth and increasing consumption per capita, as well as the limitations of traditional sources such as oil and hydroelectric power, constitute one of the major problem areas faced by the world today. Canada is a privileged country in that it has been able to generate enough energy to satisfy domestic demand, thanks to abundant hydroelectricity (e.g. the James Bay and Manicouagan River developments), and to the deposits of oil, natural gas and tar sand in the Prairies. Projections of the consumption and demand curves, however, have shown that in 1980 Canada will have to import energy, which will make the country dependent upon outside suppliers and will affect the balance of payments.

For this reason, Canada, in company with many other countries, has expended considerable effort on the development of nuclear reactors for energy production. Although there is a growing awareness of the environmental dangers associated with the use of nuclear reactors, they appear to be the only readily available alternative for at least two decades. New processes for producing energy such as hydrogen fusion or solar energy still appear to be in the early stages of development.

The Canadian CANDU nuclear reactors system is based on natural uranium dioxide as a fuel. For this reason, a strict neutron economy must be achieved in order to maintain the fission chain reaction. Zirconium-base alloys have been used extensively in the construction of the core elements, as they combine in an almost unique way good mechanical and corrosion properties with very low neutron absorption. The improvement in

the mechanical properties of these alloys is the key to cheaper energy, as the net efficiency increases substantially with operating temperature.

The original aim of the present investigation was to study the effects of niobium and molybdenum on the high temperature properties of zirconium alloys. In this way the study would provide a contrast to the work of Luton on zirconium-tin alloys, as tin is an α-stabilizer, whereas niobium and molybdenum are β-stabilizers. Thus it was intended to carry out a detailed activation analysis of the flow behaviour in an attempt to see if niobium and molybdenum act as direct strengtheners, i.e. whether the Nb and Mo atoms are themselves the obstacles to dislocation flow, or whether they modify the effect of other obstacles such as dislocation nodes and sub-boundaries.

Once the investigation was underway, however, it soon became apparent that flow curves differing considerably from the regular ones observed by Luton were frequently obtained. There were several unusual aspects to these stress-strain curves. In the zirconium-molybdenum alloys, yield drops and a continuous decrease of stress with strain were commonly observed. When the tests were interrupted after a certain strain interval and then reloaded, appreciable strengthening was detected, which increased with delay time before reloading. This behaviour suggested that some strengthening effect other than solution hardening was taking place. In the zirconium-niobium alloys, sharp yield drops were not observed, nor was there an interruption strengthening effect. The flow curves, on the other hand, displayed even more marked flow softening, of an extent not usually encountered in investigations of this type. The cause of the flow softening was not known, but could have been a result of various mechanisms such as precipitate coarsening, dynamic recrystallization, the intensifica-

tion of grain boundary sliding, texture modification during straining, for instance. It was clear at this point that the original aim of activation analysis had to be abandoned and that the object of the investigation would instead be that of determining the causes of the unusual behaviour of the two families of alloys. It is fortuitous that the factors responsible for the abnormal flow curves were different for the two alloy systems. The way in which they were determined, and the conclusions that were drawn, will be described in the sections that follow.

CHAPTER 2

FUNDAMENTAL ASPECTS OF THE DEFORMATION OF METALS AND THE OXIDATION OF ZIRCONIUM AND ITS ALLOYS AT ELEVATED TEMPERATURES

The purpose of this chapter is to review some of the background literature that is relevant to an understanding of the present work. The first section is concerned with the phenomenology of the high temperature deformation of metals, and also deals with the theories and mechanistic models used to account for the observed phenomena. In a second section, particular emphasis is placed on those mechanisms that are capable of producing pronounced softening during high temperature flow. The last two sections are devoted to the oxidation of zirconium and its alloys, and describes the effects of oxidation on the mechanical properties of materials.

2.1 THE DEFORMATION OF METALS AT HIGH TEMPERATURES

The deformation of metals at elevated temperatures has been extensively studied during the past two decades. Several good reviews dealing with the characteristics and properties of metals under hot working conditions have been published recently (1-6). The present review will therefore be limited to a brief survey of the main features of high temperature deformation. Of particular interest in the present work are the flow curves, which will be dealt with first. These curves are affected by the accompanying microstructural changes, which will be considered together with some models for high temperature deformation in the sections that follow. The empirical relations between the deformation parameters will be surveyed briefly in the last section.

2.1.1 The High Temperature Flow Curve

High temperature flow curves have been determined for a large number of pure metals and alloys. They fall into two main categories: the dynamic recovery curves and the dynamic recrystallization curves.

2.1.1.1 The dynamic recovery curve

This type of flow behaviour has been observed in aluminum (7-9), α-iron (10-15) and ferritic alloys, in b.c.c. refractory metals (16), in zirconium alloys (17) and in other h.c.p. metals (18-19). The flow curve can be divided into three stages (Figure 2.1.a). First, a micro-strain region can be observed in which the plastic strain rate of the sample increases from zero to the nominal strain rate. The loading slopes in this region range from E/50 at low strain rates and high temperatures to E/5 at high strain rates and lower temperatures. The slopes are lower than the modulus E because of the plastic strain produced during initial loading by the operation of thermally activated dislocation sources. A work-hardening region follows in which the net work-hardening rate decreases with increasing strain. The net work-hardening rate near the onset of gross plastic flow varies from E/500 at high temperatures and low strain rates to E/100 at low temperatures and high strain rates. In the third region, the net rate of work-hardening falls to zero and the stress remains constant with increasing strain, provided the true strain rate is constant. The strain at which the steady state regime is achieved increases with strain rate and decreases with temperature.

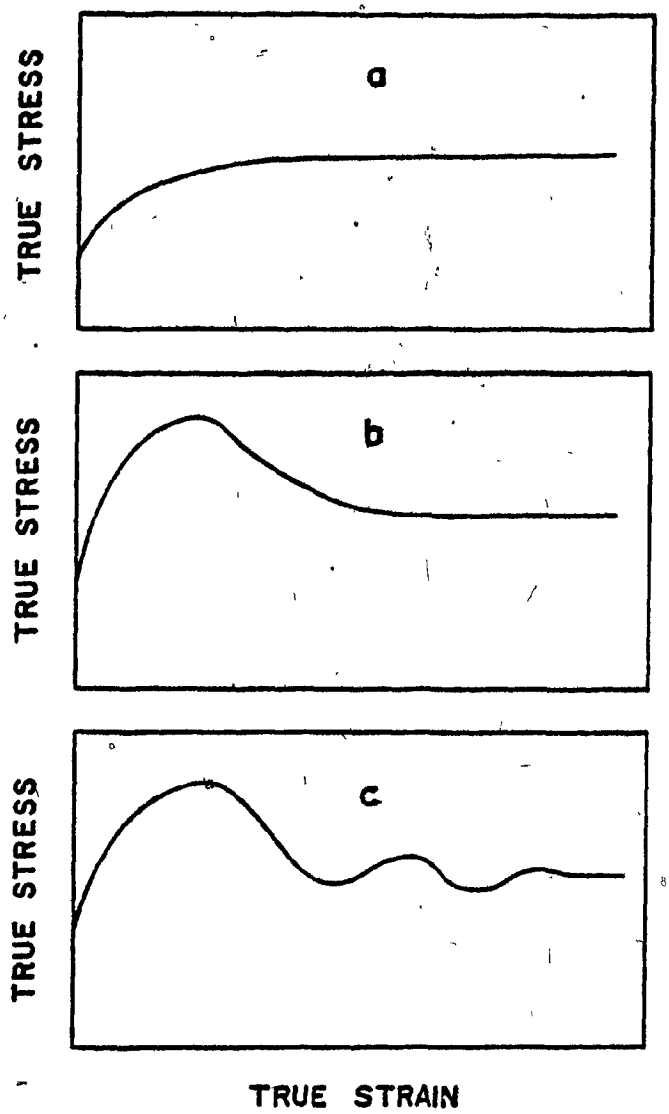

FIGURE 2.1 Schematic representation of flow curves obtained for different types of materials:
a. materials that dynamically recover only
b. materials that dynamically recrystallize continuously
c. materials that recrystallize periodically

2.1.1.2 The dynamic recrystallization curve

This behaviour has been encountered in nickel (7,20-24) and nickel-base alloys (21,22-25), in copper (7,20,21,26), in γ-iron (27) and austenitic alloys (28-33) and is shown schematically in Figure 2.1.b. The early part of the curve also exhibits a microstrain region which turns gradually into a work-hardening region in a manner similar to that observed in the dynamic recovery curves. As the strain increases, however, the work-hardening rate, after decreasing with strain to zero, subsequently becomes negative and eventually settles back to zero. In other words, the stress goes through a peak value at a strain ε_p, then decreases with strain and finally stabilizes at a value that is normally lower than the peak stress. At low strain rates a steady state stress may not be attained directly after the peak, but only after some oscillations of the flow stress with strain have taken place; see Figure 2.1.c (22). The strain to the peak ε_p increases with strain rate and decreases with temperature.

2.1.2 Dynamic Recovery

2.1.2.1 Microstructural changes associated with dynamic recovery

During the strain interval required to reach steady state flow, the dislocation structure, which consists of randomly distributed dislocations, evolves into an orderly subgrain structure. The subgrains may be characterized by dislocation "walls", in which dislocations are very tightly knit and have a very high density; these walls in turn separate cells in which the dislocation density is much lower. The overall dislocation density increases during deformation from about $10^{11} m^{-2}$ in the undeformed state to about $10^{14} m^{-2}$ in the steady state condition. The

subgrains appear better defined at higher temperatures and lower strain rates than at lower temperatures and higher strain rates.

Once steady state flow is obtained, the subgrains remain equiaxed, whereas the grain structure becomes more and more elongated with further deformation. Below 0.6 T_m the subgrains may get somewhat elongated as the strain is increased, but only to a limited extent. Stüwe (26,34) has explained the dynamic stability of subgrains during concurrent deformation as being due to the attainment of a dynamic equilibrium between the rate of dislocation generation in the subgrain interiors and the annihilation rate in the subgrain boundaries. Another interpretation was proposed by McQueen et al (35) who viewed the equiaxed subgrains as resulting from the continuous break-up and reformation of the sub-boundaries during steady state flow.

2.1.2.2 Stress and subgrain size

The subgrain size can be correlated with the developed stress according to an equation of the type

$$\bar{d} = k\sigma^{-M} \qquad (2.1)$$

where $\bar{d}$ is the average subgrain size, σ is the steady state stress and k and M are constants.

The exponent M is usually close to unity (1,2,36). Equation 2.1, however, does not imply any causal relationship between $\bar{d}$ and σ, but only that the steady state size of subgrains attain a certain value for each combination of stress, temperature and strain rate. The initial grain size does not seem to have an effect on either the subgrain size or the

steady state flow stress.

The dislocation density within subgrains ρ has been successfully related to the high temperature flow stress σ through the relation (37)

$$\sigma = \alpha\mu b\sqrt{\rho} \qquad (2.2)$$

where α is a constant, μ the shear modulus and b the Burgers vector.

In the subgrains formed in certain metals, such as Al, the dislocation density has been found to be very low (36,38); whereas in others, such as 20% Cr - 35% Ni steel (39), it can remain quite high. This has been related to the stacking fault energy changes, which will be considered later. The misorientation between subgrains does not appear to vary with the strain; strain rate and temperature on the other hand have a modest influence, the smallest misorientations being observed at the highest temperatures and the lowest strain rates. The detailed nature of the sub-boundaries has not been clearly characterized to date. Although sub-boundaries of tilt, twist or mixed nature have been reported in various studies, the occurrence of these types has not been clearly related to material or experimental variables. The dislocation density in the subgrain walls is also largely unknown, due to the experimental problems involved in its determination, and the rate controlling annihilation mechanisms have not been unequivocally determined.

2.1.2.3 Effect of solute addition on dynamic recovery

In general, alloying increases very markedly the resistance of metals to creep as well as increasing the flow stress under constant strain rate conditions. The effect is most marked when the first few per cent solute is added than it is at higher solute concentrations.

Solutes have been thought to affect the flow stress either by acting as point obstacles on the slip planes or by decreasing the stacking fault energy. The decrease in SFE leads to a decrease in the recovery rate and thus leads to higher flow stresses.

Empirically, it has been shown that the creep rate is proportional to $\gamma 3.5$, γ being the SFE (40-43). In zirconium-tin alloys Sastry et al (44) were able to relate the observed variation of SFE with solute concentration to the characteristics of the rate-controlling obstacles, as determined from mechanical tests. They showed that in these alloys, where the unzipping of attractive junctions is proposed as the rate controlling mechanism, the free energies of the obstacles in the absence of stress calculated from the stacking fault energies were in very good agreement with those determined from the strain rate and temperature dependence of the flow stress. Although similar studies have not been carried out on other alloy systems, it appears possible that SFE changes promoted by alloying may, in general, be the cause of the change in mechanical behaviour. Changes in diffusivity and in the elastic moduli with solute content may also be expected to influence the mechanical behaviour, but have so far been found to be of relatively little importance. Nevertheless, sharp decreases in creep rate with solute addition have been observed in α-brass (45) and in Nb-Mo alloys (46), and these cannot be explained by SFE changes alone.

It has been shown (47) that the addition of silicon to iron causes strengthening at low temperatures ($< 800^{o}C$) and appears to soften the material at higher temperatures. Immarigeon (47) was able to obtain the variation of both the probability of activation of a dislocation over the obstacles and that of the density of activatable sites with temperature,

from the thermal activation analysis which will be described in Section 2.1.5. He found that, at high temperatures, the increase in the pre-exponential factor of the rate equation caused by silicon addition (which is related to the density of activatable sites) was overpowering the corresponding increase in obstacle strength.

This result is of some importance since it shows that solute addition may induce, apart from an increase in obstacle strength, a variation in other parameters which may reduce and even overcome the strengthening component.

2.1.2.4 Dynamic recovery models

None of the present models explains in an entirely satisfactory manner all the features of dynamic recovery. However, three of the principal types will now be examined in turn.

2.1.2.4 (a) The dislocation climb model (48,49)

The situation considered is that of dislocations emitted by a source, but subject to strong interactions with neighbouring pile-ups in adjacent slip planes. Further pile-ups are produced, and dislocation motion by glide becomes inhibited until the leading dislocations in the pile-ups begin to climb and be annihilated by dislocations of opposite sign on neighbouring planes. When a dislocation is annihilated, the corresponding source emits a new dislocation and the old configuration is re-established after a strain increment. The strain rate can be expressed as

$$\dot{\varepsilon} = b.A.N.\frac{\dot{c}}{h} \qquad (2.3)$$

where N is the density of dislocation sources, c the climb rate, h the distance between adjacent pile-up groups, A the area swept out on the slip plane by the leading dislocation and b the Burgers vector. The rate of climb is controlled by the rate at which vacancies can be supplied or removed. The climb rate obtained by Weertman is

$$\dot{c} = \frac{2D_s.\sigma^2.L.b^4}{\mu.k.T} \qquad (2.4)$$

where D_s is the self-diffusion coefficient, L is the length of the pile-up, and the other symbols have their usual meaning.

In order to obtain the strain rate $\dot{\varepsilon}$, h must be estimated from the stress $\sigma = \mu b/4\pi h$ required to force two parallel pile-ups to pass each other and L^2 is estimated to be proportional to σ. Under these conditions, Weertman arrived at:

$$\dot{\varepsilon} = \frac{BD_s\sigma^{4.5}}{b^{\frac{1}{2}}.N.^{\frac{1}{2}}\mu^{3.5}.k.T} \qquad (2.5)$$

The above stress exponent agrees reasonably well with empirical observations in pure metals and in some solid solutions. Some of the assumptions, however, render this equation less than appealing (1,5,50,51). $\hat{N}$ is not likely to be a constant but rather is expected to increase with stress. The stress dependence of L can be questioned as well, and a more refined analysis leads to stress exponent of 5, for example. Finally, the dislocation pile-ups which constitute the ground for the theory have never been observed. The activation energy predicted is that of self-diffusion, which agrees with those determined experimentally only in high temperature creep, and then not for the h.c.p. metals (52).

2.1.2.4 (b) Dislocation jog models (53-58)

When screw dislocations intersect each other, they become jogged with edge components which restrict their motion. If the jogs are to keep up with the dislocations, these must move in a non-conservative manner. They emit or absorb vacancies. A chemical force, due to the deviation of the vacancy concentration from equilibrium, is exerted on the dislocations at the jogs. Its value is given by:

$$f_e = \frac{kT}{b^2} \ln(c_e/c_o) \tag{2.6}$$

for vacancy emitting jogs; and

$$f_a = \frac{kT}{b^2} \ln(c_o/c_a) \tag{2.7}$$

for vacancy absorbing jogs. Here c_o is the equilibrium vacancy concentration in a dislocation-free crystal and c_e is the local vacancy concentration near the vacancy emitting jog. c_a is the counterpart of c_e for a vacancy absorbing jog and the other symbols have their usual meaning. Barrett and Nix (58) have related the excess vacancy concentration to the jog emission through the term:

$$c_e - c_o = \frac{V_e}{4\pi D_v b^2} \tag{2.8}$$

For vacancy absorbing jogs, the equivalent expression is:

$$c_a - c_o = \frac{V_a}{4\pi D_v b^2} \tag{2.9}$$

These equations imply that only bulk diffusion occurs.

By appropriate substitution of the above four equations, and considering that, in the steady state, $\sigma b\lambda = f_e$

$$V_e = 4\pi D_V b^2 c_o \left[\exp\left(\frac{\sigma b^2 \lambda}{kT}\right) - 1\right] \tag{2.10}$$

$$V_a = 4\pi D_V b^2 c_o \left[1 - \exp\left(\frac{\sigma b^2 \lambda}{kT}\right)\right] \tag{2.11}$$

where λ is the distance between the jogs, D_V is the vacancy diffusion coefficient and V_e and V_a the velocities of the emitting and absorbing jogs.

Relating now the velocities to the strain rate through the Orowan equation, and assuming equal densities of absorbing and emitting jogs, both contributing to the strain rate, Barrett and Nix obtained the relation

$$\dot{\varepsilon} = bD_V \rho_m \sinh\left(\frac{\sigma b^2 \lambda}{kT}\right) \tag{2.12}$$

where ρ_m is the mobile dislocation density and b is a constant.

The stress dependences of ρ_m and λ are unfortunately unknown. Assuming they are not stress dependent, which limits the generality of the equation, it fits the type of creep data generally obtained reasonably well. A similar strain rate expression is obtained when rapid dislocation core diffusion is taken into account. Recently, more rigorous treatments have been proposed (59-61), which lead to an expression of the type

$$\dot{\varepsilon} \alpha \rho_m \tanh(\lambda b^2 \sigma / kT) \tag{2.13}$$

In these models, the stress dependence of the mobile dislocation density is still not spelled out, and it is apparent that the tanh law is not in agreement with experimental observations at high stresses.

2.1.2.4 (c) Recovery creep models (3,14,62-65)

These models are based on the knowledge that materials harden with strain and soften with time. High temperature creep is considered as resulting from the simultaneous operation of these two mechanisms. The strain hardening and the rate of recovery are defined as

$$h = \left(\frac{\partial\sigma}{\partial\varepsilon}\right) \quad , \quad r = -\left(\frac{\partial\sigma}{\partial t}\right) \tag{2.14}$$

respectively. Under steady state deformation conditions the strain rate can be written as:

$$\dot{\varepsilon}_s = \left(-\frac{\partial\sigma}{\partial t}\right)/\left(\frac{\partial\sigma}{\partial\varepsilon}\right) = r/h \tag{2.15}$$

In stage I creep, the dislocation density increases with strain, and hence so does the rate of recovery, until a balance is achieved between work-hardening and recovery. McLean (3) expressed the process by the Arrhenius equation

$$\dot{\varepsilon} = \dot{\varepsilon}_o \exp\left[-\frac{bA(h\varepsilon - rt)}{kT}\right] \tag{2.16}$$

where $\dot{\varepsilon}_o$ is a pre-exponential factor similar to that in the expression for thermally activated deformation and A an activation area. This equation describes satisfactorily the primary and secondary creep stages.

Lagneborg (65), however, pointed out that this model was over-simplified in that it treated h and r as constants. He proposed a model taking into account the fact that r increases as the dislocation density increases with strain, and that the rate of work-hardening tends to decrease with strain. In accord with direct observations, he also considered the r and h parameters to vary with the geometry of the three dimensional dislocation network. During creep, the distribution of link sizes varies as a result of three processes. The first one is the release of dislocation links by thermally activated node unpinning. The second process is work-hardening, which arises as new dislocation links are supplied by the expansion of the released links until their arrest against the network. The last event is recovery, which is postulated to occur by the climb-controlled shrinkage of small meshes in the network and the accompanying growth of the large ones, in analogy with grain growth. This model was found to be capable of simulating the strain-time as well as the dislocation density-time behaviour (66).

2.1.3 Dynamic Recrystallization

2.1.3.1 Microstructural changes during dynamic recrystallization

In metals that are prone to recrystallize dynamically, the early stages of deformation are accompanied by the formation of a cellular dislocation substructure. In these materials, the cell sizes tend to be smaller and the boundaries more tangled than those formed in materials that only dynamically recover during the deformation. Beyond a critical strain, dynamic recrystallization starts to occur. In this process, nuclei form and new grains begin to grow. The driving force for the growth of new grains is the strain energy difference between the heavily deformed region outside the nuclei and the essentially dislocation free regions

within them. The new grains grow fast, consuming the severely strained old grains.

If the rate of straining is low, the new grains can grow to their full extent without being themselves appreciably strained. The driving force does not decrease significantly as the deformation is pursued at a low strain rate and thus permits the rate of migration to remain nearly constant until recrystallization is completed. The flow stress drops during the process from that of a heavily strained material to that of a statically recrystallized or annealed metal. As straining continues, the dislocation density builds up again, until nucleation again comes into play, leading to a repetition of the cycle. Under such conditions, the flow stress keeps oscillating with strain.

At high strain rates, the situation is quite different. The cellular structure evolved in the early strain history is more dense and the sub-boundaries pin the grain boundaries more effectively, so they cannot supply new grains through the boundary bulging mechanism. Nucleation is now originated throughout the deformed grains and recrystallized grains begin to grow. The centers of the new grains, however, become strained as deformation continues. As the new grains start to experience dislocation build-up, the driving force decreases, and causes a concurrent decrease of the rate of migration of the boundary. The recrystallized grains can accumulate enough strain to begin to recrystallize again even though the first recrystallization cycle is incomplete.

The material thus exhibits a distribution of regions with different degrees of deformation, but none exceeding the peak strain. The peak stress arises because the material, in the first recrystallization cycle, is strained as far as it can be without recrystallization. Further

straining causes a stress drop as the new grains grow. The steady state stress reached is characteristic of a dynamic average of all the strain conditions in the material, and lies between the yield stress of statically recrystallized material and the peak stress (22,67,68,70).

2.1.3.2 Critical strains for the nucleation and completion of recrystallization

The critical strain for dynamic recrystallization ε_c is somewhat less than the peak strain ε_p at which dynamic recrystallization already balances work-hardening (22). The relation between ε_c and ε_p has been approximated by (69):

$$\varepsilon_c = \frac{5}{6}\varepsilon_p \qquad (2.17)$$

Recrystallization kinetics follow a sigmoidal curve on a plot of volume recrystallized versus log time. At constant strain rate, a plot of volume recrystallized versus log strain has a similar shape. As the strain for complete recrystallization is hard to define, since the fraction recrystallized does not reach 100% in a finite time, for practical purposes ε_r is taken as the strain for 95% recrystallization.

The strains ε_c and ε_r decrease with increasing temperature, and this has been attributed to the increase in the rate of recovery, and therefore of nucleation at higher temperatures. The increase in ε_c and ε_r with strain rate has the same origin. The effect of the two variables on ε_c and ε_r can be expressed as (6)

$$\varepsilon_c = K_1 Z \qquad (2.18)$$

$$\varepsilon_r = K_2 Z \tag{2.19}$$

where Z is the Zener-Hollomon parameter.

The strain for the completion of recrystallization ε_r is affected by strain rate not only through the nucleation rate, but also through the decrease in driving force and consequently through the rate of grain boundary migration with increasing strain rate. The result is that ε_r is far more sensitive to strain rate than ε_c.

2.1.3.3 Grain and subgrain size in dynamic recrystallization

The grain size d_g during steady-state deformation remains constant with strain, and has been correlated with the steady state stress through the relation:

$$\sigma_s = K_3 d_g^{-M} \tag{2.20}$$

where K_3 is a constant and M varies between 0.75 and 1.0. This relation, however, does not signify that the steady state stress level is determined by the grain size. In reality the situation is more complex, and we can expect three factors to act on σ_s. These are the subgrain size in the recrystallized grains, the dislocation density within the subgrains and finally the grain size. The subgrains add a component to the flow stress σ_{sg} of the type:

$$\sigma_{sg} = K_4 \bar{d}_{sg}^{-1} \tag{2.21}$$

where d_{sg} is the average subgrain size and K_4 a constant. This relation is the same as the one relating subgrain size and flow stress in dynamically recovered metals.

A second component σ_{ds} comes from the dislocation density within subgrains ρ_{sg}, in the form:

$$\sigma_{ds} = \alpha \mu b \rho_{sg}^{1/2} \tag{2.22}$$

where α is a constant, μ the shear modulus and b the Burgers vector.

The distinction between these two components has been discussed by McQueen and Jonas (6). It is useful from a conceptual point of view but one could argue that it is an arbitrary one since the dislocation density within subgrains is not independent of the subgrain size, so that the term $K_4 d_{sg}^{-1}$ already contains the dislocation density term. The two views may be reconciled, however, if we consider that $\rho_{sg}^{1/2}$ is proportional to d_{sg}^{-1}, so that the terms σ_g and σ_{ds} can be combined to give:

$$\sigma_{sg} + \sigma_{ds} = K_4 d_{sg}^{-1} + \alpha \mu b \rho_s^{1/2} \tag{2.23}$$

$$= K_5 d_{sg}^{-1} \tag{2.24}$$

A further term arises from the contribution of the grain boundaries. The limited evidence for this component is that a Hall-Petch relation appears to apply, thus:

$$\sigma_{gb} = K_6 d_g^{-1/2} \tag{2.25}$$

where σ_{gb} is the flow stress component arising from grain boundaries, d_g is the grain size and K_6 a constant. As a result, the steady state flow stress during dynamic recrystallization will have two structural components and can be written, if we call σ^* the effective stress:

$$\sigma_s = \sigma^* + K_5 d_{sg}^{-1} + K_6 d_g^{-1/2} \qquad (2.26)$$

The nuclei density will be inversely proportional to the subgrain size and, in turn, the larger the nucleus density, the smaller the grain size. The outcome of this sequence is that the recrystallized grain size is proportional to the subgrain size. Equation 2.26 can thus be rewritten:

$$\sigma_s = \sigma^* + K_5 d_g^{-1} + K_6 d_g^{-1/2} \qquad (2.27)$$

It appears that the Hall-Petch contribution is smaller than the subgrain contribution, as the variation of σ_s with d_g follows the experimentally determined relation given in Equation 2.24; that is, the term d_{sg} in Equation 2.26 seems to predominate over the d_g term.

2.1.3.4 Effect of alloying

Alloying affects dynamic recrystallization in two opposite ways. On the one hand it greatly reduces the rate of recovery (see preceding section), which promotes an increase in the driving force for dynamic recrystallization. On the other hand, it reduces the rate of migration of grain boundaries, and as a consequence slows down the kinetics of recrystallization. In OFHC copper tested at 500°C, the steady state flow

stress is achieved after a strain of about 0.14, whereas it can take a strain of over 0.5 to reach the same condition in tough pitch copper under the same testing conditions (70). In Cu-9.5%Ni, the nickel addition considerably decreases the rate of recovery and, at a strain of 0.7, the peak in stress has not yet been reached, let alone the strain for the onset of steady state flow (6). Similar trends have been reported in brass (71), monel (72), Ni-base superalloys (73) and austenite (74).

2.1.4 Empirical Flow Stress Relationships

The main parameters that affect high temperature deformation are the temperature, stress and strain rate. Strain has an effect only as long as steady state flow has not been achieved. The structure obviously has some influence on the stress but it is difficult to define it. Grain size will add one component, stacking fault energy another, but the largest contributions can be expected from the sub-boundary density and dislocation density as discussed above. It is usually assumed that the structure factor remains constant as long as the flow stress is constant, independently of strain rate and temperature, although this may not be exactly valid. More rigorously, the structure factor can be expected to depend on σ/E or τ/μ rather than on σ alone.

2.1.4.1 Stress dependence of the strain rate (1)

At very low stresses (very high temperature creep), it is found that the strain rate is proportional to the flow stress :

$$\dot{\varepsilon} = \alpha_1 \sigma \qquad (2.28)$$

At intermediate stresses (creep, moderate strain rates), the relation:

$$\dot{\varepsilon} = \alpha_2 \sigma^n \tag{2.29}$$

is found to apply. At still higher stresses, the best fit of the stress strain rate relation appears to be of the type :

$$\dot{\varepsilon} = \alpha_3 \exp(\beta\sigma) \tag{2.30}$$

It has also been proposed that the latter two relations are contained in the simple equation :

$$\dot{\varepsilon} = \alpha_4 \left[\sinh(\alpha\sigma)\right]^n \tag{2.31}$$

We shall restrict our considerations to the most usual equation found in practice, which is Equation 2.29. The value of n, determined from $n = (\partial \log\dot{\varepsilon}/\partial \log\sigma)_T$ is typically between 4 and 5 for pure metals and solid solutions. The stress exponent is in the range 5-10 for precipitation hardened alloys and is even higher for dispersion hardened materials, where values up to 40 have been observed (75-78).

2.1.4.2 Temperature dependence of the strain rate

High temperature deformation is thermally activated and can therefore be represented by an equation of the type:

$$\dot{\varepsilon} = A(\sigma)\exp(-\frac{Q}{RT}) \tag{2.32}$$

The value of Q is found to vary with temperature (and therefore with stress) in creep. It appears to pass through some plateaus, and above 0.5 T_m reaches a temperature independent value about equal to the activation energy for self-diffusion in some metals (2). In the hexagonal metals, the activation energies are generally higher (4,52) than the self-diffusion values. Under hot working conditions, Q appears stress dependent, indicating that the self-diffusion activation energy probably represents a limiting case. Moreover, Q increases with alloying content, a result which cannot easily be explained by variations in the self-diffusion coefficient.

2.1.5 The Application of Reaction Rate Theory to High Temperature Flow

The empirical relations, unfortunately, cannot be used directly to obtain an understanding of the rate controlling mechanisms of plastic flow. The dynamic recovery models, on the other hand, are very specific and their derivation requires assumptions which probably oversimplify the relations between the various mechanisms involved in the deformation. Thermal activation analysis avoids these difficulties because it is based on a rate equation in which dislocations overcome unspecified obstacles; according to this method, there is no a priori knowledge of the obstacle geometry. The utility of the approach, which is very widely used, is to yield information about the properties of the rate-controlling obstacles (i.e. their density and shape) through the activation parameters and thereby to enable the researcher to get closer to their identification.

A brief description of the main features of the theory will be given, and for a more complete treatment the reader is referred to Evans and Rawlings (79), Li (80), Gibbs (81), Surek et al (82-84) and Kocks et al (85).

2.1.5.1 Thermodynamics of dislocation-obstacle interactions

The analysis considers a glide dislocation which is resting against a localized obstacle. The obstacle is characterized by its free energy profile, an example of which is shown in Figure 2.2.a. In the absence of applied stress, the change in free energy of the system when the dislocation moves from its rest position to the saddle point is ΔG_o, which is equal to ΔF, the Helmoltz free energy change, since no mechanical work is done during the process. For this reason the curve is labelled F.

The free energy change that takes place during the dislocation movement generates a local back stress τ_b where :

$$\tau_b = \frac{1}{b}\left(\frac{\partial F}{\partial A}\right)_{T,l} \qquad (2.33)$$

and b is the Burgers vector, $A = lx$ the area swept by the dislocation, l being the length of the free dislocation between obstacle pinning points and x the displacement coordinate along the glide direction. The back stress corresponding to the free energy curve of Figure 2.2.a is shown in Figure 2.2.b.

When a stress is applied to the dislocation, it moves against the obstacle until the effective stress τ^* † is balanced by the back stress τ_b due to the obstacle, the new rest position being characterized by the displacement coordinate x_1^* or better A_1^*. The dislocation cannot move any further under this stress until it reaches the position A_2^* where

† The local effective stress τ^* is related to the applied stress τ_a and the local value of the internal stress τ_i through $\tau^* = \tau_a - \tau_i$.

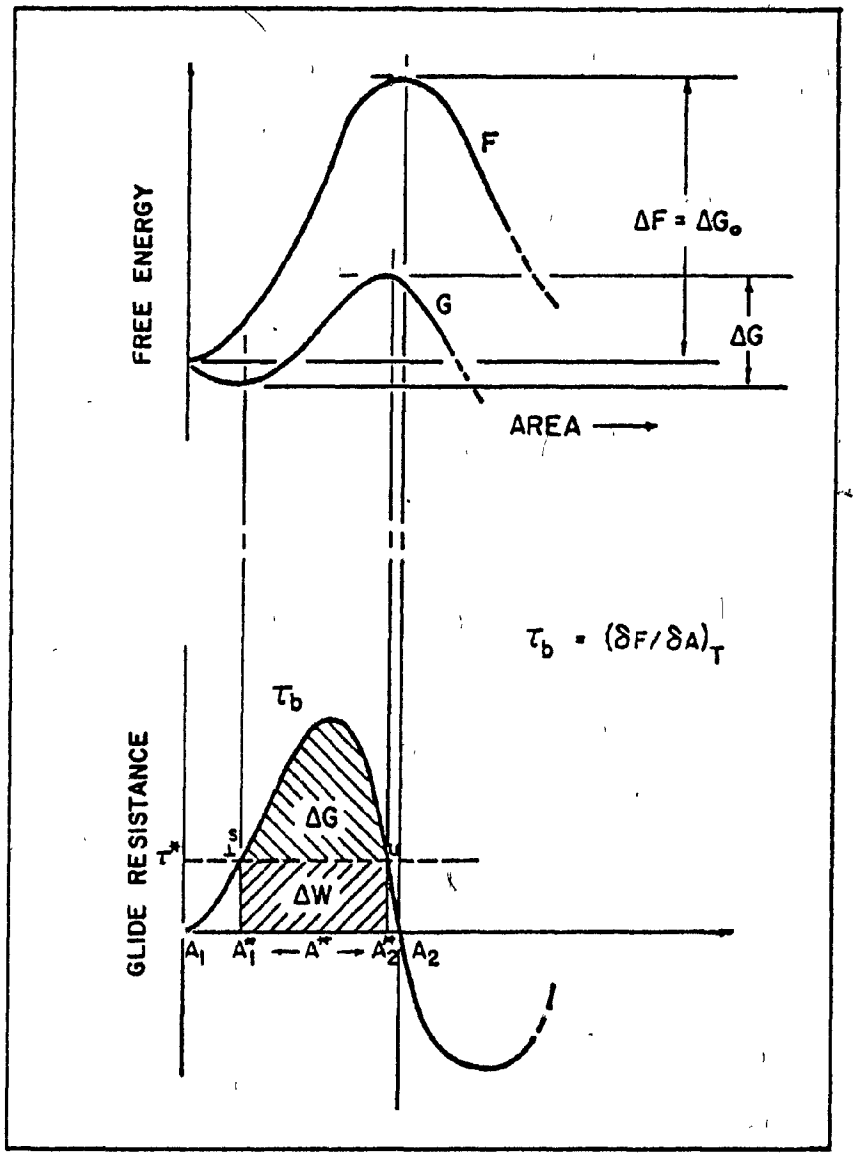

FIGURE 2.2 Schematic representation of the obstacle-dislocation interaction:
a. Helmholtz free energy (F) and Gibbs free energy (G) barriers as a junction of the area swept by the dislocation
b. back stress profile felt by the dislocation in the vicinity of the obstacle as a function of slipped area.

glide would again be possible. During the activation event, thermal fluctuations supply the free energy necessary to move the dislocation from A_1^* to A_2^*, The Helmoltz free energy change during activation is therefore:

$$\Delta F_i(T,\tau^*) = b\int_{A_1^*(T,\tau^*)}^{A_2^*(T,\tau^*)} \tau_b(A,T)dA \tag{2.34}$$

The work done by the effective stress during the same event is given by:

$$\Delta W = bA^*(T,\tau^*)\tau^* \tag{2.35}$$

so that the change in Gibbs free energy during the process becomes:

$$\Delta G_i(T,\tau^*) = \Delta F_i(T,\tau^*) - \Delta W \tag{2.36}$$

$$= b\int_{A_1^*(T,\tau^*)}^{A_2^*(T,\tau^*)} \tau_b(A,T)dA - bA^*(T,\tau^*)\tau^* \tag{2.37}$$

and is shown in Figure 2.2.a. In this equation, both ΔF_i and A^* are functions of τ^*, which presents a serious difficulty.

Another approach was taken by Li (80) and gives:

$$\Delta G_i = \Delta F(T) - b\bar{A}\tau^* \tag{2.38}$$

where ΔF is the previously defined Helmoltz free energy in the absence of stress, or

$$\Delta F(T) = b \int_{A_1}^{A_2} \tau_b(T,A)dA \qquad (2.39)$$

and $\overline{A}$, the average activation area is defined as:

$$\overline{A} = \frac{1}{\tau^*} \int_0^{\tau^*} A^* \, d\tau^* \qquad (2.40)$$

The significance of these various quantities can be seen easily on Figure 2.2.b.

2.1.5.2 Derivation of the rate equation

Having now described the obstacle-dislocation interaction, it is possible now to derive the rate equation. The probability p that the dislocation arrested at its stable position A^*_1, will move to A^*_2 is proportional to the attempt frequency ν and to the probability of success given by the Boltzmann term $\exp(-\Delta G(T,\tau^*)/kT)$. Thus:

$$p = \nu \exp(-\Delta G(T,\tau^*)/kT) \qquad (2.41)$$

The value of the attempt frequency is limited by two extreme frequencies: the atomic frequency of vibration of an atom in the lattice, i.e. the Debye frequency ν_D and the ground state dislocation vibration frequency $\nu_o = \nu_D \frac{b}{4l}$, l being the length of the dislocation segment. Kocks et al (86) have discussed the question of which attempt frequency should be used and concluded that the best value was about $\nu_D/100$ or $\nu \simeq 10^{11} s^{-1}$. If the distance over which the dislocation moves after a successful activation event is L, then the average dislocation velocity can be written

$$\bar{V} = V_o \exp(-\Delta G/kT) \tag{2.42}$$

where $V_o = \nu \cdot b\ L$. The macroscopic strain rate $\dot{\varepsilon}$ may then be obtained through the Orowan relation:

$$\dot{\varepsilon} = \alpha b \rho_m \bar{V} \tag{2.43}$$

where α is a constant and ρ_m the mobile dislocation density. Finally,

$$\dot{\varepsilon} = \dot{\varepsilon}_o(T,\tau^*) \exp(-\Delta G(T,\tau^*)/kT) \tag{2.44}$$

where $\dot{\varepsilon}_o = \alpha \rho_m b L \nu$. From Equation 2.44 it can be seen that the pre-exponential factor $\dot{\varepsilon}_o$ is a function of stress and temperature through the dependence of the mobile dislocation density on these variables, as well as through the dependence of the mean distance travelled after a successful activation on the stress and structure.

2.1.5.3 Determination of the activation parameters

Once $\dot{\varepsilon}$, τ_a and T have been determined by mechanical tests, the activation parameters can be calculated using the method described below.

Activation free energy

The activation free energy, ΔG, obtained by rewriting Equation 2.44 as follows:

$$\Delta G(T,\tau^*) = -kT \ln(\dot{\varepsilon}(T,\tau^*)/\dot{\varepsilon}_o(T,\tau^*)) \tag{2.45}$$

The use of this equation requires knowledge of the stress and temperature dependence of $\dot{\varepsilon}_o$, which will be discussed below.

Activation enthalpy

The activation enthalpy $\Delta H(T, \tau^*)$ is given by the thermodynamic relation:

$$\Delta H_{\tau^*} = \partial(\Delta G/T)/\partial(1/T)_{\tau^*} \tag{2.46}$$

From Equation 2.45 it is equivalent to:

$$\Delta H_{\tau^*} = -k\left(\frac{\partial \ln \dot{\varepsilon}}{\partial\, 1/T}\right)_{\tau^*} + k\left(\frac{\partial \ln \dot{\varepsilon}_o}{\partial\, 1/T}\right)_{\tau^*} \tag{2.47}$$

Activation area

It can be seen that, by combining Equations 2.38 and 2.40, the activation area A* may be obtained from:

$$A^* = -\frac{1}{b}(\partial \Delta G/\partial \tau^*)_T \tag{2.48}$$

which, using Equation 2.45, becomes

$$A^* = \frac{kT}{b}\left(\frac{\partial \ln \dot{\varepsilon}}{\partial \tau^*}\right)_T - \frac{kT}{b}\left(\frac{\partial \ln \dot{\varepsilon}_o}{\partial \tau^*}\right)_T \tag{2.49}$$

Activation entropy

The activation entropy at constant stress is given by

$$\Delta S_{\tau^*} = -(\partial \Delta G/\partial T)_{\tau^*} \tag{2.50}$$

which becomes, using Equation 2.45 again,

$$\Delta S_{\tau^*} = -k \ln\dot{\varepsilon}/\dot{\varepsilon}_o + kT\left(\frac{\partial \ln\dot{\varepsilon}}{\partial T}\right)_{\tau^*} - kT\left(\frac{\partial \ln\dot{\varepsilon}_o}{\partial T}\right)_{\tau^*} \qquad (2.51)$$

In this equation, not only the temperature and strain rate dependence of $\ln \dot{\varepsilon}_o$ is required but its magnitude as well, which renders the determination of the activation entropy more difficult than that of the other parameters.

Stress and temperature dependence of the pre-exponential

The determination of the activation parameters cannot be achieved without some further assumption regarding the stress and temperature dependence of the pre-exponential since the latter appears in all the equations giving the activation parameters. Two approaches have been taken:

i. The pre-exponential $\dot{\varepsilon}_o$ is assumed to be constant with stress (87,88). The above equations are then very simple as the $\partial \ln \dot{\varepsilon}_o$ term drops out. In this case

$$\Delta H_{\tau^*} = kT^2\left(\frac{\partial \ln \dot{\varepsilon}}{\partial T}\right)_{\tau^*} = \Delta H_{exp} \qquad (2.52)$$

$$A^* = \frac{kT}{b}\left(\frac{\partial \ln \dot{\varepsilon}}{\partial T}\right)_{\tau^*} = A^*_{exp} \qquad (2.53)$$

$$\Delta S_{\tau^*} = \Delta H_{\tau^*}/T + k \ln(\dot{\varepsilon}/\dot{\varepsilon}_o) \qquad (2.54)$$

The subscript exp refers to a quantity that can be measured directly from experimental quantities. Similarly,

$$\Delta G = -kT \ln(\dot{\varepsilon}/\dot{\varepsilon}_o) \qquad (2.55)$$

Calculation of the activation entropy and energy still require knowledge of the magnitude of $\dot{\varepsilon}_o$, and in the absence of this knowledge it has often been assumed that ΔS_{τ^*} is equal to zero.

These assumptions, however, oversimplify the situation and for this reason a second approach has been suggested.

ii. The other alternative, proposed by Surek et al (82-84) is to assume that the obstacles are not only rigid (i.e. ΔF is independant of τ^*) but that their free energy varies with temperature according to

$$\Delta F(A,T) = g(A) \ldots \mu(T) \qquad (2.56)$$

Here g is a shape function and μ is the shear modulus. In this case, the obstacles are elastic in nature, a hypothesis which appears to be physically more realistic.

Under these assumptions, they showed that $\dot{\varepsilon}_o$ could be determined through an iterative procedure. An important special case is when $\dot{\varepsilon}_o$ is a function of the modulus reduced stress τ^*/μ only, e.g. $\ln \dot{\varepsilon}_o = f(\tau^*/\mu)$. In this case the activation parameters are given by

$$\Delta H_{\tau^*} = \Delta H^{\tau^*}_{exp} - k\tau^* \cdot \frac{T^2}{\mu^2} \cdot \frac{d\mu}{dT} \cdot \frac{df}{d(\tau^*/\mu)} \qquad (2.57)$$

$$= \Delta H^{\tau^*}_{exp} \quad \text{when} \quad df/d(\tau^*/\mu) = 0 \qquad (2.58)$$

$$A^* = A^*_{exp} + \frac{kT}{b\mu} \cdot \frac{df}{d(\tau^*/\mu)} \qquad (2.59)$$

$$= A^*_{exp} \quad \text{when} \quad df/d(\tau^*/\mu) = 0 \qquad (2.60)$$

$$\Delta G_i = \frac{\Delta H^{\tau^*}_{exp} + bA^*_{exp} \cdot \tau^* \cdot \frac{T}{\mu} \cdot \frac{d\mu}{dT}}{1 - \frac{T}{\mu} \cdot \frac{d\mu}{dT}} \qquad (2.61)$$

where $\Delta H^{\tau^*}_{exp}$ and A^*_{exp} are the quantities of Equations 2.52 and 2.53. ΔG_i can thus be determined from experimental quantities alone, and the function f can subsequently be obtained graphically or numerically through Equation 2.54. This approach has been successfully applied to α-zirconium (84), zinc (84), polycrystalline ice (84) and is more physically realistic and self-consistent than previous analyses.

By these methods, both $\dot{\varepsilon}_o(T,\tau^*)$ and $\Delta G_o = \Delta F$ can be calculated. The dependence of $\dot{\varepsilon}_o$ on stress and temperature, as well as on strain and solute concentration, for example, leads to information about the obstacle density and to its response to deformation and to alloying. Similarly, the value of $\Delta G_o = \Delta F$, as well as the detailed form of the force-distance curve, can be interpreted in terms of the geometry of the obstacles. This can also be dependent on solute concentration and on other experimental parameters.

In Zr-Sn alloys, as well as in Cu (89) and Fe (47), this method has led to the conclusion that the rate-controlling mechanism was the unzipping of dislocation nodes or attractive junctions. The effect of solute addition on the node free energy was also determined (44).

2.2 FLOW SOFTENING MECHANISMS

A gradual decrease in flow stress with strain at elevated temperatures is not an unknown phenomenon. There are several mechanisms which are capable of causing such a softening effect. They can be classified in two categories, the first one involving only dislocation interactions, whereas in the second, a second phase is present. In the latter case, an interaction between the dislocations and one of the phases is usually responsible for the softening behaviour. Flow softening can also take place in potentially superplastic materials, during the transition to superplastic behaviour. In this case, the microstructure can either be single or two-phase.

2.2.1 Mechanisms Involving Dislocations Only

2.2.1.1 Dynamic recrystallization

A description of dynamic recrystallization has been given earlier in this chapter. Flow softening due to dynamic recrystallization arises from a sharp dislocation density decrease as the new recrystallized grains proceed to grow at the expense of the severely strained grains. The nucleation of these new grains requires the accumulation of a critical strain ε_c, which increases with strain rate and decreases with temperature. In turn, the temperature and strain rate dependence of ε_c cause a similar variation of the peak strain ε_p, since these two strains have been observed to be related through Equation 2.17. In solid solutions, ε_c, and thereby ε_p increase with solute content, because the increase in the driving force for recrystallization caused by the enhancement of the dislocation density due to alloy addition is more than compensated by a decrease in the rate of grain boundary migration. Microstructural observations of deformed

samples show in this case a roughly equiaxed structure, the grain size bearing no relation to the original one. As has been discussed earlier, the grain size obtained as a result of dynamic recrystallization is inversely related to the flow stress.

2.2.1.2 Substructure softening

The mean subgrain size during steady state flow is a unique function of the deformation temperature and strain rate. The subgrain size can also be correlated with the steady state flow stress. However, sudden decrease in the strain rate or an increase in temperature will lead to a sudden change in σ, as well as to a dispersion of the original substructure in order to allow the formation of a coarser one corresponding to the new testing conditions. On the sudden change in strain rate or temperature, the effective stress σ^* is changed immediately; the internal stress σ_i can only change, however, when the substructure geometry is changed. The adjustment of the substructure, and of the internal stress contribution resulting from it is not instantaneous. Immarigeon (15) has shown that, in Armco iron, a strain of 0.2 was required to transform the substructure from one steady state to another when the strain rate was decreased from $10^{-1}s^{-1}$ to $10^{-3}s^{-1}$. The corresponding behaviour of the flow stress is shown in Figure 2.3. The deformation of a material in which a strong substructure is present as a result of prior hot-working will lead to flow softening until the stable, coarser, substructure is established.

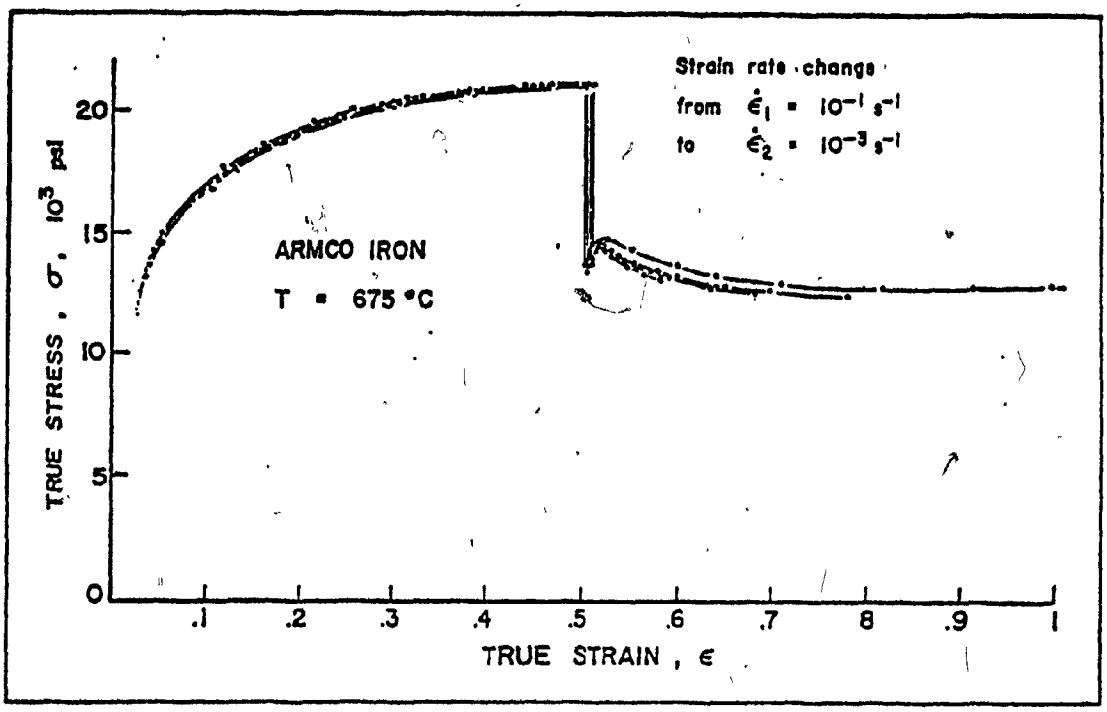

FIGURE 2.3 Flow softening in Armco iron, resulting from substructure coarsening, caused by a sudden strain rate decrease from 10^{-1} to $10^{-3}s^{-1}$, after Immarigeon (15).

2.2.1.3 Texture softening

In polycrystalline materials having a strong preferred orientation, it may happen that the texture is such that all the slip systems have a very low Schmidt factor and are therefore difficult to put into operation. This requires the application of a high uniaxial stress in the early stages of deformation in order to balance the unfavourable slip conditions. As deformation proceeds, the grains rotate with respect to the load axis, and evolve into a new texture that has a higher Schmidt factor for its slip systems. This will result in a softening effect, which will be more or less pronounced depending upon the extent and type of the initial and final textures and, above all, upon the anisotropy of the metal. Face-centered cubic metals, which have 12 close-packed slip systems are the least likely to show any marked effect. Hexagonal metals, on the other hand, have only three close-packed slip systems. For example, zinc and cadmium deform easily by basal glide, while prismatic slip for these metals is very difficult. Thus these metals are very prone to texture effects. Although α-zirconium and α-titanium deform primarily by prismatic slip, and even though pyramidal slip can also be activated under higher stresses, their strength is also very dependent upon the texture.

In Ti-6Al-4V, Lowden and Hutchison (90) have related yield stresses to the rolling texture of the alloy. A very large basal pole density in the transverse direction was found to give tensile yield stress values of 1400 MN/m^2 in the transverse direction and only 800 MN/m^2 in the rolling direction. Under similar conditions, compressive yield stress values went from 1050 MN/m^2 to 780 MN/m^2 respectively. The large difference in stress values between tension and compression was attributed to the asymmetric glide of partial dislocations, but in any event the stress differential between the transverse and rolling directions was large.

In zirconium 5% tin tested in compression at 775°C Luton (4) observed two types of stress-strain curves. A "normal" one characteristic of dynamic recovery alone was observed on samples having equiaxed grains and a $(\bar{1}010)$ pole texture. A dropping flow curve appeared on samples which had a large (0001) pole density along the compression axis, and showed a Widmanstatten type of structure. This has been interpreted as being due to texture softening (91).

2.2.1.4 Adiabatic softening

During deformation, if the strain rate is high, the sample will not remain at constant temperature but will heat up adiabatically, causing the substructure to coarsen and the flow stress to decrease in a process similar to that of substructure softening. The strain rates required to produce this effect are above 1/sec., and high strains favour it as well. The low work hardening rates at high strain rates observed on aluminum by Hockett (92) have been attributed to this effect.

2.2.2 Mechanisms Involving a Second Phase

2.2.2.1 Spheroidization of lamellar structures

The deformation of pearlite at high temperatures considerably accelerates the rate of spheroidization. Spheroidization, in turn, has been found to be associated with very marked strain softening. The rate of softening with strain increases with temperature and decreases with strain rate (93-95).

2.2.2.2 Spheroidization of Widmanstatten structures

The deformation of a 'hard' Widmanstatten structure into a more equiaxed structure leads to softening in zirconium - 2.5% niobium (96), and has also been observed in the deformation of zircaloy (97) and of Ti-6Al-4V in the $\alpha + \beta$ phase field (97).

At constant temperature, the strain necessary to achieve a state of dynamic equilibrium during flow at constant strain rate increases with strain rate and with the size of the Widmanstatten α-plates. At high strain rates, the transformation of the initial structure into roughly equiaxed α and β phase particles does not occur even after strains of about 1; however, some flow softening is present. In this case it seems that the re-orientation of the Widmanstatten α-plates during deformation is responsible for the decrease in flow stress with strain.

The mechanism whereby the Widmanstatten structure evolves into an equiaxed one during deformation is not very well known. Diffusion is clearly involved in the process but the mechanisms have not yet been clearly defined. The drastic enhancement of spheroidization by concurrent deformation suggests that short circuit diffusion paths, such as dislocation pipe diffusion, or vacancy-assisted diffusion are likely to play an important role. Results on $\alpha + \beta$ brass (98) have led to the hypothesis that during deformation break-up of the second phase plates could occur by the diffusion of solute along the subgrain walls. This, in turn, would cause the subgrain boundaries to progressively become grain boundaries. From this model, it can be predicted that the size of the second phase spheroidized grains will depend on the size of the subgrains formed during the early stages of deformation. However, a relationship between the subgrain size within the plates and the subsequent equiaxed particle size has not yet been established.

2.2.2.3 Softening by Ostwald ripening

In the alloys in which precipitation takes place, the flow stress increases with time as the volume fraction of the fine precipitates increases and the matrix becomes depleted in supersaturated solute. The amount of strengthening caused by precipitation depends not only on the volume fraction, but also on the size and to a lesser extent on the shape of the precipitates. When the volume fraction of the precipitates approaches the equilibrium value, the precipitation rate decreases towards zero. The alloy, however, is not in its lowest free energy state due to the appreciable surface free energy contribution from the finely divided precipitate. This term can be reduced if the largest precipitates grow at the expense of the smallest ones. This process, called Ostwald ripening (99), is controlled by solute diffusion.

The formal theory of the process has been given by Wagner (100) and Lifschitz and Slezov (101). Their treatment assumes a constant volume of precipitate phase, and supposes that the particles are normally distributed around a mean value $\bar{r}(t)$ which varies with time. The particle radius distribution function is shown to take the asymmetric shape shown in Figure 2.4 and to remain constant thereafter. The variation of the average radius with time was demonstrated to follow the relation

$$\bar{r}^3 - \bar{r}_o^3 = kt \qquad (2.62)$$

where $\bar{r}$ is the average radius at the time t, $\bar{r}_o$ the average radius at $t = 0$ and k is a constant. Agreement with experiment was found to be satisfactory in the Ni-Al (102,103), Ni-Si, and Fe-Cu (104) systems, as well as in the $\gamma'(Ni_3(Al,Ti,Si))/\gamma$ superalloy system (105). It must be

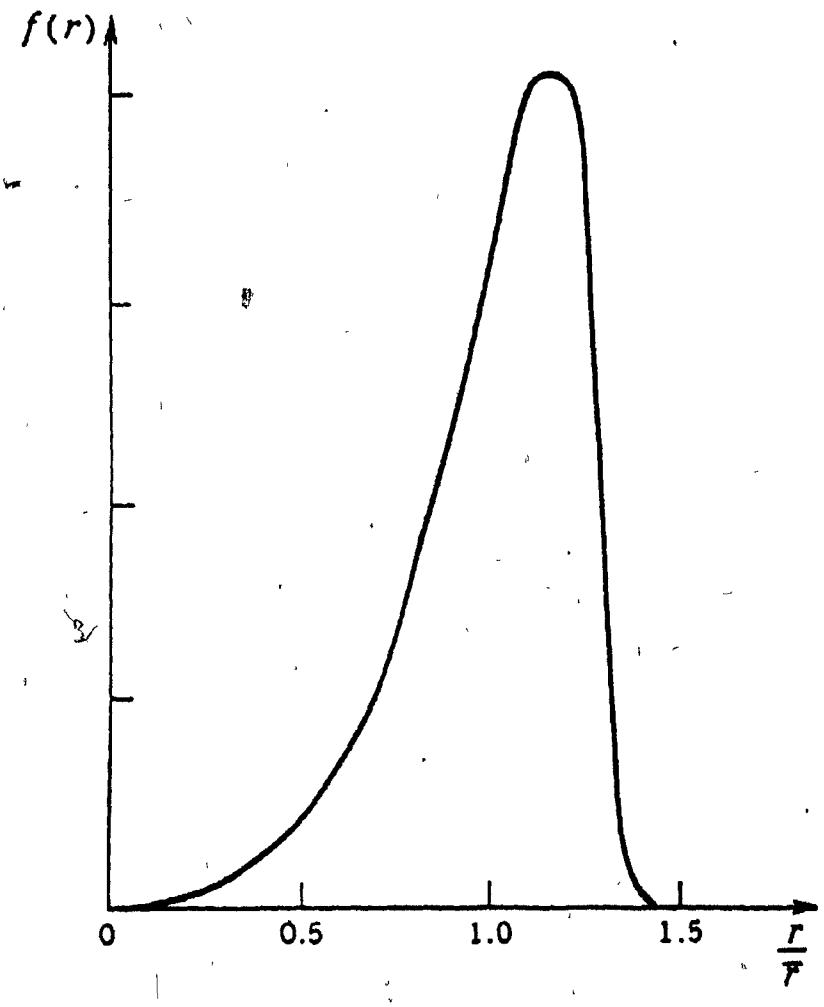

FIGURE 2.4 Particle size distribution during Ostwald ripening of precipitates. $\bar{r}$ is the average radius of the precipitates at time t.

pointed out that this theory neglects the strain energy due to volume changes during precipitate growth, as well as the distortion components arising in the case of coherency between the precipitate and the matrix.

When an alloy is deformed in a situation where Ostwald ripening takes place, the particle coarsening process becomes accelerated by vacancies and dislocation pipe diffusion. The kinetics of the process can be increased by several orders of magnitude by the deformation. As a result, the role of precipitates as obstacles to dislocation movement decreases with strain, thus leading to pronounced softening. Such an effect has been observed in steels (106), in tough pitch copper (107) and in Al-Mg-Pb alloys (108).

From the standpoint of characterizing the features of the stress-strain curves obtained under such conditions, one can expect for this process a larger stress exponent for the flow stress at yield than that obtained from steady state deformation, where precipitates do not contribute significantly to the flow stress (109-113).

2.2.3 Superplastic Materials

The deformation of superplastic materials may be characterized by very large elongations which take place without an appreciable tendency to neck. This type of deformation is encountered either under special conditions (such as thermal cycling through a temperature range in which the material undergoes a phase change) or, as is usually the case, in very fine grained (1-10 μm) metals and alloys. Many materials have been found to be superplastic and good reviews of the compositions and properties have been given by Underwood (114) and by Johnson (115).

Microstructural observations on superplastic metals and alloys have revealed that the grains remain essentially equiaxed during the deformation, and do not exhibit any grain growth. Stable grains of a very small diameter are more easily obtained in two-phase alloys than in pure metals. The former require extensive solute diffusion for structural coarsening to take place whereas the latter only require grain growth. For this reason, and because grain boundary sliding occurs more readily at the interface between two phases, two-phase alloys constitute a very large portion of the known superplastic materials (115). During straining the grains undergo large rotations and deformations, these having been evidenced by the curvature of previously inscribed straight lines during straining.

The mechanical behaviour of superplastic materials may be characterized by a stress exponent of about 2, which is much lower than that found during the conventional hot working of metals. The value of 1, which corresponds to Newtonian viscous flow, constitutes a limit at which necking cannot occur. A few alloys approach this value but never reach it. The activation energies for superplastic deformation are either in the range of the values obtained in climb-controlled creep (116), or they may be lower and have been identified with the grain boundary diffusion energy (117,118). It is of interest to note that the effect of grain size d on the strain rate at constant stress and temperature is very large and usually follows a d^{-2} dependence (116).

The stress strain curves obtained in superplastic materials often show very pronounced softening (119). Most of the curves reported in the literature to date, however, have been determined at constant crosshead speed which, in tension leads to an ever-decreasing true strain

rate. This in turn leads to lower stresses and thus most of the softening observed is only apparent.

In summary, the deformation mechanisms in superplastic materials are still controversial and cannot explain fully all the features of the deformation behaviour. A few models have been proposed to explain the characteristics of flow. These are:

i. The vacancy migration model which attempts to interpret the deformation as arising from assisted vacancy migration through the lattice (120) or along the grain boundaries (121). This theory predicts a stress exponent of 1, which is never observed in practice, and does not explain how the grains remain equiaxed during deformation.

ii. The grain boundary sliding model (122-130), which explains most of the features of the deformation. It does not, however, account for the experimental observation that grains are deformed during straining. Moreover, the rates predicted for this model appear in some instances to be much lower than the observed ones (131).

iii. The dislocation movement models which have been proposed (132) are largely inadequate in that they do not explain how the grains remain equiaxed during deformation. Mukherjee (133) has suggested a model based on grain boundary sliding with dislocation motion as the predominant mode of deformation within the grains but this model lacks experimental support so far.

Clearly, more experimental work is required in the field of superplasticity to determine which, if any, of these models is applicable.

2.3 OXIDATION OF ZIRCONIUM AND ZIRCONIUM ALLOYS

The behaviour of unalloyed zirconium under oxidizing conditions has been studied in some detail during the past twenty years and is now relatively well characterized. Zirconium-base alloys, however, have received very little attention as far as their oxidation resistance at high temperatures is concerned. The paragraphs that follow will therefore be devoted to a description of the prominent characteristics of the oxidation of pure zirconium. Later, the oxidation behaviour of alloys, and in particular those used in the present investigation, i.e. the binary Zr-Mo and Zr-Nb systems, will be considered.

2.3.1 The Zr-O Phase Diagram

The oxygen-zirconium equilibrium diagram shown in Figure 2.5 is reproduced from the Metals Handbook. The oxide ZrO_2 has a monoclinic structure up to about 1010°C and changes above that temperature to a tetragonal structure. The deviation from stoichiometry that the oxide structure allows is not very clearly defined, but is appreciable. The α-phase can dissolve up to 29.2% atomic oxygen, the maximum solubility being nearly temperature insensitive. The solubility of oxygen in the β-phase increases with temperature, but remains fairly small. Only about 4 atomic % can be dissolved in the β-phase at 1000°C. It thus appears that oxygen acts as a very effective α-stabilizer.

2.3.2 Rate of Oxidation of Zirconium

2.3.2.1 Oxidation rate in the 10-760 torr range

The rate of oxidation is usually represented by the increase Δm of mass of a sample of unit area as a function of time. This relationship

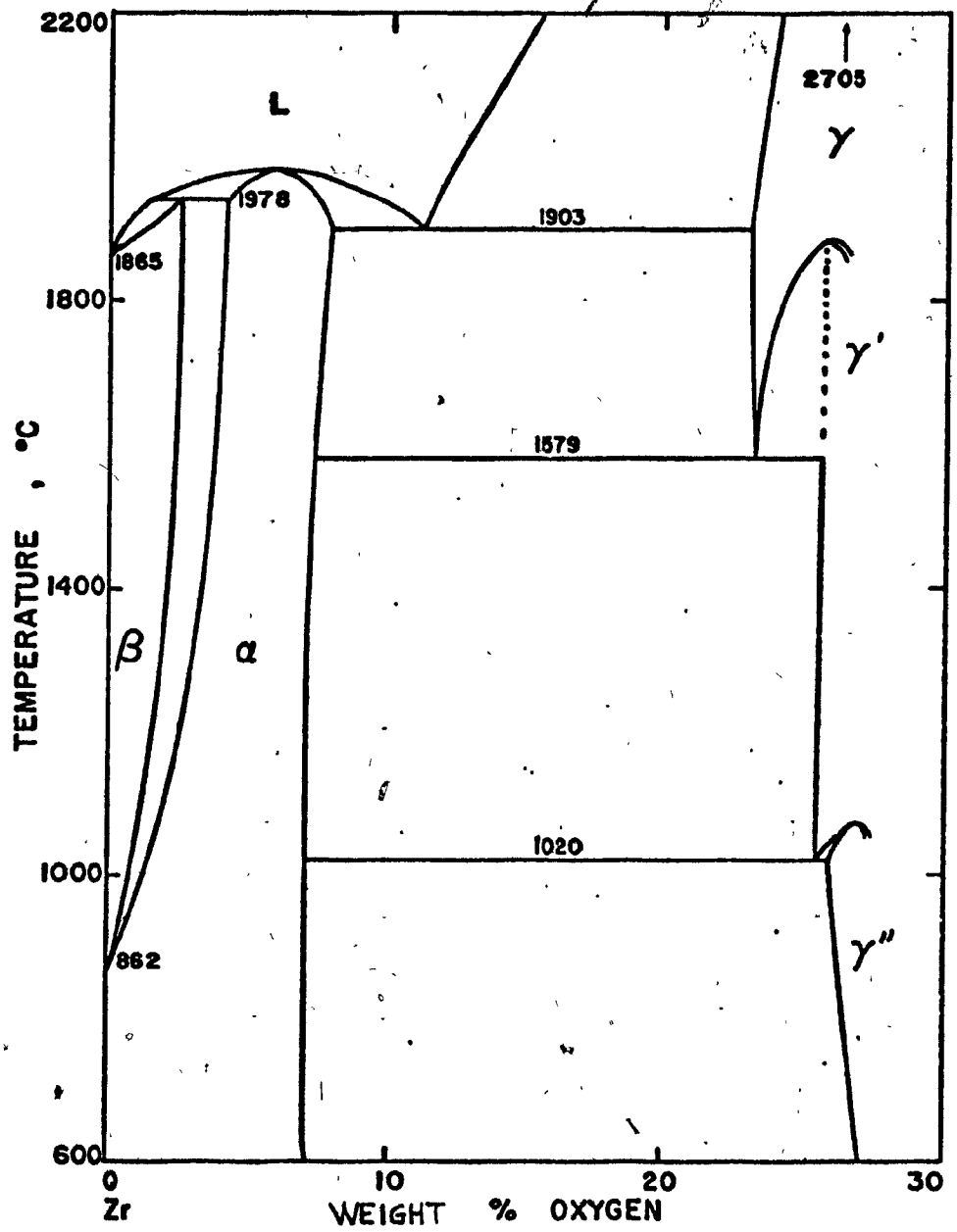

FIGURE 2.5 The zirconium-oxygen binary phase diagram, redrawn from the Metals Handbook.

$$\Delta m = k t^{n} \qquad (2.63)$$

can nearly always be applied to describe the oxidation of pure metals. The above equation was found to apply to the oxidation behaviour of low-hafnium zirconium under a 760 torr oxygen pressure. Belle and Mallett (134) observed n values lying in the range 0.31 to 0.38 for temperatures above 575 and below 950°C. They concluded that zirconium obeyed a cubic law ($1/n = 3$); it is of interest to note that their data do not show any effect of the crystal structure of the metal (fcc or hcp) on the oxidation rate. Charles et al. (135), under the same oxygen pressure, observed that a cubic law also fitted their data in the 350 - 450°C temperature range. These results were challenged by Gulbransen and Andrew (136), who suggested that surface condition could modify the rate of oxidation. This conclusion was based on their results for mechanically abraded specimens, which fitted a cubic oxidation law, whereas their results for chemically polished ones obeyed a parabolic oxidation law ($1/n = 2$). They interpreted the change in behaviour brought about by chemical polishing as possibly being due to the formation of a passive oxide film on the smoother surface. The oxygen pressure used was 76 torr, compared to 760 torr in the previous investigations. Under similar surface conditions, the absolute weight increases in the two sets of studies were comparable, indicating that there was little pressure dependence.

Porte et al (137) carried out some experiments to check the findings of Gulbransen and Andrew regarding the effect of surface condition on the oxidation rate. Below 600°C and oxygen pressures varying from 50 and 800 torr, they observed a slower reaction rate for chemically polished zirconium; they found no appreciable difference above 600°C, however. In

addition, they concluded that their results could best be expressed by a cubic law, in agreement with earlier investigators.

Another study, which also led to diverging observations, was that of Osthagen and Kofstad (138). They detected a considerable increase in the mass pick-up rate with oxygen concentration in the metal and they estimated that, after 100 minutes of oxidation at 800°C under 760 torr oxygen, only about 20% of the oxygen picked up remained in the oxide scale, the remainder being dissolved in the metal. The enhancement of oxygen pick-up with oxygen content in the alloy seems difficult to rationalize. Since the oxygen diffusion flux is proportional to the oxygen gradient, it follows that the diffusion rate will decrease as the oxygen concentration is raised in the alloy. As a consequence it could be expected that the oxide layer would build up at a faster rate, leading to a decrease in the oxygen pick-up rate.

In attempting to verify Porte's findings, Sense (139) also studied the oxidation of zirconium in the 400 - 500°C range under a pressure of about 50 torr. He observed no effect of surface condition on the oxidation rate, in contradiction with the results of both Gulbransen and Andrew (136) and Porte (137). In analyzing his data, he found that his rate law varied with time from linear, to parabolic, to cubic. This result, however, is not necessarily in opposition to earlier investigations, as the parabolic rate lasted for times not exceeding 15 minutes, compared with several hours or more for the cubic law in the other investigations.

In order to explain the variation in the oxidation kinetics from parabolic to cubic, Smeltzer et al (140) developed a model applicable at moderate temperatures (i.e. 300 - 600°C). This theory assumes that the oxygen ions migrate through the oxide lattice under a concentration gradient (as in Wagner's model) and that the diffusion takes place along short

circuit paths whose density f decreases with time according to the rate equation:

$$f = f_o \exp(-kt) \tag{2.64}$$

The effective diffusion coefficient D_{eff} is therefore:

$$D_{eff} = D_e(1 - f) + D_b f \tag{2.65}$$

where f_o is the initial fraction of oxygen sites within the low resistance paths, f the fraction at any time t, and D_e and D_b are the lattice and short circuit (boundary) diffusion coefficients for oxygen. On the assumption that $D_b >> D_e$, Smeltzer et al (140) derived the following equation for oxide growth:

$$x_1^2 = k_p\left(t + \frac{D_b f_o}{D_e k}(1 - \exp(-kt))\right) \tag{2.66}$$

Here x_1 is the thickness of the oxide layer and k_p is the parabolic rate constant. This equation has an adjustable parameter k, and proves to be capable of predicting or fitting in a satisfactory manner the oxidation behaviour. It is important to point out that this model does not take into account the dissolution of oxygen in the metal, and is thereby inapplicable at high temperatures.

In a later investigation, Hussey and Smeltzer (141) determined the partition of oxygen between metal and oxide. They found that after long anneal times in the 500 - 600°C range, e.g. up to 600 hours, 15 to 25% of the oxygen picked up went into the metal phases, the remainder

constituting the oxide scale. Their observations on the rate of oxidation permitted them to conclude that, after an initial transient, the behaviour was parabolic and that it was independent of the surface condition of the specimen. This conclusion contradicts some of the earlier results discussed above, but no interpretation of the discrepancy was offered.

Somewhat earlier, Akram and Smeltzer (142) reported that they observed a transition from parabolic to linear oxidation after 60 hours of heating at temperatures between 800 and 850°C. The linear oxidation behaviour was found to be associated with layers of porous and compact oxide, whose presence was not explained. These results may, however, be overlooked, since subsequent work by Wallwork et al (143) again supported a parabolic law even after long reaction times in the oxygen pressure range 400 - 700 torr.

In summary, then, the results on the rate of oxidation of zirconium appear to fall into two groups, one of which favours cubic rate kinetics for intermediate and long times, the other supporting the view that a parabolic rate predominates.

All the investigations described above were carried out under an atmosphere of nominally pure oxygen. However, it is possible that some of the observed discrepancies can be attributed to traces of nitrogen and water vapour in the gas, both of which have been shown capable of causing an increase in the oxidation rate (144).

2.3.2.2 Oxidation rate under low pressures

The results discussed so far were obtained under oxygen pressures ranging from 10 to 760 torr. The study of the oxidation of zirconium under still lower pressures shows a different behaviour, which is associated with

the early stages of oxidation and in particular with the formation of a thin oxide film. Under these conditions, i.e. at oxygen pressures between 10^{-2} and 10^{-5} torr, Deschamps et al (145-147) found that linear oxidation kinetics prevailed, followed by a parabolic rate of reaction. They did not, however, come to any conclusion regarding the rate-controlling process.

Under similar pressures, Niederlich and Paidassi (148) found also by gravimetry that the oxidation rate varied continuously with time in the initial stages of oxidation. They hypothesized that the chemisorption rate was the controlling process. Recently, Horz and Hammel (149), observed a linear oxidation rate in the temperature range 1100 - 1600°C, and under oxygen pressures of $1x10^{-5}$ to $8x10^{-4}$ torr. The oxidation rate appeared to be almost independent of temperature; it was therefore concluded that the rate controlling parameter was the transport of oxygen atoms to the sample surface, a contention supported by the high pressure dependence of the oxidation rate.

2.3.3 Effect of Temperature

The oxidation of metals, and zirconium in particular, is temperature dependent. The temperature dependence follows an Arrhenius law, and values of the experimental activation energy have been reported by many investigators. In an early work, Cubiciotti (150) deduced an activation energy of 75 kJ/mol, from data in the 600 - 920°C range. In the same range of temperature, Belle and Mallett (134) published a value of 195 kJ/mol, but could not explain the discrepancy observed. Support to the latter value was brought by the work of Charles et al (135), who obtained an energy of 159 kJ/mol in the 350 - 650°C temperature range.

The results of Gulbransen and Andrew (136) cited above yielded several values of activation energy. Chemically polished specimens led to Q = 135 kJ/mol throughout the temperature range from 400 to 800°C. By contrast, a break in the line on the log k versus 1/T plot occurred when the results obtained on mechanically abraded specimens were plotted. Below 525°C, the slope yielded Q = 76 kJ/mol, whereas above 525°C a value of 120 kJ/mol was found. Gulbransen and Andrew were not able to explain the origin of the change in slope that they observed. They attempted to correlate the activation energies with possible oxide growth mechanisms, but without conclusive results.

Under 200 torr oxygen, Porte et al (137) obtained an activation energy of 178 ± 3 kJ/mol from a very wide temperature range, extending from 400 to 900°C. Their results agree with those of Charles et al (135) and Belle et al (134), and it is of interest to note that no break in the slope was found throughout the domain investigated. Sense (139) obtained an activation energy of 122 kJ/mol in the parabolic oxidation region and 176 kJ/mol in the cubic region, but could not relate these values to any physical process. The first value appears in agreement with that of 133 kJ/mol reported by Hussey and Smeltzer (141). In a more recent paper (151), the latter investigators analyzed the oxygen gradient in the metal and applied a model based on simultaneous diffusion in both oxide and metal. From the oxygen gradient, they were able to determine the activation energy for oxygen diffusion in α-Zr and obtained a value of 223 kJ/mol, in good agreement with published values (152). As was pointed out earlier, however, this model does not explain why the oxidation appears to accelerate with an increase in the oxygen concentration in the metal. To the author's knowledge, there has not been a satisfactory explanation for these large

differences in activation energy. This jeopardises the attempts made to determine the rate controlling mechanism. For this reason, perhaps, further studies of the oxidation behaviour of Zr have been concerned with aspects that are more amenable to physical interpretation.

2.3.4 Mechanism of Oxidation

Many investigators have attempted to interpret the cubic and parabolic rate laws, as well as the small pressure dependence of the oxidation rate. In early studies, this effort was based on the assumption that oxidation was controlled by diffusion through the oxide film. Marker experiments showed that zirconium oxide grows at the metal-oxide interface (153), from which it was concluded that anion diffusion constituted the most important transport mechanism. Since the movement of interstitial O^{--} in the ZrO_2 lattice is likely to be a slow process, with a very large activation energy, it was postulated that the diffusion of oxygen ions occurred via O^{--} vacancies (136). This was confirmed by measurements of the thermoelectric power of the film, which led to the conclusion that ZrO_2 is an n-type semiconductor (134).

Nevertheless, the low temperature activation energies of Gulbransen and Andrew (136) did not agree well with computed values based on anion diffusion through the oxide lattice. Moreover, other difficulties based on entropy considerations also arose (136). The model proposed by Smeltzer et al (140), in spite of its success in predicting the oxidation rate, could not provide a theoretical value for the activation energy.

Partly as a result of these difficulties, the main thrust towards an understanding of the oxidation behaviour under moderate pressures (10-760 torr) was directed to a consideration of the simultaneous diffusion

of oxygen in the metal (143,154-156) and through the oxide. For example, Rosa and Smeltzer (155) and Rosa (156) have analyzed the oxygen concentration profiles given in Figure 2.6a and b. In a, in the α-phase, oxygen diffuses through the oxide and arrives at the metal-oxide interface. Part of it remains and contributes to film thickening, whereas the remainder simply diffuses into the metal. If the abscissa of the metal-oxide interface is denoted by x_1, this situation can be described by the following relation

$$D_{II}\left(\frac{\partial c}{\partial x}\right)_{x = x_1 - 0} = \left(c_{II_{x_1}} - c_{I_{x_1}}\right)\frac{dx_1}{dt} - D_I\left(\frac{\partial c}{\partial x}\right)_{x = x_1 + 0} \quad \ldots\ldots(2.67)$$

where D_{II} and D_I are the oxygen diffusion coefficients in the oxide and the metal respectively, and $c_{II_{x_1}}$ and $c_{I_{x_1}}$ the oxygen concentration in the oxide and the α-phase at the point x_1, respectively. No oxygen accumulation takes place within the oxide during diffusion, and as a consequence

$$\frac{d}{dt}(\Delta m) = -D_{II}\left(\frac{\partial c}{\partial x}\right)_{x = 0 \text{ or } x = x_1} \quad (2.68)$$

where Δm is the mass pick-up per unit area.

Figure 2.6b, representing the situation when oxidation occurs in the β-phase is complicated by the presence, between the oxide and the thermodynamically stable β-phase of an α-layer. The description of the process involves, in addition to the above equations, which still apply at the α/oxide interface, a relation similar to Equation 2.67 at the α/β interface. If the abscissa here is x_2, we can write that:

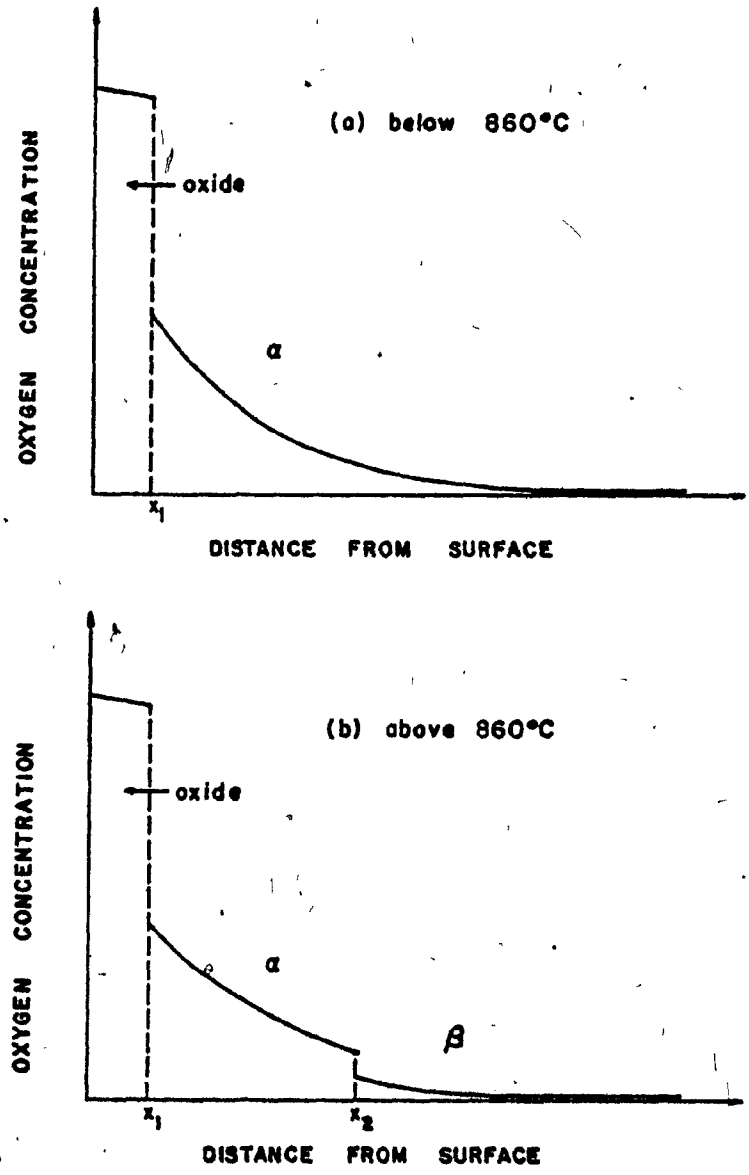

FIGURE 2.6 Oxygen concentration profile near the surface for zirconium in the β-phase in an oxidizing atmosphere
a. below 860°C
b. above 860°C

$$- D_I\left(\frac{\partial c}{\partial x}\right)_{x = x_2 - 0} = (c_{I_{x_2}} - c_{o_{x_2}}) \frac{dx_2}{dt} - D_o\left(\frac{\partial c}{\partial x}\right)_{x = x_2 + 0} \quad (2.69)$$

where D_o is the diffusion coefficient of oxygen in the β-phase, and c_o the oxygen concentration.

Another relation relating the fluxes at the boundaries of the α-phase can be derived; it states that the difference between the fluxes of oxygen at the two interfaces serves to increase the oxygen concentration. This equation has the following form:

$$\left(\frac{\partial c}{\partial x}\right)_{x = x_1 + 0} - \int_{x_1}^{x_2} \left(\frac{\partial^2 c}{\partial x^2}\right) dx + \left(\frac{\partial c}{\partial x}\right)_{x = x_2 - 0} \quad (2.70)$$

Differential Equations 2.67-2.70, applied both above and below the transus, have been solved, in particular by Rosa (156). We shall, however, restrict the presentation of the solution to the case where the temperature is above the α/β transus, as it is relevant to the present work. The solution of these equations can be achieved numerically for preset boundary conditions, or can be obtained analytically if some further assumptions are made. In Rosa's treatment, the variation in concentration in the α and β phases was taken as:

$$c_\alpha = c_o + B_I(1 - \mathrm{erf}(x/2\sqrt{D_I t})) \quad (2.71)$$

$$c_\beta = c_o + B_o(1 - \mathrm{erf}(x/2\sqrt{D_o t})) \quad (2.72)$$

The assumption involved here is that the boundaries x_1 and x_2 move slowly enough that the oxygen concentration profile remains fixed, as if no moving boundaries were present. Since the physical situation is unique,

a particular solution should permit the determination of the general solution. If it is now assumed (as suggested by experimental results) that

$$x_1 = 2m_1\sqrt{D_{II}t} \qquad (2.73)$$

and

$$x_2 = 2m_2\sqrt{D_I t} \qquad (2.74)$$

where m_1 and m_2 are constants, and if Equations 2.71 and 2.72 are combined with Equations 2.67, 2.68 and 2.69, integration leads to:

$$\Delta m = \left[2m_1(c_{II_{x_1}} - c_{I_{x_1}})\sqrt{D_{II}} \quad 2B_1\sqrt{D_I/\pi}\, \exp(-\, m_1{}^2 \frac{D_{II}}{D_I})\right]\sqrt{t} \qquad .....(2.75)$$

which can be written, after substitution of Equations 2.68 to 2.74 into 2.67,

$$\Delta m = \left[k_{p(oxide)} + k_{p(alpha)} + k_{p(beta)}\right]\sqrt{t} \qquad (2.76)$$

where

$$k_{p\ oxide} = 2m_1(c_{II_{x_1}} - c_{I_{x_2}})\sqrt{D_{II}} \qquad (2.77)$$

$$k_{p\ alpha} = 2m_2(c_{I_{x_2}} - c_{o_{x_2}})\sqrt{D_I} + 2B_I\sqrt{D_I/\pi}(\exp(-\frac{m_1{}^2 D_{II}}{D_I}) - \exp(-\, m_2{}^2)) \qquad .....(2.78)$$

$$k_{p\ beta} = 2B_o\sqrt{D_o/\pi}\, \exp(-\frac{m_2{}^2 D_I}{D_o}) \qquad (2.79)$$

This treatment thus predicts a parabolic rate of mass pick-up, and furthermore permits an estimate to be made of the oxygen partition between oxide, α-phase and β-phase.

If a small oxygen gradient is now assumed to exist in the oxide,

$$\Delta m_{oxide} = (c_{II} - c_o)x_1 \tag{2.80}$$

In a similar way, the mass pick-up in the α-phase can be obtained from

$$\Delta m_\alpha = \int_{x_2}^{x_1} (c - c_o)dx \tag{2.81}$$

$$= 2B_1\sqrt{D_1 t}\ (\text{ierf}\ \frac{x_1}{2\sqrt{D_1 t}} - \text{ierf}\ \frac{x_2}{2\sqrt{D_I t}}) \tag{2.82}$$

and, in the β-phase from

$$\Delta m_\beta = 2B_o\sqrt{D_o t}\ \text{ierfc}(\frac{x_2}{2\sqrt{D_o t}}) \tag{2.83}$$

The diffusion coefficients required for these calculations are available in the literature. The activation energies for oxygen diffusion in the oxide, and α and β phases are about 117-138, 213 and 118 kJ/mol, respectively.

From Equations 2.75 to 2.79 we see that the measured temperature dependence will depend critically upon the relative importance of the three terms. Although not pointed out in the original paper (156), this can perhaps offer some means of rationalizing the widely different Q values reported. A disadvantage of this treatment, however, is that it does not consider the expansion caused by the formation of oxide, which causes x_1 to increase faster than indicated.

From Equations 2.80 to 2.83, Rosa was able to obtain the relative proportions of oxygen in each phase. He found that at 950°C, more than 65% of the oxygen was confined to the stabilization and growth of the oxide

layer. In his experiments, he found that the oxide layer/alpha phase thickness ratio decreased from about 0.1 to 0.05 after about 40 hours, and subsequently remained constant with time, in satisfactory agreement with his theoretical treatment. It should be added that in a later treatment, Rosa considered the volume change that takes place during oxide formation, and arrived at essentially similar results.

2.3.5 Effect of Oxygen Pressure on the Oxidation Rate

The effect of oxygen pressure on the oxidation kinetics of zirconium has been observed to be negligible in the 1-760 torr range (141,143,154,157,158). This is to be expected if the transport of oxygen through the oxide is achieved by defect migration in the lattice. The change in pressure only changes the density of defects, thereby introducing a pressure component which was shown by Wagner to be proportional to $P^{1/n}$, where $6 < n < 8$.

However, below 10^{-3} torr, not only is the oxidation rate very sensitive to oxygen pressure, but the activation energy becomes pressure dependent as well (145). Such an effect may also be expected from the assumed change in the mechanism controlling oxidation at low pressures. At low pressures, oxidation proceeds first by the formation of a chemisorbed layer, and then by the formation of oxide nuclei on the surface which later spreads to form a continuous film. Subsequent oxidation proceeds by the thickening of the oxide film. Diffusion of oxygen in the metal also takes place and may completely impede oxide formation. Under such circumstances, it is understandable that the particular conditions of temperature and pressure may favour different rate controlling mechanisms. An extreme case, perhaps, is that reported by Horz and Hammel (149), where the oxidation rate is nearly temperature independent, and for which the rate

controlling mechanism was hypothesized to be the transport of oxygen atoms to the surface of the solid.

In the transition pressure range, which extends from 10^{-2} to 1 torr approximately, conflicting results have been reported concerning the effects of pressure on the oxidation kinetics. A marked pressure dependence on the oxidation rate has been found by some investigators (159), whereas other researchers do not observe any pressure effects (145). This discrepancy has not yet been fully resolved.

2.3.6 Effect of Alloying

According to the semiconductor theory of oxidation (160), the introduction of foreign ions of lower valence than zirconium should increase the rate of oxidation since it leads to a higher density of positively charged oxygen vacancies. By contrast, the presence of ions of higher valence than zirconium will decrease the oxidation rate by means of the opposite effect. This argument of course breaks down if a new oxide phase is formed, or if the oxide film becomes blistered or cracked as a result of the presence of an alloying element.

Data on the effect of alloying on the oxidation rate are very scarce. The most extensive work is that of Porte et al (137) who investigated the effects of twenty alloying elements on the oxidation kinetics at 700°C. The observed changes resulting from alloying were classified into four groups, according to their behaviour, as shown in Figure 2.7. Group I alloys oxidized according to the cubic rate law, and did not exhibit a breakaway. This group contains the largest number of alloying elements. In Group 2. the alloying elements only promote change from a cubic to a parabolic rate law, but no breakaway is detected. Group 3

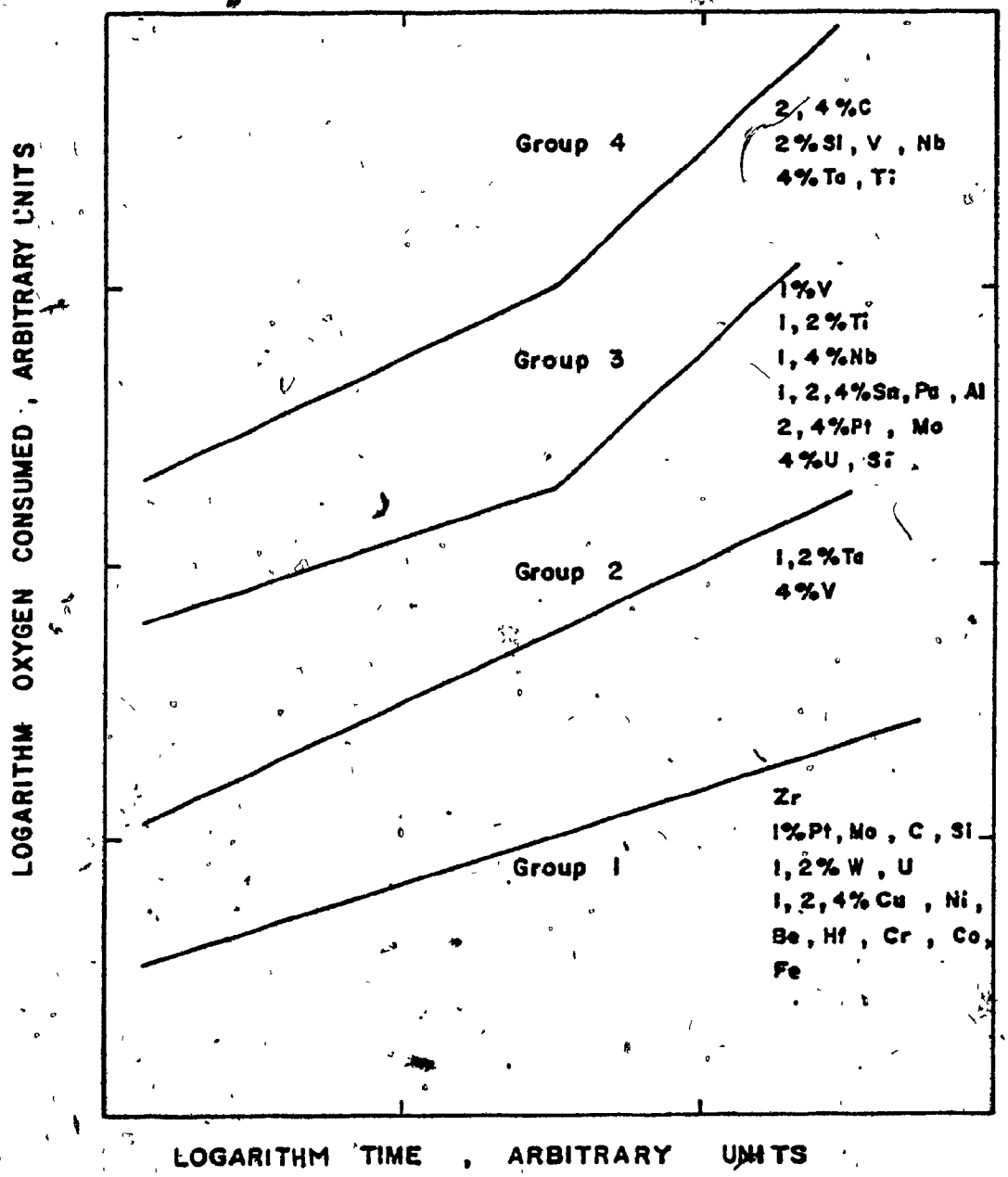

FIGURE 2.7 Oxidation rate of zirconium alloys at 700°C under a 200 torr oxygen pressure, after Porte et al (137).

alloys oxidize first as Group 1, then subsequently exhibited a breakaway to linear oxidation rates. Finally, a transition to linear oxidation from the parabolic rate law is observed in Group 4. Molybdenum in small concentrations (1%) does not affect the rate of oxygen pick-up, but from 2% to at least 4% it changes the alloy behaviour from Group 1 to Group 3, introducing a breakaway. Niobium appears to have a more complex effect since at 1 and 4% the alloy is classified in Group 3, whereas for 2% it is found in Group 4. These results were confirmed by an independent investigation by De Gelas et al (161).

In the conclusions of their work, Porte et al (137) stated that those alloying elements which had appreciable solubility generally followed the behaviour predicted by the semiconductor theory of oxidation at low solute concentration. They also showed that the occurrence of breakaway was usually related to the atomic radius. It appears that when the solute atomic radius differs by more than 15% from that of zirconium, breakaway will occur. It should be noted, however, that the alloying elements which meet the above criterion but which have little solubility in zirconium display a behaviour which cannot be rationalized by the Wagner-Hauffe theory.

2.3.7 Oxidation Behaviour in the Zr-Mo and Zr-Nb Systems

The oxidation of Zr-Nb alloys in the β-phase has been studied by Zmeskal and Brey (162). The oxidation rate at 900°C was determined under an oxygen pressure of 200 torr. It was found that it could not be represented by Equation 2.63 for any of the experimental compositions. The slope n appeared to decrease continuously with time from about 3 to about 1, indicating a transition towards a linear oxidation behaviour.

Pure zirconium was the least reactive species, the increase in weight being about 5 times less than that of alloys having niobium contents ranging from 5 to 20%. The oxidation rate increased with niobium content up to about 10-20%, then decreased as the concentration went up to about 30%. For niobium contents up to 50%, the oxidation rate remained constant then climbed rapidly as the niobium concentration was increased towards pure niobium.

Experiments conducted at 1090°C led to similar results, except that the oxidation rate was higher, but appeared not to be very sensitive to temperature. The presence of a breakaway transition suggests that the oxide scale is not likely to be single phase since the atomic radius of Nb, being only 8% smaller than that of Zr would not be expected to modify drastically the zirconium dioxide structure.

The oxidation behaviour of Zr-Mo alloys above 800°C has not been determined. The reactivity of the alloy can to some extent be predicted from the properties of the molybdenum oxides MoO_2 and MoO_3. Molybdenum dioxide sublimates to some extent above 1000°C without decomposition, the larger part reacting to give MoO_3 and Mo. The oxide MoO_3 sublimates appreciably above 650°C and evaporates above 1000°C. The Mo-O phase diagram predicts the persistence of liquid phases down to 800°C. The oxidation resistance of Zr-Mo alloys is thus likely to be very poor, especially if the oxide layer becomes porous as the molybdenum oxides evaporate.

2.4 EFFECTS OF GASEOUS ENVIRONMENT ON MECHANICAL PROPERTIES

The effects of gaseous environments on the mechanical properties of metals and alloys have been known for some time. The very large variety of materials, atmospheres and testing methods renders a classification of

the effects produced difficult. However, two main categories may be distinguished. At elevated temperatures, the atmosphere usually produces a scale, whose deformation behaviour determines the modification of the strength properties. At room temperature, on the other hand, no oxidation or similar reaction normally occurs, but the surface absorption of gases may cause some modification of the mechanical properties. The latter category is not relevant to the present review, but for comprehensive articles, the reader may refer to Kramer and Demers (163), Machlin (164), and Cook and Skelton (165).

2.4.1 Effects of Atmospheres on High Temperature Properties

The effects of atmospheres on the high temperature properties reported in the literature concern mostly alloys designed for high-temperature applications, under service conditions where creep or fatigue occurs. Rather than presenting a detailed report of the observed effects, a brief account of typical observations on creep and fatigue will be given.

2.4.1.1 Effects on creep

The presence of air tends to increase the rupture life of nickel at high temperatures and low stresses, whilst a high vacuum environment produces the longest life at low temperatures and high stresses (166-168). The bridging of cracks by oxide particles seems to be the cause of the improvement of high temperature life in air. At low temperatures, no ready explanation is available for the deterioration of the rupture life in air, but it may be associated with oxygen absorption on the crack surface, thereby reducing the surface energy, and enhancing its growth. Nickel-base alloys such as Inconel (168), Hastelloy C (169), Inconel X (170)

and Ni-20Cu alloys (171,172), behave similarly to nickel in this respect.

Austenitic steels are also affected by the oxygen partial pressure, but the creep behaviour under different conditions cannot easily be rationalized (168,169,173). One of the reasons for the complexity of the effects observed may lie in the change in the oxide structure brought about by a variation in oxygen pressure. The creep resistance of plain carbon steels is increased by trace impurities in an inert atmosphere (169). Furthermore, short time tests give longer rupture lives in 1.25Cr-0.5Mo and 12Cr-1V steels in air and in oxygen than for their counterparts in helium, nitrogen or vacuum (170).

2.4.1.2 Effects on fatigue

At high temperatures, the fatigue lives of Pb, Co-base alloy S 816 and of Inconel 550 are best in vacuum, worst in oxygen and intermediate in air (174). A temperature decrease results in a convergence of the endurance limit obtained in various environments. A cross-over may even be obtained in some cases (175). As in creep, atmosphere effects arise primarily by affecting crack propagation.

2.4.2 Mechanisms of Interaction of Surface Films

The more fundamental studies attempting to explain the effect of surface films on strength have been all carried out at room temperature and mostly on single crystals. Most of these studies have concerned the influence of metallic films of various thicknesses on the strength. A few studies, however, have reported on the effects due to the presence of oxide films.

In all cases, the CRSS is increased by the presence of a surface film, the strengthening then persisting up to over 20% strain. Typically, an increase of 25% in the CRSS is brought about by a 1 μm coating (163). The extent of stage I is reduced in FCC metals but remains unchanged in HCP metals (164) such as zinc, where the stress-strain curve is dominated by easy glide.

An estimation of the CRSS increase due to the transfer of load to the surface film has shown that the expected flow stress increment is much lower than the observed one (176-179). In many cases, the strength of the film would have to be of the order of the theoretical elastic limit, or even higher, to match the observed effect (180,181).

The interpretation of the observed increase in flow stress that is generally agreed upon is that surface films constitute a barrier to the egress of dislocations. Brame and Evans (182) have shown that dislocation transfer from the metal to the film is impossible unless: i) the film is epitaxial; ii) the lattice parameter of the film differs from that of the substrate by less than 5% (i.e. the accomodating dislocations are spaced more than 20b apart).

These conditions never prevail under normal conditions, and are excluded in the case of oxide films in which the volume change (Pilling-Bedworth ratio) is much larger than 5%. Hence, surface films are essentially impervious to dislocations, and during deformation, dislocation pile-ups form at the film/substrate interface, until the shear stress evolved at the head of the pile-up is sufficient to shear the film. The pile-ups adjacent to the crack line are then released, causing a spurt of strain (183).

The increase in dislocation density underneath the surface film is not limited to short-range effects. Quantitative measurements of dis-

location density on chromium-plated copper single crystals strained to 2.5% have led to densities double those of unplated crystals (184). This dislocation density increase was found to extend to depths over 1200 times that of the plated layer. The shear stress at 2.5% strain was raised from 240 g/mm^2 to 380 g/mm^2. An important finding of these experiments was the recognition of the role of plastic constraint in film strengthening. The presence of a strengthening component after a few percent strain (i.e. after the film had already cracked in some places) indicated that a cracked film could still prevent dislocation egress to a significant extent, and that it would cease to act as a dislocation barrier only when the crack network is very dense.

The surface films also block the dislocation lines ending in the surface, thereby creating singly-pinned Frank-Read sources, whose contribution to the dislocation density increase is added to that of the normal sources (185). A theoretical prediction of the magnitude of the flow stress increase has not yet been achieved on this basis, in spite of the simplified situation in single crystals. For polycrystals, the situation is much more complicated since firstly, multiple slip operates from the initiation of flow; secondly, pile-ups exist near the grain boundaries and not only at the surface; and, lastly, the number of sources is certainly large in polycrystals.

The behaviour of surface films at high temperatures cannot be simply extrapolated from that observed at room temperature. For one thing, the dislocation density increase during straining will be partly offset by the operation of recovery mechanisms. Moreover, even if the oxides are still likely to be brittle, the metallic phases formed on the surface (such as the oxygen-stabilized α-layer on the β-core in zirconium) may be

very ductile and will simply deform by slip. It can be seen that the description of the effect of a surface film on the strength at high temperatures is extremely complex and that an adequate model is still lacking.

2.4.3 Internal Oxidation

Internal oxidation is the process by which oxygen diffuses into an alloy and causes subsurface precipitation of the oxides of the alloying elements. This situation arises when the alloying elements are much less noble than the matrix.

2.4.3.1 Thermodynamics

The thermodynamic expression of the condition for internal oxidation is derived from the equilibrium

$$Me_{(solute)} + \nu O_{(solute)} \rightleftharpoons MO_{\nu (precipitate)} \qquad (2.84)$$

where ν is the stoichiometric ratio of oxygen to metal atoms in the oxide. If the free energy of oxide formation is $\Delta G^{T}_{o_{oxide}}$, and assuming that the surface energy and lattice constraints of the oxide are negligible, then

$$\left[a_s^{Me}\right]\left[a_s^{o}\right]^{\nu} = k_p = \exp\left(-\frac{\Delta G^{T}_{o_{oxide}}}{RT}\right) \qquad (2.85)$$

where a_s^{Me} and a_s^{o} are the activities of the metal solute and dissolved oxygen in the matrix. If the alloy is in equilibrium with an oxygen pressure p_{O_2}, it follows that the equilibrium

$$\tfrac{1}{2}\, O_2 \rightleftharpoons O_{(solute)} \qquad (2.86)$$

is achieved, that is

$$\left[p_{O_2}\right]^{\frac{1}{2}} = a_s^{\,o} \qquad (2.87)$$

Equation 2.2 can then be rewritten

$$p_{O_2} = \left[a_s^{\,Me}\right]^{2/\nu} \exp\left(-\frac{2\Delta G^{\,T}_{o\,oxide}}{\nu RT}\right) \qquad (2.88)$$

Oxide precipitation will thus take place if p_{O_2} is larger than the equilibrium value. From Equation 2.88, it can be seen that p_{O_2} will depend to some extent upon the activity of the metal in solution, but will be much more sensitive to the oxide stability. For this reason we see that oxide precipitation will be achieved in systems containing solutes such as Al, Si, Zr, in a matrix of Cu or Fe.

2.4.3.2 Kinetics

If an alloy susceptible to internal oxidation is placed in contact with an oxygen pressure larger than the equilibrium pressure, internal oxidation will occur. The kinetics of the process will be governed by the rate at which oxygen diffuses into the alloy and thereby precipitates the solute oxide. The matrix being depleted in solute, a counter diffusion of solute will take place.

The mathematical analysis of the process carried out by Wagner (186) predicts that the thickness ξ will vary according to the time law:

$$\xi = 2(D_o t)^{\frac{1}{2}}/\gamma \qquad (2.89)$$

where D_o is the diffusion coefficient of oxygen in the metal matrix and γ is a constant called the parabolic rate constant, which can be obtained from

$$\frac{N_o^s}{N_{Me}^o} = \frac{\nu \exp(\gamma^2) \cdot \operatorname{erf}(\gamma)}{(D_o/D_{Me})^{\frac{1}{2}} \cdot \exp(\frac{\gamma^2 D_o}{D_{Me}}) \cdot \operatorname{erfc}(\gamma(\frac{D_o}{D_{Me}})^{\frac{1}{2}})} \qquad (2.90)$$

In this equation,

N_o^s is the atom fraction of oxygen at the surface,

N_{Me}^s the atomic fraction of solute in the alloy, and

D_{Me} the diffusion coefficient of the metal in the alloy.

In the limiting case, where oxygen diffusion predominates,

$$\gamma = \frac{N_o^s}{2\nu N_{Me}^s}^{\frac{1}{2}} \qquad (2.91)$$

whereas when counterdiffusion is the most important

$$\gamma = \frac{N_o^s (\pi D_o/D_{Me})^{\frac{1}{2}}}{2\nu N_{Me}^s} \qquad (2.92)$$

Parabolic rates of internal oxidation have been observed in copper-base alloys (187) and nickel-base alloys (188), and support the predictions of the theory.

2.4.3.3 Morphology

The morphology of the oxide depends on its stability and upon the diffusion rate, inasmuch as these affect the rates of nucleation and growth. Rhines (187) observed that the oxide particle size decreased with oxide free energy and increased with temperature and depth from the surface. Classical nucleation theory easily explains these results qualitatively. The higher the $\Delta G_{o\ oxide}^{T}$, the larger the number of nuclei, and thus the number of particles. On the other hand, as the oxidation front moves proportionally to the square root of time, low supersaturation conditions leading to few nuclei and large particles will prevail at large distances from the surface. Raising the temperature increases the diffusion coefficients and decreases the oxide free energy. The quantitative treatment of Bohm and Kahlweit (189) predicted that the particle diameter will increase linearly with depth. This has been observed to be in agreement with results on Cu-Al alloys (189), but disagrees with results obtained on other Cu alloys (190).

Depending upon the degree of coherency of the oxide and the anisotropy of the surface energy, the particle shape may vary widely. In copper-base alloys, SiO_2 and TiO_2 particles were found to be spherical, MgO tetrahedral (190,191), BeO triangular (190). When large precipitates are formed, the effect is even more marked and Widmanstatten patterns have been observed (192). Cycling in temperature or in partial pressure may result in a periodic structure of oxides (193,194).

2.4.3.4 Strengthening

Internal oxidation can lead to strengthening if the dispersion of the particles is very fine with a sufficiently close interparticle spacing.

Typical particle sizes that are effective in strengthening are of the order of 50-1000Å. The particles constitute obstacles to dislocation glide which cannot be overcome by thermal activation. An Orowan mechanism may then operate, leading to a flow stress that is inversely proportional to the average interparticle spacing. Secondary slip may also occur around the particles (195). The change in particle diameter with distance from the surface limits the preparation of internally oxidized commercial alloys to thin sections. Creep life has been found to increase by a factor of 10 in Nb-1%W-1%Zr at 1200°C following internal oxidation (196). In nickel containing dispersed Al_2O_3, produced by powder metallurgy, the stress for 100-hr rupture life was about 10 times higher than that of extruded nickel powder (188).

The temperature dependence of the creep rate at constant stress or of the stress at constant strain rate is considerably lower than that of conventional alloys, particularly at high temperatures. The strain rate sensitivity of these materials is lower than that of alloys at hot working temperatures.

CHAPTER 3

EXPERIMENTAL EQUIPMENT

3.1 MECHANICAL TESTING METHODS

Various methods are used to obtain information on the mechanical behaviour of metals at high temperatures. The advantages and limits of each method have already been discussed by several authors (197-200). The most widely used types of test are torsion, tension and compression, and these will now be discussed briefly.

Torsion testing allows large strains to be reached (several hundred true strain units) and permits constant strain rates to be achieved simply by keeping the angular velocity constant. However, the strain varies from the center to the surface of the torsion sample which means different portions of the sample undergo different strains. As a consequence, the torsion test does not permit the determination of the initial flow stress. Similarly, the strain rate varies across the sample radius, which constitutes another difficulty.

The tensile test is probably the most accurate method of determining the initial flow stress or yield. Furthermore, a constant true strain rate may be obtained during uniform elongation of the sample by causing the crosshead velocity to be proportional to the instantaneous length of the sample. Unfortunately, uniform elongation is only maintained at low strains (less than 0.5) because of the onset of necking. The tensile test cannot therefore be used for the determination of steady state flow stresses.

Compression testing achieves more of a compromise. The determination of initial stress is relatively easy, a constant strain rate can be achieved, and strains up to about 1 can be currently obtained. The limit imposed to the strain arises from friction at the faces of the compression sample, leading to inhomogeneous flow, which in most cases appears as "barrelling" of the sample.

3.2 TESTING APPARATUS

The equipment available was basically a standard 100 kN Instron testing machine equipped for hot compression. This machine was capable of operating at a constant true strain rate, and was interfaced with a GE 4020 process control computer for test control and data acquisition purposes. The following sections describe the equipment in more detail.

3.2.1 Hot Compression Testing

The compression train was designed by Luton (4) and is shown schematically in Figure 3.1. The upper compression anvil is made of a Udimet 700 bar, which is water-cooled over half its length and is connected directly to the moving crosshead of the Instron machine. The lower anvil is made of the same material, and is fixed to a stainless steel base, which is, in turn, located on top of the load cell. The upper and the lower anvil faces are of alumina. The alumina inserts are in the form of truncated cones which are held in position on the anvil ends by means of retaining conical nuts. The design of the lower anvil also features a quench device, which consists of an ejection arm that is used to push the sample into a hole on the side of the anvil. The latter is connected to a hollow anvil column, which leads to a water bath through a door in the

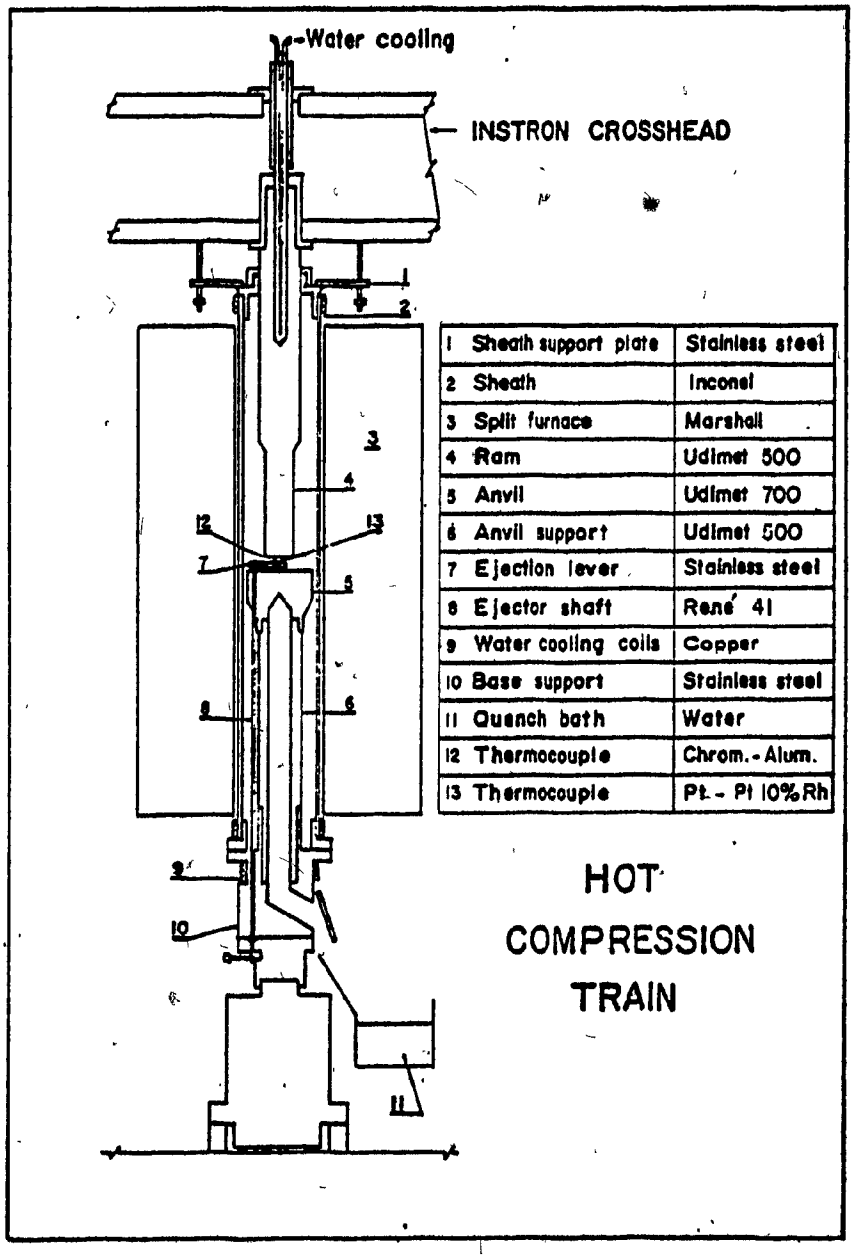

1	Sheath support plate	Stainless steel
2	Sheath	Inconel
3	Split furnace	Marshall
4	Ram	Udimet 500
5	Anvil	Udimet 700
6	Anvil support	Udimet 500
7	Ejection lever	Stainless steel
8	Ejector shaft	Rene' 41
9	Water cooling coils	Copper
10	Base support	Stainless steel
11	Quench bath	Water
12	Thermocouple	Chrom.-Alum.
13	Thermocouple	Pt - Pt 10%Rh

FIGURE 3.1 Cross-section of the hot compression train.

base. The temperature is measured by an Inconel sheathed chromel-alumel thermocouple placed close to the sample and connected to a Thermo-Electric digital display meter.

The whole testing train is enclosed in an Inconel tube. The test chamber is sealed by means of "O" rings. The chamber and testing train are heated by means of a platinum-wound split furnace. The test chamber permits tests to be carried out in a controlled atmosphere, or in a primary vacuum. In order to insert a sample, the Instron crosshead is raised, thus raising the furnace, the test chamber and the upper anvil. The sample is then placed with tweezers on the lower anvil and the crosshead lowered again until the test chamber is closed.

3.2.2 Temperature Control

The heating unit consists of a platinum-wound, three-zone split furnace, with a maximum power rating of 7.8 kVA. Control is achieved by means of a Leeds-Northrup Electromax II current-proportioning temperature controller, which drives three independent SCR power controllers. Control of the temperature during a test is kept to within $\pm 3^{\circ}C$ of the desired temperature by this means. A diagram of the temperature control system is given in Figure 3.2.

3.2.3 Atmosphere Control

The standard atmosphere consists of high purity argon*, which is passed through drying columns in order to eliminate moisture. The gas

---

* Supplied by Liquid Air of Canada Ltd., with the following impurities: O_2 = 10 ppm; N_2 = 23 ppm; H_2 = 2 ppm; CO_2 = 0.5 ppm; H_2O = 5 ppm; and hydrocarbons > 0.5 ppm.

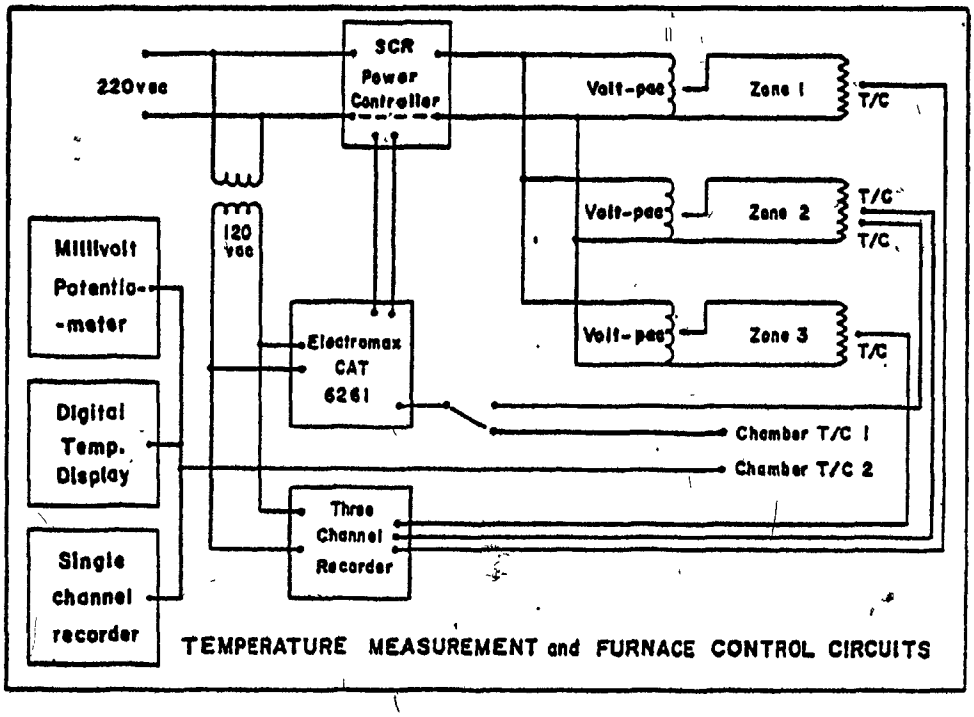

FIGURE 3.2 Schematic diagram of the furnace control circuit.

is kept flowing at a rate of about 30 cm^3/min and is allowed to escape to atmosphere through an oil trap. The gas pressure in the chamber is always kept slightly greater than the outside pressure so as to prevent back diffusion of air through the seals and small leaks. This atmosphere has proved to be satisfactory for the testing of most materials (copper and its alloys, carbon steels, HSLA steels, pure zirconium), but was found to be insufficiently pure for zirconium-molybdenum alloys (Chapter 5). Some possible causes of the presence of oxygen in the chamber are: back diffusion through the "O" ring seals, desorption of gases from the tooling, decomposition of oxides formed on the tooling and in the chamber (chiefly nickel oxide), and decomposition of some glasses (such as those containing PbO).

The best method for solving this environment problem is, of course, to have a testing system in which the chamber can be evacuated down to 10^{-6} torr or less. However, the present system could not be adapted to such standards without extensive modification and redesign. The first improvement in the atmosphere was achieved by removing the remaining oxygen in the incoming high purity argon. This was done by flowing the argon over a bed of zirconium chips placed in a silica tube and heated up to about 900°C. This procedure, however, was felt to be insufficient, since minute amounts of oxygen released in the chamber can produce a significant oxygen concentration increase over the sample surface, as its volume is very small compared to that of the chamber.

Consequently, for the tests that were carried out under the highest purity atmosphere, a thin-walled zircaloy tube of about 6 cm in diameter and 15 cm in height was placed around the upper anvil. This tube had the function of absorbing most of the oxygen that was left in the

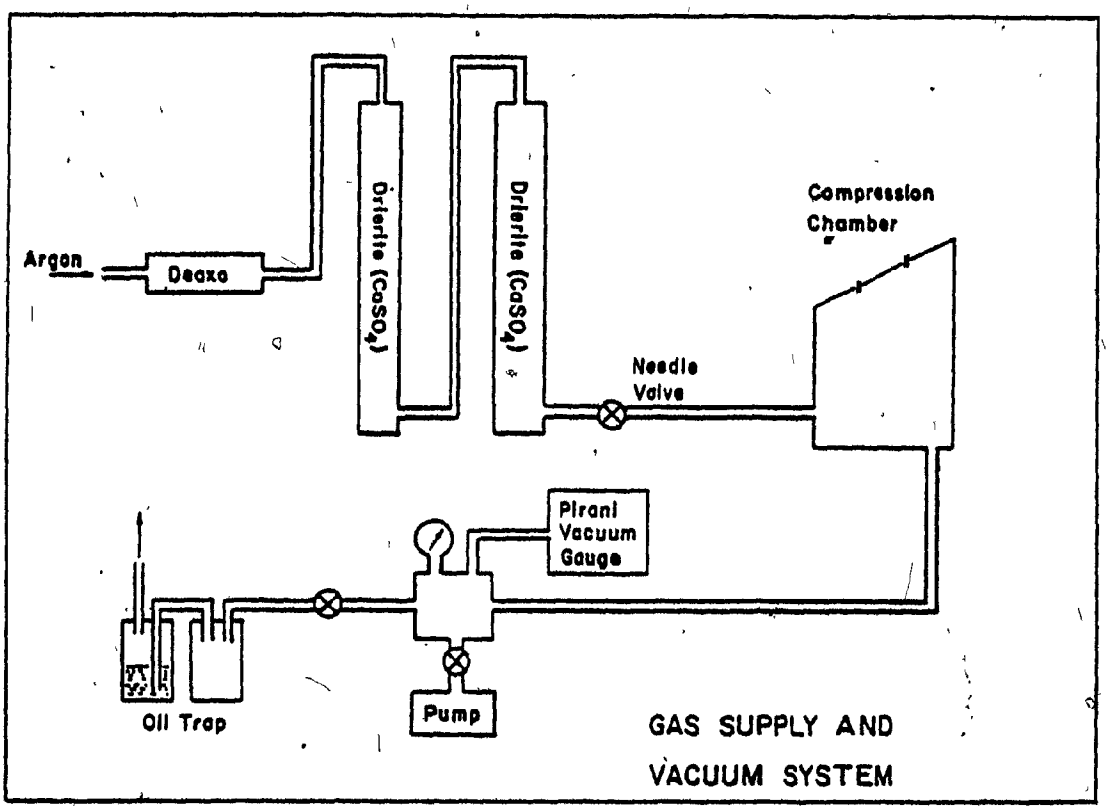

FIGURE 3.3 Schematic diagram of the vacuum and argon supply system.

testing chamber, so that very little could be picked up by the sample. The surface area of the tube was about 500 cm^2, which was about 500 times that of the sample. In this way, the oxygen pick-up of the sample could be reduced to 1% of its previous value, assuming oxygen pick-up per unit area to be identical for the tube and the sample. This gettering system proved to be very effective. A diagram of the vacuum and gas system is shown in Figure 3.3. For the tests carried out under the highest purity argon the sample was always inserted in the chamber while the latter was at room temperature.

3.3 STRAIN RATE CONTROL

The flow stress of metals at high temperatures is very sensitive to strain rate. However, a constant deformation rate (i.e. dh/dt) does not produce a constant true strain rate. In the case of compression, a constant deformation rate causes the true strain rate to increase continuously during the test. The true strain rate is defined as $\dot{\epsilon} = dh/hdt$ where h is the height of the sample at any instant. The true strain rate can therefore be kept constant by causing the deformation velocity to be proportional to the instantaneous sample height.

The Instron machine was equipped with a constant strain rate apparatus (CSRA) designed and built at McGill by Luton, Immarigeon and Jonas (201), which operates in conjunction with an Instron variable speed unit. In the variable speed unit, the crosshead speed is proportional to the angular position of a 10 turn potentiometer. The CSRA converts the linear displacement of a probe following the crosshead position into an angular motion imparted to a potentiometer replacing that of the variable speed unit. A speed decrease proportional to the crosshead displacement

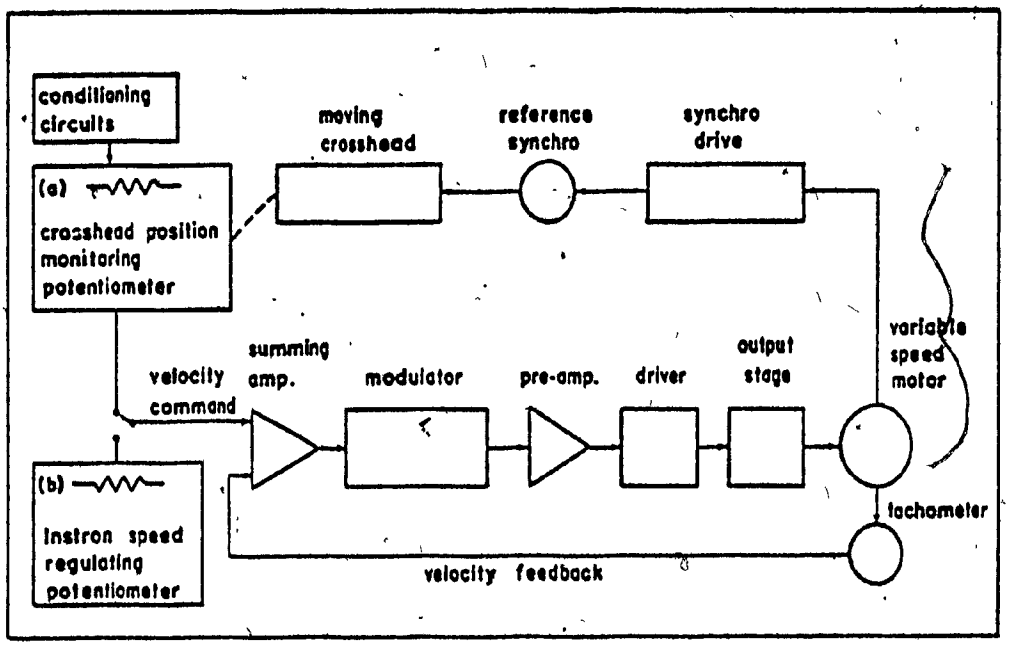

FIGURE 3.4 Block diagram of the crosshead speed control system incorporating the constant true strain rate device.

is thus achieved. By means of conditioning circuits and mechanical adjustments, a variation of crosshead speed from the nominal strain rate to zero can be achieved by moving the crosshead from the point where the ram first touches the sample to the contact point with the lower anvil. A schematic view of the CSRA is shown in Figure 3.4. The performance of the CSRA is very good, as far as keeping the crosshead velocity proportional to the sample height is concerned, assuming perfectly stiff anvils. However, the deflection of the anvils during the initial loading part of the stress-strain curve leads to the specimen strain rate differing from the nominal one by as much as 20%. Nevertheless, at low strain rates and high temperatures, the error drops to less than 1%. A more detailed discussion of the system is available elsewhere (202).

3.4 COMPUTER MONITORING AND AUTOMATIC DATA ACQUISITION

To obtain true stress-strain curves from the load-displacement curves on a paper chart is tedious work. It consists of reading from the chart a large number of data pairs, one for load and one for displacement, and then punching them onto data cards, in order to get eventually a plot of the true stress-true strain curve with the aid of a suitable computer program. In the present experiments, fortunately, such a problem was avoided because the Instron was interfaced with a remote Canadian General Electric 4020 process control computer. The computer is used to perform two types of duties: control of the test and monitoring and acquisition of the load and displacement data.

3.4.1 Test Control

Computer control of the Instron test machine is achieved by means of a relay interface unit resident in the Instron and the Multiple

Output Controller (MOC) of the GE 4020. The control functions of the Instron, such as UP, DOWN, STOP, and RETURN are produced by the coded positions of three switches in the MOC. This code is interpreted by the interface unit which then causes the Instron to perform the desired function.

3.4.2 Test Monitoring

If, for example, the DOWN mode is required on the Instron, the main program generates the proper OUT command at the MOC (Multiple Output Controller). This activates the 5V TTL (Transistor to Transistor Logic), which in turn transmits the excitation voltage required to switch on the desired mode. For a continuous test at a constant true strain rate, the computer program sends the DOWN command to initiate the test, and when the test is completed (that is, after the time to produce a given strain has elapsed), sends a STOP command, followed by UP, STOP and eventually NORMAL, which restores the machine to manual operation.

3.4.3 Data Acquisition

The original 100 kN Instron load cell was of too large capacity for the present experiments. We used instead a 25 kN Lebow load cell*, whose output signal was amplified 100 times by a conditioning circuit. The displacement was measured by a Direct Current Displacement Transducer (DCDT) manufactured by the Hewlett-Packard Co. Ltd., and which gives a DC

---

* Manufactured by Lebow Associates Ltd., Troy, Michigan. Sensitivity 2 mV/V_{exc} at rated capacity, linearity 0.2% full range, repeatability 0.05% of capacity.

output signal that does not require further amplification. The readings of these signals were taken via a multiplexed analog-to-digital converting system. This consisted of a VIDAR 610 low level scanner, whose purpose was to select the proper channel to be read, followed by a VIDAR 521 integrating digital voltmeter. The two signals (load and displacement) cannot be scanned simultaneously with such an arrangement, and so scanning must be effected sequentially. The time lag involved between the two scans was 1.66 ms in the present case. This was considered to be of no effect, for practical purposes, since the error involved was negligible compared to the uncertainty in the load and displacement.

The main program obtained load and displacement readings with the scanning system in the following way. A scanning instruction generated an OUT command at the MOC (scanning group). A TTL logic circuit activated the low level scanner which identified the channel to be read (250 for load), the nature of the signal (3 for voltage) and its magnitude (say 1000 mV), according to the instruction. The signal was then fed into the digital voltmeter, and an IN command transferred the signal value into core memory. Figure 3.5 shows a block diagram illustrating the test monitoring and data acquisition system. Figure 3.6 shows a drawing of the load conditioning circuit. The gain of the load amplifier was adjusted to 100 with an external resistor, and the Cal button, placing a resistor on one of the arms of the load cell bridge, was used to check the overall calibration.

3.5 DATA RETRIEVAL

The conversion of the data into stress-strain curves was achieved by means of a plotting program. This program, designed by Luton, took the load and displacement values into core memory, then converted them into

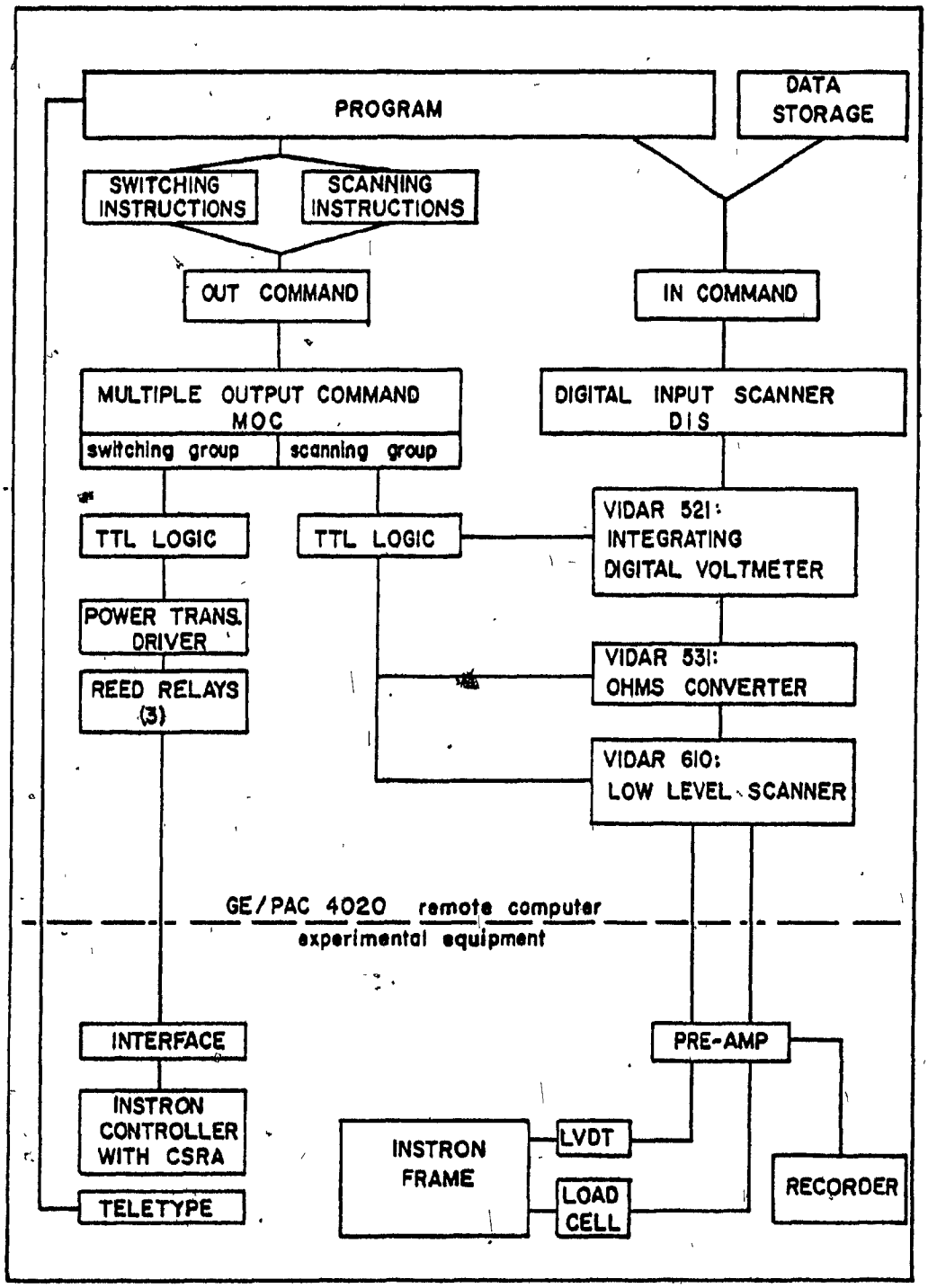

FIGURE 3.5 Schematic diagram of the test monitoring and data acquisition system.

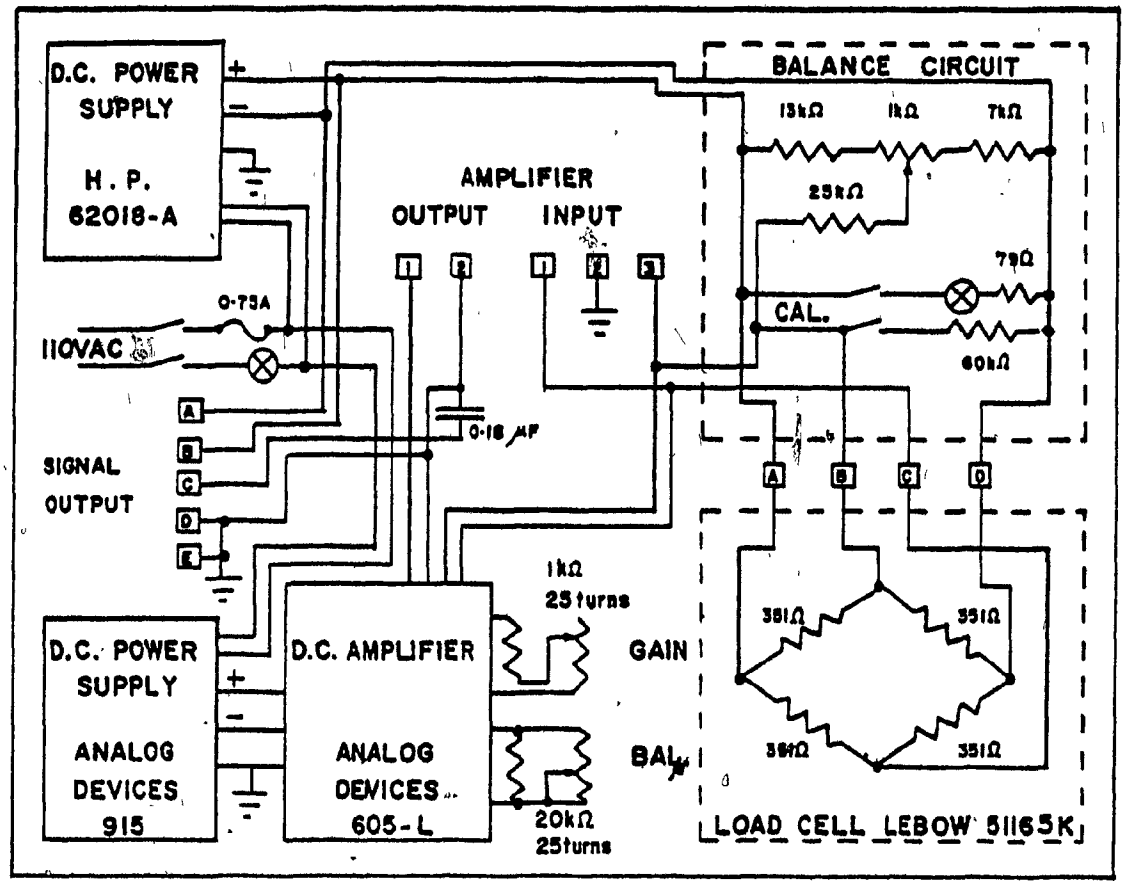

FIGURE 3.6 Drawing of the load conditioning circuit.

loads and displacements, the latter being corrected for the elastic distortion of the anvils. The load and displacement values were then turned into stress-strain data and plotted by means of a digital plotter. The plotting program also offered an expanded plot of the first 0.10 strain which allowed precise determination of the yield values. The data in the core memory were transferred onto a 1/2 inch magnetic tape*, on which they were kept for further use such as later plotting on a normalized scale.

3.6 ERRORS AFFECTING THE STRESS AND STRAIN VALUES

3.6.1 Errors Associated with the Testing Apparatus

The strain ε is obtained through the relation

$$\varepsilon = \ln \frac{h_o}{h} \tag{3.1}$$

where h_o is the initial height of the sample and h the instantaneous height. An error in strain can arise because of the uncertainty in h. The error in strain can, in turn, affect that of the stress σ which is calculated from the relation

$$\sigma = \frac{L}{A} = \frac{L}{A_o} \exp(\varepsilon) = \frac{L}{A_o} \frac{h_o}{h} \tag{3.2}$$

where L is the load, A_o the initial cross section of the sample and A its "instantaneous" cross section.

---

* BASF storage tape.

3.6.1.1 Error in the determination of the strain

The first error involved in this calculation is simply associated with the accuracy and sensitivity of the displacement transducer. The unit used was a Hewlett-Packard model 7DCDT-500, which is a linear displacement transformer having a non-linearity less than 0.5% of the total stroke (0.5") and an electrical output of 3.3 Volts full-scale. The non-linearity may therefore introduce a systematic displacement error of the order of 50 μm at the most. It is the sensitivity of the digital voltmeter that in theory limits resolution of the displacement. In practice, however, owing to some noise and some drift, it was found that displacements of less than 25 μm could not be determined reliably.

The second error arises from the way the height of the sample is calculated. The plotting program takes as the start of the deformation the displacement for which the load is 1% of the maximum load. Calculation of the sample height then involves subtracting from the output voltage at a given time t that at the onset of deformation, and multiplying this difference by the calibration factor. In this way the error n is twice that of any particular displacement reading and is about 50 μm. At large strains, when the displacement exceeds 5 mm, the error in the strain is very small; however, at low strains

$$\Delta\varepsilon \sim \frac{\Delta(h_o-h)}{h_o} \qquad (3.3)$$

and thus $\Delta\varepsilon \sim 4\times10^{-3}$. The absolute error is thus not very significant, even at low strains.

3.6.1.2 Error in the determination of the stress

This error has two components, one which arises from the load cell itself and another that comes from the error in the strain. The load cell that was used has a capacity of 25 kN and has a non-linearity of less than 0.5% of full scale. The sensitivity is 2 mV/V excitation at rated capacity. In the present application, the non-linearity could be as high as 125 N and the sensitivity, for a 17 V excitation voltage and after an amplification of 100, 0.14 mV/N.

The resolution is, in theory, that of the voltmeter which was 0.1 mV on a 100 mV scale or 1 mV on a 1000 mV scale, and should lead to a resolution of 1 N and 10 N, respectively. Practically, however, there was some noise pick-up on the signal line as well as some drift in the output, which raised the effective minimum measurable load to about 30 N. In terms of stress, this value corresponds to a stress of about 0.5 MN/m^2 when a sample of circular cross-section having a diameter of 8.6 mm is tested.

The error in strain affects the stress through the correction for the cross-section area (Equation 3.2) and as a consequence,

$$\frac{\Delta\sigma}{\sigma} = \frac{dh}{h} \qquad (3.4)$$

Thus, the value of the relative error in stress varies from 0.4% at the onset of deformation to 0.8% at 0.7 strain.

3.6.1.3 Error in the strain rate

The true strain rate device which was used to achieve a constant true strain rate constituted a fairly stable and reliable piece of equipment

and its calibration was checked regularly. The calibration itself can be done only when the sample height is being measured, so that the position of the upper anvil with respect to the sample top is known. This was done by bringing the anvils in contact, the contact being detected by a load increase. Prior to the sample insertion, a reading was taken of the linear transducer voltage V_o. In order to determine the position of the upper anvil once the sample was inserted, only a reading of the voltage V_1 of the displacement transducer was necessary, as the gap G between the top of the sample and the upper anvil could then be obtained from:

$$G = (V_1 - V_o) \times D_{cal} - h_o \tag{3.5}$$

where D_{cal} is the DCDT conversion factor from volts to mm.

The error involvediin calculating G was essentially that of estimating the contact between the anvils, which was about ±250 μm. The true strain rate, $\dot{\varepsilon}$, determined from $\dot{\varepsilon} = \frac{CHS}{h_o}$ where CHS is the nominal crosshead speed, was modified by the error in G in that the calibration was effected as if the sample was not of a height h_o, but $h_o + \Delta G$. Thus,

$$\frac{\Delta\dot{\varepsilon}}{\dot{\varepsilon}} \approx \frac{\Delta G}{h_o} = 1.8\% \tag{3.6}$$

The error in the strain rate affected in turn the stress through the rate sensitivity n and taking $n = \frac{1}{4}$,

$$\frac{\Delta\sigma}{\sigma} = 0.4\%$$

3.6.2 Errors Involving the Sample Geometry

3.6.2.1 Effect of lubrication

Some tests were carried out on crystal bar zirconium at 1000°C, at a strain rate of $1.5 \times 10^{-3} s^{-1}$ in order to investigate the effect of glass lubricant viscosity on the mechanical properties. The samples were placed in the hot chamber preheated for 1/2 hour at 1000°C and tested under a dynamic high purity argon atmosphere. The glasses used were those manufactured by Corning Glass Ltd. and glasses of various viscosities, as well as mixtures of glasses were tried out. The stress-strain curves obtained in this way are shown in Figure 3.7. The numbers are arranged in order of decreasing viscosity; and the glass numbers refer to those in Figure 4.6.

The curves show that there is no systematic variation of apparent flow stress with glass viscosity in the range investigated, whether one considers yield stress, steady state stress, or any other stress. Repeats were done on glasses #7050 and #0010. The scatter in the stress values under nominally identical testing conditions was about 0.5 MN/m^2, and appeared to be higher than any viscosity effect. Sample deformation was least homogeneous for the most viscous glass (#1720), and for a very fluid glass (#9776) which was tried out as well. It was noted in a few cases that towards the end of the deformation, the stress increased markedly. This can be attributed to the breakdown of the glass lubricant film. The results of Figure 3.7 thus indicate that, even if the material flows in an inhomogeneous manner, the mechanical properties as measured are not significantly altered. At 1000°C, it appears that glass #0010 is the best one, with a viscosity of 10,000 poises.

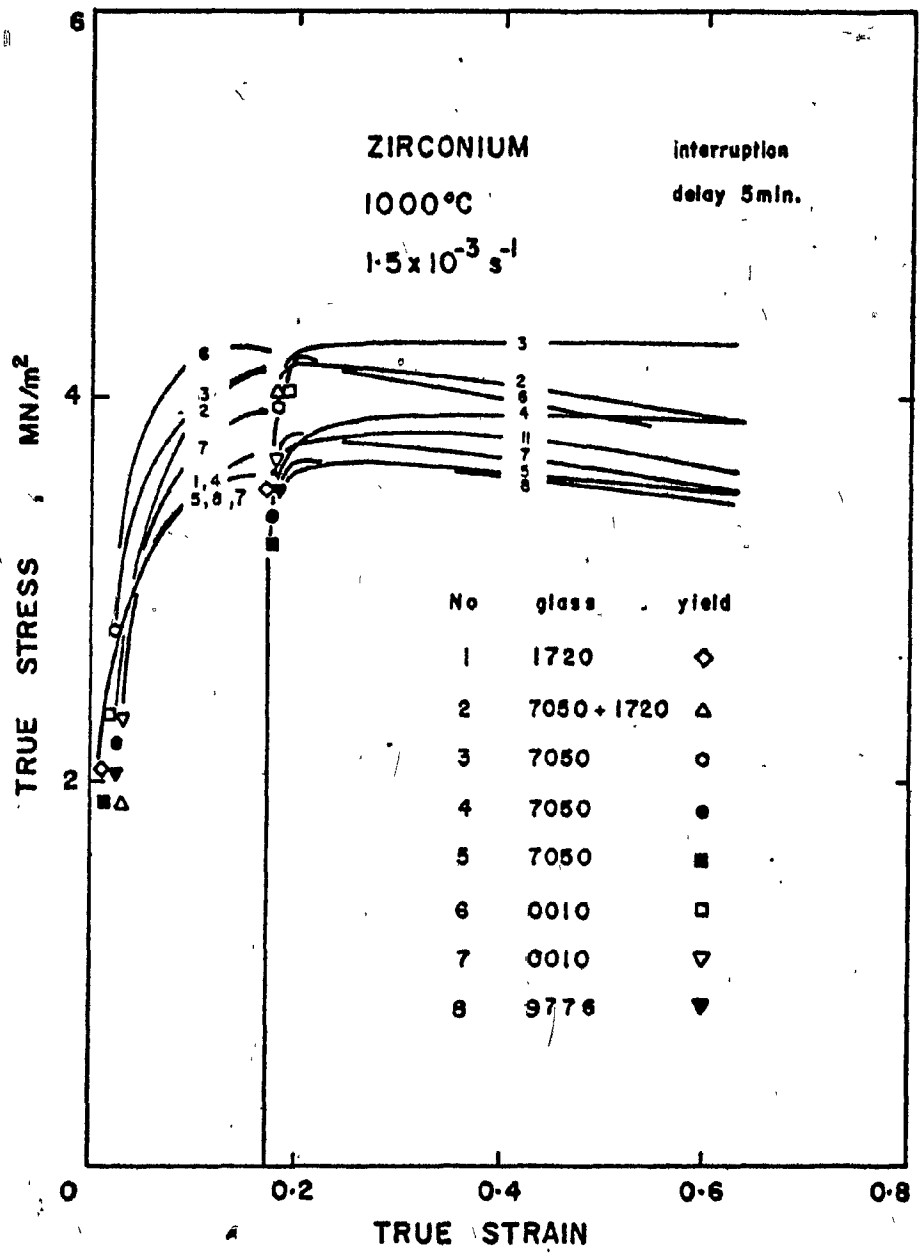

FIGURE 3.7 Effect of lubricating glass viscosity on the stress-strain curve of zirconium at 1000°C.

3.6.2.2 Effect of groove geometry

The groove geometry was patterned after that of Luton (4), who showed that for the hot compression of cylindrical samples, a trapezoidal groove section gave the best results.

3.6.2.3 Effect of anvil hardness

Under ideal testing conditions, the anvil surface is perfectly hard. In early tests, where ceramic inserts were not used, but Udimet superalloy constituted the anvil surface, imprints of the sample could sometimes be detected on the anvil after deformation. This resulted in poor flow of the sample and a slight error in the displacement values. As soon as this problem was recognized, a ceramic insert was mounted on the anvils and completely suppressed this effect.

3.6.3 Error Bars

In summary, the errors due to instrumentation lead to the following uncertainties

$\Delta\varepsilon = 4\times10^{-3}$

$\Delta\sigma = -0.5$ MN/m^2 0.8 to 1.2%, consisting of the following three components: first an absolute component arising from the resolution of the load cell - $\Delta\sigma \approx 0.5$ MN/m^2; second, a relative component derived from the strain error - $\Delta\sigma/\sigma = 0.4\%$ at low strains to 0.8% at high strains; and third, a component arising from the strain rate error - $\Delta\sigma/\sigma = 0.4\%$. The relative error in the stress values thus hardly exceeds 1%. On the other hand, Figure 3.7 shows that the repetition of a test under similar conditions

of temperature, strain rate, lubrication, and preheat yields an uncertainty of about 0.8 MN/m^2, i.e. somewhat in excess of that predicted by the calculated error bars, suggesting that specimen inhomogeneities are also involved.

A check of the repeatability and accuracy of the overall testing equipment and procedure was carried out by testing several samples of 304 stainless steel under similar conditions. This material is very resistant to oxidation and has a mechanical behaviour known and characteristic of dynamic recovery. The flow stresses were found to be around 100 ± 2 MN/m^2, which was considered very satisfactory.

CHAPTER 4

EXPERIMENTAL MATERIALS AND PROCEDURES

4.1 EXPERIMENTAL MATERIALS

4.1.1 Crystal Bar Zirconium

Crystal bar zirconium, supplied by Atomic Energy of Canada Ltd., was manufactured by the Wah Chang Corp., Albany, Oregon. The metal was supplied in the form of 15 mm square bars about 35 cm long, cut from a worked ingot. The chemical analysis of the as-received material is given in Table 4.1.

4.1.2 Zirconium-Molybdenum Alloys

These alloys were supplied by Atomic Energy of Canada Ltd., and manufactured by Westinghouse Canada Ltd. Each composition was prepared in ∿2 Kg buttons, which were twice arc-melted under vacuum so as to insure a satisfactory homogeneity. In spite of these precautions, however, some composition inhomogeneities were still present, but were somewhat reduced in the forming process. The buttons were hot swaged to 9.5 mm bars in about 10 passes, after having been clad with copper to minimize oxidation during the process. The compositions and oxygen analyses are given in Table 4.2. The oxygen concentration is quite low, but there is a considerable spread in the molybdenum content.

4.1.3 Zirconium-Niobium Alloys

The zirconium-niobium alloys were made by the Wah Chang Corp., Albany, Oregon. The 2.5% Nb alloy was part of their standard stock, whereas the high Nb alloys were specially made in 100 lb ingots.

TABLE 4.1

Chemical Analysis of the Crystal Bar Zirconium

Element	Impurity Analysis (ppm)
Al	< 25
B	< 0.2
C	50
Cd	< 0.3
Co	< 5
Cr	42
Cu	< 25
Fe	376
H	9
Hf	135
Mg	< 5
Mn	< 10
N	34
Ni	32
O	160
Pb	< 5
Si	< 40
Sn	10
Ti	< 20
U	< 0.5
W	75

TABLE 4.2 Chemical Analysis of the Zirconium-Molybdenum Alloys

Element	Nominal Molybdenum Concentration 1.9 (weight %)	4	6
Mo	1.9 - 3.5	3.64 - 4.10	5.6 - 6.11
	Impurity Analysis (ppm)		
O	1210	1290	1165
N	38	60	40
Al	8	20	20
B	<0.2	<0.2	<0.2
Ca	<20	<20	<20
Cd	0.25	0.25	0.25
Co	20	20	20
Cr	50	50	50
Fe	100	120	100
Hf	50	100	80
Mg	<10	<10	<10
Mn	15	15	10
Nb	<10	<10	<10
Ni	<10	<10	<10
Pb	< 5	< 5	< 5
Si	20	30	30
Sn	5	5	5
Ta	80	100	80
Ti	<10	15	<10
V	< 5	< 5	< 5

The detailed chemical analyses of the Nb alloys are given in Table 4.3. The compositions appear to be close to the 2.5, 10, 15 and 20% Nb specified and do not vary very significantly over the ingot. Apart from the fairly high oxygen content, the alloys seem to be reasonably satisfactory as far as impurities are concerned.

The ingots were formed into 9.5 mm cylindrical rods by hot extrusion and swaging.

4.2 SPECIMEN PREPARATION

The compression samples were cylinders machined on a lathe from the as-received bars. The end faces were grooved to promote proper lubrication of the contact surfaces.

The sample geometry is given in Figure 4.1. The height of the samples, 13.8 mm, was chosen as being the best height for optimal performance of the constant true strain rate apparatus. The diameter of the sample was chosen to be 2/3 of the sample height, on the basis of successful experiments by Uvira (11) and Luton (4,17).

The choice of flat-bottomed grooves was based on the results of Luton (4,17) who obtained the best lubrication for this particular sample geometry. The grooves were machined with a thread chaser which had had 16 μm ground off the tips of the teeth.

4.3 SPECIMEN PLATING

In the experiments carried out on the Zr-Mo alloys, it was found (Section 5.1) that residual oxygen in the atmosphere affected the mechanical properties. Specimen plating offered one method of assessing the environment effects and of reducing environment interactions. Two types of pro-

TABLE 4.3

Chemical Analysis of the Zirconium-Niobium Alloys

Element	Alloy Analysis (weight %)			
Nb	2.5	10.3	15.1	19.6
	Impurity Analysis (ppm)			
Al	< 20	< 35	< 35	< 35
B	< 0.2	< 0.25	< 0.25	< 0.25
C	110	100	90	80
Cd	< 0.2	< 0.25	< 0.25	< 0.25
Co	< 10	< 10	< 10	< 10
Cr	58	103	95	< 80
Cu	< 20	12	18	17
Fe	420	668	707	398
H	10	13	18	18
Hf	105	< 80	< 80	< 80
Mg	< 10	< 20	< 20	< 20
Mn	< 20	< 25	< 25	< 25
Mo	-	< 25	< 25	< 25
N	45	13	18	18
Ni	< 35	< 35	< 35	< 35
O	1060	1330	1580	1370
Pb	< 20	< 50	< 50	< 50
Si	< 30	71	< 60	78
Sn	< 25	< 20	< 20	< 20
Ta	-	< 200	< 200	< 200
Ti	< 20	< 25	< 25	< 25
U	< 1	< 0.5	< 0.5	< 0.5
V	< 20	< 25	< 25	< 25
W	< 50	< 25	< 25	< 25

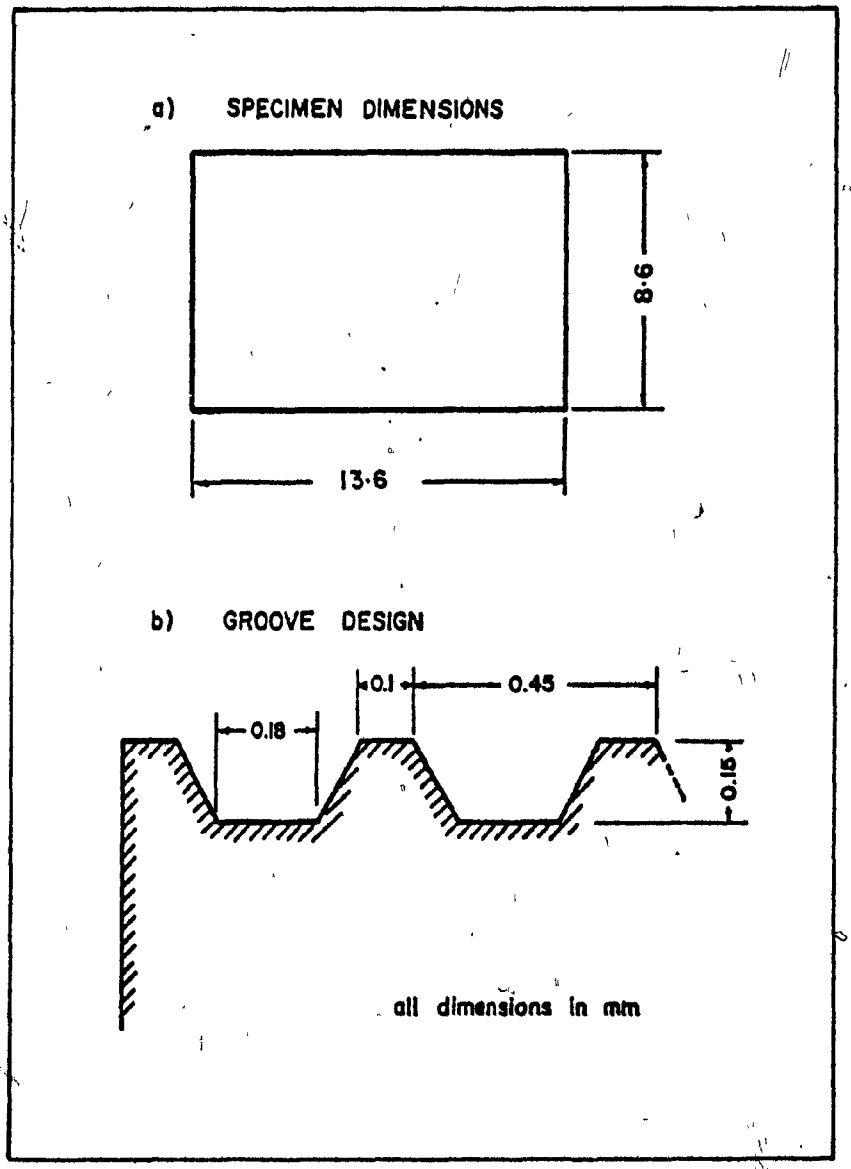

FIGURE 4.1 Drawing of the sample showing dimensions and lubrication grooves geometry.

tective coating were tried; these were copper plating and chromium plating. Copper plating could be used for testing below 900°C on zirconium. The upper limit of temperature arises because of the existence of a liquid phase in the binary Cu-Zr phase diagram. Such a liquid phase is to be avoided since diffusion can occur orders of magnitude faster in a liquid phase than in the solid state, and as a consequence no protection is ensured by the coating. For higher temperature tests, however, chromium could be safely used up to 1370°C, at which a liquid phase is formed. The thickness of the coatings was kept below the thickness that would contribute 1% to the maximum load, assuming simple load sharing between the coating and the sample. The plating thickness e was estimated from the increase in weight Δm of the sample, through the relation:

$$e = \frac{2\Delta m}{\rho(2\pi d_o h_o + \pi d_o^2)} \qquad (4.1)$$

where ρ is the density of the deposited metal and d_o and h_o are the diameter and height of the sample, respectively. The above equation neglects the surface area variation introduced by the grooves present at the ends of the sample. No check was carried out to assess uneven coating thickness or coating porosity other than low magnification microscopic examination. The latter defect was considered to be likely to occur in the chromium plate.

Copper plating was achieved in a solution of the following composition:

copper sulfate:	75 g/l	
sulfuric acid:	187.5 g/l	(∿10% volume)
chloride (typically HCl):	50 ppm	

and a brightener, Lea-Ronal Copper Gleam PC*: 1.2% by volume

The other plating conditions were:

temperature:	24°C
agitation:	moderate
current density:	20 mA/cm^2
anode:	OHFC copper
filtration:	intermittent

These plating conditions yielded a very bright and ductile deposit. The deposition rates were very high, typically of the order of 7 μm per minute.

Chromium plating was achieved with a commercial solution known as SPS 515 SELECTRON†, which had a good throwing power and yielded the best results. The solution was used under the following conditions:

temperature:	∿ 60°C
agitation:	the sample was rotated slowly during the process to get a more uniform plating
current density:	200 mA/cm^2

The computed thicknesses deposited in this way never exceeded 1-2 μm. The surface finish remained dull, indicating rather uneven deposition. However, these coatings proved to be reasonably effective in minimizing oxidation (see Figure 5.13 below).

A last type of coating used on the Zr-Nb alloys was ≈1 μm gold. This plating was carried out by Electro-Loh Plating Company, and yielded a bright shiny finish.

---

* Manufactured by Lea-Ronal, Inc., 272 Buffalo Avenue, N.Y. 11520 (U.S.A.).
† Manufactured by SELECTRONS LTD., 116 East 16th Street, N.Y. (U.S.A.).

4.4 HIGH TEMPERATURE LUBRICANTS

Lubrication must be provided during compression testing in order to suppress or minimize the inhomogeneous flow that results from the friction between the anvils and the specimen end surfaces. Powdered glass lubricants have been successfully used for this purpose (4,10).

The optimum flow conditions are met when the glass is not too fluid, thereby being retained in the sample grooves. On the other hand, it must not be too viscous in order to be able to flow properly. This ideal viscosity lies around 10^4 poises (203) but it does not, as seen in Section 3.6.2.1, prove to be a very sensitive parameter.

The glasses employed for lubrication were manufactured by Corning Glass Ltd. and were supplied in a -325 mesh powder. Figure 4.2 gives the manufacturer's data on the viscosity of the various glasses as a function of temperature.

The powdered glasses were placed in suspension in acetone, and the mixture was applied to the specimen ends with a brush. Care was taken to avoid the painting of any glass on the specimen sides.

4.5 TESTING PROCEDURE

Prior to a series of tests, the testing chamber was heated up to the desired temperature. The anvils were then manually brought to contact, the contact point being determined by the increase of the load signal to a value corresponding to about 50 lbs. The linear displacement transducer output V_o was then read by the digital voltmeter and stored, using a special computer program.

At this point the sample was ready to be placed onto the lower anvil. This was done by raising the crosshead, thereby lifting the upper

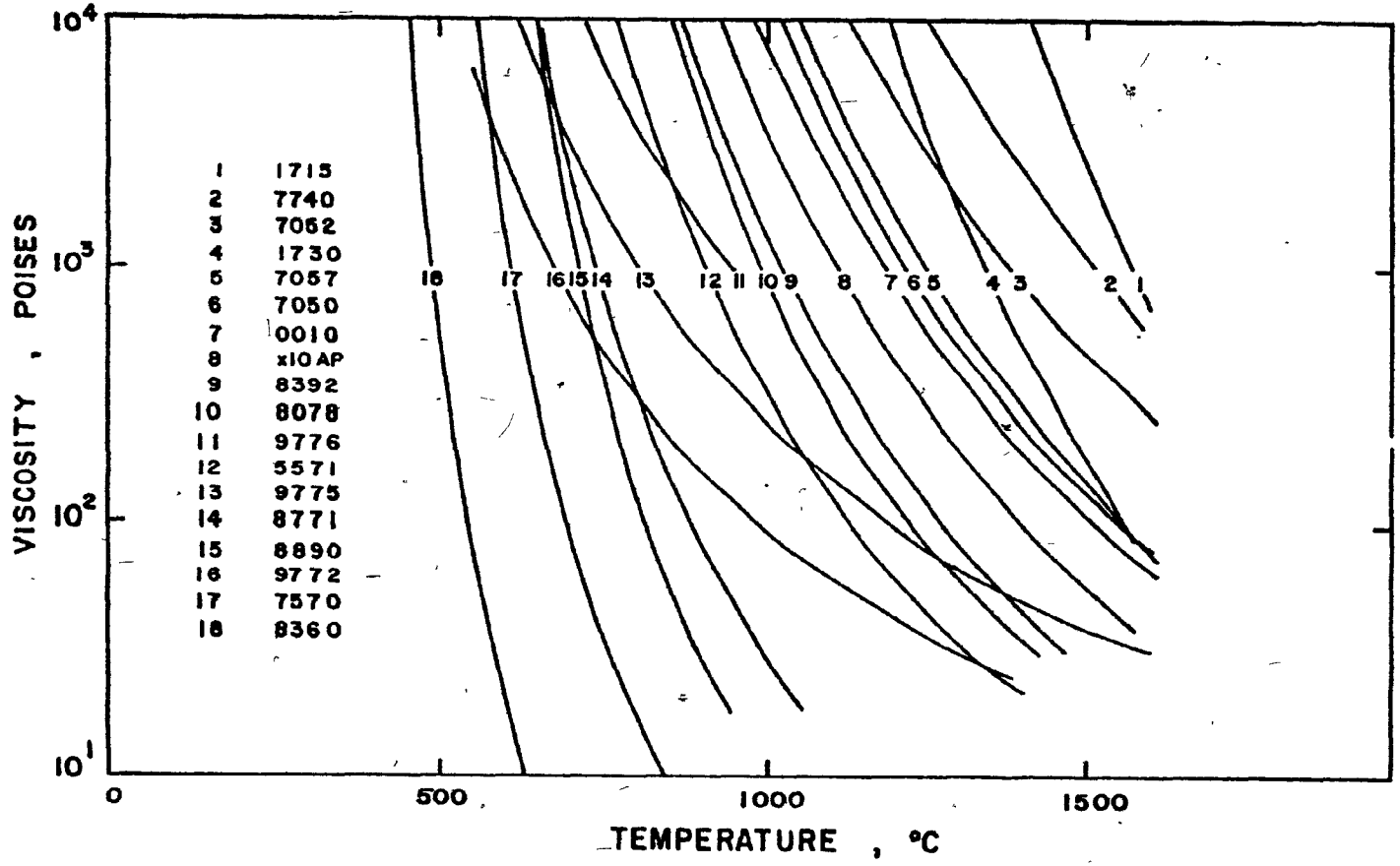

FIGURE 4.2 Plot of viscosity versus temperature, for various Corning Glass lubrication glasses.

anvil, the chamber enclosure sheath and the furnace. After the sample, having been lubricated at both ends, had been placed in position with tweezers, the crosshead was lowered. As soon as the chamber was closed, the chamber was evacuated by means of a vacuum pump, then high purity argon was flushed into the chamber. The pump down-flush sequence was repeated three times to insure that no air was left in the testing chamber.

When the chamber had again reached the set temperature, the calibration adjustments were carried out, and the test parameters were entered into the computer in a conversational mode, through a teletype. The calibration of the constant strain rate device was done once the gap G between the upper anvil and the sample was determined by the computer. The test program calculated this quantity after the computer had converted the linear transducer output V by means of the relation

$$G = (V - V_o) \times D_{cal} - h_o$$

In addition, the program displayed pertinent data such as test duration, maximum crosshead travel, and the number of data points determined. When calibration was completed, the compression test was initiated simply by pressing the break button on the teletype. The test was then started and performed automatically. At the end of the test, when the load was removed, the sample was manually quenched into a water bath by actuating the quench lever arm.

CHAPTER 5

EXPERIMENTAL RESULTS

This chapter describes, in a first part, the experimental results obtained on the zirconium-molybdenum alloys. The second part is devoted only to the behaviour of zirconium-2.5% niobium, since the mechanical response of this alloy differs markedly from that of the higher niobium alloys. The latter results are presented in a third part.

5.1 ZIRCONIUM-MOLYBDENUM ALLOYS

5.1.1 The Flow Curve

The true stress-true strain curves determined for zirconium-molybdenum alloys exhibit a maximum in stress which usually takes place after a small work-hardening region. With further increases in strain, the flow stress decreases continuously up to the maximum applied strain of 0.8. Typical stress-strain curves are shown in Figure 5.1. The extent of the work-hardening region was found to increase with the strain rate and thus was minimal at low strain rates. Some tests showed a marked stress drop at the onset of plastic flow; this was followed by the behaviour described above. The upper yield point and stress drop usually obscured part of the work-hardening region. On the other hand, the curves obtained in some cases showed no work-hardening at all.

For practical reasons, the maximum strain achieved was typically 0.8. The curves show that even at such strains, the flow softening persisted although not to such a marked extent as during the earlier stages of deformation. It was also observed that, at a strain rate of $1.5 \times 10^{-3} s^{-1}$,

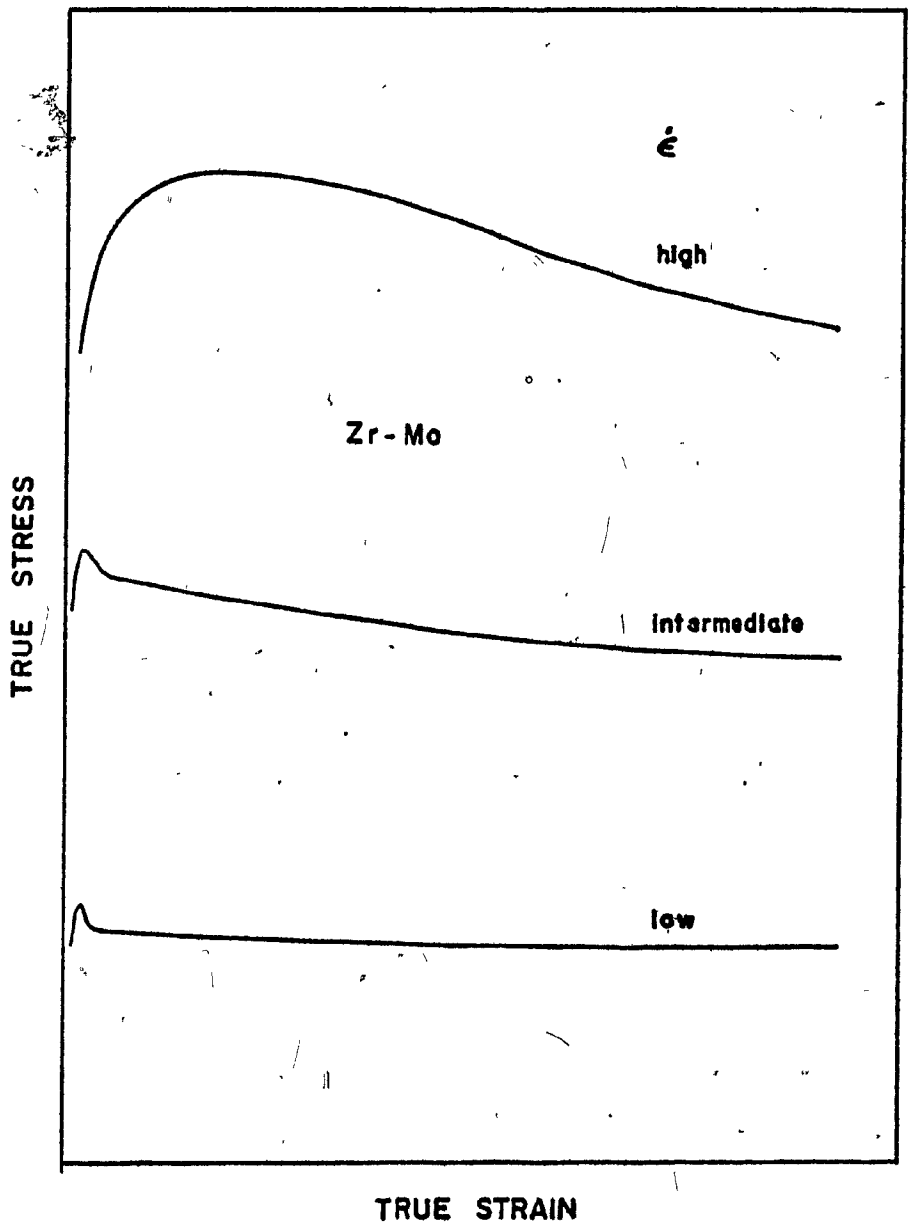

FIGURE 5.1 Schematic representation of the stress-strain curves of Zr-Mo alloys in the β-phase

the initial rates of work-hardening are very high, typically of the order of 2100 MN/m^2 compared with 280 MN/m^2 in unalloyed zirconium.

5.1.2 Effect of Strain Rate on the Flow Curves

Figures 5.2, 5.3, 5.4 and 5.5 show the stress-strain curves obtained at strain rates varying between 6.2×10^{-5} and $1.5 \times 10^{-1} s^{-1}$, for alloys containing 0, 1.9, 4.0 and 6.0% molybdenum, respectively, and tested at 1000°C. The preheat time in the furnace was kept constant for all tests and was equal to 30 minutes.

It is clear that the stress level at any strain is strongly affected by strain rate; the higher the strain rate, the higher the stress. Some of the curves indicate a slight increase in stress at large strains. This effect is most probably due to a breakdown of the lubricating glass film towards the end of the test. The yield and steady state stress data obtained from the stress-strain curves are given in Tables 5.1-5.4. Yield stresses were obtained by means of the 0.2% offset method, using the expanded plots of the first 10% strain of the flow curves. The overall stress sensitivity of the strain rate n can be defined as $n = (d\log\dot{\varepsilon}/d\log\sigma)_T$ and was obtained from the slope of the curve of $\log\dot{\varepsilon}$ versus $\log\sigma$ at constant temperature*. These curves for the zirconium-molybdenum alloys tested at 1000°C are shown in Figures 5.6 and 5.7 for the yield and steady state data, respectively. The value of 0.7 strain was taken as the strain at which near steady state flow conditions were achieved. This assumption is a compromise since at larger strains, where a truly constant flow stress

---

* The "true" stress sensitivity of the strain rate is given by $(\partial\log\dot{\varepsilon}/\partial\log\sigma)_{T,\varepsilon}$, and is generally higher than n.

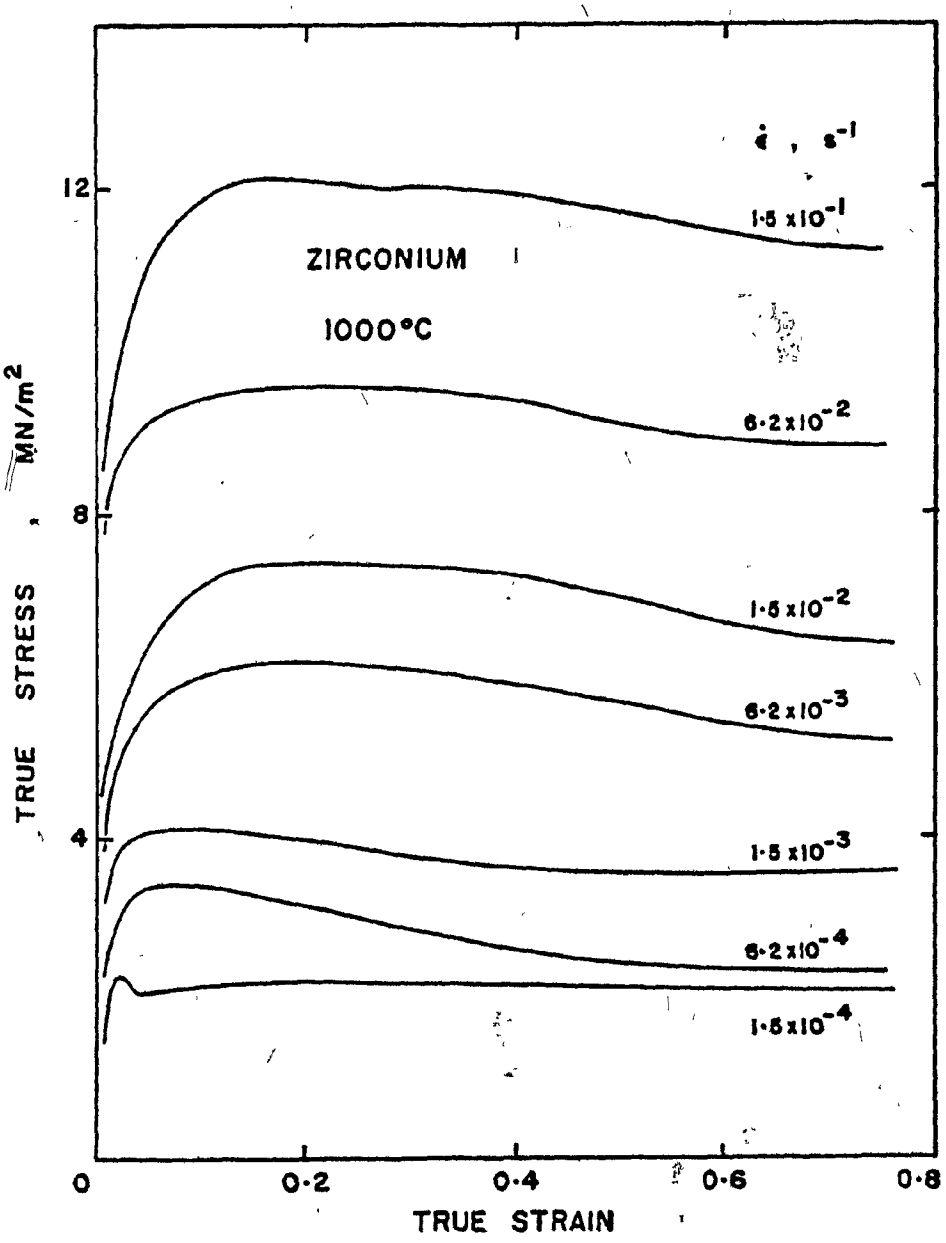

FIGURE 5.2 Experimental stress-strain curves of crystal bar zirconium obtained at 1000°C for various strain rates.

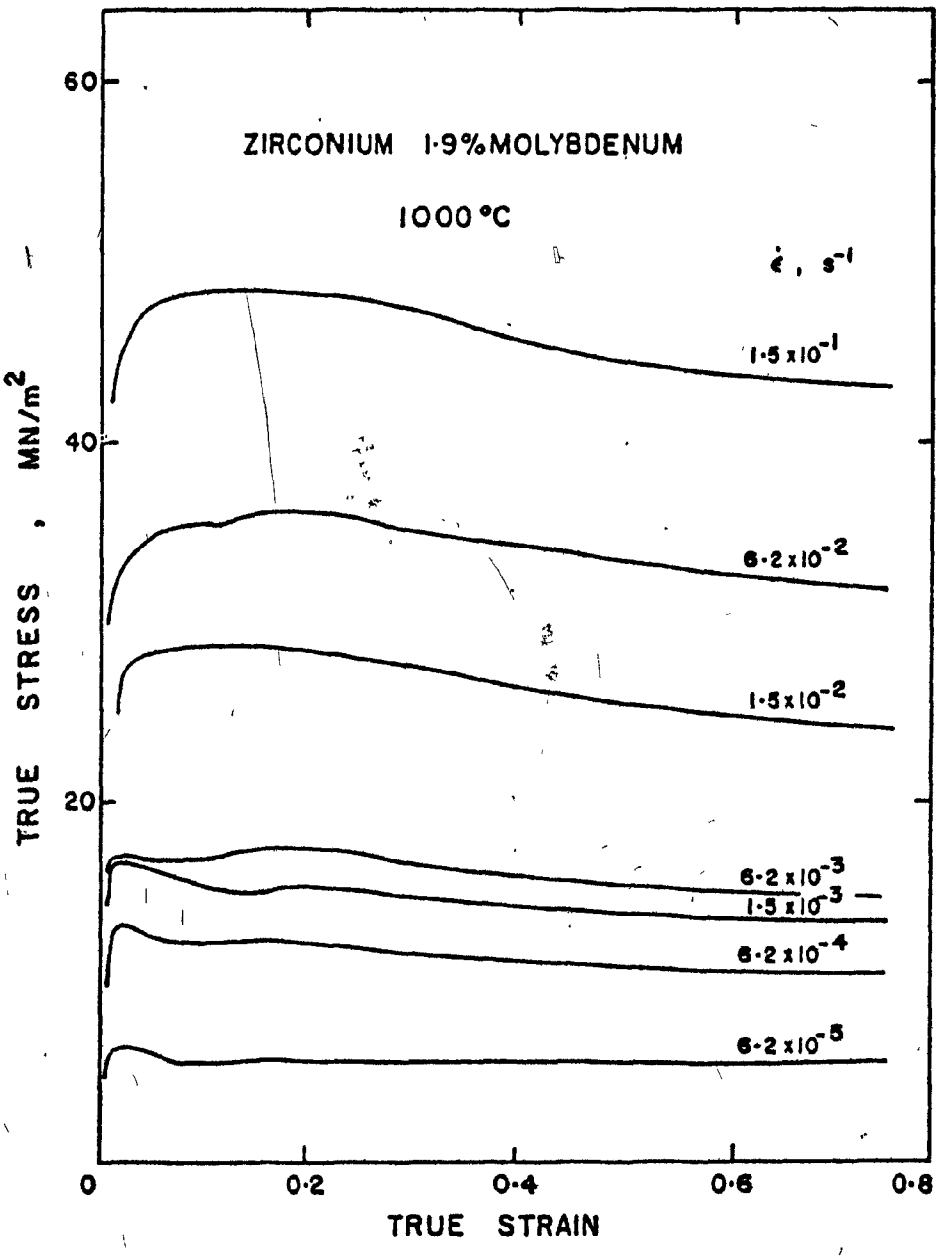

FIGURE 5.3 Experimental stress-strain curves of the Zr-1.9% Mo alloy, obtained at 1000°C for various strain rates.

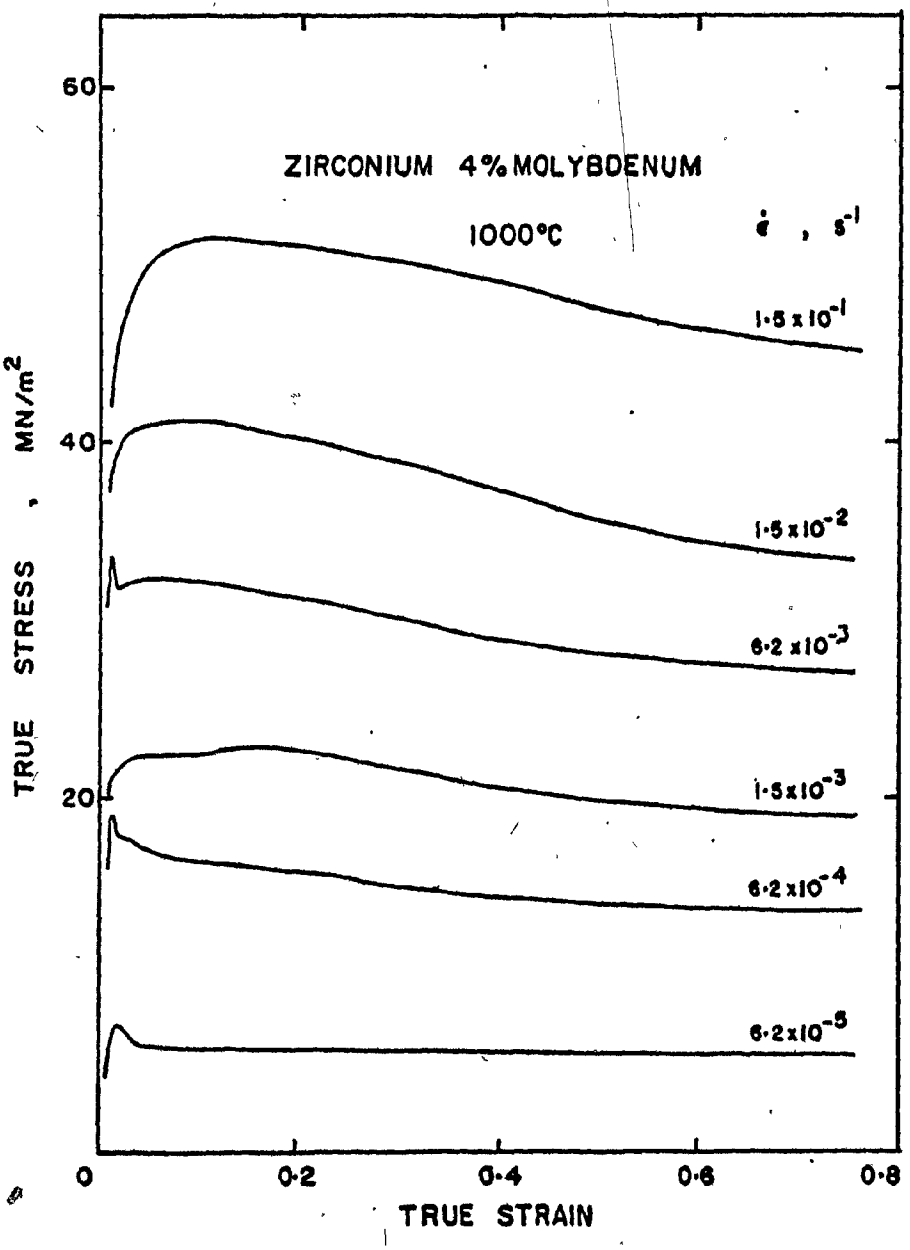

FIGURE 5.4 Experimental stress-strain curves of the Zr-4% Mo alloy, obtained at 1000°C for various strain rates.

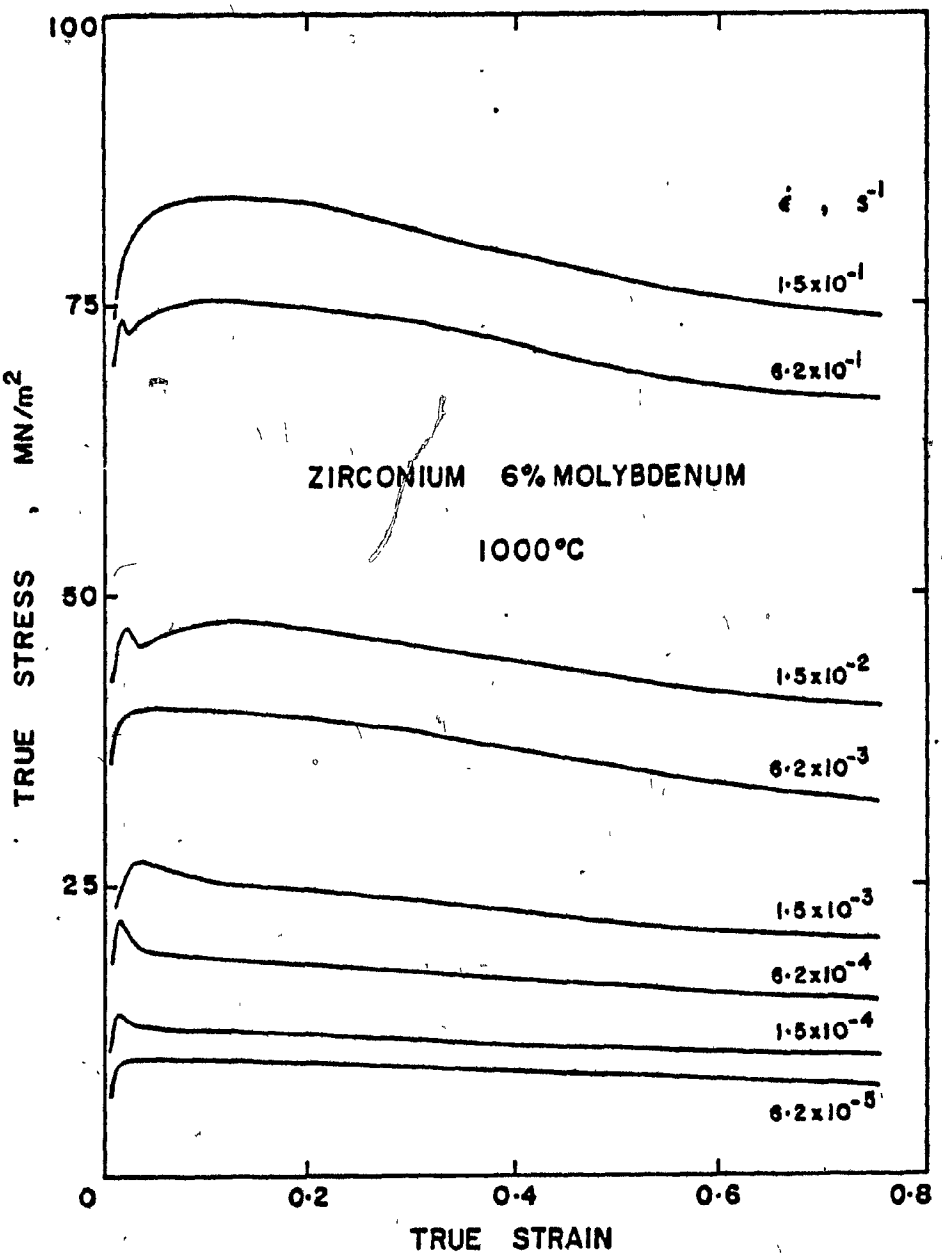

FIGURE 5.5 Experimental stress-strain curves of the Zr-6% Mo alloy, obtained at 1000°C for various strain rates.

TABLE 5.1

Mechanical Data for Crystal Bar Zirconium at 1000°C, for Various Strain Rates

$\dot{\varepsilon}$, s^{-1}	stress (MN/m^2)	
	Yield	$\varepsilon = 0.7$
1.5×10^{-1}	10.5	11.2
6.2×10^{-2}	7.5	9.5
1.5×10^{-2}	4.5	6.4
6.2×10^{-3}	$\sim$ 4.5	5.2
1.5×10^{-3}	3.5	3.5
6.2×10^{-4}	2.0	2.4
1.5×10^{-4}	2.0	$\sim$ 2.0

TABLE 5.2

Mechanical Data for Zirconium 1.9% Molybdenum at 1000°C

$\dot{\varepsilon}$, s^{-1}	stress (MN/m^2)	
	Yield	$\varepsilon = 0.7$
1.5×10^{-1}	44	43.2
6.2×10^{-2}	32.5	31.8
1.5×10^{-2}	26.2	24.1
6.2×10^{-3}	16.1	14.8
1.5×10^{-3}	17.3	13.5
6.2×10^{-4}	13.2	10.6
1.5×10^{-4}	-	-
6.2×10^{-5}	5.7	5.5

TABLE 5.3

Mechanical Data for Zirconium 4% Molybdenum at 1000°C

$\dot{\varepsilon}$, s^{-1}	stress (MN/m^2)	
	Yield	$\varepsilon = 0.7$
1.5×10^{-1}	44.1	45.5
6.2×10^{-2}	-	-
1.5×10^{-2}	38.0	34.0
6.2×10^{-3}	33.5	27.1
1.5×10^{-3}	20.4	15.9
6.2×10^{-4}	18.9	13.6
1.5×10^{-4}	9.4	9.9
6.2×10^{-5}	6.3	5.6

TABLE 5.4

Mechanical Data for Zirconium 6% Molybdenum at 1000°C

$\dot{\varepsilon}$, s^{-1}	stress (MN/m^2)	
	Yield	$\varepsilon = 0.7$
1.5×10^{-1}	80.0	74.5
6.2×10^{-2}	69.0	66.2
1.5×10^{-2}	45.0	40.6
6.2×10^{-3}	38.7	32.5
1.5×10^{-3}	24.0	20.4
6.2×10^{-4}	15.5	12.4
1.5×10^{-4}	11.5	10.5
6.2×10^{-5}	8.5	8.0

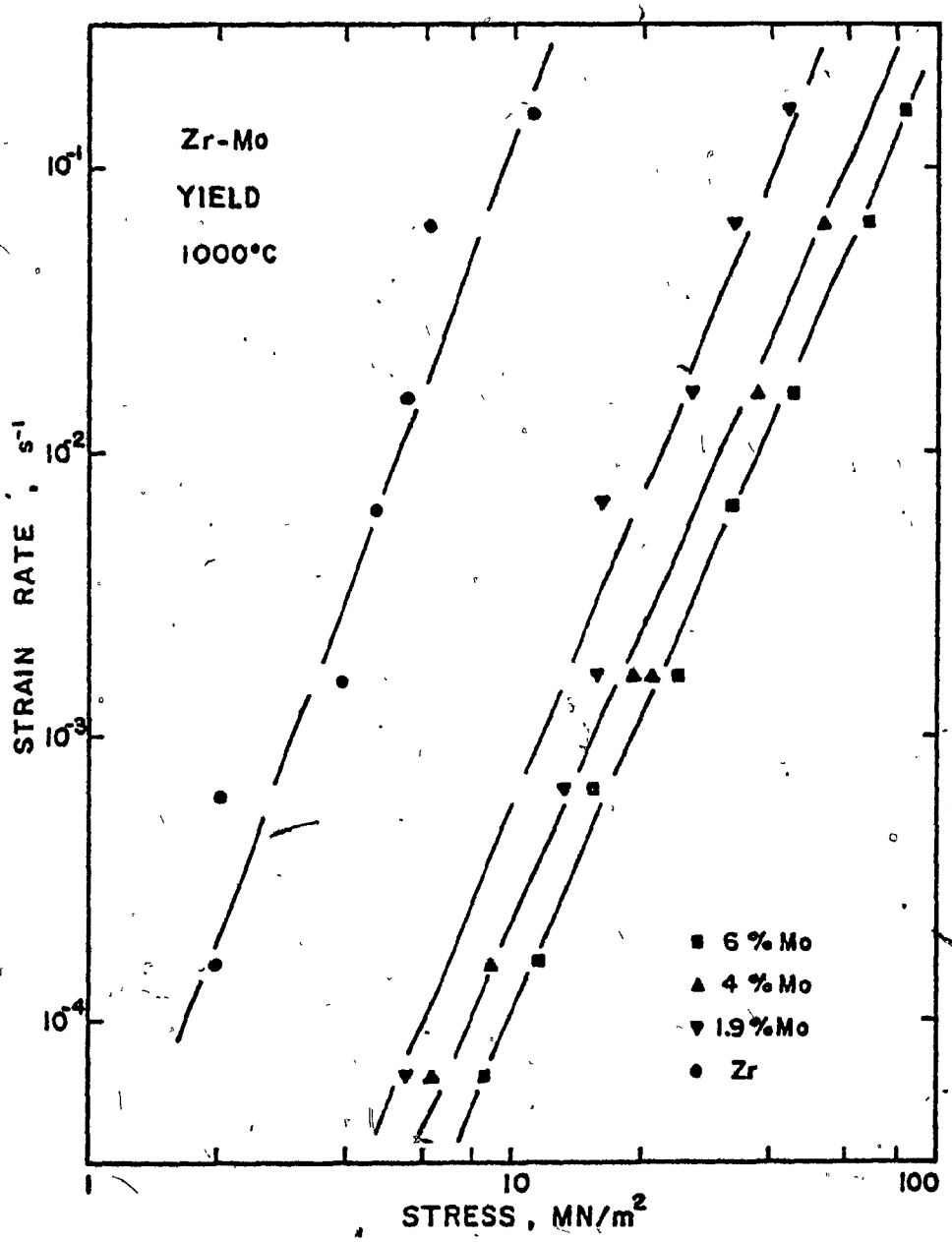

FIGURE 5.6 Logarithmic plot of the strain rate dependence of the yield stress, for various molybdenum contents.

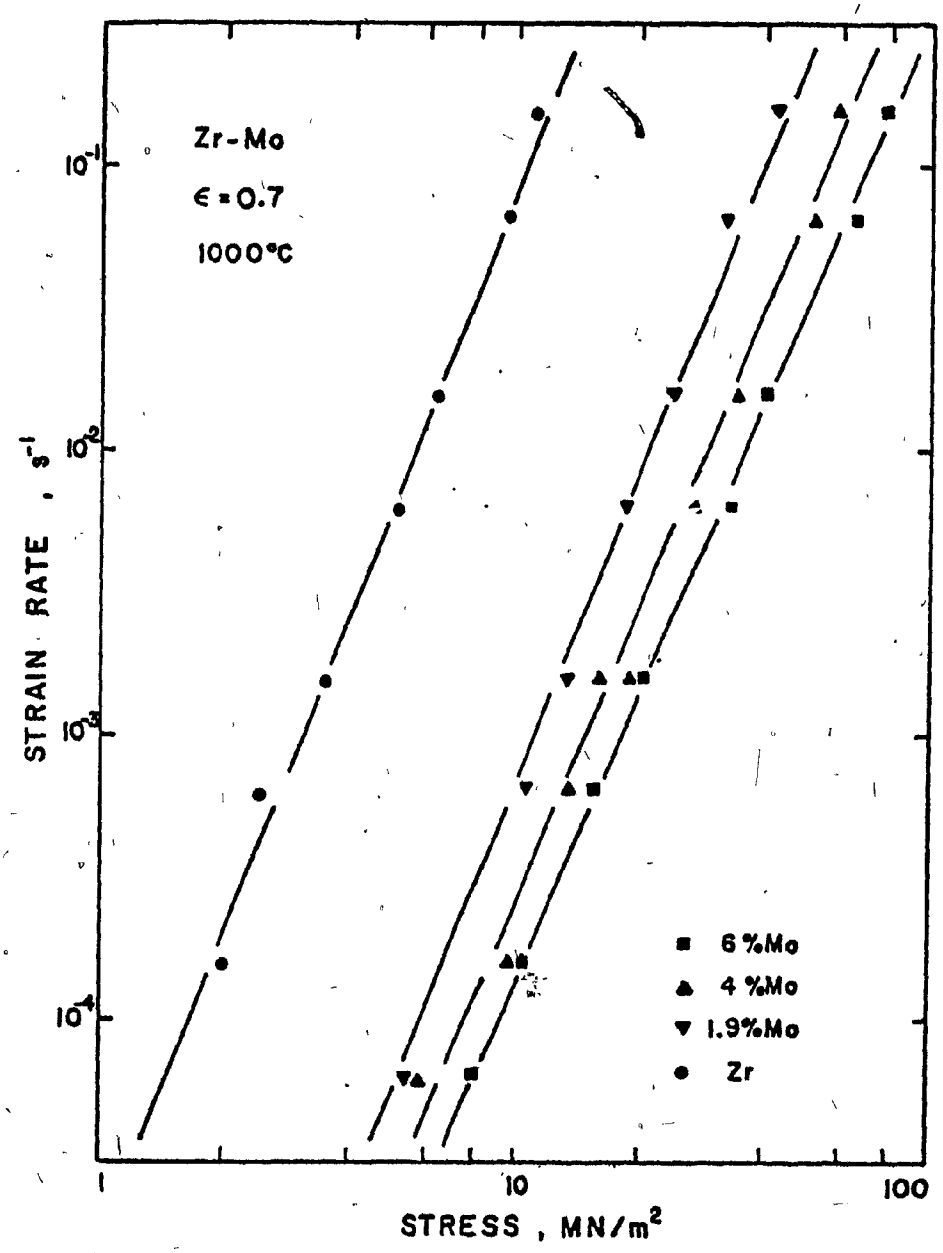

FIGURE 5.7 Logarithmic plot of the strain rate dependence of the stress at 0.7 strain, for various molybdenum contents.

might be obtained, there are effects on the flow stress due to poor lubrication. Lubricant break-up effects typically become significant around strains of 0.8.

From Figure 5.7, the value of n under steady state conditions was found to decrease with molybdenum content, i.e. from 4.0 in unalloyed zirconium to 3.4 in the 6% molybdenum alloy. The value of n determined from Figure 5.6 for the yield stresses decreases similarly from 4.0 to 3.4 as the molybdenum content is increased from 0 to 6%. The yield stress values tend to be more scattered than steady state values; this additional variability presumably arises because of the occasional occurrence of the "yield drop" effect. When the yield drop occurs, the amount of stress decrease was found to vary considerably from sample to sample.

5.1.3 Effect of Temperature

The stress-strain curves obtained at 900°C on the 1.9 and 6% Mo alloys are shown in Figures 5.8 and 5.9. Comparing the stress levels with the curves obtained at 1000°C (Figures 5.3 and 5.5), it can be seen that the flow stresses are increased markedly as the temperature is decreased. However, insufficient data were obtained to permit the accurate determination of activation energies and the other activation parameters. Nevertheless, the experimental activation energy was estimated from the data for the 1.9% and the 6% Mo alloys. At a stress of 30 MN/m^2, for example, the activation energies for the 1.9% Mo alloy are 160 and 105 kJ/mol for the yield and steady-state flow levels, respectively. Similar values for this parameter were found for the Zr-6% Mo alloy, these being 150 and 105 kJ/mol, respectively, for the yield and steady-state regimes, at a stress of 55 MN/m^2.

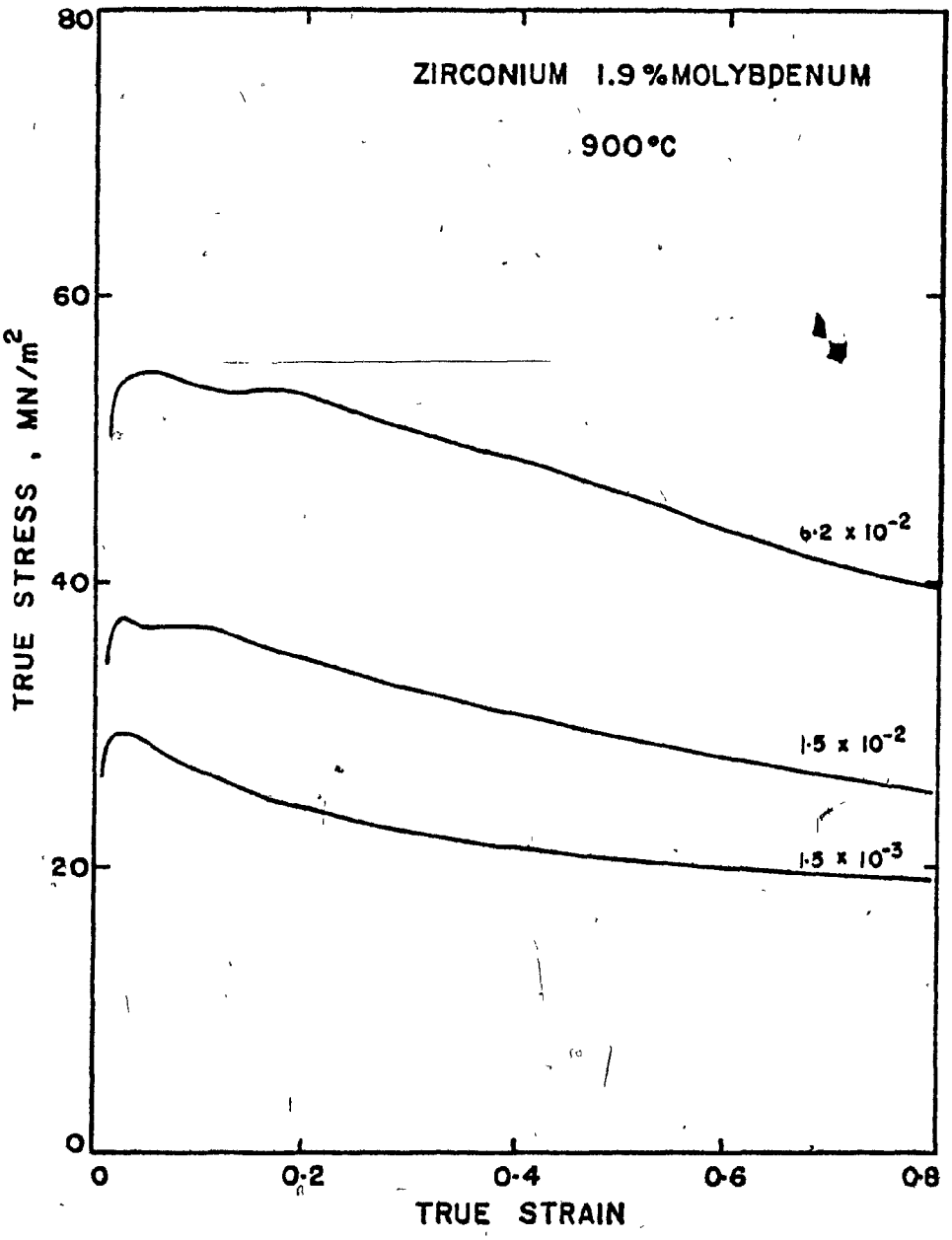

FIGURE 5.8 Experimental stress-strain curves of the Zr-1.9% Mo alloy, obtained at 900°C for various strain rates.

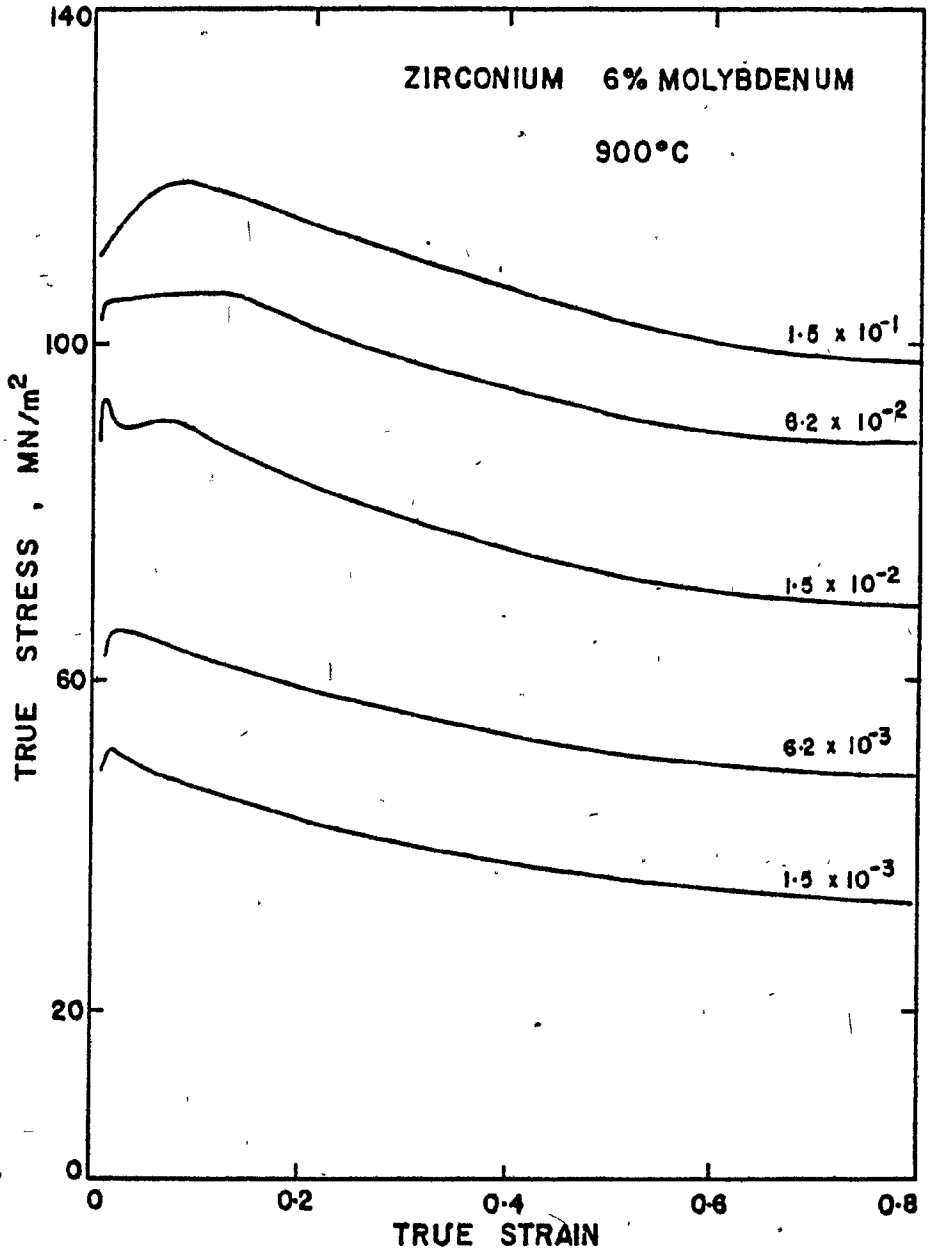

FIGURE 5.9 Experimental stress-strain curves of the Zr-6% Mo alloy, obtained at 900°C for various strain rates.

It is of interest to note that flow softening occurs at 900°C; the flow curves appear similar to those obtained at 1000°C. At low strains very little work-hardening is observed. At higher strains, the stress decreases continuously up to the maximum of 0.8 applied in the present work.

5.1.4 Effect of Alloy Content

A stress versus composition curve, determined at constant strain rate and temperature, is shown for yield strain and 0.7 strain in Figures 5.10a and 5.10b. The data points appear somewhat scattered, particularly at low strain rates. The presence of this scatter renders the determination of the molybdenum concentration dependence of the flow stress very uncertain. It appears, however, that the stress level increases with c^m, where m takes a value in the range 0.5 to 1.0. The significance of this result is not clear, although a $c^{1/2}$ dependence is normally assumed to be followed (204) when the solute atoms act as individual obstacles to dislocation movement. On this basis, for the 2, 4 and 6% wt molybdenum alloys the average spacings calculated are 7.5, 5.3 and 4.3 interatomic distances, respectively. It is likely that the dislocation does not move by overcoming the strain field of a single atom at a time, but rather by passing several of them concurrently. If solute atoms act as groups which must be overcome collectively, then the relationship between the stress and the solute concentration would be complex (205). This is not unexpected since the size and distribution of the solute groups must be taken in account as well as the effects of concentration changes on these parameters. Alternatively, the type of strengthening observed may arise from the indirect effect of the molybdenum atoms (44). An indirect proof of this hypothesis would have been obtained if the activation volume had been

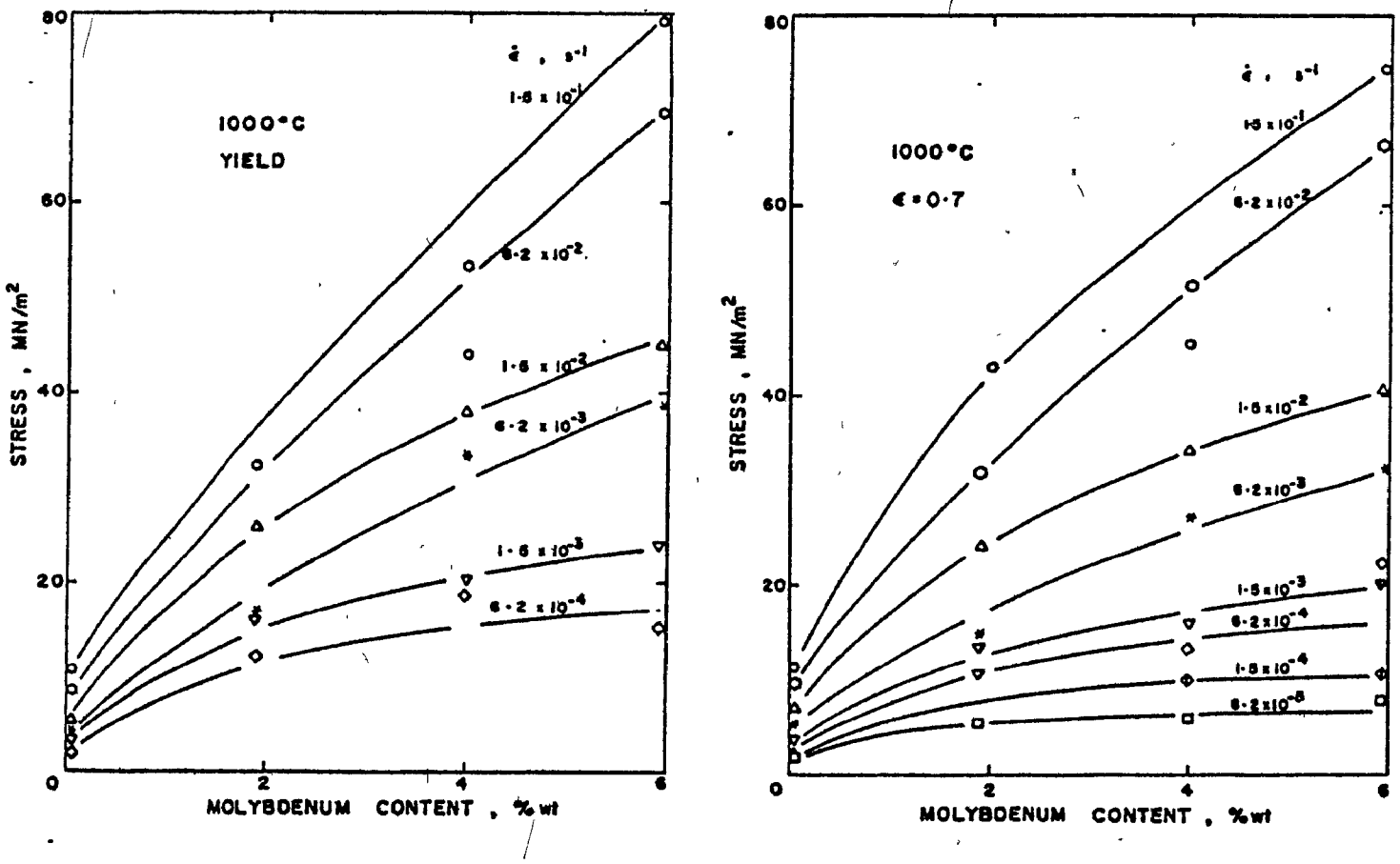

FIGURE 5.10 a) Plot of the yield stress variation with molybdenum content at 1000°C for various strain rates.
b) Plot of the stress at 0.7 strain versus molybdenum content at 1000°C for various strain rates.

calculated, and found to be large. (This is indicated in a qualitative way by the magnitude of the stress sensitivity n.)

5.1.5 Microscopic Examination

Temperature-time-transformation curves for various zirconium molybdenum alloys have been determined by Domalaga et al (206). Their results show that the decomposition of the ω-phase cannot be avoided even by the most rapid quenching in the 1.3 and 3.3% wt alloys. Although water quenching of the 5.4% wt molybdenum alloy from the β-field can retain the β-phase to room temperature, a small quantity of ω-phase is expected to be formed during cooling. In view of this, most of the optical and electron microscopy was carried out on the 6% molybdenum alloy, water quenched from the β-phase. Under such conditions, the microstructure is expected to consist of β-phase with a small quantity of ω-phase present.

5.1.5.1 Optical Microscopy

Samples were ground down to 600 grade paper and then polished and etched in a solution containing 45 parts HNO_3, 45 parts H_2O and 6 parts HF. The solution was swabbed on to the sample surface with a cotton pad for about 10 seconds. Microscopic examination of a sample maintained for one-half hour and subsequently water quenched revealed a microstructure of roughly equiaxed grains. The grain size, measured by the linear intercept method and averaged over 300 measurements was found to be about 0.15 mm. Within each grain was a network of plate-like features which appeared to be crystallographically oriented with respect to the grain. In general, most of the plates were parallel to a single direction, with the remainder oriented towards a few other well-defined directions. This Widmanstatten-

like structure is very similar in appearance to the β"-phase found in zirconium-niobium alloys (207,208). In particular, the crystal structure and the composition of the β"-phase do not differ from that of the β-phase, so that it almost appears to be an etching artefact.

The examination of samples preheated for half an hour, deformed to a strain of 0.8 and subsequently quenched showed that the grains become elongated in a direction perpendicular to the compression axis during straining. In addition, the needle-like Widmanstatten features were observed to be bent by various amounts, up to 30 degrees. No evidence was found by optical means for the presence of precipitates. However, a very thin oxide layer was found to be present on the surface of the samples. In the region immediately adjacent to the surface oxide, a layer about 0.1 mm thick consisting of α-phase was found, resulting from oxygen diffusion.

5.1.5.2 Transmission Electron Microscopy

Transmission electron microscopy was carried out on 6% molybdenum alloy samples held 30 minutes at 1000°C and quenched after true strains of 0.0, 0.15 and 0.60. These samples were used to ascertain the presence or the absence of precipitates (such as carbides or oxides) in order to establish whether an Orowan type of mechanism could play any role. Sample preparation and thinning were similar to that used for pure zirconium (209). Sections 1 mm thick were cut with a silicon carbide abrasive saw, then mounted on a brass jig using a thermoplastic cement and then ground on silicon carbide papers. The sections were removed from the jig, turned over, remounted and polished so that the thickness was reduced to about 0.6 mm. The sections were then chemically polished in a solution containing

45 parts HNO_3, 45 parts H_2O and 5 parts HF until a thickness of less than 50 μm was achieved.

The final thinning was achieved by jet electropolishing using a solution containing 20% perchloric acid and 80% ethyl alcohol, and maintained at -20°C in a dry ice bath. Despite the precautions this technique proved to lead to the formation of hydrides during thin foil preparation. In spite of these difficulties, the results confirm that in neither the deformed nor in the undeformed condition were any precipitates present in the samples examined. Selected area diffraction of the matrix material showed some reciprocal lattice streaking which suggested the presence of some ω-phase. The ω-phase detected could have been formed during cooling.

5.1.5.3 Microprobe Examination

A microprobe examination of the samples was carried out to investigate the possibility of molybdenum segregation. The samples were found to have a uniform distribution throughout, within the degree of certainty of the measurements. Both the grain boundaries and the β" type plates appeared to have the same molybdenum content as the bulk of the grains. These results suggest that segregation, if present, must be present at a level below the sensitivity of the technique that is less than 1-2% or only at a submicroscopic scale.

5.1.6 Interrupted Tests

Since the metallographic observations were not able to explain why the material softens during straining, a different approach was taken. Compression tests were carried out to a preset strain at which the deformation was interrupted and the sample unloaded. After a preset time had

elapsed, the deformation was pursued to a strain of about 0.8. By comparing the stress levels on reloading with those in the virgin material, these interrupted tests permitted some direct information to be obtained about the structural changes taking place during the interruption delay. The strain at which the interruption is introduced is arbitrary, and was chosen at 0.15; this is beyond the peak, but avoids the large strains at which flow softening is less severe in the present materials.

Figure 5.11 shows the stress-strain curves obtained from a 6% molybdenum alloy tested at a strain rate of $1.5 \times 10^{-3} s^{-1}$ for various interruption delays. For the initial 0.15 strain the stress levels vary appreciably from sample to sample. This large scatter may be attributed to some extent to molybdenum concentration variations from sample to sample. It is of interest to note that in this part of the curves the highest stresses are always associated with the existence of a peak stress around the yield region.

In spite of the initial scatter, the stresses obtained on reloading clearly show the strengthening effect of interruption, the magnitude of which increases with delay time. The longest delays, 30,000 and 60,000 seconds produce not only a very pronounced strengthening effect, but also a sharp yield drop on reloading. The strengthening imparted to the alloy by the interruption delay persists up to the largest strains obtained by compression testing, i.e. 0.8.

Similar interrupted tests were performed on unalloyed zirconium in order to assess the differences in mechanical behaviour compared to the Zr-6% Mo alloy when subjected to a 60,000 seconds delay. The curve obtained is shown in Figure 5.12. The delay caused a marked increase in the flow stress of β-Zr, from 6.3 MN/m^2 to 14.5 MN/m^2 at the peak. This increase

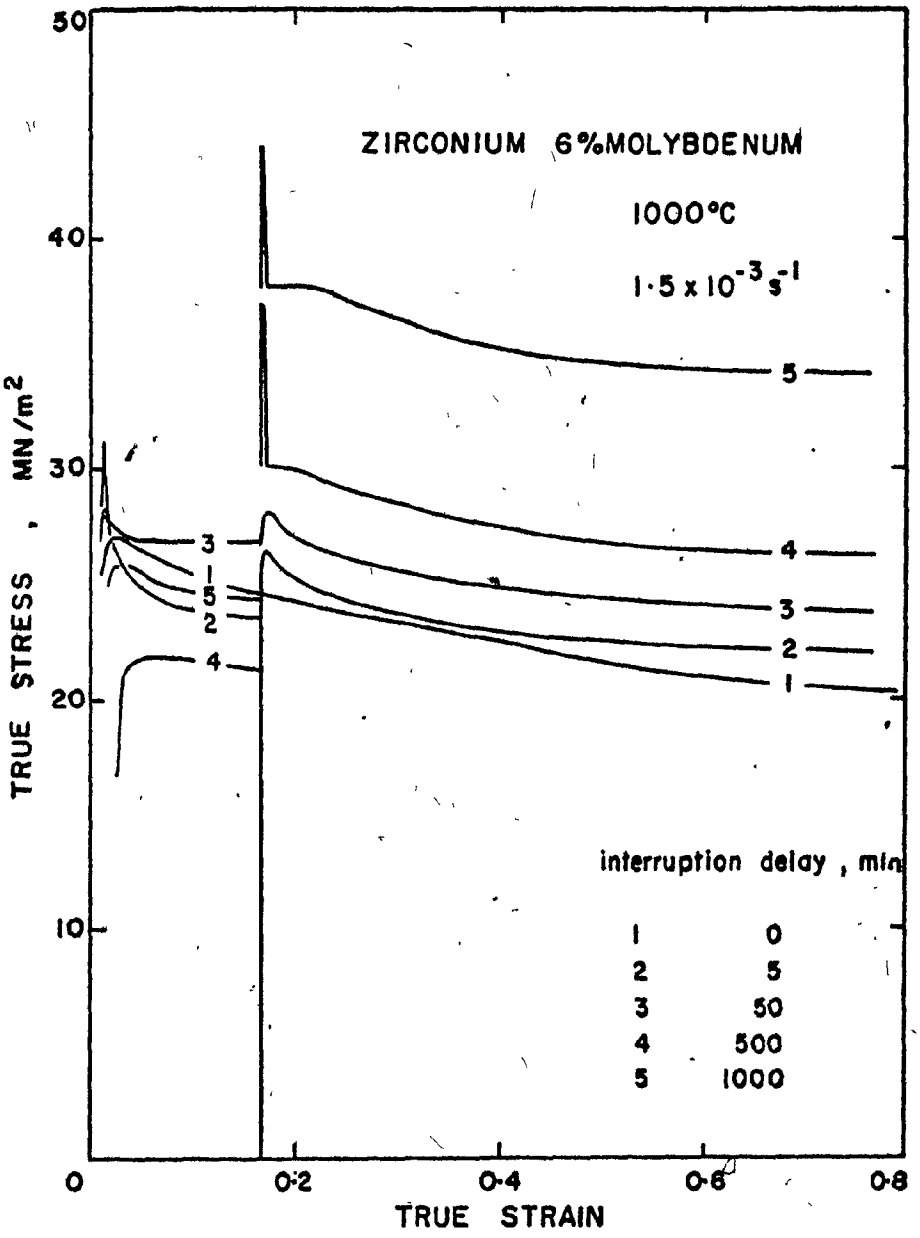

FIGURE 5.11 Interrupted stress-strain curves obtained at 1000°C for the 6% Mo alloy tested at a strain rate of $1.5 \times 10^{-3} s^{-1}$, for various interruption delays.

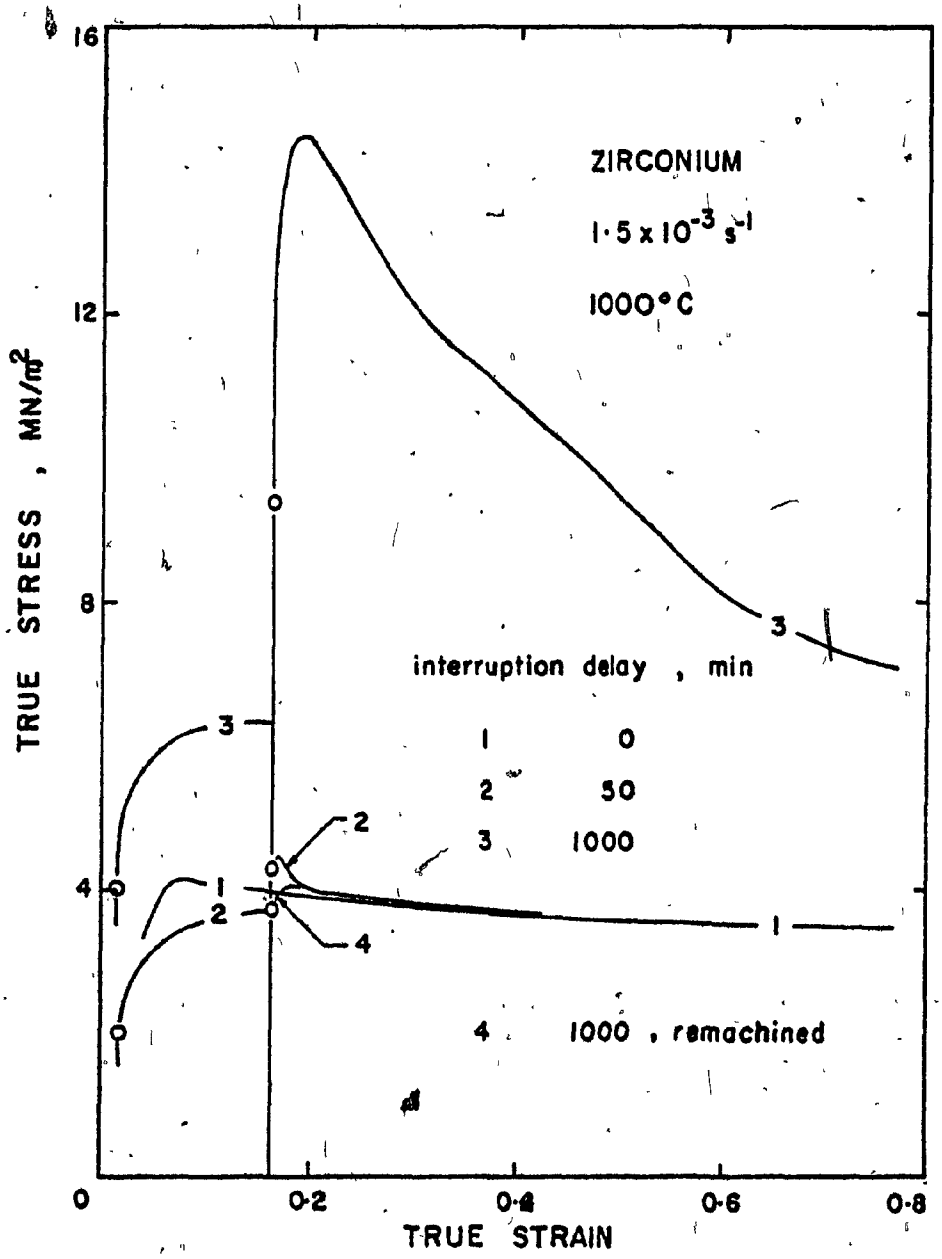

FIGURE 5.12 Interrupted stress-strain curves obtained at 1000°C for crystal bar Zr tested at a strain rate of $1.5 \times 10^{-3} s^{-1}$, for different interruption delays.

of 8.2 MN/m^2 is, however, much smaller than that in Zr-6% Mo, which reaches 19.2 MN/m^2 under the same conditions.

The increase in stress during the delay, together with the metallographic observations, suggested that environmental effects are principally responsible for the change in the mechanical properties in these materials, and the possibility of such an effect was therefore considered in more detail, as will be outlined below.

5.1.7 Atmosphere Effects

The tests described above were carried out in an atmosphere of flowing high purity argon (40 cc/min). In spite of this it was considered possible that some oxygen pick-up could take place, particularly during the insertion of the sample into the chamber. In order to assess the importance of these effects, attempts were made firstly to getter the residual oxygen from the argon stream, and secondly to minimize oxygen pick-up during sample insertion by placing the sample in a cold furnace. In addition to these major precautions, some tests were conducted on samples whose surfaces had been treated with various types of coating. A further set of experiments was carried out to study the degree to which the influence of the atmosphere on the mechanical properties was a surface as opposed to a bulk effect. The influence of these changes in test practice on the flow curves of zirconium-molybdenum alloys will now be presented in turn.

5.1.7.1 Results on coated samples

Effects of sample coating on the interruption stress-strain curves are shown in Figure 5.13; these curves are for zirconium-6% molybdenum tested at 1000°C and interrupted for 60,000 seconds. All the curves

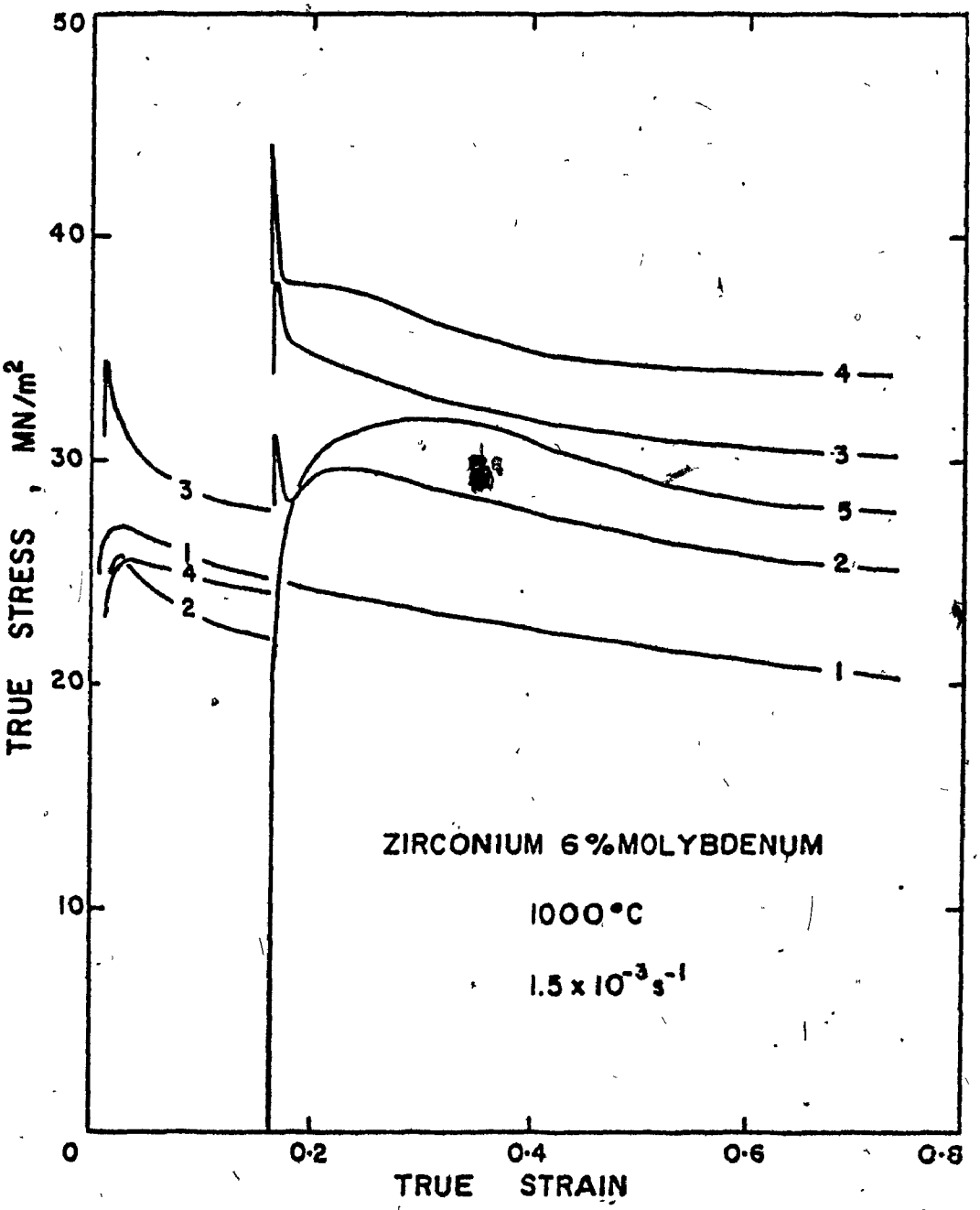

FIGURE 5.13 Interrupted stress-strain curves obtained at 1000°C for the 6% Mo alloy tested at a strain rate of $1.5 \times 10^{-3} s^{-1}$ under atmospheres of different purity for an interruption delay of 60,000 seconds (except No.1)

Sample and atmosphere conditions:

1. Sample without coating, placed in the chamber preheated to the testing temperature. No interruption was applied.
2. Sample plated with Cr and Cu, and placed in the testing chamber at room temperature.
3. Sample plated with Cr and placed in the testing chamber at room temperature.
4. Sample without coating placed in the chamber preheated to the test temperature.
5. Sample in condition 4, quenched after the delay, re-machined before being tested.

exhibit strain softening. The delay causes an increase in strength similar to the one described before when the standard testing procedure was used. However, it appears that in the tests carried out on Cr coated samples under highly purified argon, for which sample insertion was effected only when the testing chamber was cold, the amount of strengthening that occurs during the delay was decreased, but not eliminated completely. It is interesting to note that in some instances the curve on reloading appears to show a stress drop at yield followed by a work-hardening region beyond which the strain softening described earlier takes place.

The amount of flow softening during prestraining, as well as the actual stress levels, varied considerably from one testing condition to another. This scatter cannot, however, be related to the different atmosphere conditions, since the stress levels in the prestrain region do not vary in the same manner as those after the delay. It is suggested, therefore, that the variation in the stress level on prestraining probably arises from slight differences in sample composition. The influence of oxygen on the reloading curve then appears to mask any sample-to-sample variation in composition.

5.1.7.2 Continuous stress-strain curves in a high purity atmosphere

A few stress-strain curves were obtained from Zr-6% Mo samples for which the highest purity atmosphere that could be obtained with the present equipment was used. This was achieved by purifying further the high purity argon on an oxygen removal train. Also, in the testing chamber, a large zircaloy tube was installed as an oxygen getter, and the sample was placed in the chamber when cold. Heat-up was started only after purified gas was flowing. Stress-strain curves obtained under such conditions are shown in Figure 5.14. We note that the yield drop is still present except

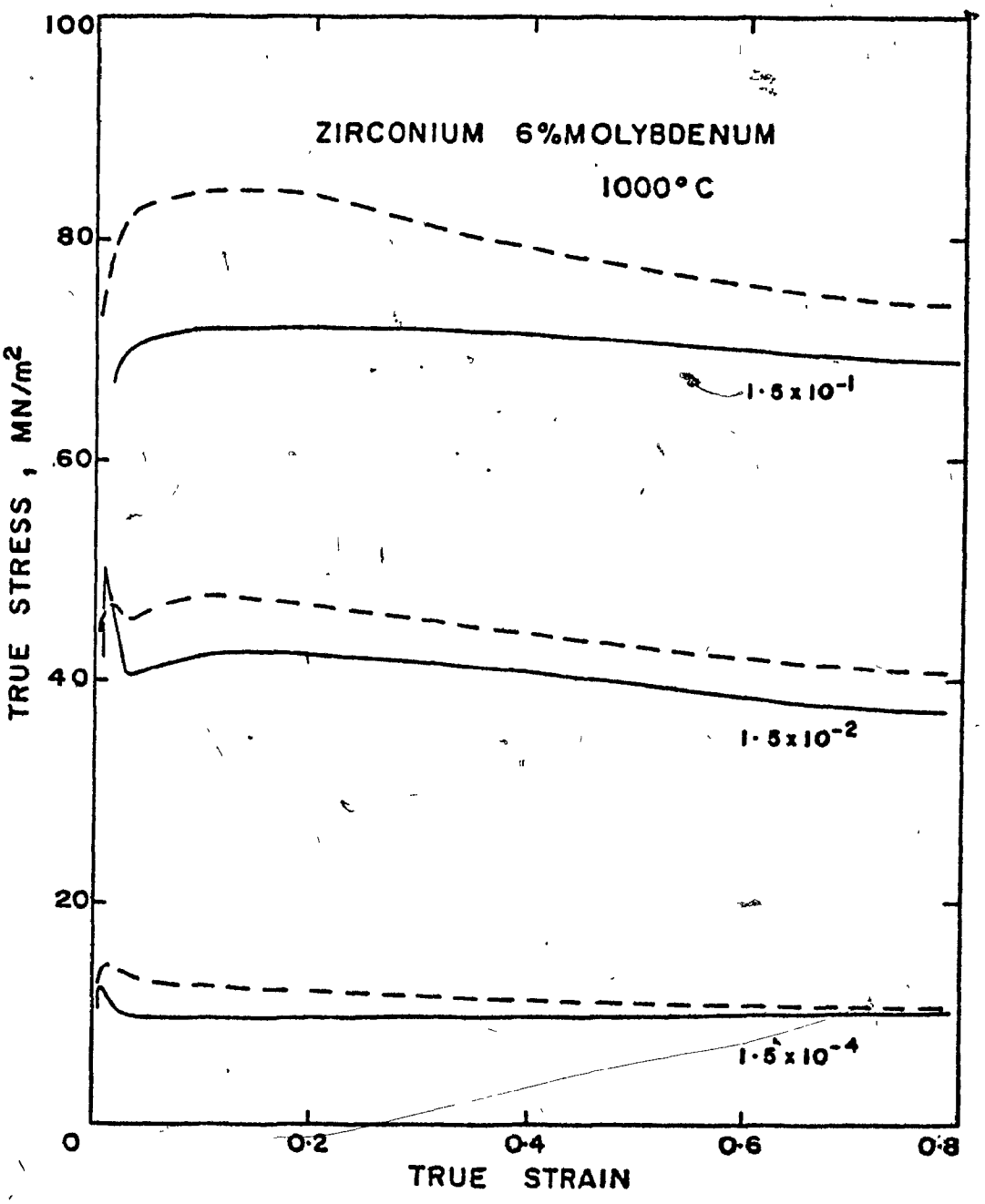

FIGURE 5.14 Stress-strain curves obtained at 1000°C for the 6% Mo alloy tested at various strain rates under the purest atmosphere obtainable with the experimental equipment.

for the test at $1.5x10^{-1}s^{-1}$. However, beyond the initial yield drop, for all strain rates of testing, no stress decrease with strain appears that does not lie within the scatter of the data points. When the curves are compared with the set obtained under the same mechanical conditions but in the "normal" atmosphere, the following observations can be made:

i. No softening appears at strains beyond 0.1 in tests carried out under a high purity atmosphere; in contrast, with the "normal" atmosphere, flow softening is evident. That is, an improvement of atmosphere purity leads to an almost complete elimination of the 'strain softening'.

ii. The stress levels at intermediate strains (0.2-0.6) are consistently lower for the tests effected under a high purity atmosphere compared to the other ones. This difference vanished at 0.7 strain except perhaps at a strain rate of $1.5x10^{-1}s^{-1}$.

5.1.7.3 Effect of sample size

It appears from these results that atmosphere conditions can strongly affect the stress-strain curves. This effect can be expected to have been localized on, or near the sample surface. For this reason, a set of interrupted curves, with varying interruption times, was carried out under similar conditions to those in Figure 5.11, but with samples of 4.5 mm in height and 3 mm in diameter; that is, about half the dimensions normally used. Figure 5.15 gives the stress-strain curves obtained under such conditions. The increase in stress associated with the delay is two to three times that obtained on reloading with "normal" samples. One sample was submitted to an interruption delay of 240,000 seconds. On re-

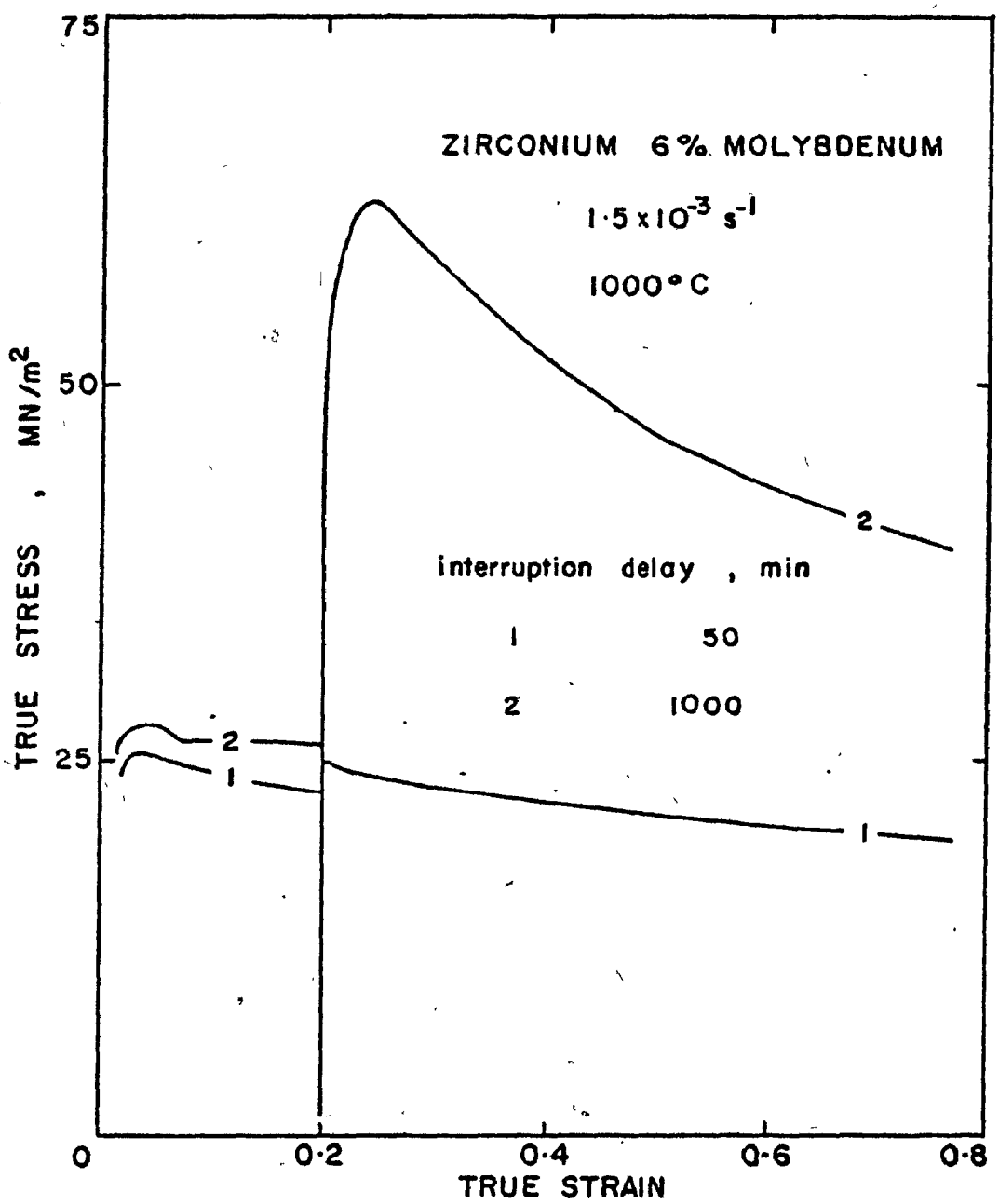

FIGURE 5.15 Interrupted stress-strain curves obtained at 1000°C for the 6% Mo alloy tested at a strain rate of $1.5 \times 10^{-3} s^{-1}$ for different interruption delays. The samples are smaller than the regular size so as to identify surface effects.

loading, the stress reached a peak value of over 200 MN/m^2 and dropped very abruptly afterwards. The sample was found after subsequent cooling to room temperature to consist entirely of oxide. In these tests the flow stress over the first 0.15 strain, again, showed a large variation in spite of the fact that the prestrain conditions were the same.

5.1.7.4 Removal of the outer layer

Since the atmosphere interaction clearly affects the mechanical properties, the following experiment was designed to assess the importance of the outer layer of the sample. Samples were strained to 0.15, unloaded and held at temperature for 60,000 seconds after which they were water quenched, thereby retaining the β-phase to room temperature. A 1.25 mm thick layer was removed on a lathe from the sides and the ends of the sample. The machined sample was then placed back in the chamber and tested five minutes after it had reached the test temperature (1000°C). The relevant stress-strain curve is also shown in Figure 5.13. The yield stress obtained on reloading was 22 MN/m^2, only 2 MN/m^2 higher than the one obtained in the pre-straining region. Flow softening, however, is not totally eliminated by this means and is still evident at larger strains, beyond a work-hardening region. However, the removal of the outer layer appears to suppress the stress drop present on reloading and reduces the stress levels down to values similar to those obtained during pre-straining.

A similar test was carried out on a crystal bar zirconium sample which had been submitted to a 60,000 second delay. The stress-strain curve obtained is shown in Figure 5.12. We note here again that the removal of the outer layer suppresses nearly completely the strength increase induced by the delay, the new yield value being now only 1.9 MN/m^2 higher than the yield stress of the virgin material.

This strength increment over that of the initially undeformed material can be explained if it is considered that some oxidation takes place during the sample insertion and preheat time. Oxidation will be proportional to the sample area, which decreased proportionally less than the sample volume when the oxygen-affected layer was removed. Moreover, the degree to which the sample oxidizes may have been different than that of the initial sample owing to sample-to-sample differences in testing technique, surface finish or impurity level in the gas stream.

5.1.8 X-Ray Analysis of Oxidized Samples

The results just described show a very strong influence of the outer layer upon the mechanical properties of the Zr-Mo alloys. X-ray diffraction was used to determine the nature of this outer layer.

A few samples of Zr-6% Mo and of crystal bar zirconium were placed in the furnace in the same manner as for tests shown in Figure 5.11, and left for 90 hours (324,000 seconds) at 1000°C without deformation. The furnace was then cooled to room temperature and the sample retrieved. After this treatment, the surface appeared grey-white over a layer which did not exceed 20 μm. Below this, there was a very brittle layer which was about 0.5 mm thick in zirconium-molybdenum and thinner in the Zr samples, and had a metallic appearance. The sample core was ductile and optically homogeneous.

5.1.8.1 Ductile Core

The samples for diffraction were prepared by cutting away the outer layer with a lathe, and then filing the ductile part to -50 mesh. The diffraction peaks obtained from the crystal bar zirconium samples are

those of α-zirconium as shown in Table 5.5. The Zr-6% Mo alloy, on the other hand, produced peaks which were identified as α-zirconium, plus some weak peaks which were found to be those of $ZrMo_2$. These findings are in agreement with the equilibrium phase diagram which suggests that, at room temperature, the zirconium-6% molybdenum alloy consists of intermetallic $ZrMo_2$ and α-zirconium containing less than 0.1% molybdenum.

5.1.8.2 Brittle layer

The brittle layer could not be separated from the grey-white outside layer, so they were analyzed together. The layers were broken off the inner core with gentle hammer strokes and were then ground to a -50 mesh powder. The diffraction peaks for pure zirconium are given in Table 5.6, and those for Zr-6% Mo under similar conditions in Table 5.7.

The peaks present in the diffractometer trace listed in Figure 5.6 were indexed and identified as belonging to two compounds: ZrO_2 (monoclinic) and α-Zr (hexagonal), the latter being by far the most important one by volume. It is important to note that, whereas the d spacings measured for ZrO_2 were spread on both sides of the values given in the ASTM files, the d spacings measured for the α-Zr were always larger than those of the ASTM files. This suggests that the lattice parameters of α-Zr present in the brittle layer differ from those obtained in oxygen-free zirconium. The variation of the lattice parameter of zirconium with oxygen concentration has been given by Holmberg (210) and is reproduced in Figure 5.16.

TABLE 5.5

X-Ray Diffraction Pattern of Crystal Bar Zirconium (Ductile Core)

2θ	I	d (A°)	index $d_{(\alpha\text{-Zr})}$	(hkl)
32.11	M	2.787	2.796	$(10\bar{1}0)$
35.06	S	2.559	2.573	(0002)
36.64	VS	2.452	2.459	$(10\bar{1}1)$
48.19	M	1.888	1.894	$(10\bar{1}2)$
57.0	M	1.616	1.616	$(11\bar{2}0)$
63.79	S	1.459	1.463	$(10\bar{1}3)$
68.73	M	1.366	1.363	$(11\bar{2}2)$
69.57	M	1.351	1.350	$(20\bar{2}1)$
73.81	VW	1.284	1.287	(0004)
77.60	VW	1.229	1.2296	$(20\bar{2}2)$
82.58	VW	1.168	1.169	$(10\bar{1}4)$
90.64	VW	1.084	1.0842	$(20\bar{2}3)$
96.09	VW	1.037	1.036	$(21\bar{3}1)$

TABLE 5.6

X-Ray Diffraction Pattern of Crystal Bar Zirconium (Brittle Layer)

			Index			
			αZr		ZrO_2	
2θ	I	d(A°)	d(A°)	hkl	d(A°)	hkl
28.22	VW	3.162	-	-	3.157	$(11\bar{1})$
31.86	W	2.809	2.796	$(10\bar{1}0)$	-	-
34.65	S	2.589	2.573	(0002)	-	-
36.42	VS	2.467	2.459	$(10\bar{1}1)$	-	-
38.55	VW	2.335				
47.75	S	1.905	1.894	$(10\bar{1}2)$	-	-
56.72	S	1.623	1.616	$(11\bar{2}0)$	-	-
63.12	S	1.473	1.463	$(10\bar{1}3)$	-	-
66.45	VW	1.407	1.399	$(20\bar{2}0)$	-	-
68.08	S	1.377	1.363	$(11\bar{2}2)$	-	-
69.16	S	1.358	1.350	$(20\bar{2}1)$	-	-
72.91	VW	1.297	1.287	(0004)	-	-
77.14	VW	1.236	1.2296	$(20\bar{2}2)$	-	-
81.74	VW	1.178	1.169	$(10\bar{1}4)$	-	-
89.88	W	1.091	1.0842	$(20\bar{2}3)$	-	-
95.47	M	1.042	1.0360	$(21\bar{3}1)$	-	-
98.97	M	1.014	1.0063	$(11\bar{2}4)$	-	-
103.15	W	0.9840	0.9783	$(21\bar{3}2)$	-	-
104.62	W	0.9742	0.9660	$(10\bar{1}5)$	-	-
107.79	VW	0.9541	0.9474	$(20\bar{2}4)$	-	-
110.54	VW	0.9380	0.9327	$(30\bar{3}0)$	-	-
116.65	M	0.9044	0.9003	$(21\bar{3}3)$	-	-
121.84	M	0.8821	0.8771	$(30\bar{3}2)$	-	-

TABLE 5.7

X-Ray Diffraction Pattern of Zr-6% Mo (Brittle Layer)

			ZrO_2		α-Zr		$ZrMo_2$	
2θ	I	d(A°)	d(A°)	hkl	d(A°)	hkl	d(A°)	hkl
28.32	M	3.15	3.157	$(11\bar{1})$	-	-	-	-
31.92	S	2.80	2.834	(111)	2.796	$(10\bar{1}0)$	-	-
33.50	VW	2.675	2.617	(002)			2.69	(220)
34.64	M	2.589	2.598	(020)	2.573	(0002)		
36.40	VS	2.468			2.459	$(10\bar{1}1)$		
39.52	M	2.280					2.28	(311)
40.84	VW	2.209	2.213	$(21\bar{1})$				
41.43	VW	2.179	2.182	(102)			2.18	(222)
47.74	S	1.905			1.894	$(10\bar{1}2)$		
49.32	VW	1.848	1.845	(022)				
50.22	VW	1.817	1.818	(220)				
54.26	W	1.690	1.691	(300,(202)				
56.91	VS	1.618	1.608	$(3\bar{1}1)$,(212),$(13\bar{1})$	1.616	$(11\bar{2}0)$		
59.91	VW	1.543					1.54	(422)
63.09	S	1.474			1.463	$(10\bar{1}3)$	1.46	(333,(511)
66.50	W	1.406			1.369	$(20\bar{2}0)$		
68.15	VS	1.376			1.363	$(11\bar{2}2)$		
69.20	VS	1.358			1.350	$(20\bar{2}1)$		
70.23	VW	1.340					1.342	(440)
72.87	W	1.298			1.287	(004)		
77.18	M	1.236			1.2296	$(20\bar{2}2)$		
81.75	VW	1.178			1.169	$(10\bar{1}4)$		
89.92	S	1.091			1.0842	$(20\bar{2}3)$		
92.91	W	1.064			1.0588	$(21\bar{3}0)$		
95.45	S	1.042			1.036	$(21\bar{3}1)$		
99.06	M	1.013			1.0063	$(11\bar{2}4)$		

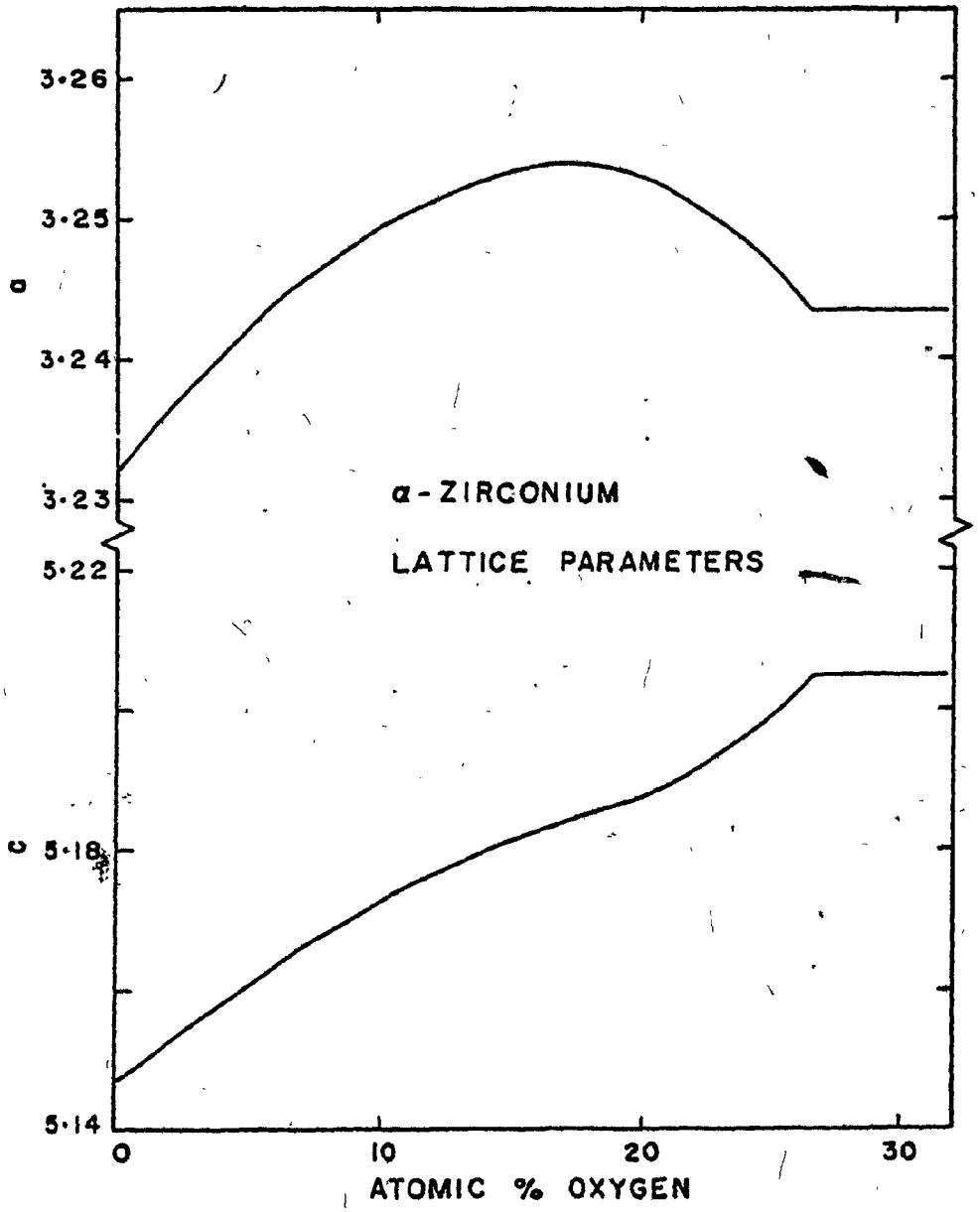

FIGURE 5.16 Plot of the lattice parameters of α-zirconium versus oxygen content, after Holmberg (210).

The lattice parameters vary with oxygen content in a complex way. The c parameter increases monotonically, but not linearly as the oxygen content goes up from 5.147Å to 5.204Å at the solubility limit. The parameter increases from 3.232Å to 3.255Å as the oxygen content rises from 0 to 23% atomic oxygen then decreases down to 3.244 as the oxygen concentration increases to 28.5% atomic limit of solubility.

The 2θ values of the diffraction charts permit a more accurate determination of the lattice parameters and this was done using the method described in Appendix 1. The set of 2θ values corresponding to the brittle layer of α-Zr yields for lattice constants:

$$a = 3.256 \pm 0.005\text{Å}, \qquad c = 5.195 \pm 0.007\text{Å}$$

A similar calculation based on the indexed reflections of α-Zr in the Zr-6% Mo alloy gives:

$$a = 3.27 \pm 0.03\text{Å}, \qquad c = 5.17 \pm 0.04\text{Å}$$

The errors in the lattice parameter are larger in this case as a result of the lower number of reflections.

Taking the variation in lattice parameter from the α-Zr as arising from interstitial oxygen pick-up, the oxygen content in the brittle layer of α-Zr is found to be 22 ± 3% atomic oxygen (4.72% wt), which is quite close to the saturation value (28.5% atomic). It can be seen that a large oxygen content must be present in spite of the relatively large error bars on the lattice parameters. The error bars in the values of the brittle layer parameters for Zr-Mo are larger and cannot permit an accurate

determination, but they nevertheless suggest a similar oxygen content.

The diffraction peaks of the ductile core, analyzed in the same manner yielded the following values for α-Zr:

$$a = 3.237 \pm 0.005\text{Å}, \quad c = 5.14 \pm 0.005\text{Å}$$

Within the error bars on the lattice parameters it can be concluded that the oxygen content is much lower than before (i.e. 22%) in agreement with the results of chemical analysis (see Section 4).

It is possible to conclude therefore that the α-zirconium present in the outer layers of the sample is saturated with oxygen, so that when interrupted tests are carried out, oxygen diffuses inwards from the surface of the sample. First an outer shell of ZrO_2 is formed, followed by a thicker, oxygen-stabilized α-zirconium layer. The core of the sample is of course β at the testing temperature. Increasing the delay time only serves to thicken the oxygen-stabilized layer of the α-phase, and decrease the proportion of the softer β-phase. It is of interest to note that, although some nitrogen traces could also have been present, no nitrides were detected by the X-ray analysis.

5.1.9 Hardness Curve

The experiments described thus far have made clear the influence of oxygen on the mechanical properties. They do not give, however, any information on how the strengthening arises in the material. Hardness tests were chosen to give some indication of the local oxygen strengthening across the sample after deformation, thereby permitting an estimate of the local mechanical properties. Figure 5.17 gives the micro-hardness profile

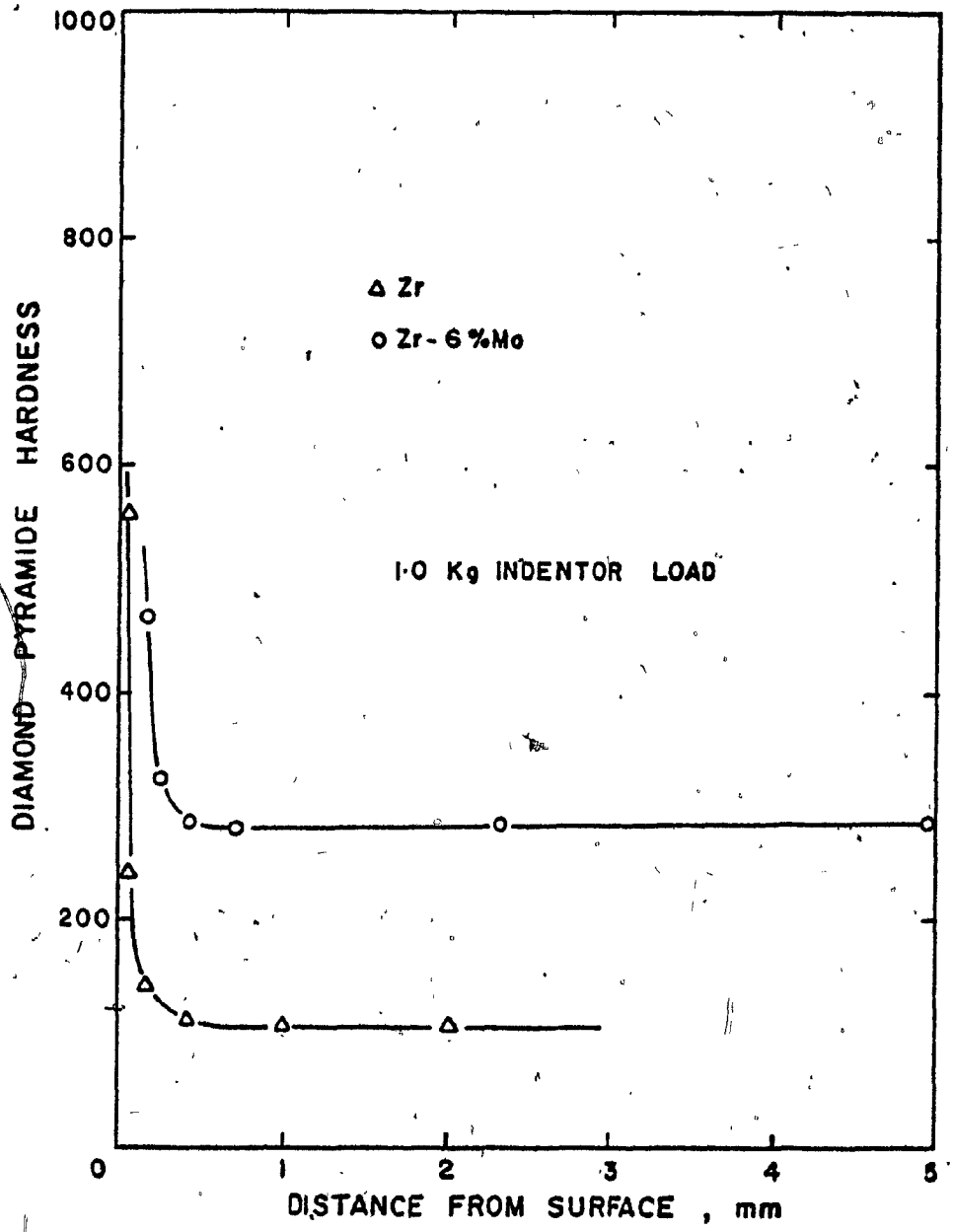

FIGURE 5.17 Plot of the microhardness versus distance from surface for Zr and Zr-6% Mo materials having undergone interrupted compression with a 1000-minute delay time.

for samples of Zr and Zr-6% Mo deformed to a strain of 0.15, maintained for an interruption delay of 60,000 seconds, and then deformed to 0.7 strain and subsequently quenched. We remark that for both zirconium and Zr-6% Mo, the α-layer persists up to 0.7 strain, although it appears to be thinner for zirconium than for Zr-6% Mo. The hardness values appear to decrease very sharply in the α-phase with the distance from the surface, indicating the presence of a very large oxygen gradient through the α-layer. By contrast, below 0.5 mm from the surface, that is, in the β-phase, no hardness variations are detected, supporting the view that no appreciable oxygen gradient is present. Furthermore, it appears likely from the absence of hardness variation in the β-phase that the strength is not influenced markedly by the plastic constraint exerted by the α-phase on to the β-core.

5.2 ZIRCONIUM 2.5% NIOBIUM

5.2.1 Prior Heat Treatment

The as-received material had been hot swaged and subsequently air cooled to room temperature. The samples were therefore annealed for 30 minutes at 1025°C and control cooled at a rate of 1°C/sec to room temperature. The preheat time at the test temperature was kept constant and was chosen to be 25 minutes.

5.2.2 Appearance of the Stress-Strain Curves

The stress-strain curves of the 2.5% Nb alloy tested in the β-phase exhibited a very marked work-hardening region, followed by a steady state flow region. A small decrease in flow stress was sometimes observed with further deformation. Such mild flow softening can arise in the course of high temperature deformation in metals that exhibit the classical dynamic recovery curve.

5.2.3 Effect of Strain Rate

The stress-strain curves obtained at true strain rates ranging from 1.5×10^{-1} to $6.2 \times 10^{-4} s^{-1}$ are given in Figures 5.18, 5.19 and 5.20 for testing temperatures of 925, 975 and 1025°C, respectively. The stress levels appear strain rate sensitive; in Figures 5.21, 5.22 and 5.23 are shown the log-log plots of strain rate versus flow stress, for the yield and steady state stresses, at testing temperatures of 925, 975 and 1025°C, respectively. The stress sensitivity, n, determined from the slopes appears to decrease from ∿5.0 for the yield data to 4.3 for the steady-state data at 925°C. A similar trend is observed at 975°C, although the slopes are steeper, giving n values of 6.0 at yield and 4.8 at steady state. At 1025°C, the experimental points suggest a curved fit, but in view of the limited range of testing rates, the suggestion is tentative. For this reason, a straight line was fitted, yielding slopes of 5.9 and 4.2 for the yield and the steady-state stresses, respectively.

The flow curves obtained at $6.2 \times 10^{-4} s^{-1}$ and $1.5 \times 10^{-3} s^{-1}$ and at a temperature of 1025°C (Figure 5.20) show much less work-hardening beyond the yield than those obtained at similar strain rates and lower temperatures or same temperature but higher strain rates. This indicates that the yield stress under these conditions is influenced by surface effects, which reduce the difference between steady-state and yield stresses, an effect which is apparent in Figure 5.23.

5.2.4 Effect of Temperature

Both the steady-state and the yield stresses are very sensitive to strain rate but appear to be considerably less sensitive to temperature.

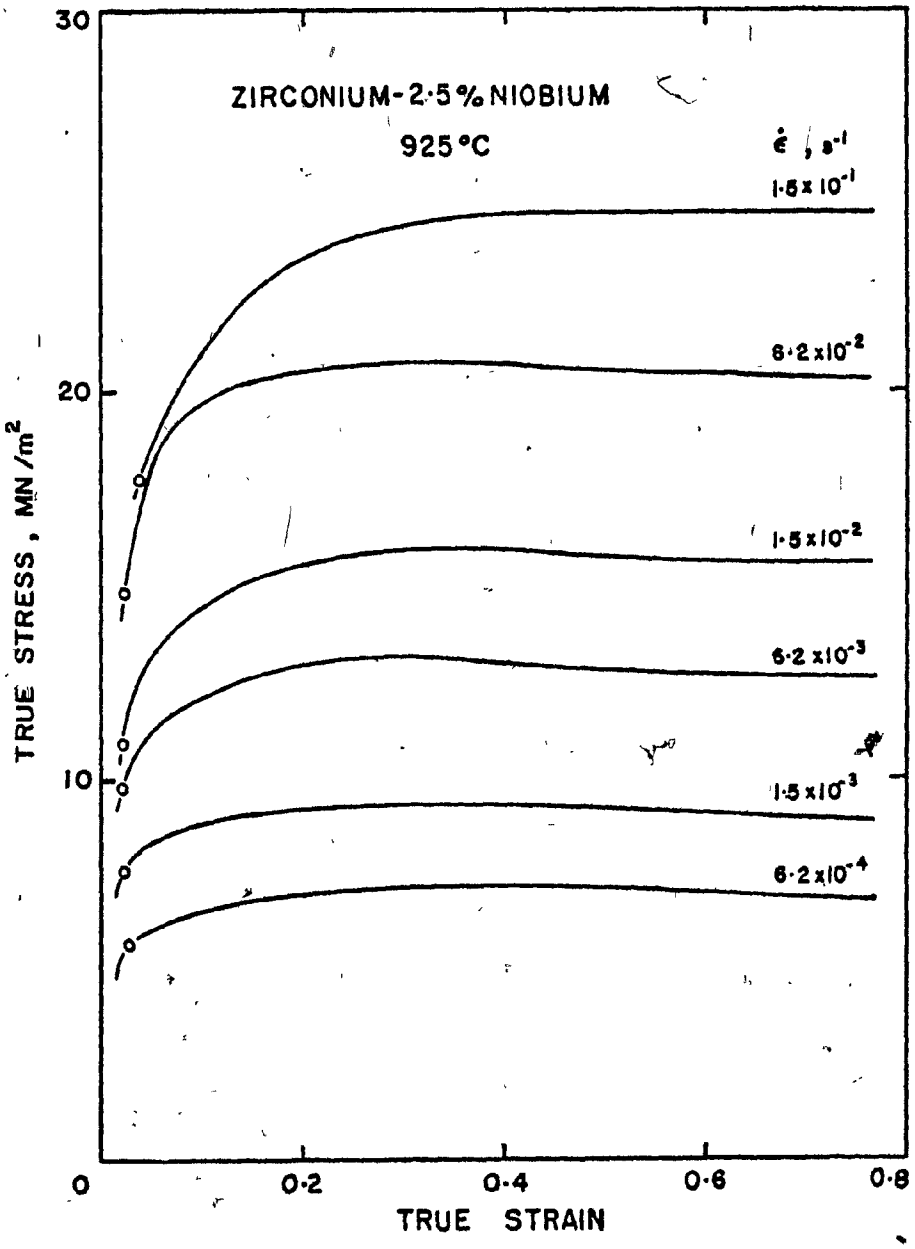

FIGURE 5.18 Experimental stress-strain curves of the Zr-2.5% Nb alloy, obtained at 925°C for various strain rates.

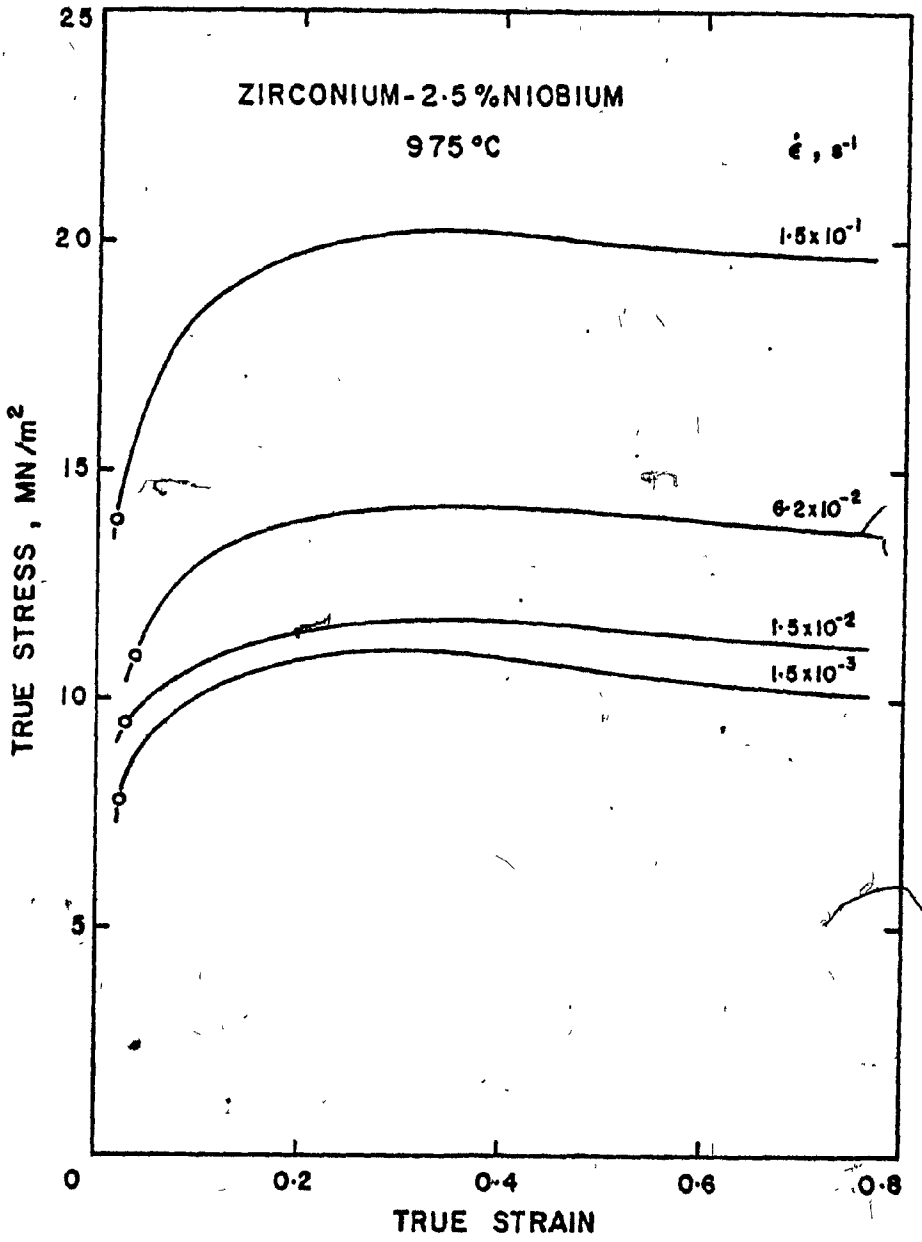

FIGURE 5.19 Experimental stress-strain curves of the Zr-2.5% Nb alloy, obtained at 975°C for various strain rates.

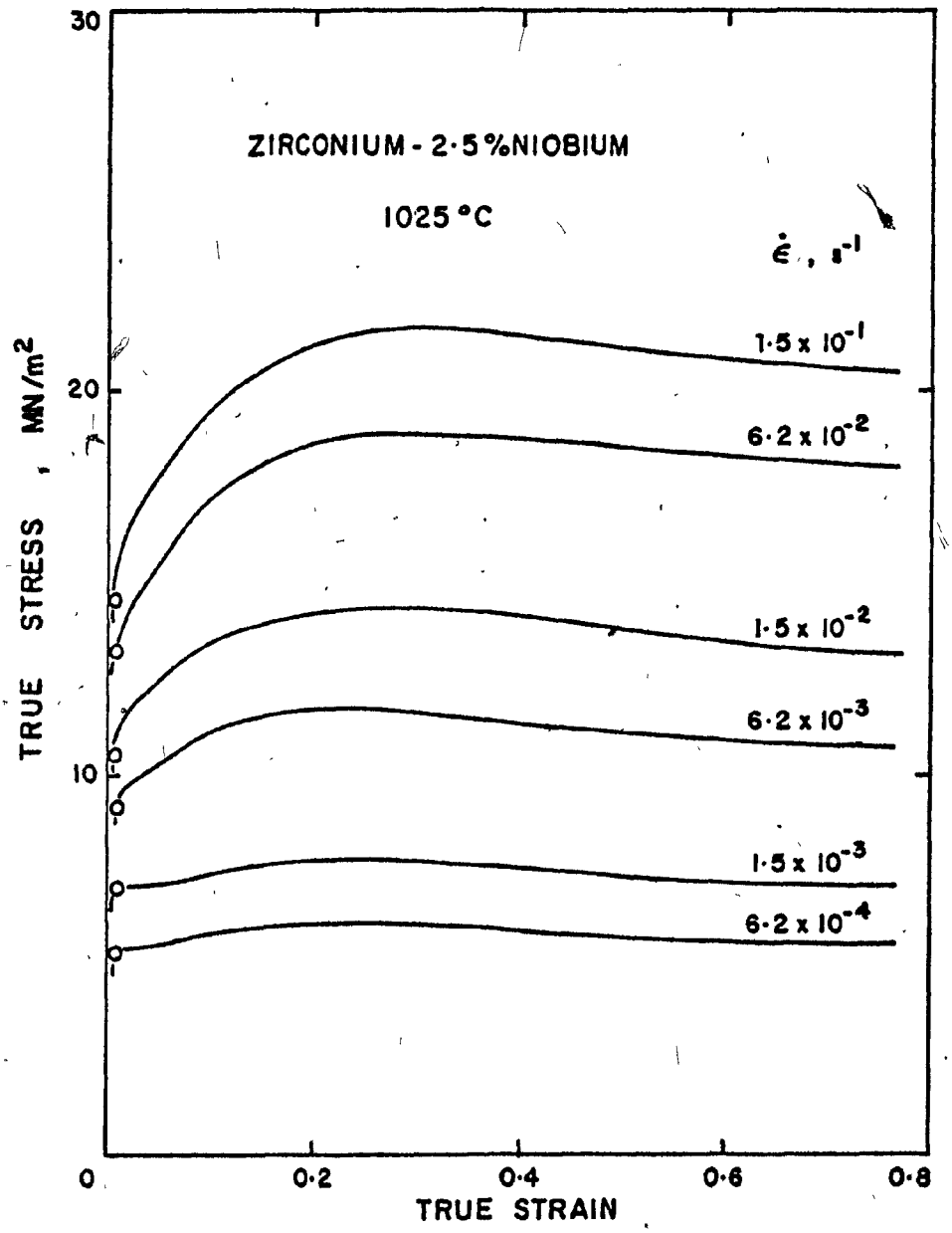

FIGURE 5.20 Experimental stress-strain curves of the Zr-2.5% Nb alloy, obtained at 1025°C for various strain rates.

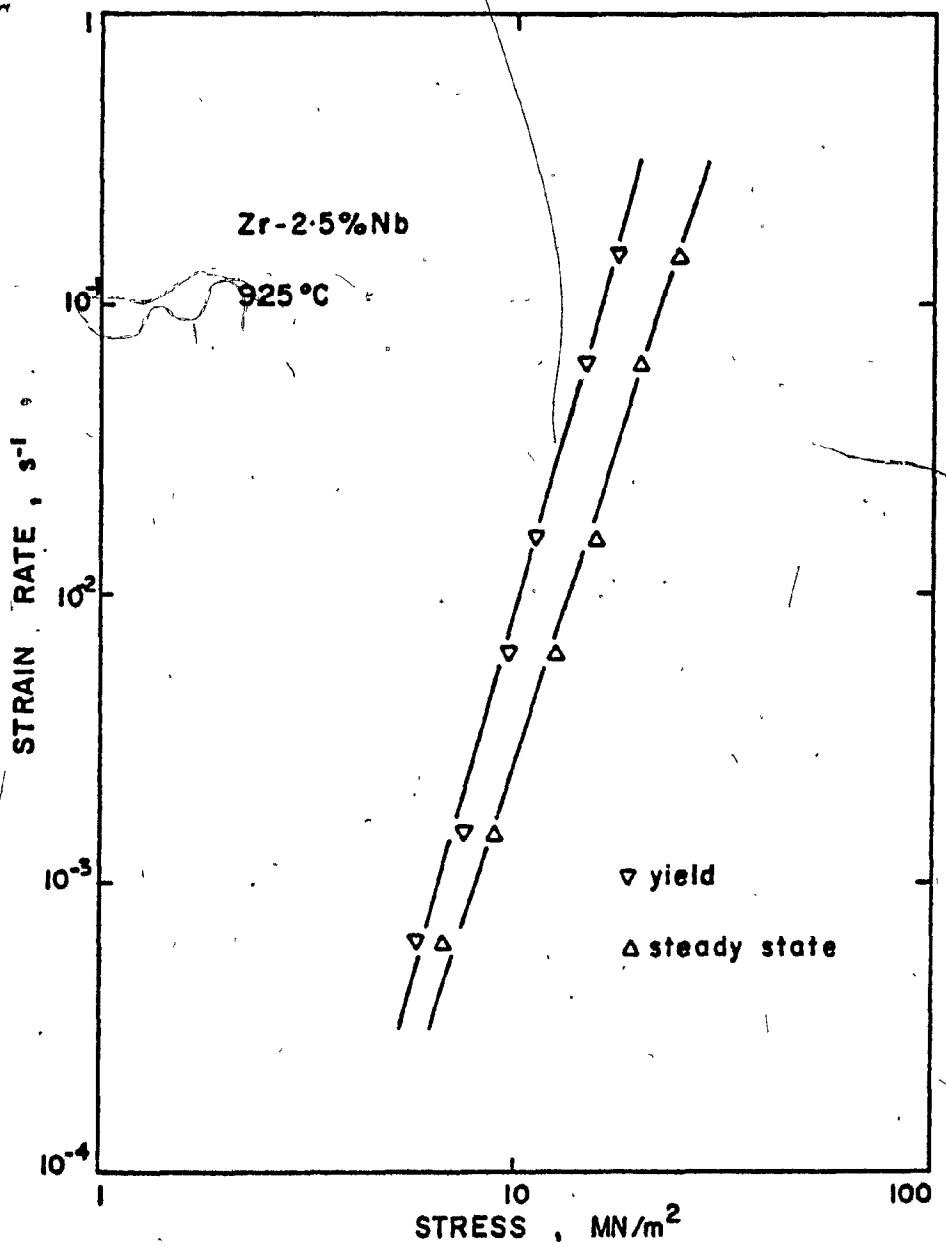

FIGURE 5.21 Logarithmic plot of the strain rate dependence of the yield and steady state flow stresses at 925°C, for the Zr-2.5% Nb alloy.

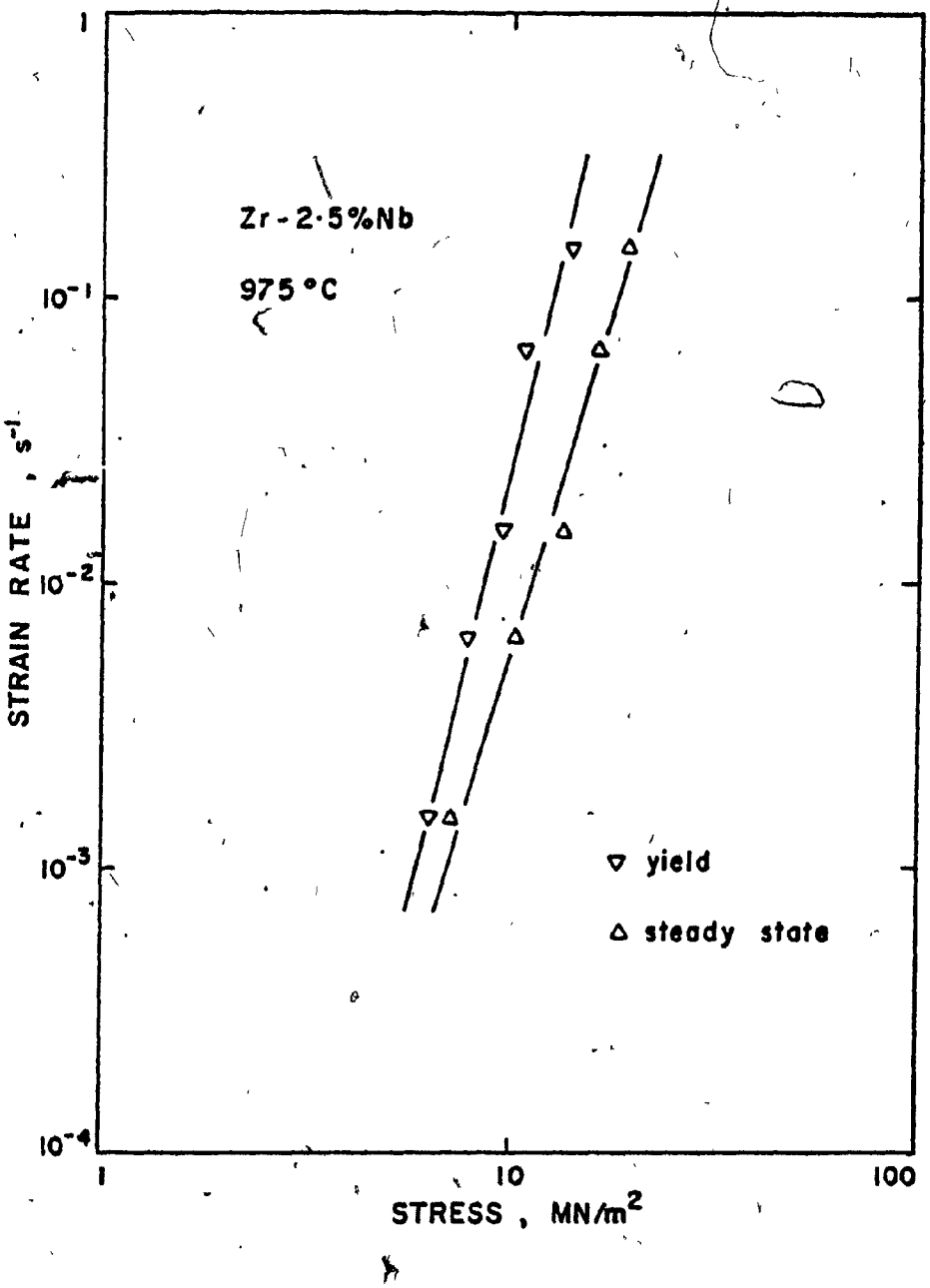

FIGURE 5.22 Logarithmic plot of the strain rate dependence of the yield and steady state flow stresses at 975°C, for the Zr-2.5% Nb alloy.

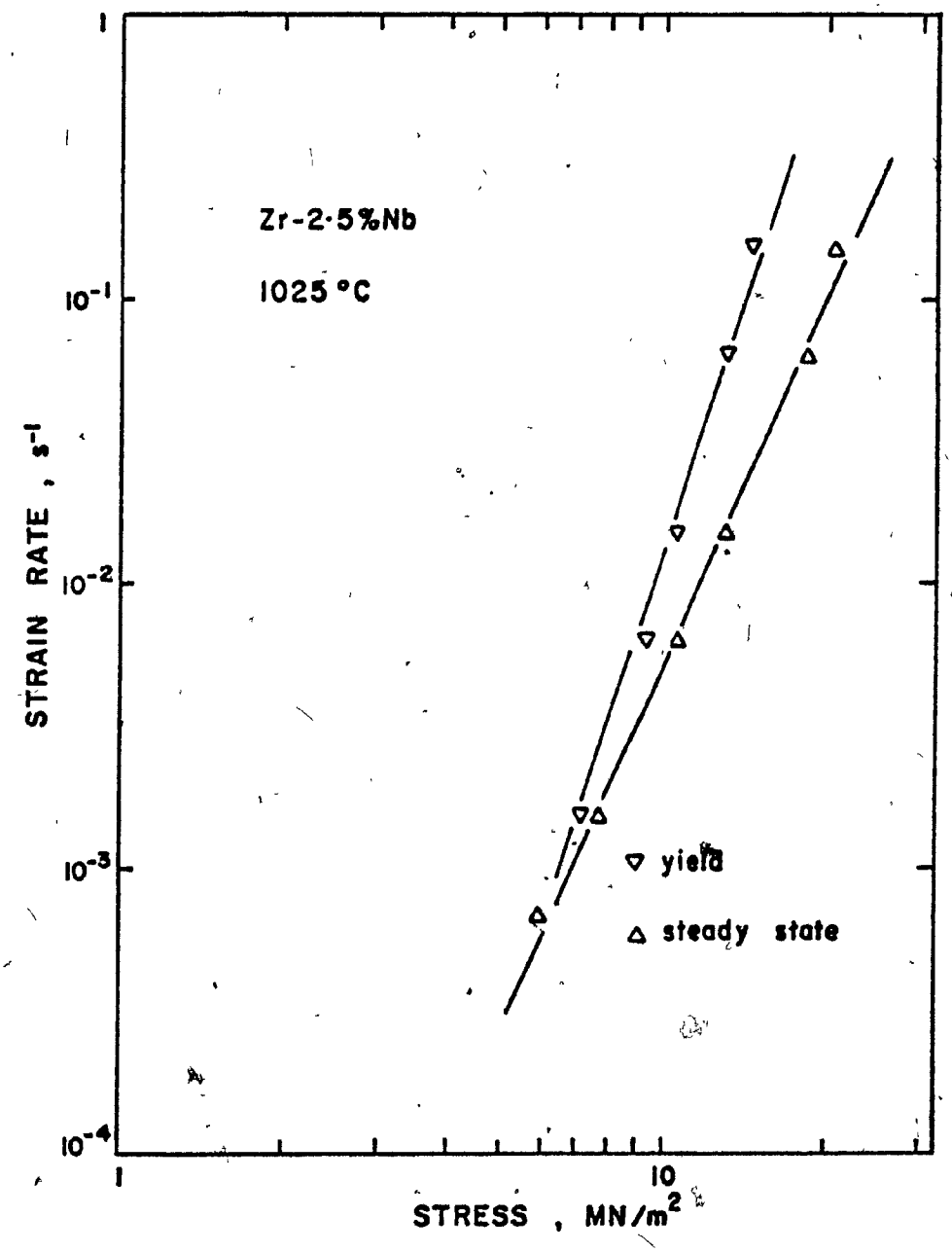

FIGURE 5.23 Logarithmic plot of the strain rate dependence of the yield and steady state flow stresses at 1025°C, for the Zr-2.5% Nb alloy.

A maximum of a 20% stress decrease takes place as a result of a 100°C temperature increase. This renders the determination of experimental activation energies rather inaccurate and of questionable physical significance. Moreover, the present data even indicate that the stress levels at 1025°C are higher than those at 975°C. This may have arisen from a material difference, since the samples tested at 1025°C came from a different bar than those used at 925 and 975°C. In the former samples, no significant grain growth was found prior to testing, and the grain size of the tested material was about 0.15 mm.

5.3 HIGH NIOBIUM ALLOYS

This section will describe the results obtained on the 10, 15 and 20% Nb alloys. The mechanical behaviour of these alloys appears similar, but differs considerably from that of the 2.5% Nb alloy. These alloys, which were received in the as-extruded condition, were given a standard heat treatment consisting of a 10-minute anneal at 1000°C, followed by cooling in inert atmosphere at a rate of 5°C/sec. In all the alloys, the β-phase was retained to room temperature, except possibly for some decomposition of the 10% Nb alloy, as concluded from the TTT diagrams of Hehemann (211) related to Zr-Nb alloys.

5.3.1 The Stress-Strain Curve

A typical stress-strain curve is shown in Figure 5.24 for the 20% Nb alloy tested at $1.5 \times 10^{-3} s^{-1}$. The flow curve exhibits very little work-hardening before arriving at a maximum in stress, beyond which the stress decreases continuously with strain. On the curve obtained at 725°C, the yield stress is 173.4 MPa, the peak stress 180.4 MPa and the flow

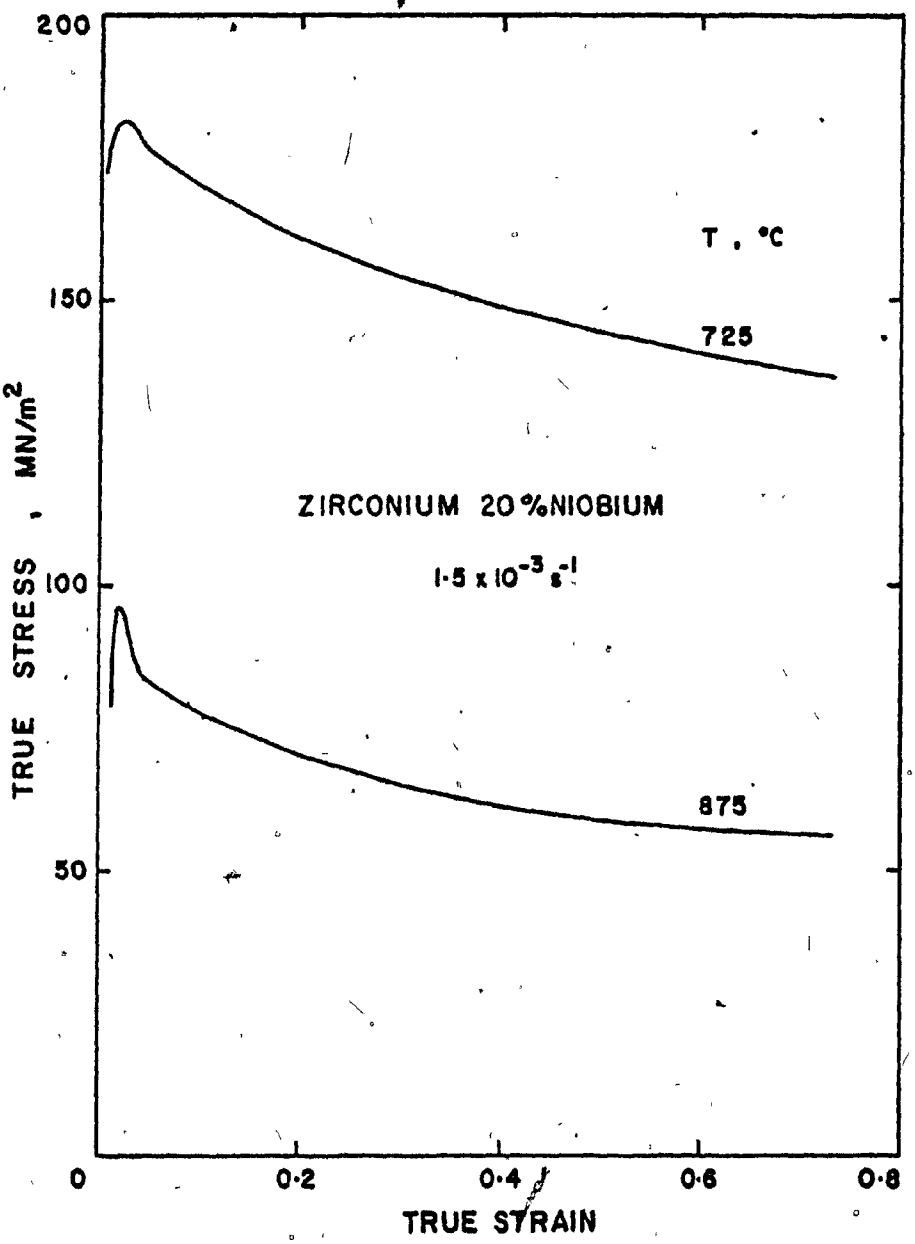

FIGURE 5.24 Typical stress-strain curves of the Zr-20% Nb alloy exhibiting marked flow softening behaviour.

stress at 0.7 true strain 136.2 MPa. The amount of softening is large and appears to be present at 875°C as well. Figure 5.25 shows that similar behaviour is obtained at 825°C for the 15% Nb alloy. In the 10% Nb alloy, again, flow softening occurs at all temperatures and strain rates, as shown in Figure 5.26. In the last alloy, attempts were made to reduce the softening observed by strain-annealing the samples prior to testing so as to produce a fairly large grain size. It appears that this treatment results in an increase in the flow softening effect, and furthermore, it causes an increase in flow stress, as can be seen from Figure 5.26. It is of interest to note that two types of flow softening are observed: a severe one, typified in Figure 5.24 and Figure 5.25, and a mild one, typified in curves 1 to 4 of Figure 5.26. Depending upon the thermal pre-treatment, the material can change from one type of behaviour to another, as will be seen in more detail in Section 5.3.4.

The flow stress of the high niobium alloys appears both temperature and strain rate sensitive, as is the case in the hot working of metals. The effects of heat treatment suggest that some as yet unspecified variables affect the flow curve. The following paragraphs describe the results of the investigations carried out in order to discover the source of the softening behaviour.

5.3.2 Effect of Testing Atmosphere

The presence of a sharp decrease in flow stress which often occurred shortly after yielding, as well as the subsequent flow softening, could have been due to an oxidation effect, in a manner similar to that observed in the Zr-Mo alloys described above. The influence of the oxygen present in the argon atmosphere on the mechanical properties was therefore

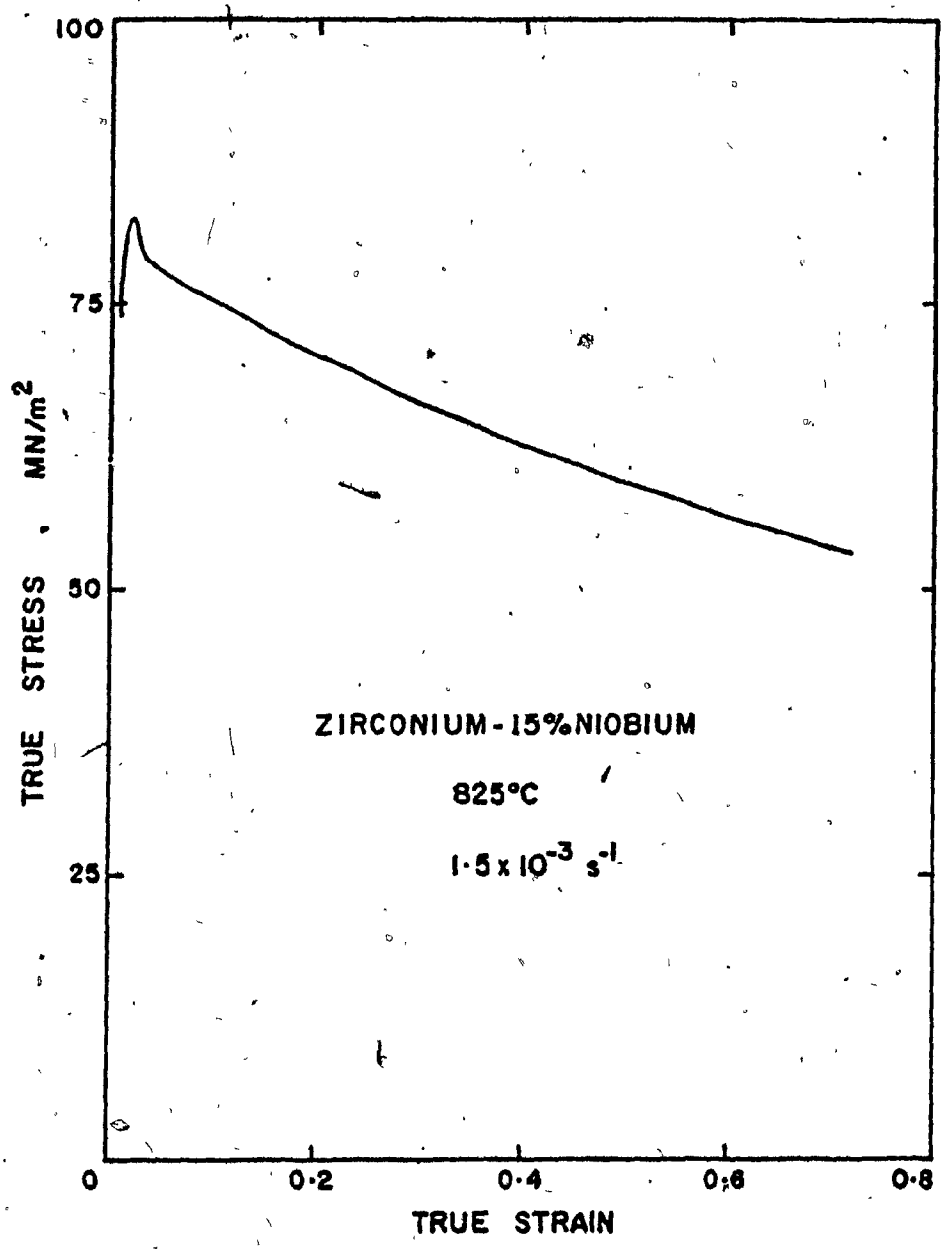

FIGURE 5.25 Typical stress-strain curve of the Zr-15% Nb alloy tested at 825°C exhibiting a marked flow softening effect.

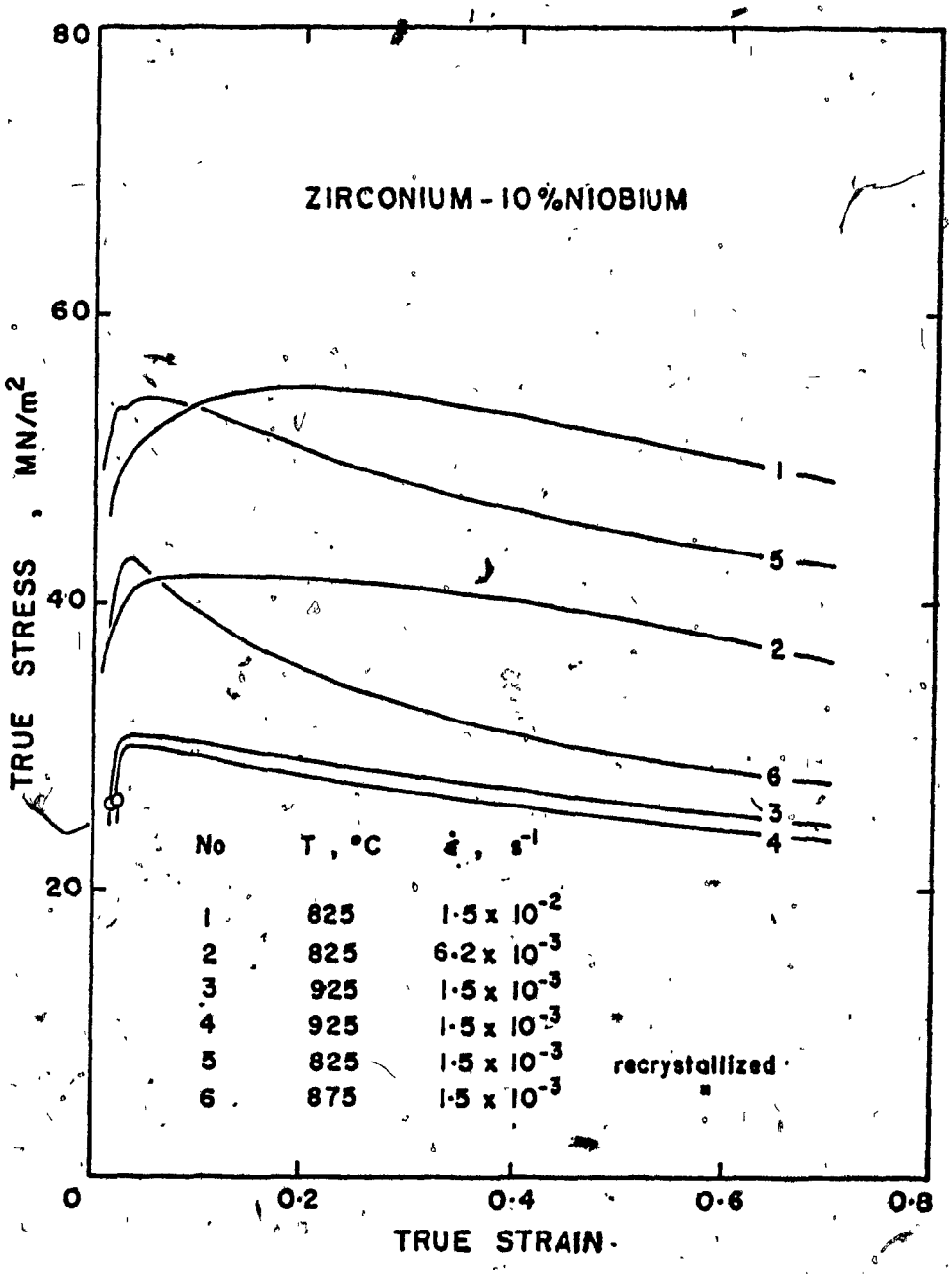

FIGURE 5.26 Stress-strain curves of the Zr-10% Nb alloy tested at various temperatures and strain rates, and showing the transition from mild to severe softening with annealing treatment.

assessed by investigating the effects due to variations in preheat time, delay time during intermediate unloading tests, and those produced by the plating procedure.

5.3.2.1 Effect of preheat time

Samples of Zr-20% Nb were held at the test temperature of 725°C for 1800, 10800 and 72000 seconds prior to being deformed at $1.5 \times 10^{-3} s^{-1}$. The stress-strain curves obtained on these samples are shown in Figure 5.27. The influence of prolonged holding at the test temperature is to increase the magnitude of the initial peak in flow stress and to promote subsequent flow softening. This increase appears relatively small from 1800 to 10800 seconds. The flow curve obtained after 1800 seconds preheat, however, shows a slight drop shortly after yield. It is possible that this drop arises from oxygen effects during the preheat time and, to test this hypothesis, interrupted tests were carried out.

5.3.2.2 Interrupted tests

The effect of increasing delay times during intermediate unloading on the reloading stress was investigated on the 20 and 15% Nb alloys in order to evaluate the strengthening that can be caused by oxidation. This method was described in detail in Section 5.1.6 pertaining to the Zr-Mo alloys. Figure 5.28 shows the stress-strain curves obtained using 10 and 65 minute delays. The yield stress caused by the 65 minute delay is only about 8 MN/m^2 higher than that due to the 10-minute delay. In both cases, the yield stress is lower than the unloading stress and the flow stress on reloading settles back almost immediately to the level of the uninterrupted curve. This indicates that at 725°C there is no significant oxida-

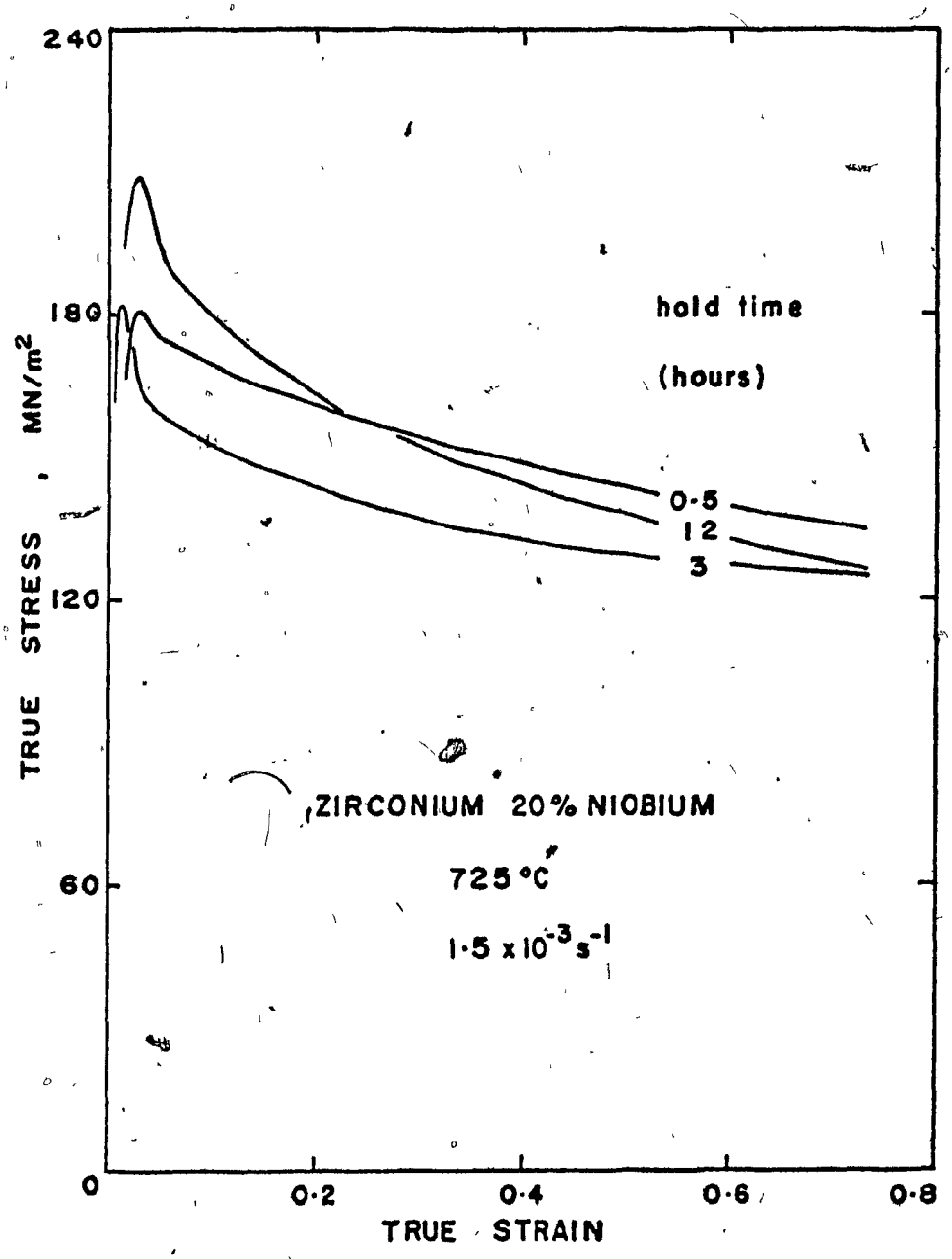

FIGURE 5.27 Effect of preheat time upon the aspect of the flow curve for the Zr-20% Nb alloy tested at 725°C.

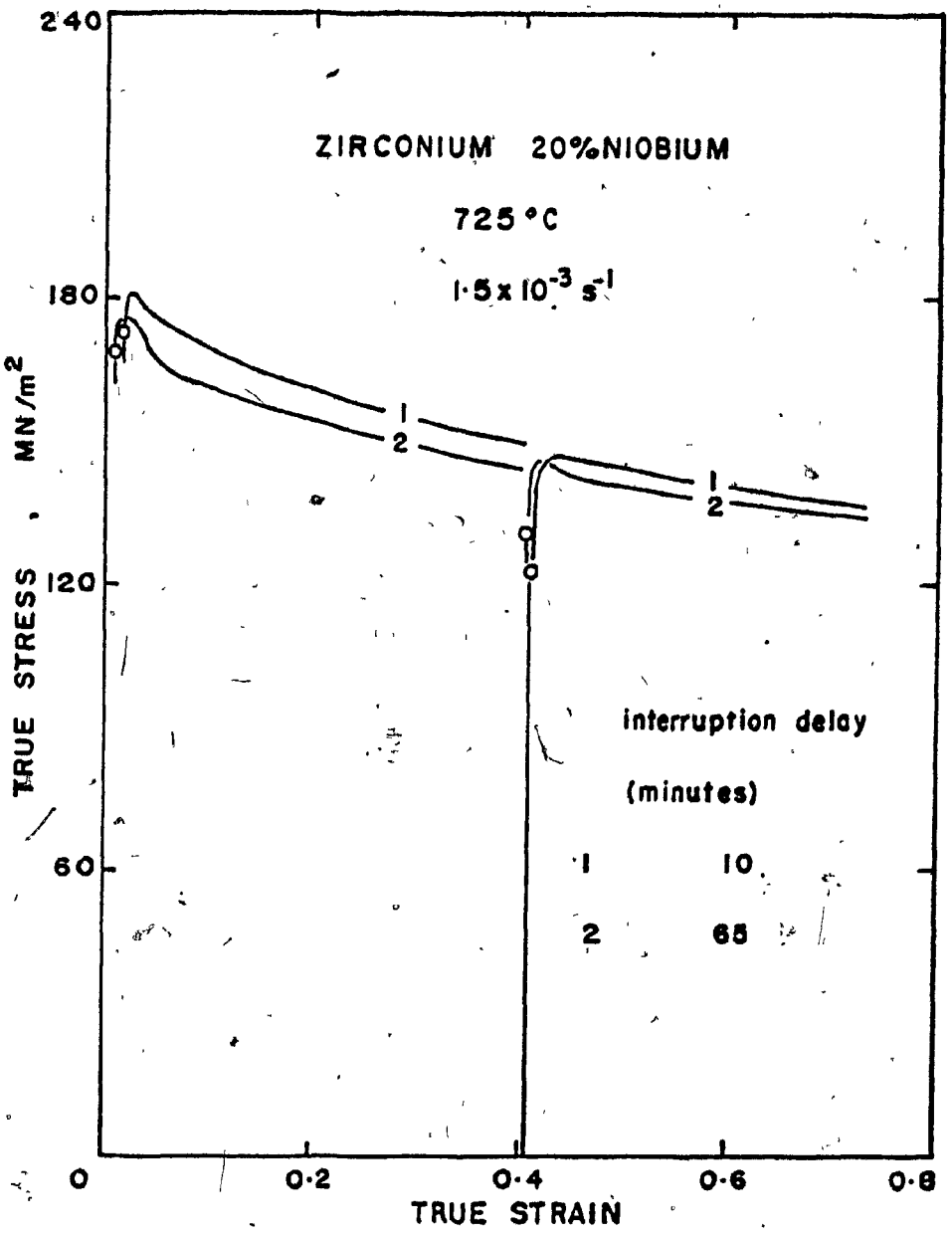

FIGURE 5.28 Effect of the interruption delay upon the subsequent flow of the Zr-20% Nb alloy, tested at 725°C and $1.5 \times 10^{-3} s^{-1}$.

tion effect, as might be expected for such a low temperature. These results confirm the results obtained by varying the preheat time and furthermore indicated that within the first 60 minutes, no oxidation effects similar to those observed in Zr-Mo alloys are present, at least at 725°C.

The stress-strain curve for Zr-15% Nb tested at 825°C and interrupted for 30 minutes is shown in Figure 5.29. During the delay, the chamber was opened and the sequence of operations carried out during the insertion of the sample into the hot chamber repeated, so as to check whether the few minutes following sample insertion had a large influence on the flow stress. Upon reloading, the flow stress appears unperturbed by the delay.

5.3.2.3 Gold plating

Finally, the deformation of the 15% Nb alloy at 825°C was carried out on gold plated (0.2 μm) and unplated samples, as shown in Figure 5.30. There is little difference in the softening behaviour and in stress levels. The most apparent difference is a slightly lower loading rate in the gold-coated sample, which is expected to be a parameter very sensitive to oxidation effects. The results of these investigations lead to the conclusion that the testing atmosphere did not contribute significantly to the flow stress in the lower temperatures of the β-range. The unusual deformation behaviour of the 10, 15 and 20% Nb alloys thus cannot be explained by atmosphere effects, as was the case for the Mo alloys. At higher temperatures, the effects of oxygen were not ascertained, but are unlikely to increase sharply enough to be responsible for the flow softening effects.

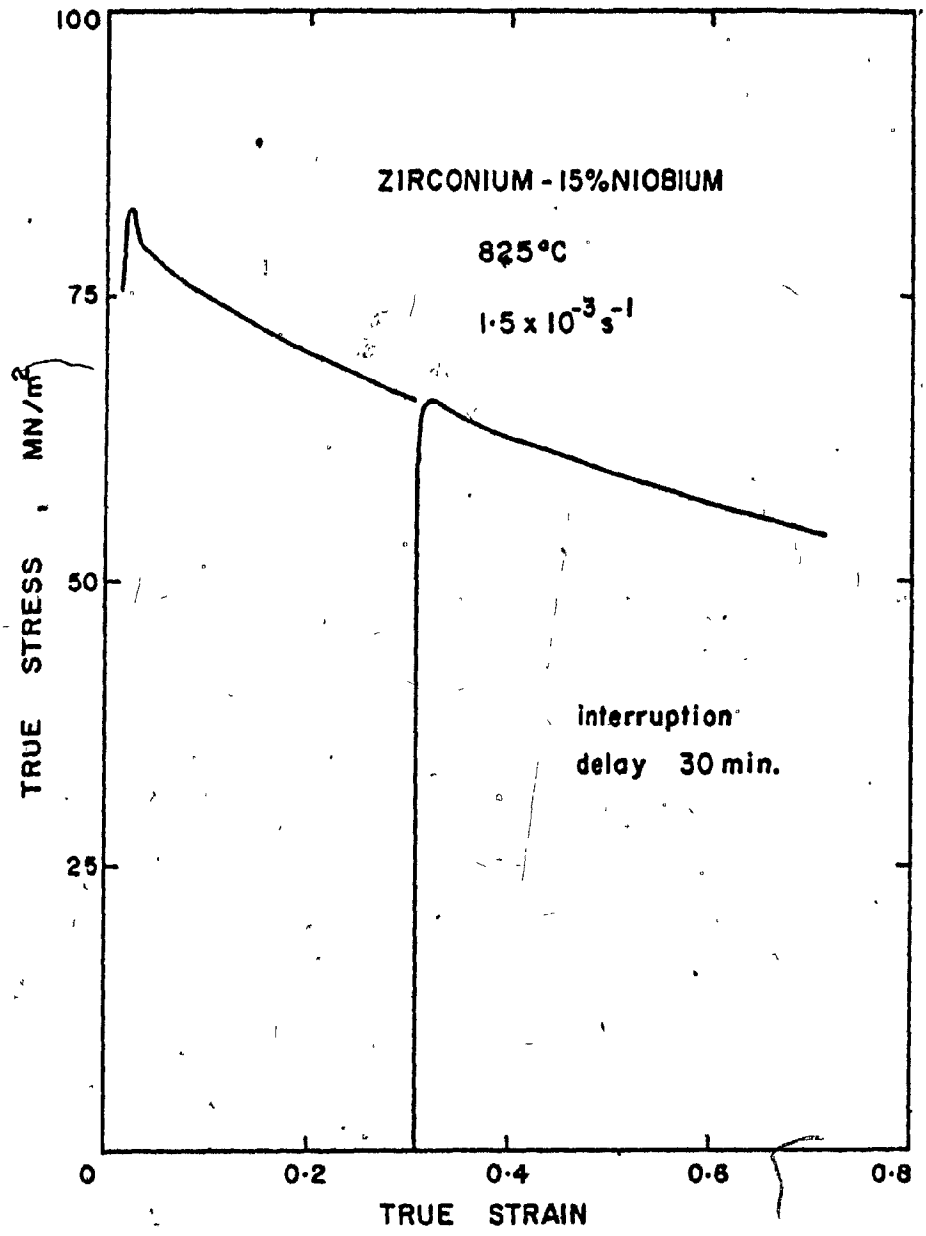

FIGURE 5.29 Effect of interruption delay upon the subsequent flow of the Zr-15% Nb alloy, tested at 725°C and $1.5 \times 10^{-3} s^{-1}$.

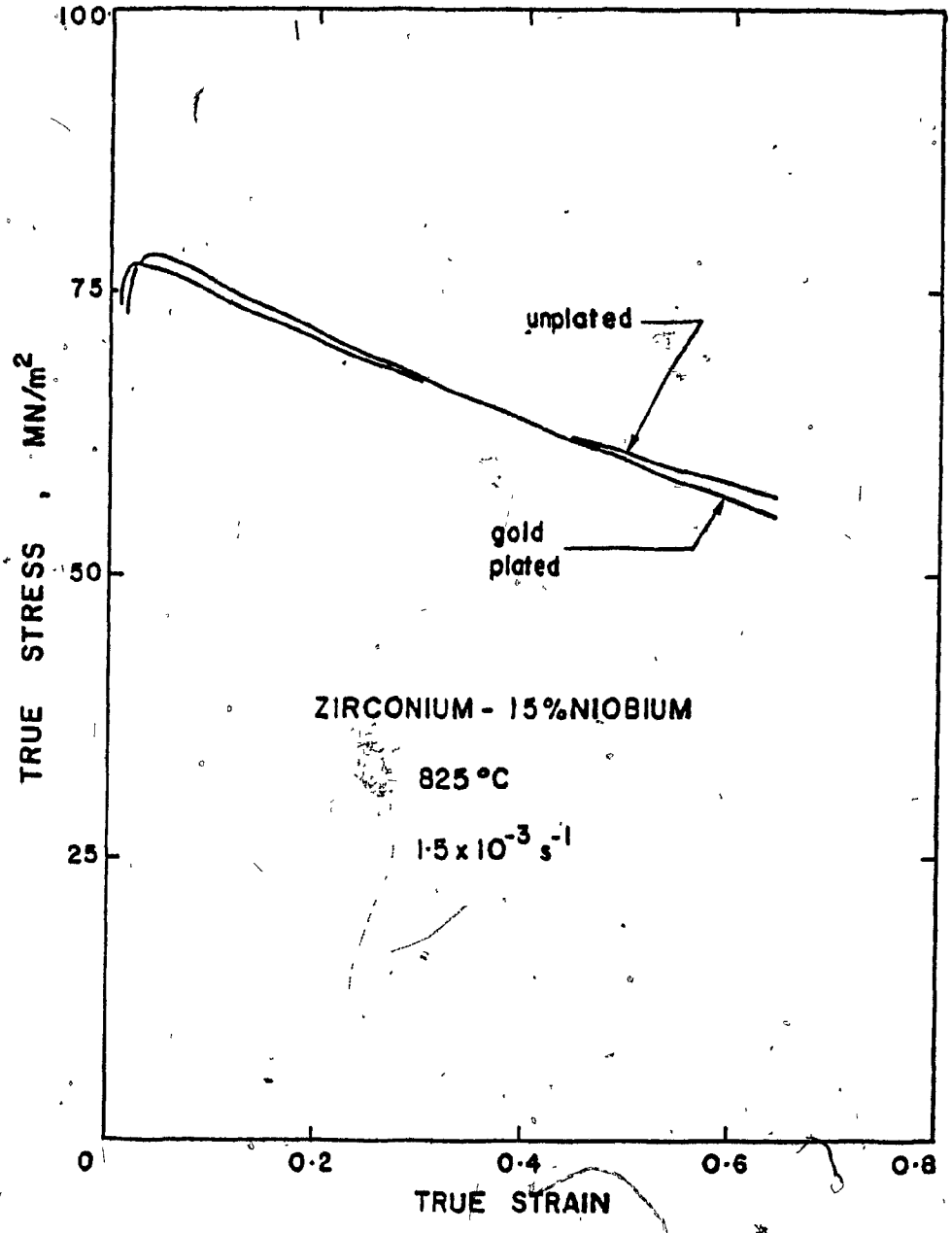

FIGURE 5.30 Effect of gold plating on the stress-strain curve of the Zr-15% Nb alloy.

5.3.3 Texture Determination

The marked strength increase that arose as a result of recrystallization and grain coarsening (Figure 5.26) and the increased softening on deformation suggested that texture variations during deformation could be responsible for the flow softening that was observed. This hypothesis was consistent with the results of the interrupted tests, which showed no tendency for a return to the undeformed condition during an interruption delay, and the observation that flow softening seemed present at all temperatures. The β-phase, being bcc, is not very prone to strong texture effects, but an unusual texture development could have occurred in the present material, and for this reason texture determination was carried out.

The (110) pole figures were determined in the 10% Nb alloy tested at 825°C as a function of strain as well as in the standard heat treatment condition (i.e. 10 minutes at 1000°C) but water quenched instead of slowly cooled and in the fully recrystallized condition. Determination of the pole figures was based on the assumption that the texture was symmetrical about the compression axis. Details of the sample preparation and texture determination are given in Appendix 2.

Figure 5.31 shows the pole development observed as a function of strain for the alloy maintained for 10 minutes at 1000°C. In the upper left quadrant is given the texture prior to testing ($\varepsilon = 0$), and the textures obtained for strains of 0.1, 0.4 and 0.8, respectively, are distributed clockwise. In no case were the values of the pole density higher than 2, indicating only a fairly weak variation in texture. The spread of the poles in the undeformed condition indicates a nearly random texture. After a true strain of 0.1, the (110) poles tend to shift away from the

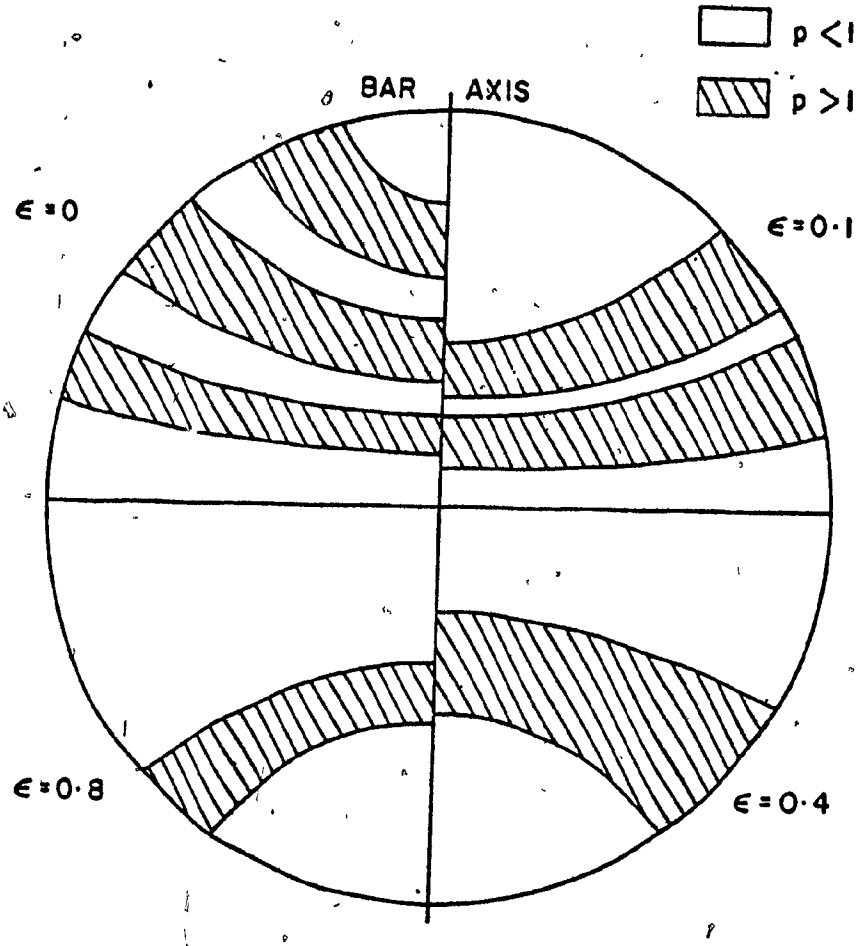

FIGURE 5.31 (110) pole figure of the Zr-10% Nb, showing the evolution of the texture with strain.

bar axis. At a true strain of 0.4, the poles are located mostly in a wide zone which narrows somewhat when the strain reaches 0.8. In this latter texture, the (110) poles are located about 30-40° from the bar axis.

The texture evolution with strain appears to be from nearly random to a (111) fiber texture, as seen from the angle between the (111) and (110) planes. This angle is 35.26° the angle around which are spread high (110) pole densities.

Turning our attention now to the pole figures obtained for the recrystallized material, these were obtained in a similar way and are presented in Figure 5.32. It can be seen that similar results were obtained, except that the (110) poles are more evenly spread around the mean angle 35.26°.

It is now possible to estimate qualitatively the effects of these textures on the mechanical strength. In a random texture, which can be considered to be approximated in the undeformed material, the relation between the flow stress σ_r and the average shear stress τ on a (110) plane is

$$\sigma_r = M_T \tau \qquad (5.1)$$

where M_T is the Taylor factor, equal to 3.06 in bcc metals. On the other hand, for a perfect (111) fiber texture, the relation between the flow stress σ_t and the shear stress τ on the operating $[11\bar{1}]$ (110) slip system is

$$\sigma_t = M_S \tau \qquad (5.2)$$

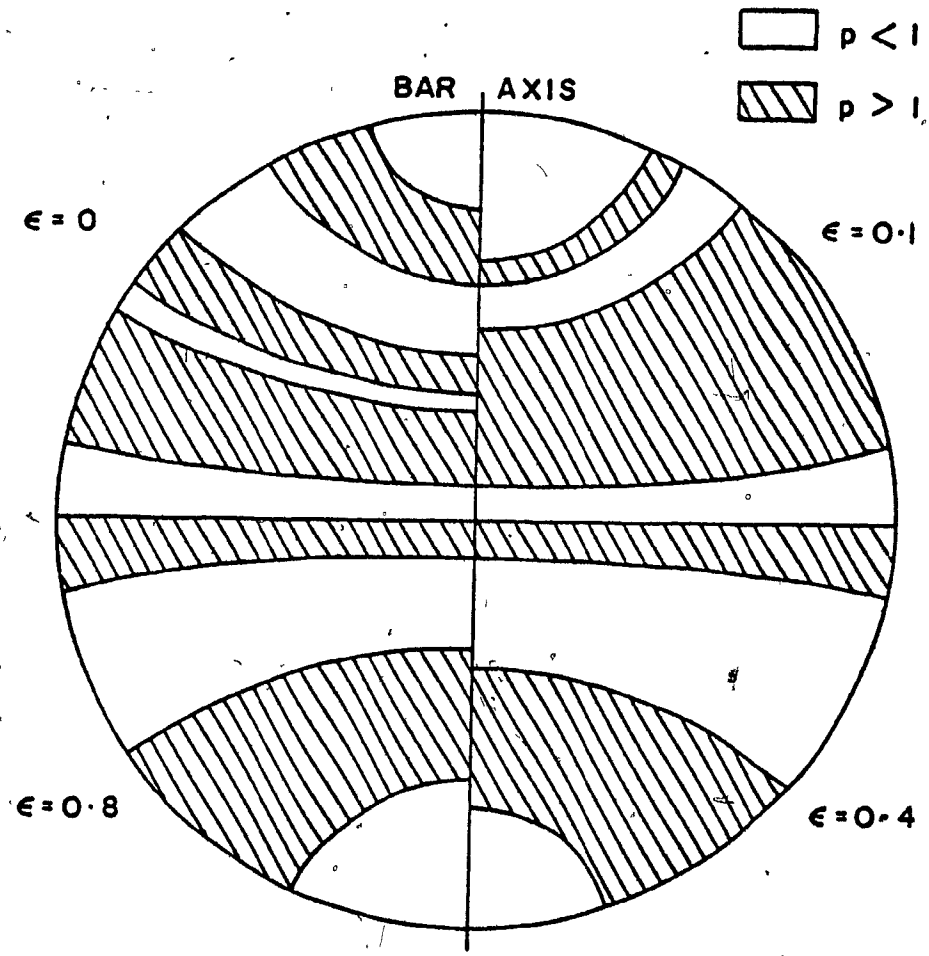

Zr - 10%Nb recrystallized

FIGURE 5.32 (110) pole figure of Zr-10% Nb, strain annealed, showing the evolution of the recrystallized texture with strain.

where M_S is the inverse of the Schmidt factor and is equal to 3.67. If it is assumed that a constant resolved shear stress is required to initiate flow, the flow stress of the fiber texture will be

$$\sigma_t = \frac{M_S}{M_T} \sigma_r = 1.20\, \sigma_r \qquad (5.3)$$

that is, 20% higher than that required to deform a random structure. The development of the hard (111) fiber texture should lead to an increase in flow stress and in consequence should oppose the softening behaviour.

The determination of the pole figures in the other Zr-Nb alloys has not been attempted since texture evolution is a geometric property and should therefore lead to similar results. The finding that a (111) fiber texture is developed by compression on bcc Zr-Nb is in agreement with data reported in the literature (212).

5.3.4 Effect of Annealing Time

The experiments described in this section were designed to investigate the influence of β-annealing treatments on the flow curves of β-Zr-Nb alloys. In preliminary tests it was apparent that the type of flow softening was dependent on the testing temperature. At the higher temperatures, flow softening was abrupt at low strain and became rather mild at higher strains. On the other hand, at lower temperatures the flow softening was more gradual in character, the rate of softening being comparable at all strains. The influence of annealing time on the flow curve was first investigated in the 15% Nb alloy. Samples were annealed at 1000°C in a 3" quartz furnace tube chamber evacuated down to 8×10^{-6} torr, for various times, and were then cooled to room temperature by rolling

the furnace off the tube. The samples were then deformed at a strain rate of $1.5 \times 10^{-3} s^{-1}$ at 825°C after a standard preheat of 20 minutes. Figure 5.33 shows the stress-strain curves obtained after the various annealing times, and Figure 5.34 gives the stresses at yield and at 0.7 strain plotted versus the logarithm of the anneal time.

The flow stress levels appear to increase sharply with time of the anneal at 1000°C. The as-received material (no anneal) was found to flow at the lowest stresses, and did not exhibit any significant flow softening. A five-minute anneal at 1000°C increases the yield stress over that of the as-received material from 19.6 to 52.2 MPa and the corresponding stresses at 0.7 strain from 19.7 to 37.8 MPa. In addition to the increase in the flow stress level, a significant amount of strain softening is introduced by this short anneal. The strength of the material increases further as the time of annealing is increased, although not as markedly as during the first five minutes; this is indicated by the curves obtained for 90 and 240 minutes. The amount of stress increase brought about by annealing seems to reach a maximum value after about 240 minutes.

In order to confirm the existence of the very large strengthening resulting from annealing at 1000°C, these experiments were repeated in the same alloy (although in a different bar, labelled 15A, whereas the results described above pertained to a bar labelled D). In addition, similar experiments were carried out on samples of the Zr-20% Nb alloy. The annealing time was also extended to 64 hours in order to establish whether or not the stress would decrease at time longer than that required to reach the maximum value. Furthermore, a larger number of annealing time was chosen. All samples were prepared in a similar manner to that described above.

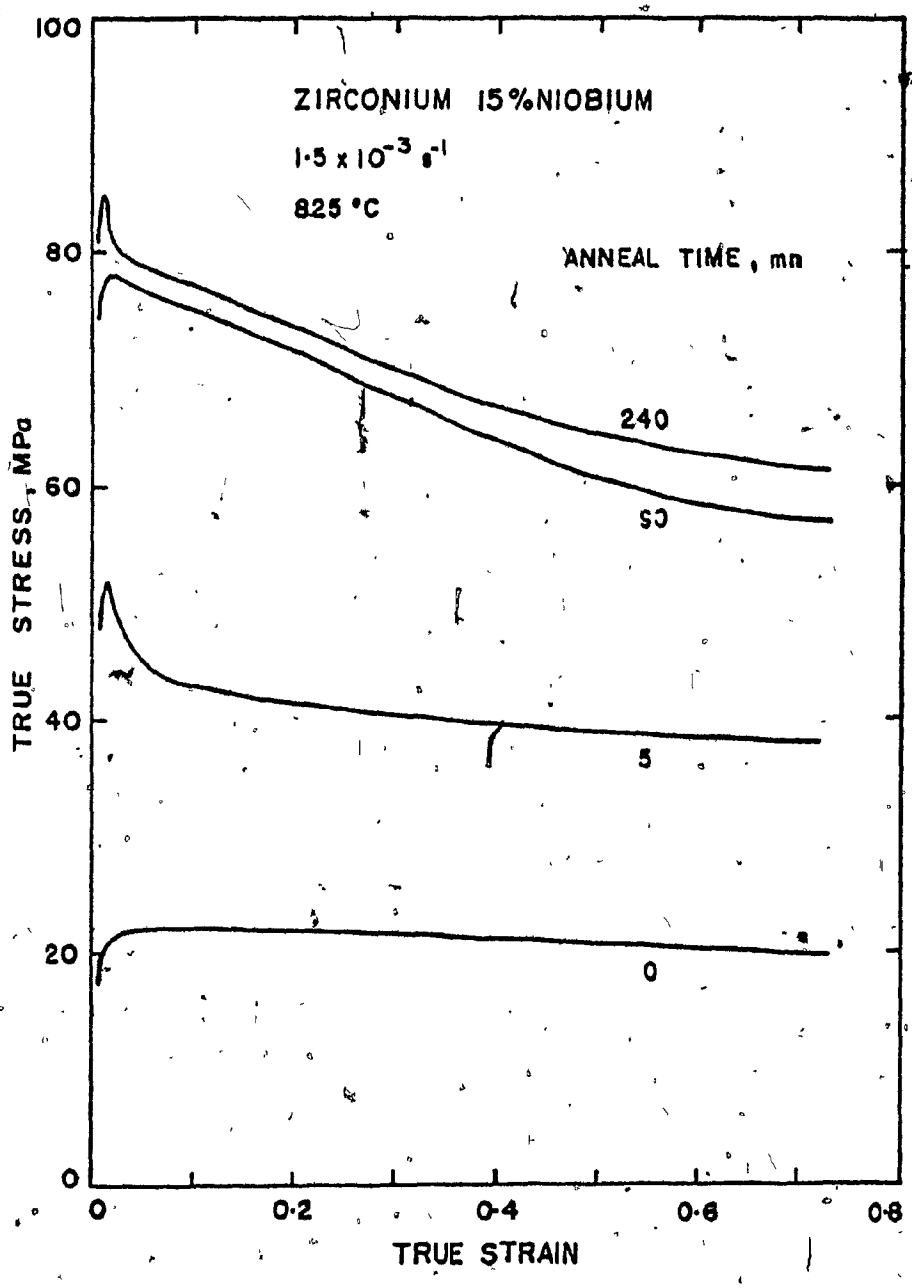

FIGURE 5.33 Effect of annealing time at 1000°C on the flow curves of Zr-15% Nb (bar D) tested at 825°C and $1.5 \times 10^{-3} s^{-1}$.

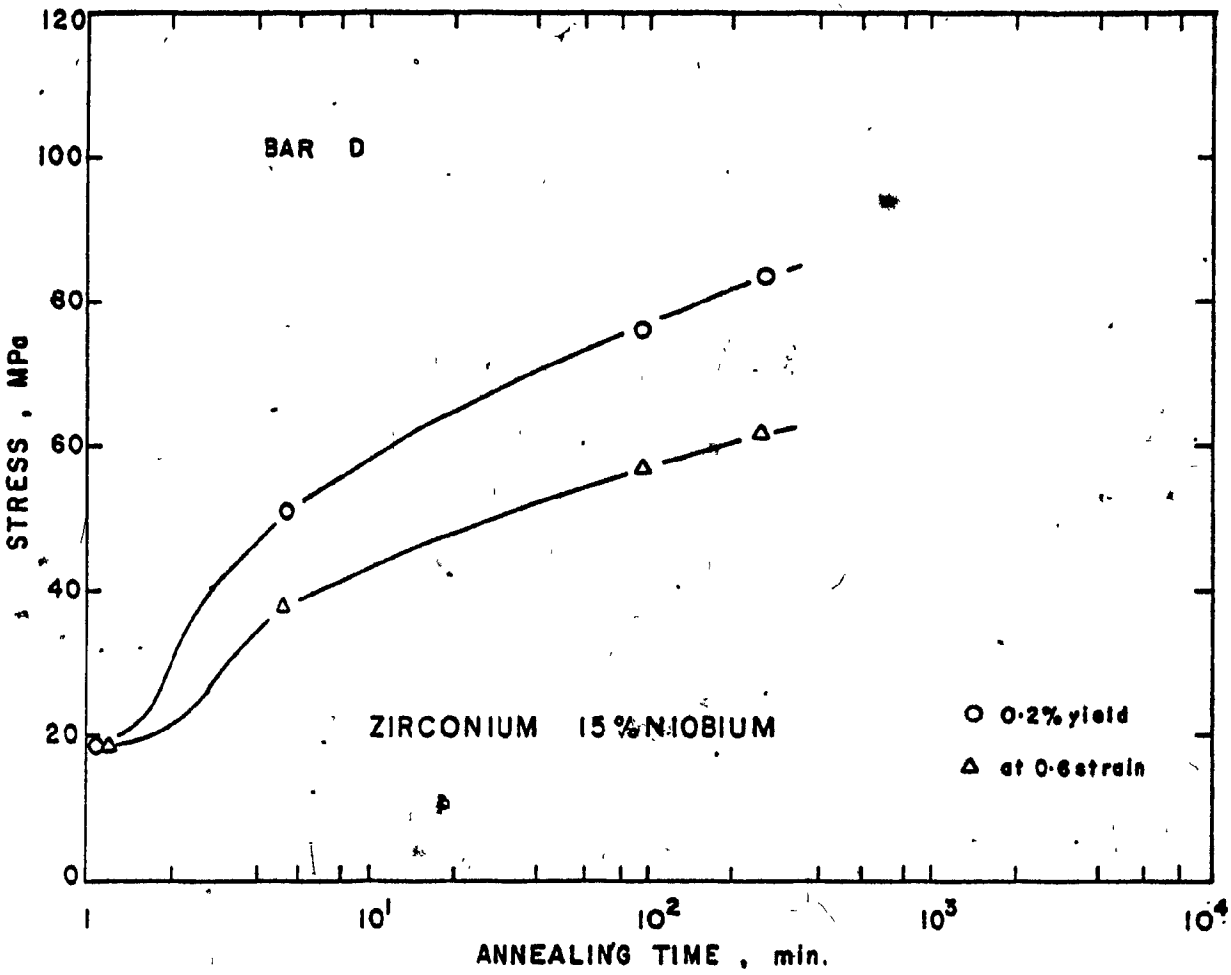

FIGURE 5.34 Yield and steady-state stresses of the flow curves of Figure 5.33, plotted versus the logarithm of the annealing time at 1000°C.

The stress-strain curves obtained under such conditions are shown in Figures 5.35 and 5.36 for the Zr-15% Nb alloy (bar 15A) and Zr-20% Nb alloy (bar 20B), respectively. The peak stress, the lower yield stress and the stress at 0.7 strain are plotted versus the logarithm of time in Figures 5.37 and 5.38 for the two alloys. From Figures 5.35 and 5.37 it can be seen that no significant change in mechanical properties takes place for anneals of less than five minutes duration. However, after ten minutes the stress increases markedly and stays approximately constant with anneal time up to four hours. Beyond this time, the stress drops again by about 20 MPa and stabilizes for longer anneal times. Comparison of Figures 5.34 and 5.37 shows that bar D in the as-received condition deforms at a stress which is approximately half that of bar 15A in similar conditions. In these two tests, bar D shows no softening, whereas bar 15A does, suggesting that flow softening and the increased strength may share a causal relationship. It is of interest in this respect to note that the difference in stress between the peak stress and the stress at 0.7 strain flow appears to be a maximum for the largest flow stress levels. For the longest anneal times, flow softening is not marked but nevertheless remains present.

The same trend is observed in the 20% Nb alloy, Figures 5.36 and 5.38. The increase in strength with anneal time appears somewhat more progressive than in the 15% Nb alloy, and the stress decrease occurs only after an eight-hour anneal, indicating a more sluggish process.

Part of the stress increase which apparently arises from an increased annealing time could be produced by oxygen contamination. If this were the case, then there would be a progressive increase in the flow stress levels with annealing time, which would mask the true effect of

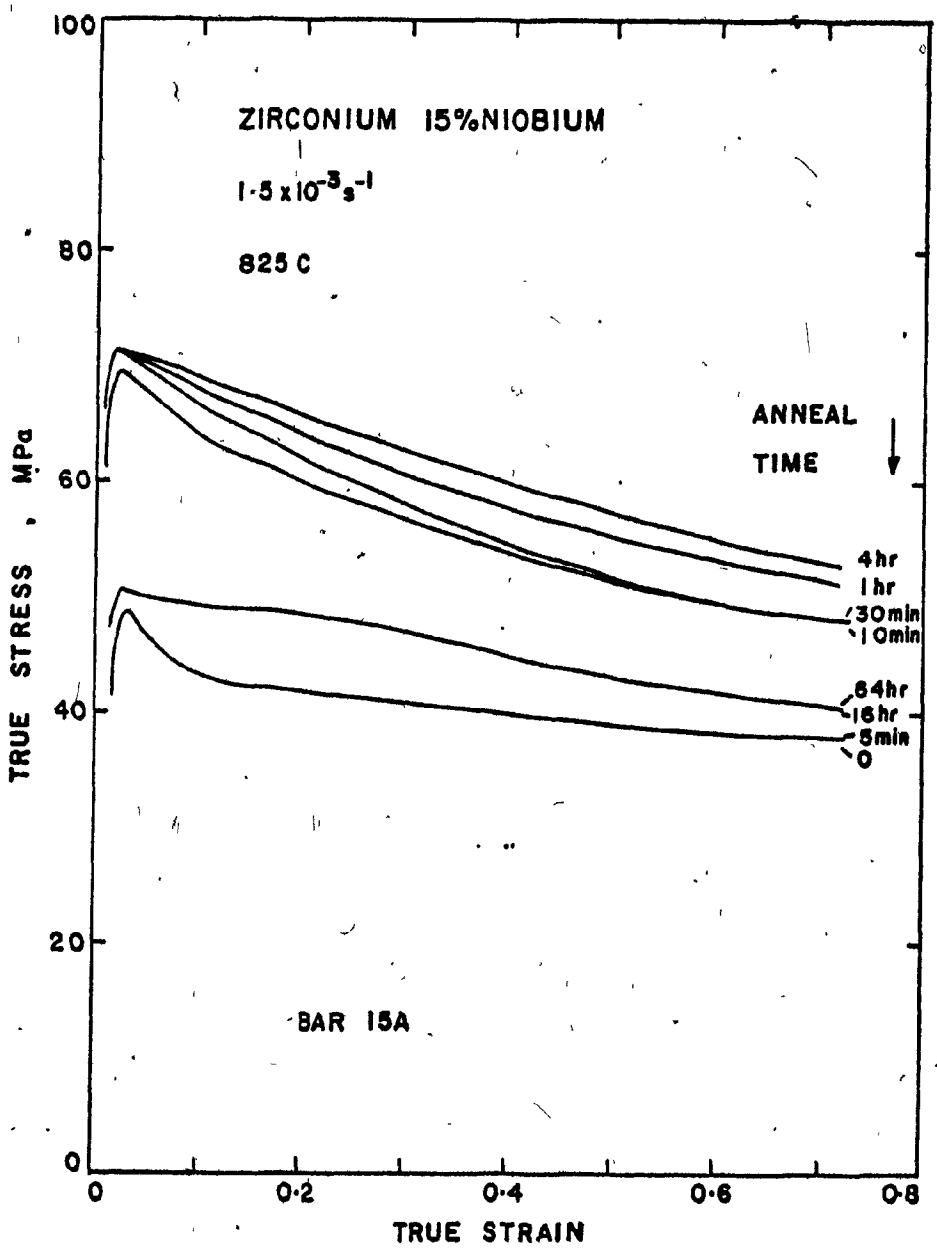

FIGURE 5.35 Effect of annealing time at 1000°C on the flow curves of Zr-15% Nb (bar 15A) tested at 825°C and at $1.5 \times 10^{-3} s^{-1}$.

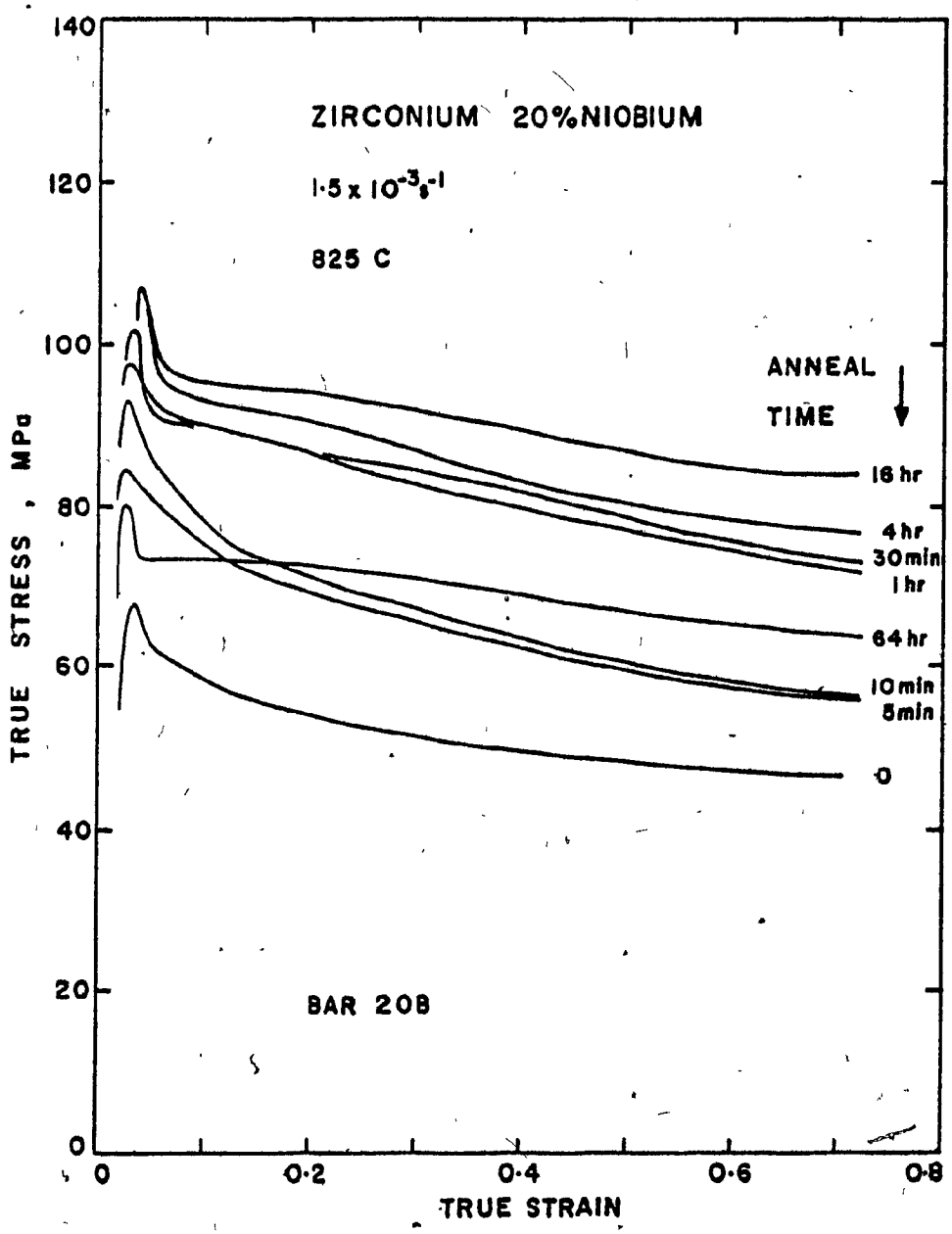

FIGURE 5.36 Effect of annealing time at 1000°C on the flow curves of Zr-20% Nb (bar 20A) tested at at 825°C and at $1.5 \times 10^{-3} s^{-1}$.

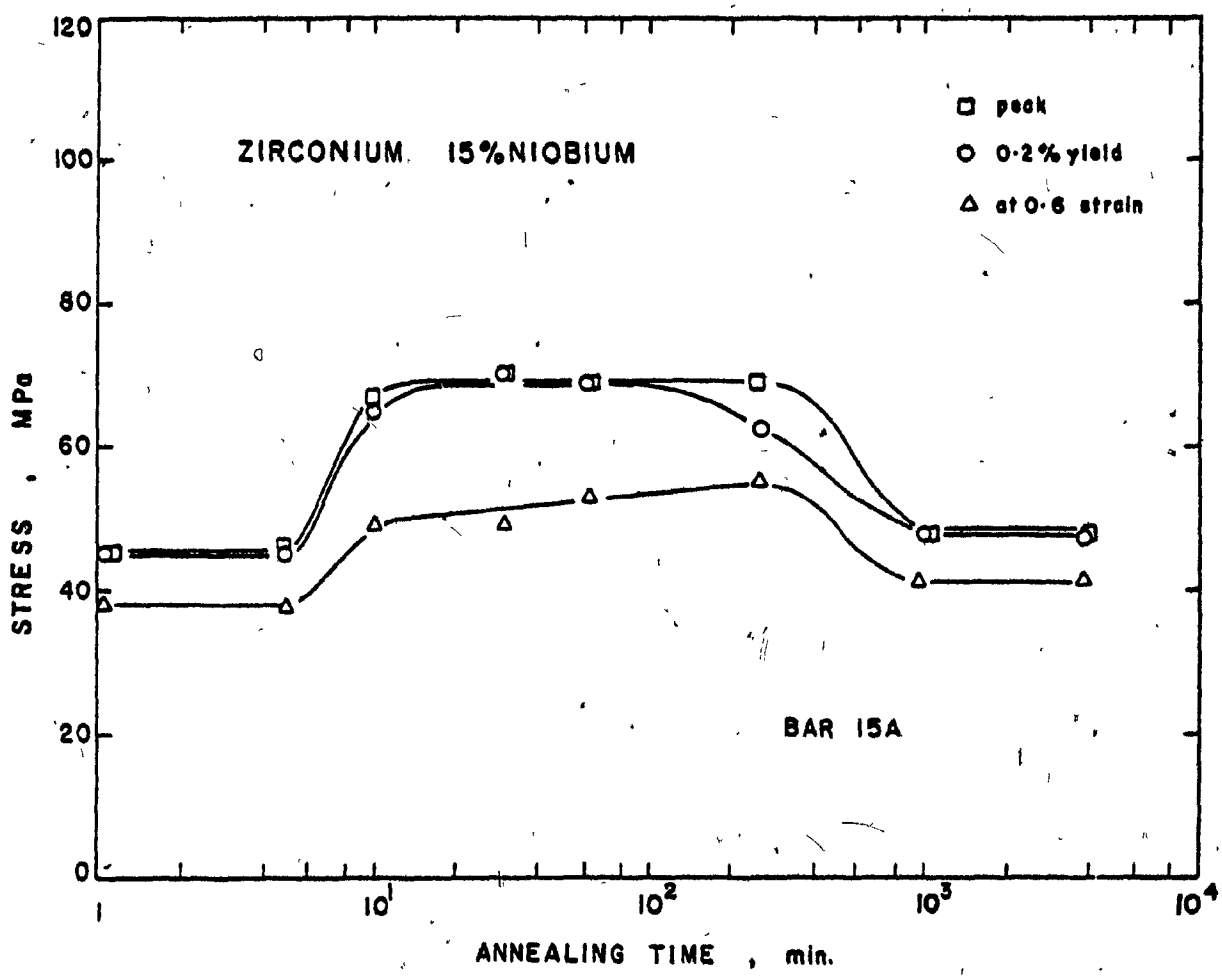

FIGURE 5.37 Yield and steady state stresses of the flow curves of Figure 5.35, plotted versus the logarithm of the anneal time at 1000°C.

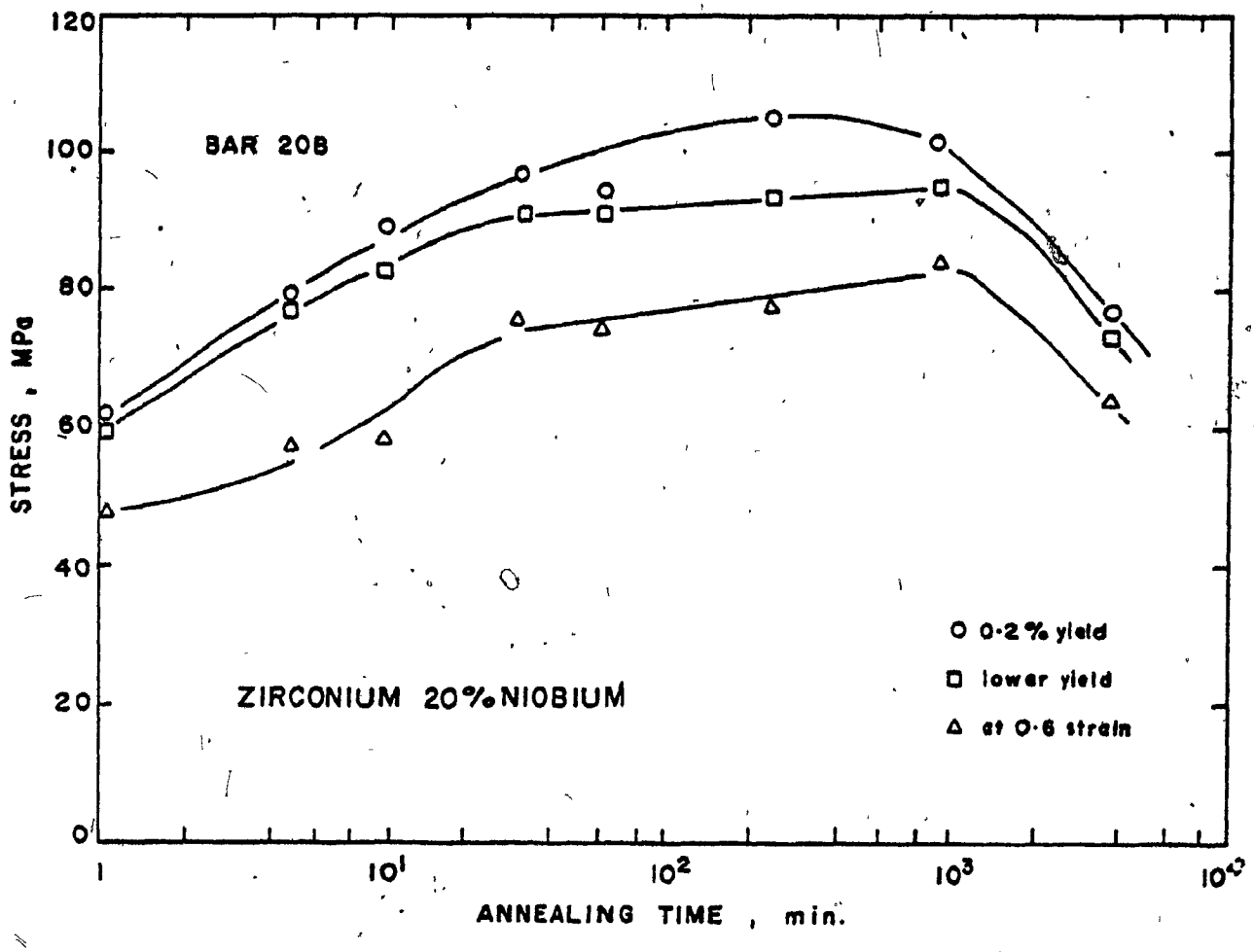

FIGURE 5.38 Yield and steady state stresses of the flow curves of Figure 5.35, plotted versus the logarithm of the anneal time at 1000°C.

annealing. The possibility of oxygen pick-up during annealing of bar D was checked by carrying out room temperature microhardness tests on a pure zirconium sample which was used as a control and annealed for four hours. The DPH values reported in Table 5.8 represent an average of 10 measurements. There is no marked difference between these values. Since hardness is very sensitive to oxygen content, these results indicate that no significant contamination took place during the anneal. In the case of bar 15A, samples which had been annealed for 4 and 64 hours as well as samples of as-received material were analyzed for oxygen concentration using a Leco oxygen analyzer. In order to avoid undesirable interference from the possible oxygen concentration gradient from the surface to the center of the specimens, thin disks of similar thicknesses were cut off on a lathe, and used for oxygen analysis. The oxygen concentrations obtained are given in Table 5.9. The values are reasonably close and indicate that the oxygen pick-up does not exceed 50 ppm even after the longest anneal. This was considered satisfactory since a 50 ppm oxygen increase would not be expected to induce a marked change in the mechanical properties.

The increase in strength of the alloys brought about by annealing was very large. In view of this it was decided to investigate the variation of the strength differential between as-received and 4 hour anneal samples of bar D with temperature. Figure 5.39 shows the stress-strain curves for bar D tested at 925 and 1025°C, in the as-received and 4 hour anneal conditions. At 925° and 1025°C the deformation of the as-received structure leads to marked softening. The flow stresses at 925 and 1025°C are lower than those obtained at 825°C. However, the difference in flow stress between the as-received and the 4 hour anneal condition is less

TABLE 5.8

Hardness Measurements Across a Section of a Zirconium Sample Annealed 64 Hours at 1000°C, Indicating the Absence of Oxygen Pick-Up During Annealing

Surface	Section	
	0.1 mm from surface	center
	(VICKERS HARDNESS)	
243	255	243
229	243	233
239		

TABLE 5.9

Oxygen Analysis of Zr-15% Nb Alloy (Bar 15A) after 0, 4 and 64 Hours of Annealing at 1000°C, Indicating the Absence of Significant Oxygen Pick-Up During Annealing

As-Received	Annealed 4 Hours at 1000°C	Annealed 64 Hours at 1000°C
in ppm weight		
1330 1350	1320 1345 1340 1360	1405 1360
Average : 1340 Standard Deviation: 24	1337 12	1382 32

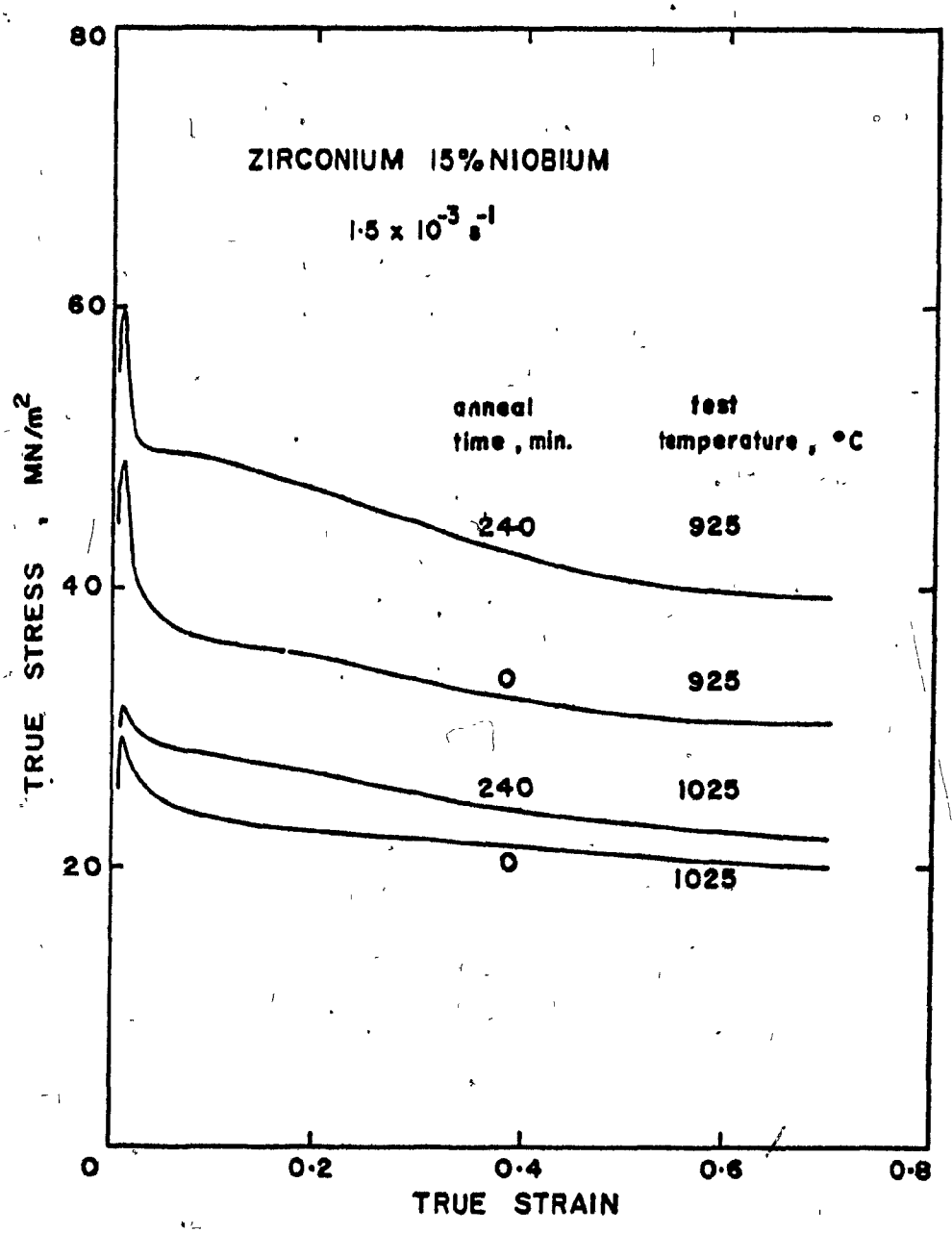

FIGURE 5.39 Effect of annealing time at 1000°C on the flow curves of Zr-15% Nb (bar D) tested at different temperatures.

than 15 MPa at 925°C and 5 MPa at 1025°C, compared to the 60 MPa resulting at 825°C. At 1025°C, the effect of hold time on the stress level appears quite small, and also the rate of softening at strains greater than 0.08 is almost independent of the annealing treatment.

5.3.5 Optical Microscopy

Metallographic examination was carried out in order to follow the microstructural changes that take place on annealing and straining. Two etchants were used, the choice of which depended upon the type of structure to be examined. The first one consisted of 45 parts H_2O, 45 parts HNO_3 and 5-10 parts HF. When samples were etched with this solution, the β grains appeared to contain a Widmanstatten-like structure, but the use of both X-ray and microprobe analysis (Sections 5.3.6 and 5.3.7) failed to indicate the presence of a second phase. These structures are similar to those found in Zr-Mo alloys and were not felt to have much influence on the mechanical properties, as they appear to be an etching artifact (207,208). The other etching solution consisted of 45 parts lactic acid, 45 parts HNO_3 and 5-10 parts HF. With this solution, the needle-like features never appeared. With both solutions, the grain boundaries were in general difficult to reveal. In some cases, they could not be clearly etched at all. Another point of interest is that there were marked differences in etch quality for samples differing only in heat treatment.

The examination of the alloys heated for 15 minutes at 925°C or 1025°C and quenched revealed the presence of β-grains only, which become elongated after deformation. The observations made on the Zr-15% Nb samples annealed for various lengths of time at 1000°C and air-cooled

showed that the β-phase was not entirely retained during cooling, but that some decomposition occurred. This suggests that the TTT diagrams determined by Hehemann for various low oxygen Zr-Nb alloys are not in fact applicable. The air-cooled structures of samples which underwent anneals of 5 minutes, 4 hours and 64 hours are shown in Figures 5.40, 5.41 and 5.42. These three conditions were chosen as typical of the treatments leading to the most marked flow stress variation, both on yielding as well as during flow, and shown before in Figure 5.37.

After 5 minutes of annealing at 1000°C, the structure remains fine-grained and the α-particles appear as small round globules. Longitudinal streaks of α parallel to the sample axis can be observed faintly. The 4 hour anneal permits a coarser grain size to be developed. The grain boundaries appear to have a continuous network of α-phase. The α-phase particles are no longer spherical but now appear as plates and rods, suggesting a low interface energy somewhat analogous to the Widmanstatten structure. The streaks observed previously appear now as lines about 10 μm wide, along which continuous α precipitation occurred. The precipitation along grain boundaries also appears more massive. Following the 64 hour anneal, the grains have not appreciably grown further. The α-precipitates now appear still more massive and less plate-like. Heavy precipitation has occurred along the grain boundary, leaving near it a precipitate-free zone. The narrow streaks have evolved into bands about 40 μm wide which have a larger precipitate density. The variation of the α-morphology with annealing time at 1000°C cannot be completely rationalized in a simple way. Although the β-grain size increase with annealing time may be expected to affect the nucleation of α upon cooling, the variation of the α-morphology with time once the grain size does not grow appreciably any more remains

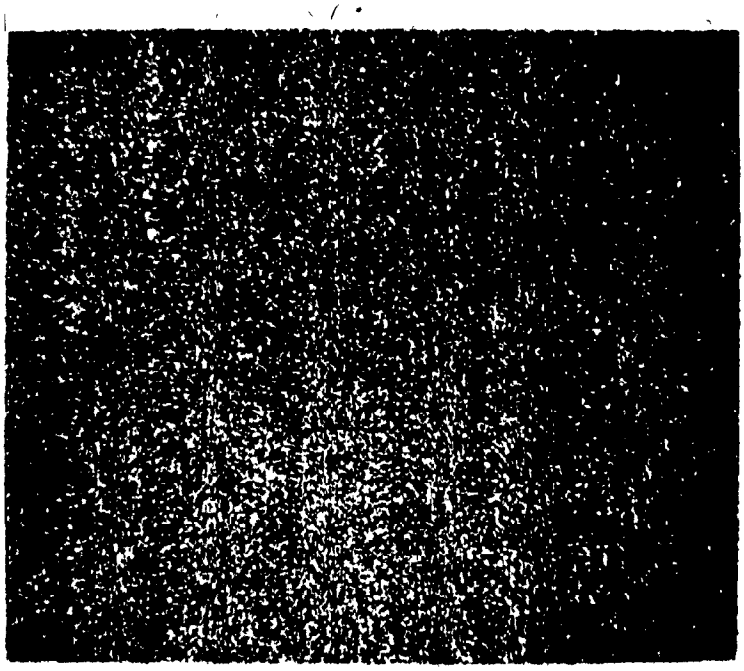

x115

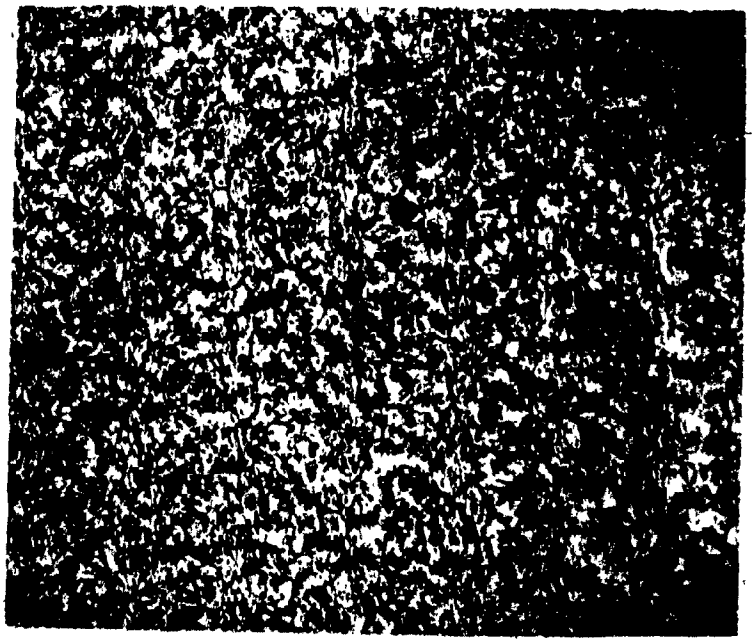

x565

FIGURE 5.40 Microstructure of Zr-15% Nb (bar 15A), annealed for 5 minutes at 1000°C and air cooled.

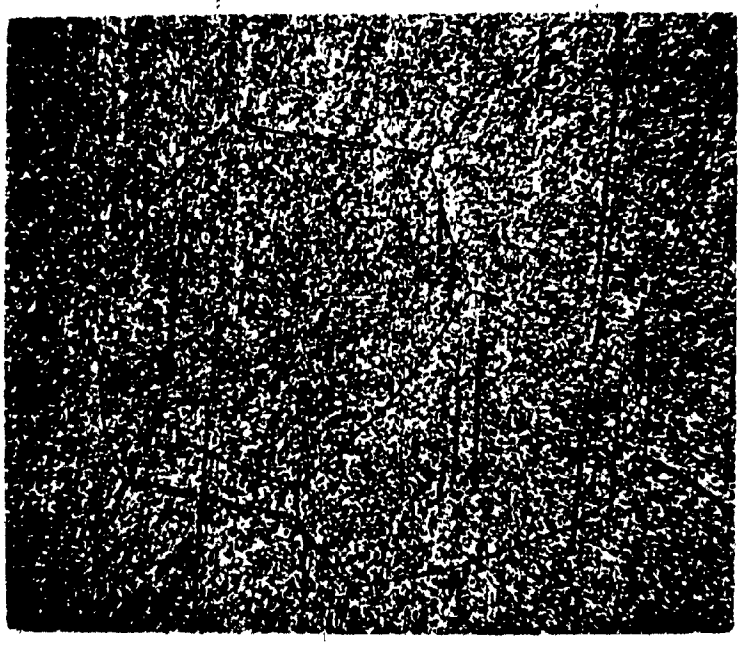

x 115

x 565

FIGURE 5.41 Microstructure of Zr-15% Nb (bar 15A), annealed for 4 hours at 1000°C and air cooled.

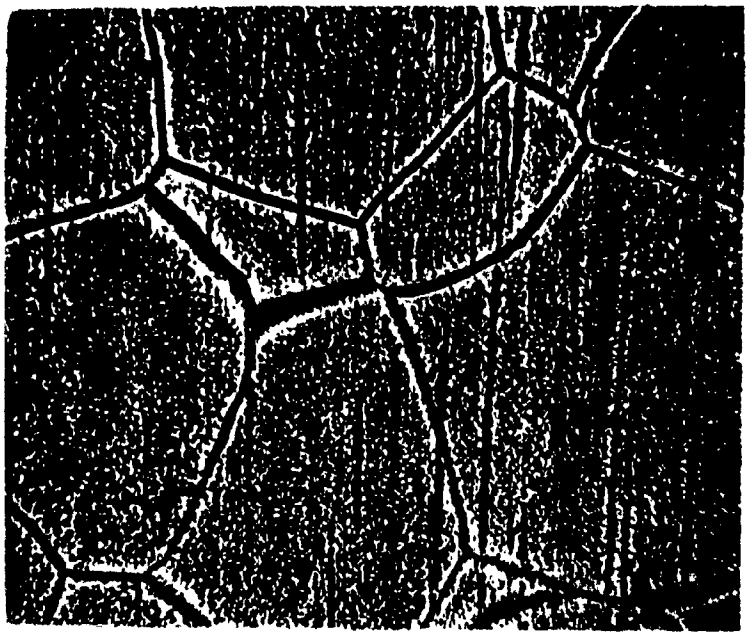

x115

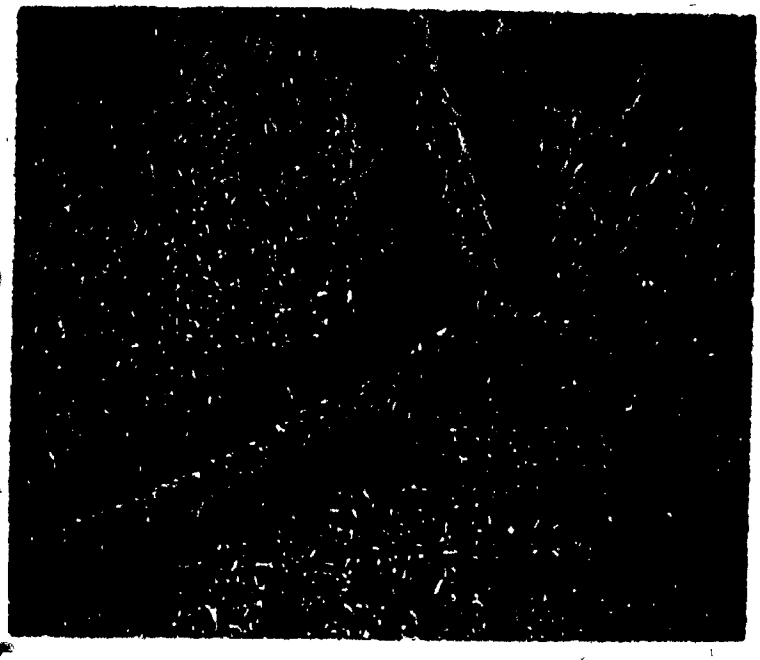

x565

FIGURE 5.42 Microstructure of Zr-15% Nb (bar 15A), annealed for 64 hours at 1000°C and air cooled.

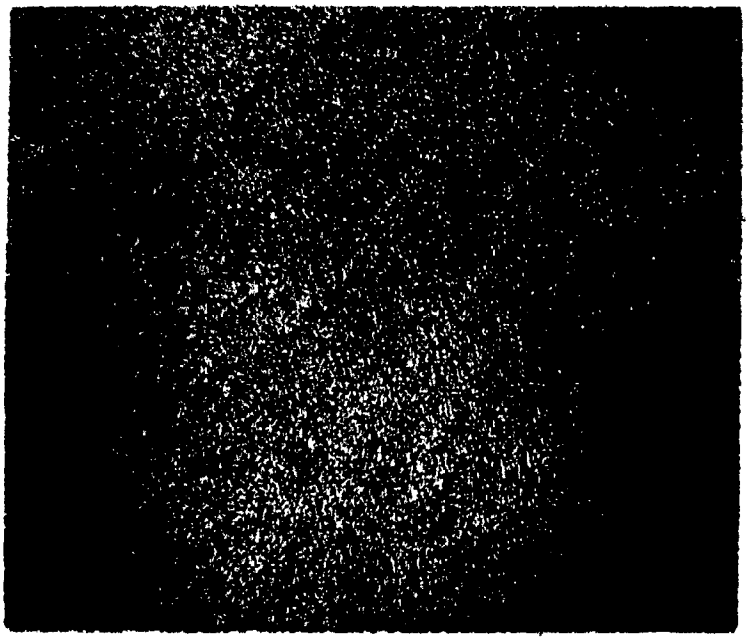

x 115

x 565

FIGURE 5.43 Microstructure of Zr-15% Nb alloy, annealed for 5 minutes at 1000°C, deformed at 825°C to 0.6 strain at a strain rate of $1.5 \times 10^{-3} s^{-1}$ and water quenched.

x115

x565

FIGURE 5.44 Microstructure of Zr-15% Nb alloy, annealed for 4 hours at 1000°C, deformed at 825°C to 0.6 strain at a strain rate of $1.5 \times 10^{-3} s^{-1}$ and water quenched.

x115

x565

FIGURE 5.45 Microstructure of Zr-15% Nb alloy, annealed for 64 hours at 1000°C, deformed at 825°C to 0.6 strain at a strain rate of $1.5 \times 10^{-3} s^{-1}$ and water quenched.

obscure. The presence of the streaks parallel to the bar axis suggests the existence of marked segregation in the as-received material.

Prior to testing at 825°C, the annealed and air-cooled samples were held for 15 minutes at the testing temperature. The metallographic examination of the alloy prior to testing showed that the α-phase had disappeared completely, except for a few α-globules (as detected by X-rays) which would not dissolve even after longer hold times. After deformation at 825°C, these particles can still be observed (Figures 5.43, 5.44 and 5.45), suggesting that they are stable at this temperature. The lack of variation in their morphology or distribution with deformation indicates that they are unlikely to be associated with the softening behaviour observed. The grains after deformation are elongated and the grain boundaries appear not to be too irregular. Finally, there is some evidence on the micrographs of Figures 5.43 to 5.45 that the features giving rise to the streaks are still present but are now distorted along the flow lines.

From the metallographic observations, it thus appears that, in the zirconium-niobium alloys:

i. no second phases are present above 825°C;

ii. some α-phase seems to be stable at 825°C in the 15% Nb alloy;

iii. there appears to have been some segregation, produced during solidification, which persists through hot working, as well as sample preparation and annealing; and

iv. there is some evidence of solute activity, i.e. diffusion, during annealing, perhaps as a result of the segregation, leading to microstructural variations.

5.3.6 X-Ray Investigations

The results reported so far indicate the need for an X-ray diffraction study of the Zr-Nb alloys. For example, the flow softening observed could have been caused by the coarsening of a suitable precipitate. Although the micrographs described above may indicate that, at least on an optical scale, there are no apparent differences in the structure of 15% Nb samples held at 1000°C for various times, X-ray analysis could provide a valuable cross-check of this hypothesis. Alternatively, the analysis could lead to the detection of sub-microscopic particles, if these are present in large enough quantities. An investigation of the nature of the precipitates formed during air cooling from the β-phase was also felt to be necessary, as was the stability of these precipitates at 825°C and at higher temperatures. Finally, more information was sought regarding the Widmanstatten-like features, which have been found by others (207-208) in Zr-Nb alloys and in Zr-Mo (Section 5.1). It was thus an objective of the X-ray investigation to verify the properties of the material, in view of the unusual behaviour of the present alloys.

The X-ray diffraction experiments were carried out on the 15% Nb alloy, which was selected as being representative of the high niobium alloy behaviour. The samples were polished and etched before being mounted in the sample holder. This method was preferred to the powder method, because it gave sharper and better defined peaks than the analogous patterns obtained from powder. The conditions used, as well as the diffraction peak angles and intensities for the samples analyzed are given in Appendix 4.

The as-received material exhibited diffraction peaks of α_{Zr} and β_{Zr}, only. No β_{Nb} or other phase was detected. From the intensities of the α-phase peaks, it appeared that the amount of α is substantial, probably

close to that pertaining to the eutectoid temperature. After a 64 hour anneal at 1000°C followed by air cooling, the treatment described earlier, the structure again appears to consist of α and β only, without the appearance of any β_{Nb} or other phase.

When these two-phase alloys are heated for 15 minutes at 825°C and subsequently quenched, most of the α is absorbed by the β, as indicated by the disappearance of all the α-phase peaks except for a very weak reflection from the $(0002)_\alpha$ plane. This peak does not disappear even when the hold time at 825°C is increased up to 3 hours. This result indicates firstly that equilibrium conditions are nearly attained after 15 minutes at 825°C, and secondly that at this temperature there is still some α present.

If now the as-received material is heated up to 925°C or 1025°C for 15 minutes and quenched, no α-phase peaks are found any more. There is no evidence either for any other high temperature phase, supporting the contention that the alloy is entirely β at this temperature.

The presence of α as a stable phase at 825°C, as described above, is in conflict with the Zr-Nb binary phase diagram of Lundin and Cox (213). However, their diagram was established for very low oxygen concentrations. For higher oxygen concentrations, Richter et al (214) have determined the Zr-Nb binary diagram by metallographic means. They concluded that oxygen concentrations as low as 200 ppm wt are sufficient to give the alloy a distinct ternary character and raise the $\alpha + \beta \rightleftharpoons \beta$ transition temperature in a marked fashion. Their phase diagram for Zr-Nb-200 ppm wt 0 is shown in Figure 5.46a. It can be seen that the $\alpha + \beta$ field is expanded by the additions of oxygen, and that an $\alpha + \beta + \beta_{Nb}$ field is created above the eutectoid temperature, and at low 0 concentrations. From the diagram it is possible to estimate the transition temperatures applicable to the

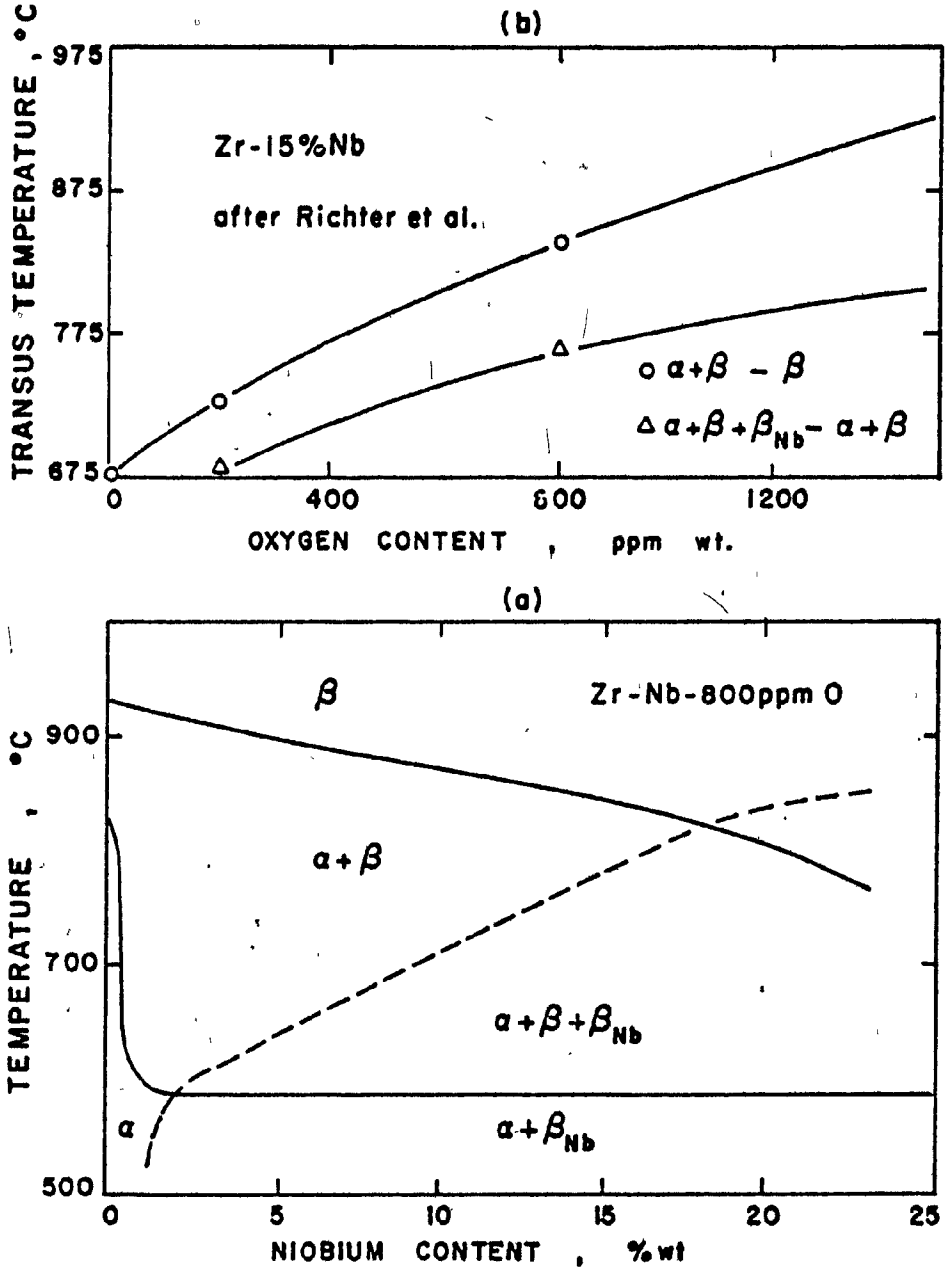

FIGURE 5.46 Effect of oxygen on the Zr-Nb phase diagram
a. pseudo binary phase diagram of Zr-Nb containing 800 ppm oxygen, redrawn from the work of Richter et al (214).
b. variation of the α β β transition temperature with oxygen concentration for the Zr-15% Nb alloy.

present 15% Nb alloy, which contains about 1500 ppm wt oxygen. This is done in Figure 5.46b by extrapolating the curve giving the variation in transition temperature with oxygen concentration obtained from Richter's data to the present oxygen level. We find that the $\alpha + \beta \rightleftharpoons \beta$ transition can be expected to occur at about 925°C whereas the $\alpha + \beta + \beta_{Nb} \rightleftharpoons \alpha + \beta$ transition may be expected around 800°C. These predictions agree with the present experimental observation, i.e. that α is present at 825°C and absent at 925 and 1025°C. It remains to be explained why no β_{Nb} is observed in the as-received material and for the annealed and air-cooled conditions. The answer to this question may lie firstly in that X-ray diffraction is incapable of detecting less than a 2% volume fraction of a second phase, and secondly in that the formation of β_{Nb} may take excessively long times, as extensive Nb diffusion is required at relatively low temperatures and at low degrees of supersaturation.

The X-ray diffraction pattern for the 15% Nb alloy annealed for 64 hours at 1000°C, air-cooled and reheated 15 minutes at 825°C did not show any phases other than β_{Zr} and some α, although under this condition, any precipitate that may have been present would have been overaged. In order to rule out, unambiguously, precipitate coarsening as the cause of softening, diffraction was carried out on this sample in the deformed condition as well. No change in pattern was detected, indicating again that the α was stable, and that neither precipitation nor precipitate coarsening occurred. Furthermore, the analysis of a 15% Nb alloy held 15 minutes at 1000°C deformed at 1000°C, and subsequently quenched, revealed the presence of β only. Since extreme overaging and deformation failed to produce a second phase (other than α) that could be detected by X-rays or optical microscopy, it was concluded from this phase of the

investigation that a precipitation and ageing mechanism cannot be invoked to explain the observed flow softening. It should be added that the occurrence of flow softening at 1000°C as well indicates that some unknown phenomenon associated with the α-phase is unlikely to be the cause of the flow stress decrease with strain. Furthermore, the plate-like features observed after attack with the water-based etchant do not appear as a distinct phase, in agreement with the results of previous investigators (207,208).

5.3.7 Microprobe Examination

The X-ray diffraction studies confirmed the metallographic observations concerning the presence of the α-phase at 825°C and the absence of any phase other than β at the higher temperatures. However, the changes in structure of the Zr-15% Nb alloys after various hold times at 1000°C and followed by slow cooling from the β-phase could not be explained by cooling rate variations. The presence of grain boundary precipitates and precipitate-free zones after long anneal times, together with the presence of longitudinal bands of precipitates somewhat similar to banding in the Mn-bearing steels (215) suggested that segregation was involved. A microprobe study was therefore undertaken to find out whether significant segregation had occurred.

Three samples were chosen for this analysis, representing the extreme conditions obtained: those having received 5 minutes (#1), 4 hours (#2) and 64 hours (#3) of annealing at 1000°C, followed by air-cooling. In order to re-dissolve the α-phase, they were heated back to 1000°C, maintained 1 hour at that temperature, then quenched. The electron beam was adjusted to be about 3 μm in diameter and the counters were set to

pick up the X-rays emitted from the main elements of the alloy, i.e. Zr and Nb. At each point, the counts were integrated over a 10-second period, then repeated at least five times. The average intensities $\overline{X}$ with their associated standard deviations are presented in Appendix 5 for each sample and area. The niobium concentrations were calculated from the intensities by means of the relation:

$$\%Nb_{(atomic)} = \frac{\overline{X}_s - \overline{X}_{Zr}}{\overline{X}_{Nb} - \overline{X}_{Zr}} \times 100 \qquad (5.4)$$

where $\overline{X}_s$ is the count average for the sample, $\overline{X}_{Zr}$ that for pure zirconium and $\overline{X}_{Nb}$ that for pure niobium. Normally a correction for differences in atomic absorption should be used in the relation above. It was omitted because, on the one hand, the correction is small, Zr and Nb being neighbouring elements in the periodic table; and, on the other, because the variations in concentration are of greater interest than the absolute value, the average value of which is known in any event from chemical analysis.

This raises the question of the accuracy of the determination of the Nb concentration. As the denominator of the above relation is constant and $\overline{X}_{Zr}$ is very small, the relative error in niobium concentration will simply arise from the error in $\overline{X}_s$ *. On the assumption that the real average is μ and that the values follow a normal distribution, the 90% confidence interval CI in μ is:

---

* This is to say that the error in niobium concentration is systematic and does not hinder the comparison of different regions.

$$CI = \overline{X}_s \pm t_{\alpha/2\ n-1} \frac{s}{\sqrt{n}}$$

Taking typical values of $\overline{X}_s = 5000$, $n = 5$, and $s = 150$

$$CI = 5000 \pm 2.132 \times \frac{150}{5}$$

$$CI = 5000 \pm 143$$

Thus, the confidence interval leads to a niobium concentration error of

$$\Delta\%Nb = \pm \frac{143}{5000} \times 0.15 \pm 0.0005$$

i.e. it will not exceed 0.5%.

It is now possible to interpret the data obtained. On the sample #3, annealed for 64 hours at 1000°C the variations in niobium concentration barely exceed the error bar, but nevertheless indicate a slight trend for low niobium contents at the grain boundaries. In sample #1, annealed for 5 minutes at 1000°C, it appears that the β" needles have a niobium content similar to that of the matrix, in agreement with the X-ray results. It seems again that the grain boundaries are somewhat poorer in niobium than the interior of the grains. In sample #2, however, the limited information available does not permit any conclusions to be drawn.

The niobium concentration seems to vary only slightly across the streaks in sample #1. This sample was chosen because the width of the streaks was the narrowest, thus leading to large possible Nb variations.

In summary, microprobe examination failed to detect massive grain boundary segregation or solute banding. The reservation must, nevertheless, be made that if the segregated zone width is below 1 μm, the microprobe beam will integrate the intensities of the segregated area and that of the grain, thus largely masking the trend.

5.3.8 Grain Size Measurements

During annealing at 1000°C, grain growth occurs, and as a result coarse-grained structures are produced. It is therefore of importance to determine whether the grain size has a marked effect on the mechanical properties. At low testing temperatures, where the Hall-Petch relation holds, the flow stress varies as $d^{-\frac{1}{2}}$, where d is the grain size. As a result, the finer the grain size, the stronger the material. At high temperatures, however, the grain boundaries can introduce a strain component by means of a sliding mechanism. In this case, the smaller the grain size, the greater the grain boundary sliding component of the strain and, therefore, the smaller the induced stress at a given strain rate. When this process is occurring, the grains tend to remain equiaxed, as in Coble creep.

Between these extreme conditions, the grain size will still play a role in two ways. On the one hand, the evolution of grain size during annealing at 1000°C will be reflected on the yield stress of the material tested at 825°C. If the initial grain size is very fine (e.g. about 20 μm), and appreciable grain coarsening occurs during annealing, then a flow stress <u>increase</u> can be expected, the kinetics of which should agree with those of grain coarsening. This would be due to the progressive loss of the grain boundary sliding component of the total strain as annealing

proceeds. Thus a grain size increase during annealing could lead to strengthening. On the other hand, the grain size may vary during straining. If it is unstable at the testing temperature, it will tend to grow during deformation. Furthermore, while the grains are small, a grain boundary sliding mechanism can operate and contribute to the total strain; this process will tend to lose importance as coarsening occurs, leading to an increase in flow stress. In a contrary way, if some grain refinement occurs during straining because of the increasing contribution of grain boundary sliding, flow softening will occur. A modest amount of flow softening can also be expected in the early stages of the straining of fine-grained samples during the period when the grain boundaries are being "smoothed out", and the conditions appropriate to grain boundary sliding are being established.

The measurements of grain size before and after deformation cannot be used directly to indicate the possible importance of grain boundary sliding and of grain growth, as the grains are in general elongated after deformation. A simple method was therefore introduced to overcome this difficulty. In the absence of either grain growth and sliding, the grains undergo on the average the same deformation as the sample itself. In the present investigation, cylindrical specimens were used which enable us to write:

$$\bar{d}_{//} = \bar{d}_o \exp(-\varepsilon_o) \qquad (5.5)$$

$$\bar{d}_{\perp} = \bar{d}_o \exp(\varepsilon_o/2) \qquad (5.6)$$

where $\bar{d}_o$ is the initial grain size, ε_o the true sample strain*, and $\bar{d}_{//}$ and $\bar{d}_{\perp}$ are the mean grain sizes in the directions parallel and perpendicular to the compression axis, respectively.

If grain boundary sliding occurs, then the grains do not deform as much as the sample and in the above equations the true applied strain ε_o should be replaced by some apparent strain ε_1 which is less than ε_o. An equiaxed grain structure would lead after straining to $\varepsilon_1 = 0$. Furthermore, if grain growth occurs concurrently with deformation, the relations are still applicable provided that $\bar{d}_o$ is replaced by the "equivalent grain size" $\bar{d}_1$ greater than $\bar{d}_o$. In the most general case, we can use the following relations:

$$\bar{d}_{//} = \bar{d}_1 \exp(-\varepsilon_1) \tag{5.7}$$

$$\bar{d}_{\perp} = \bar{d}_1 \exp(\varepsilon_1/2) \tag{5.8}$$

From these relations, we can write that:

$$\bar{d}_1 = (\bar{d}^2_{\perp} \times \bar{d}_{//})^{1/3} \tag{5.9}$$

$$\varepsilon_1 = -2/3 \ln(\bar{d}_{//}/\bar{d}_{\perp}) \tag{5.10}$$

The comparison between $\bar{d}_1$ and $\bar{d}_o$, as well as between ε_1 and ε_o can thus provide information on the extent of grain growth and of grain boundary sliding.

---

* In these equations, the convention that compressive strains are positive is followed.

Grain size measurements were carried out for various anneal times at 1000°C. The mean linear intercept grain sizes prior to deformation were measured, as were the values of $\bar{d}_{//}$ and $\bar{d}_{\perp}$ which pertain to the deformed samples. Except as otherwise stated, each grain size given represents an average taken over more than 300 grains. The results are listed in Table 5.10 and a plot of the β-grain size versus anneal time is given in Figure 5.47. The grains begin to grow after 5 minutes at 1000°C, and after 3 hours remain approximately constant in size, with a mean linear intercept value of 0.3 mm.

5.3.8.1 Grain size and yield strength

We can now attempt to relate the anneal strengthening effect to grain size by plotting the logarithm of the flow stress at yield versus that of the grain size as shown in Figure 5.48. The points first indicate some yield stress increase with grain size (with $d \log \sigma / d \log \bar{d} \simeq 0.26$), followed by a reverse effect for grain sizes larger than 0.1 mm. It may be assumed that the softening associated with the large grain sizes (i.e. those obtained after long anneal times) is partly caused by a Hall-Petch effect. The data thus indicate that in the range of small grain sizes, it is likely that a strain contribution from grain boundary sliding is produced. In the fine-grained range, conditions may not be fully developed for superplastic flow, for which a $d \log \sigma / d \log \bar{d}$ would be expected to be around 1.0 to 1.5.

5.3.8.2 Grain boundary sliding during deformation

If, for grain sizes below 100 μm grain boundary sliding is operative, at least to some degree, the computed value of the parameter ϵ_1 should

TABLE 5.10

Grain Size Measurements of Zr-15% Nb (Bar 15A) for Various Annealing Times at 1000°C, Before and After Deformation at 825°C

Prior Heat Treatment	Undeformed (mm)	Deformed at 825°C			Computed	
		ε_o	$d_{//}$(mm)	$d_{\perp}$(mm)	d_1(mm)	ε_1
as-received, 15 minutes at 825°C	0.020*	0.5	0.14*	0.25*	0.02	0.49
annealed 5 minutes at 1000°C, air cooled, reheated 15 minutes at 825°C	0.020*	0.5	0.013*	0.25*	0.02	0.5
annealed 10 minutes at 1000°C, air cooled, reheated 15 minutes at 825°C	0.070*	0.5	0.041	0.096	0.07	0.47
annealed 30 minutes at 1000°C, air cooled, reheated 15 minutes at 825°C	0.096	0.5	0.051	0.097	0.08	0.43
annealed 1 hour at 1000°C, air cooled, reheated 15 minutes at 825°C	0.172	0.5	0.100	0.190	0.15	0.43
annealed 4 hours at 1000°C, air cooled, reheated 15 minutes at 825°C	0.258	0.5	0.144	0.292	0.23	0.47
annealed 64 hours at 1000°C, air cooled, reheated 15 minutes at 825°C	0.300	0.5	0.219	0.452	0.35	0.49

*These values are approximate since the boundaries of many grains do not etch well.

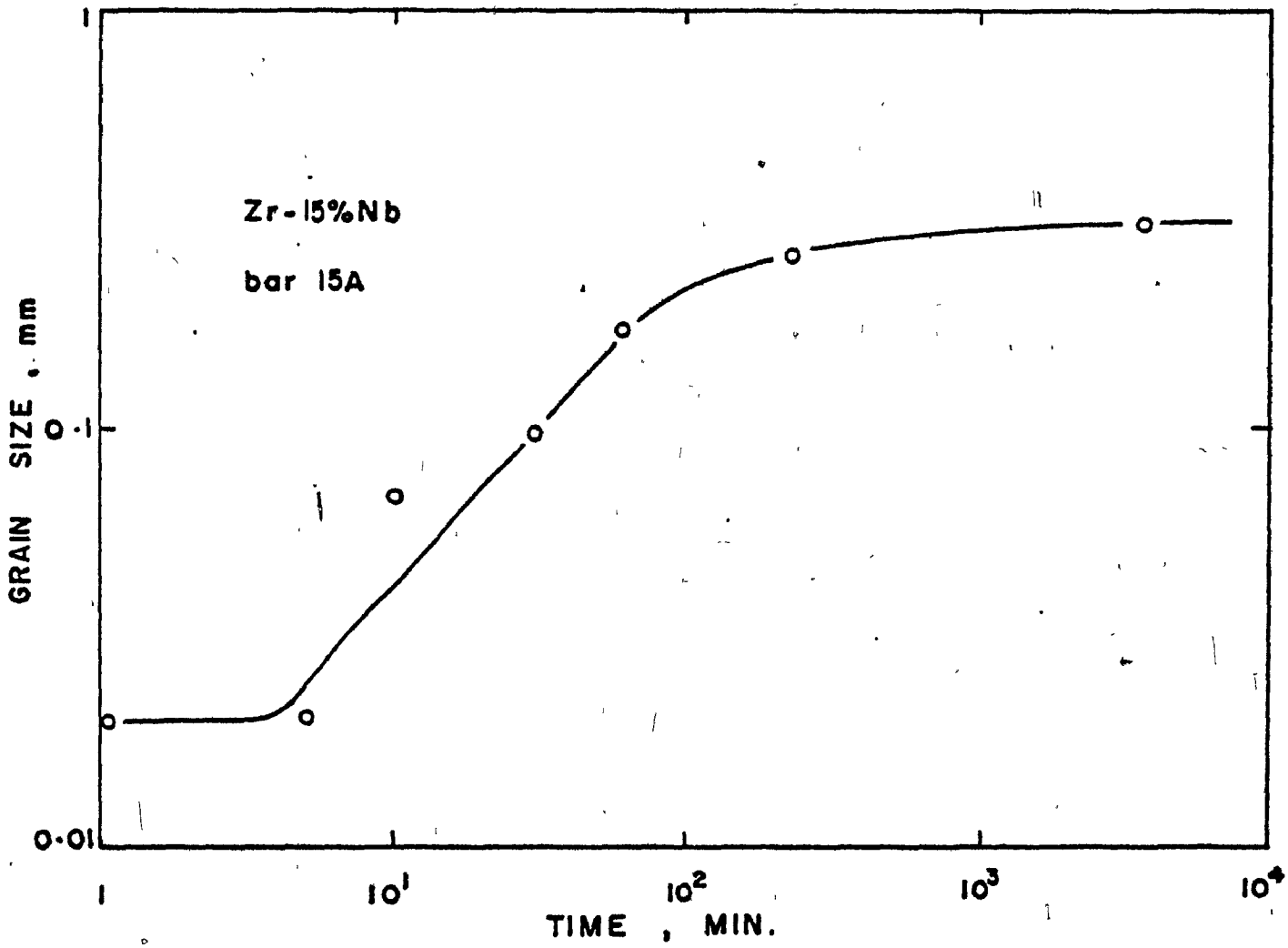

FIGURE 5.47 Plot of the increase in grain size with annealing time at 1000°C for the Zr-15% Nb alloy (bar 15A).

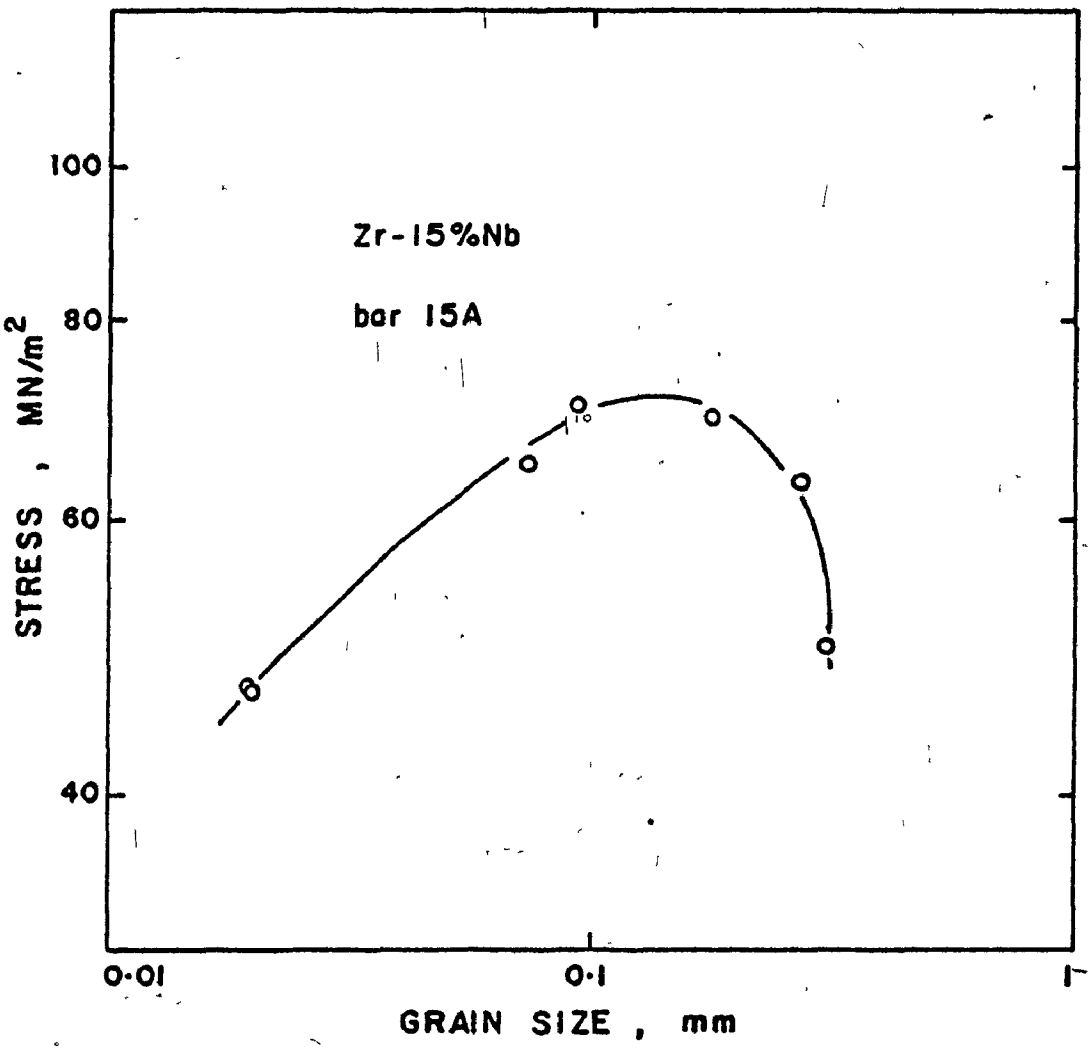

FIGURE 5.48 Plot of the variation of the yield stress versus the simultaneous grain growth, during annealing of the Zr-15% Nb alloy at 1000°C.

be less than ε_o at small grain sizes, and should become progressively closer to ε_o as the grain size increases. The data of Table 5.7 are somewhat scattered, but they are not inconsistent with the hypothesis that $\varepsilon_1/\varepsilon_o$ increases with grain size. It thus appears that grain boundary sliding probably occurs in the finer-grained specimens and that it decreases in importance as the grain size is increased.

5.3.8.3 Grain growth during straining

The grain diameters d_1 calculated from $\overline{d}_{//}$ and $\overline{d}_{\perp}$ are listed in Table 5.10. These values agree quite well with the measured ones of $\overline{d}_o$, indicating no perceptible tendency towards grain growth during deformation. Table 5.11 lists similar data for bar D, of the same Nb composition. The grain sizes obtained after five minutes and after four hours agree reasonably well with those obtained on bar 15A. However, the as-received material appeared to maintain an equiaxed structure during deformation, although its initial grain size was the same as that of bar 15A. These observations indicate that conditions of near superplastic flow, i.e. with strong strain contributions from grain boundary sliding, were attained in this material.

5.3.8.4 Grain size and testing temperature

The effect of testing temperature and annealing treatment on the initial grain size $\overline{d}_o$ and its evolution with deformation is given in Table 5.12. The results indicate that no appreciable grain growth occurs during deformation. The values of ε_1 obtained after deformation at 1000°C are similar to the corresponding values at 825°C. A comparison between the flow stresses obtained at these testing temperatures (Figure 5.38) and the initial grain size $\overline{d}_o$ suggests that the former are markedly increased by grain size increase.

TABLE 5.11

Grain Size Measurements of Zr-15% Nb (Bar D) for Various Annealing Times at 1000°C, Before and After Deformation at 825°C

Prior Heat Treatment	Undeformed (mm)	Deformed at 825°C			Computed	
		ε_o	$d_{//}$ (mm)	$d_{\perp}$ (mm)	d_{1} (mm)	ε_1
as received, 15 minutes at 825°C	0.020*	0.52	-	-	-	-
annealed 5 minutes at 1000°C, air cooled, reheated to 825°C for 15 minutes	0.020*	0.52	-	-	-	-
annealed 90 minutes at 1000°C, air cooled, reheated to 825°C, for 15 minutes	0.215	0.5	0.142	0.268	0.22	0.42
annealed 4 hours at 1000°C, air cooled, reheated to 825°C for 15 minutes	0.298	0.52	0.182	0.394	0.31	0.52

* These values are approximate since the boundaries of many grains do not etch well.

TABLE 5.12

Grain Size Measurements of Zr-15% Nb (Bar D) Before and After Deformation at Various Temperatures

Prior Heat Treatment	Undeformed (mm)	Deformed				Computed	
		ε_0	T, °C	$d_{//}$ (mm)	$d_{\perp}$ (mm)	d_1	ε_1
as-received, 15 minutes at 925°C	0.068	0.52	925	0.04*	0.08*	0.06	0.46
as-received, 15 minutes at 1000°C	0.108	0.52	1000	-	-	-	-
annealed 90 minutes at 1000°C, air cooled, reheated 15 minutes to 925°C	0.215	0.52	1000	0.142	0.268	0.217	0.42
annealed 4 hours at 1000°C, air cooled, reheated 15 minutes at 1000°C	0.298	0.52	925	0.173	0.372	0.29	0.51

* These values are approximate since the boundaries of many grains do not etch well.

CHAPTER 6

DISCUSSION

The results obtained on Zr-Mo alloys, presented in the previous chapter, show that the mechanical properties of these alloys are affected by the composition of the atmosphere during tests, whereas those of crystal bar zirconium and the Zr-2.5% Nb alloys do not exhibit such an effect. In this chapter an attempt is made first to explain the origin of the very high sensitivity to atmosphere purity displayed by the Zr-Mo alloys. A model is presented, which describes in a quantitative manner the observed flow softening. The predictions of the model are discussed in the light of the experimental results. The second part of the present chapter is devoted to the behaviour of the Zr-Nb alloys. The unusual characteristics of the high niobium alloys are discussed, and particular attention is paid to those alloys that behave in a somewhat similar manner. Various interpretations of the observed flow softening in these alloys are examined and criticized.

6.1 ZIRCONIUM MOLYBDENUM ALLOYS

The results of mechanical tests obtained in the Zr-Mo alloys have shown a marked effect of the atmosphere upon the flow properties at high temperatures. The X-ray investigations carried out on the outer layers have made clear that oxygen is the major atmospheric element responsible for this effect. We shall now turn our attention to the oxidation behaviour of Zr-Mo alloys in order to explain how these alloys can be so sensitive to atmosphere purity. In a second section of this discussion an attempt will be made to provide a model for the experimental

observations, and in the third part of the discussion, the possible mechanisms of deformation of Zr-Mo alloys in the β-phase will be considered briefly.

6.1.1 Oxidation Behaviour of Zr-Mo Alloys

It is clear that the oxidation behaviour of the present alloys will depend on the structure and properties of the oxidized layers. The oxidation products in turn can be determined from the Zr-Mo-O phase diagram, if it is known, or at least from a few isothermal sections, if these are known. Although this type of diagram is useful for the calculation of the compositions and quantities of the phases present, it does not yield directly the effect of oxygen partial pressure on the phase equilibria. For this purpose, a log P_{O_2} versus mole fraction of solute content plot is very convenient. Such diagrams have not yet been determined for the Zr-Mo-O alloy system, but can be estimated using a basic knowledge of binary systems provided a few assumptions are made. This task was carried out and is described in the following paragraphs.

6.1.1.1 The Zr-Mo-O phase diagram

Most of the tests carried out on the Zr-Mo alloys were conducted at 1000°C, and for this reason it will be useful to determine the isothermal section at 1000°C. The edges of the ternary diagram are constituted by the isothermal sections of the binary phase diagrams Zr-Mo, Zr-O and Mo-O. The first two are reproduced from the Metals Handbook in Figures 6.1 and 2.6. The phase diagram Mo-O has not been determined, but a few of its elements are known. For the present purpose, it was assumed that ZrO_2, MoO_2 and MoO_3 are stoichiometric and furthermore that the mutual solubility

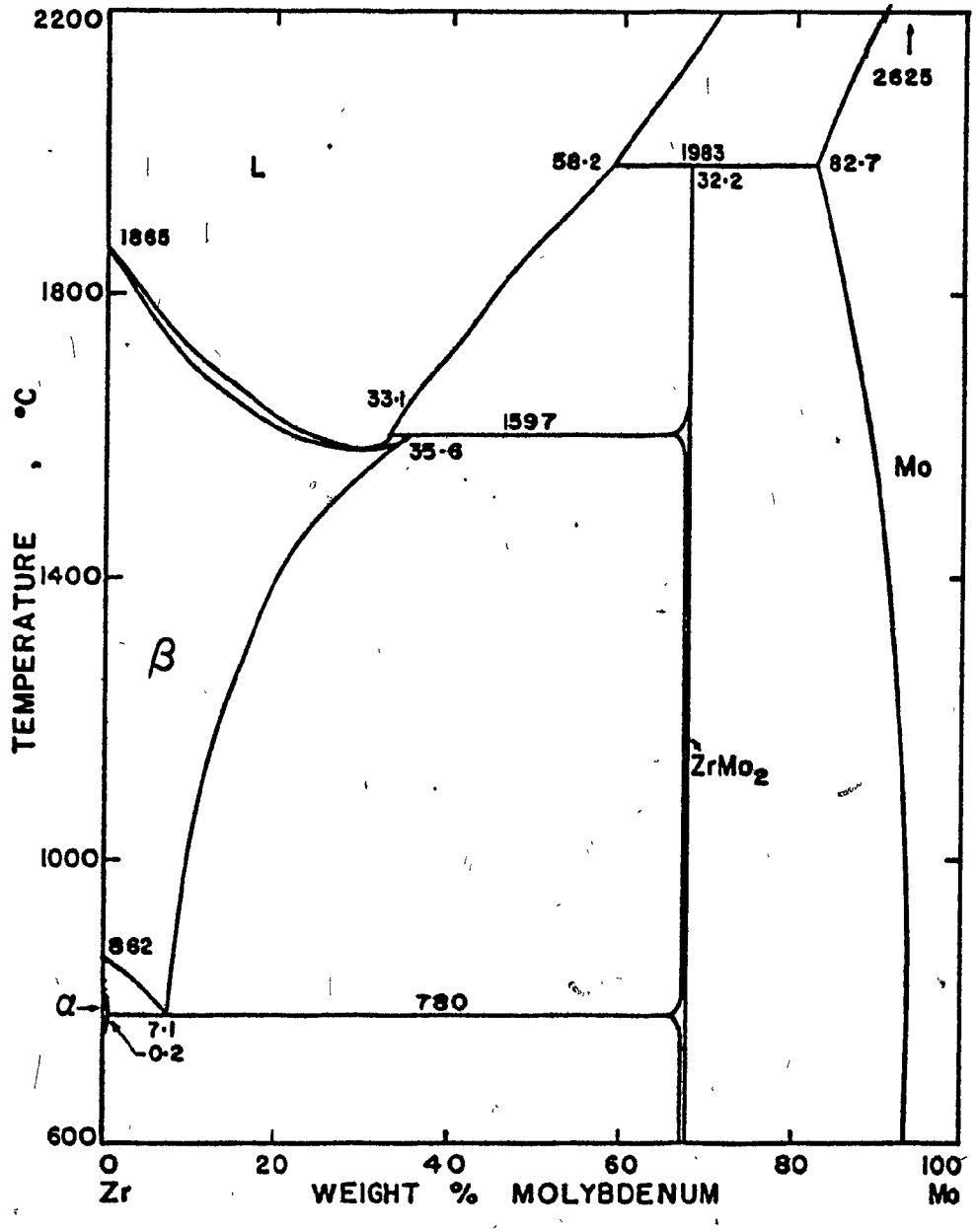

FIGURE 6.1 The zirconium-molybdenum binary phase diagram, redrawn from the Metals Handbook.

between ZrO_2, MoO_2, $ZrMo_2$ and Mo is very small. It should be noted also that MoO_3 and MoO_2 form a eutectic system, the solution being fused at 1000°C. Although the above assumptions are likely to be somewhat inexact, it is felt that since the Zr-O side of the diagram is the one of interest, the errors involved in the Mo corner will not be of serious consequence. The ternary section obtained on this basis is shown in Figure 6.2. The extent of the α, β and liquid phase fields is arbitrary since there is no available information at the present time that could permit a more precise determination. In addition to this diagram, the molybdenum oxides are known to be unstable or subject to drastic phase changes. Molybdenum dioxide sublimes partly above 1000°C without decomposition whereas the bulk disproportionates to MoO_3 and Mo. The molybdenum trioxide sublimes appreciably above 650°C, becomes liquid around 800°C and evaporates without decomposition at around 1100°C (216).

6.1.1.2 Log P_{O_2} versus Mo concentration diagram

The ternary diagram predicts the phase equilibria for an alloy of a given composition under a standard oxygen pressure, but fails to give any information about the effects of the oxygen pressure on the oxidation products of the alloy. The log P_{O_2} versus solute concentration diagrams, used extensively in corrosion studies, are very convenient, and such a diagram was estimated for the present system. The construction of this type of diagram calls for a knowledge of the various equilibria between the phases. The topological features of this diagram follow of course the phase rule. At constant oxygen pressure and temperature, there can be at most three components in equilibrium in which case the molybdenum content of each phase is fixed (horizontal lines). Two-phase

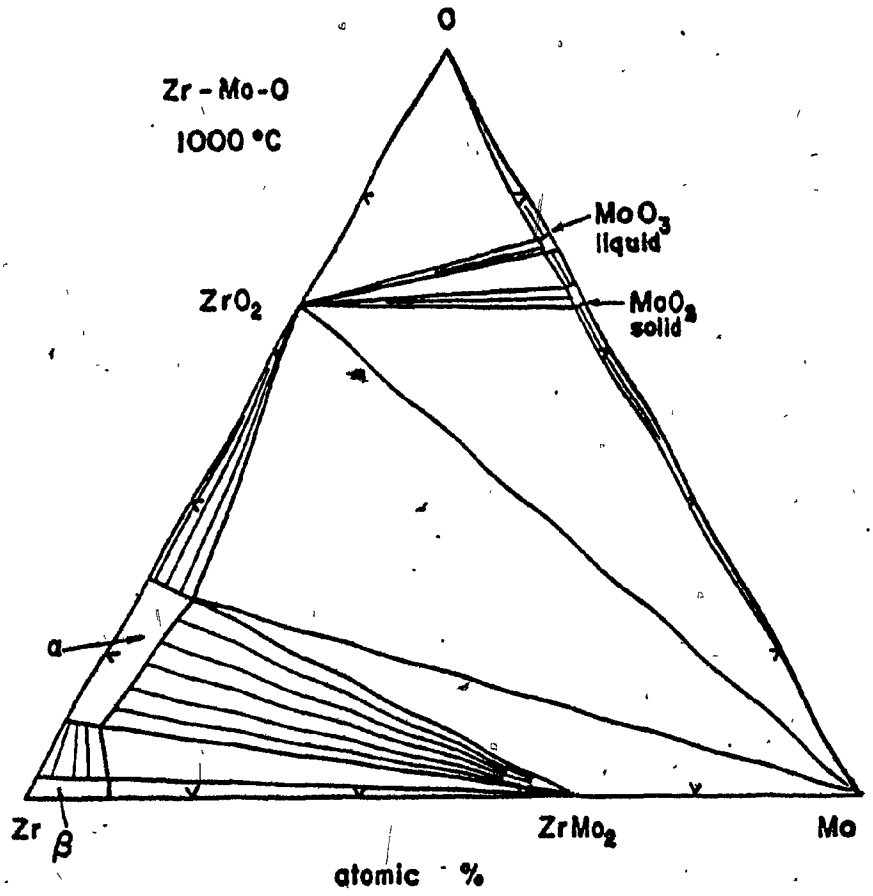

FIGURE 6.2 Estimated type III diagram for the Zr-Mo-O system at 1000°C (isothermal section of the ternary diagram).

equilibria have an extra degree of freedom, which may be either the composition of one phase; the other being thereby determined ("eutectoid"-like features) or, if the phase compositions are known, the oxygen pressure may be varied (two-phase domains). When a single phase is present, then both composition and pressure may be varied independently.

The log P_{O_2} versus %Mo phase diagram is shown in Figure 6.3. Point A was obtained from a consideration of the equilibrium:

$$ZrO_2 \rightleftharpoons Zr_\alpha + O_2 \qquad \Delta G^\circ_{1000^\circ C,\alpha} \tag{6.1}$$

where $\Delta G^\circ_{1000^\circ C,\alpha}$ represents the free energy of formation of oxide from zirconium in the α-phase. It can, in turn, be obtained from

$$\Delta G^\circ_{1000^\circ C,\alpha} = \Delta G^\circ_{1000^\circ C,\beta} + \Delta G^{\beta \rightarrow \alpha}_{1000^\circ C} \tag{6.2}$$

where $\Delta G^\circ_{1000^\circ C,\beta}$ is the standard free energy of formation of oxide, and $\Delta G^{\alpha \rightarrow \beta}_{1000^\circ C}$ the free energy of the allotropic transformation $\alpha \rightarrow \beta$ at 1000°C. Taking -845 and ∿ -5 kJ/mol respectively as the values of these quantities (216), and writing the equilibrium conditions as:

$$\log P_{O_2} = \log K_p = -\frac{\Delta G^\circ_{1000^\circ C,\alpha}}{RT \ln 10} \tag{6.3}$$

we obtain

$$\log P_{O_2} = -34.7 \tag{6.4}$$

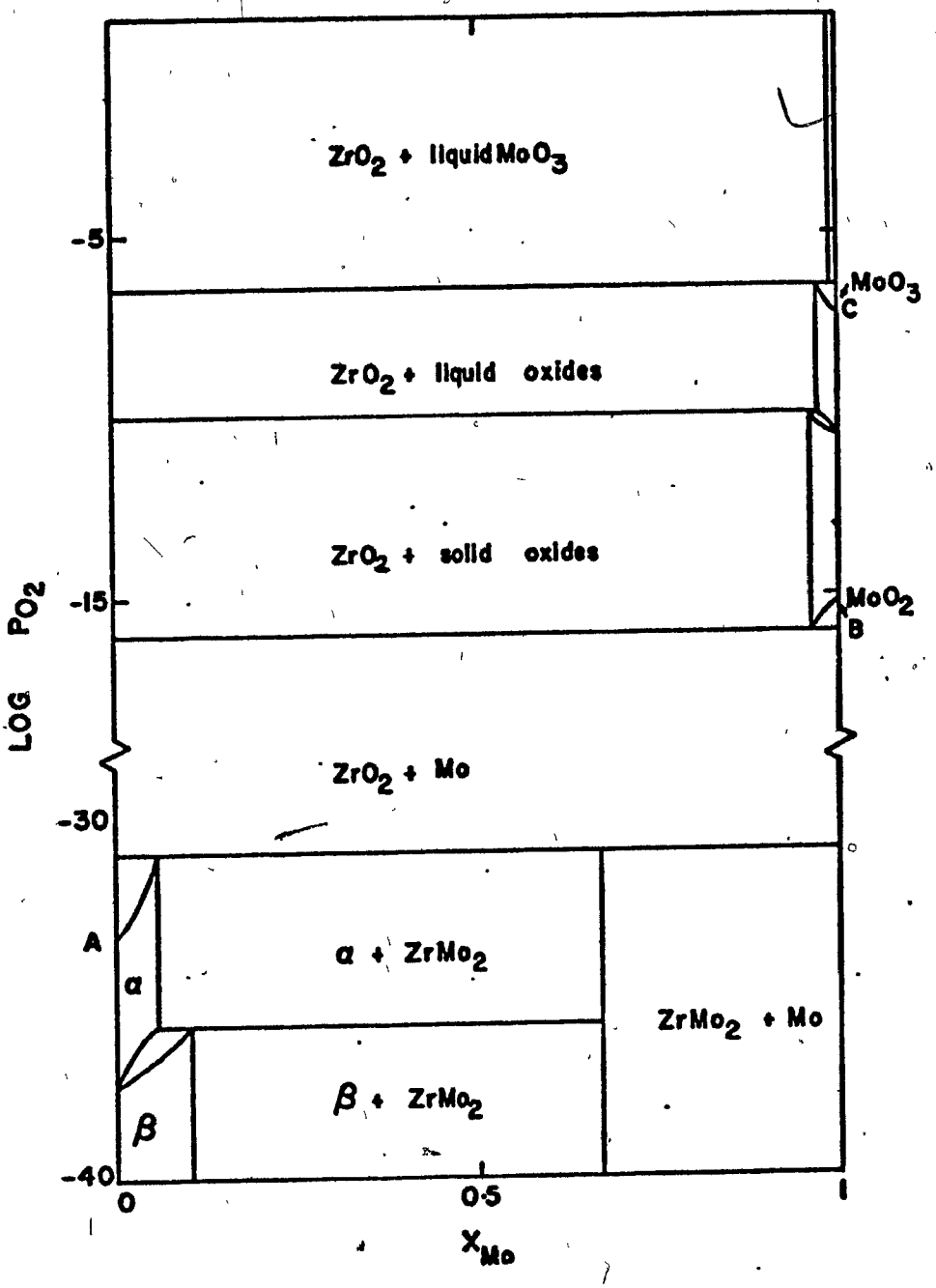

FIGURE 6.3 Estimated type II diagram for the Zr-Mo-O system at 1000°C (log P_{O_2} versus mole fraction of Mo in the binary alloy).

Point B can be calculated in a similar way, from the equilibrium:

$$MoO_2 \rightleftharpoons Mo + O_2 \qquad \Delta G^{1000^oC}_{MoO_2} = -366 \text{ kJ/mol} \qquad (6.5)$$

which yields

$$\log P_{O_2} \approx 15.0 \qquad (6.6)$$

Point C is slightly more difficult to determine since at this point the equilibrium

$$2MoO_3 \rightleftharpoons 2MoO_2 + O_2 \qquad (6.7)$$

is achieved. In a similar way, one finds, since $\Delta G^{1000^oC}_{MoO_3} = -446$ kJ/mol

$$\log P_{O_2} \approx -6.5 \qquad (6.8)$$

The thermodynamic data required to position the other points and lines is lacking, which compelled us to place them somewhat arbitrarily. It may be seen, however, that the oxygen pressure must be lowered to less than 10^{-7} atmospheres to prevent the formation of MoO_3, to less than 10^{-11} atmospheres to avoid any liquid phase, and to less than 10^{-35} atmospheres to prevent oxide formation !

6.1.1.3 Oxidation products in Zr-Mo alloys

The diagram thus indicates clearly that the testing atmosphere was never pure enough to prevent the formation of the oxides, and that the effect of atmosphere purity on the mechanical properties may have had an

effect only through the kinetics of the process.

The graphs of Figures 6.2 and 6.3 predict that as oxidation proceeds, the 6% Mo alloy in the β-phase will develop an outer layer of ZrO_2 and liquid molybdenum oxides, below which there will be another layer of ZrO_2 and a solid solution of molybdenum oxides. The oxidation layers below will be successively ZrO_2 + Mo, α + Mo, α + $ZrMo_2$, α + β before reaching the β matrix. In spite of the errors involved in the construction of the phase diagram, it can be seen that the oxidation behaviour is complex, and leads to the formation of liquid phases. The molybdenum trioxide, moreover, evaporates at a rapid rate at 1000°C, and may thus displace the equilibrium, leading to an outward diffusion of molybdenum and its subsequent evaporation.

The results of the X-ray analysis in Section 5.1 showed α to be the main oxygen stabilized phase and indicated the presence of ZrO_2 and $ZrMo_2$. No molybdenum or molybdenum oxides were detected, however, which may be explained by the small quantities of Mo as well as by the evaporation of the oxide phases. In addition, of course, there is the inaccuracy involved in the determination of the diagrams.

6.1.1.4 Oxidation kinetics of Zr and Zr alloys

The difference in the stress-strain curves obtained from Zr (Figure 5.2) and Zr-2.5% Nb (Figure 5.18) when compared to those obtained in the Zr-Mo alloys (Figures 5.3 to 5.5) have been shown to be dependent upon atmosphere purity.

These results suggest that Zr-Mo alloys oxidize at a considerably faster rate than pure zirconium and zirconium-niobium alloys. If the

structure of the oxide scale on Zr-Mo alloys contains a liquid phase, as predicted by the diagrams of Figures 6.2 and 6.3, oxygen transfer through the oxide will be achieved at a rate orders of magnitude larger than oxygen diffusion through lattice defects in a continuous oxide scale. The structure of the oxide layers on the Zr-Mo alloys will cause what has been called catastrophic oxidation. The deleterious effect of molybdenum on the oxidation resistance of certain alloys has indeed been already observed. In Fe-Mo-Ni and Fe-Mo-Cr alloys rapid oxidation occurs in a certain range of compositions (217). Rathenau and Meijering (218) have studied the catastrophic oxidation of Cu, Cu8Al, Ag, Ag4Al, Ni, Fe-25Cr and 19Cr9Ni steel when heated up in contact with molybdenum trioxide. They found that rapid oxidation started only at a definite temperature, different for each alloy, which was associated with either the appearance of liquid phases (binary or ternary eutectics) or with the liquid phase dissolving the protective oxide.

It is not clear, however, whether the oxygen mass transport through the liquid phase is entirely responsible for accelerated oxidation, and it has been shown that electron transfer in the metal/partly liquid oxides/oxygen all could affect significantly the oxidation rates (219).

The oxidation rates of the zirconium-niobium alloys, by contrast, is comparable to that of pure zirconium (see Section 2.3), being only about five times higher. The oxides that may form, ZrO_2, NbO_2, Nb_2O_5, NbO, or some mixtures of these oxides are all likely to be in the solid state up to above 1000°C and, as the oxidation rates show, offer a relatively good oxygen barrier. Pure zirconium is the least reactive material. The observation of the scales formed after 60,000s interruption on the Zr-Mo alloys indicates that the α-phase is the most important

constituent. The diffusion through the oxide must be much faster than it is for pure zirconium, on the one hand, but must be slow enough to permit the growth of the α-layer. In other words, the oxygen flux arriving at the α-oxide interface must be less or equal to the diffusion flux in the α-layer.

6.1.2 Effect of Interruption Delay in Zr-6% Mo Alloy

The strengthening effect caused by delay during interrupted compression tests increases with time (Figure 5.11). The most appropriate parameter to indicate the extent of the strengthening is $\Delta\sigma$, which is the difference between some appropriate reloading stress and the stress before unloading σ_u. $\Delta\sigma$ has the advantage of eliminating sample-to-sample differences in strength, leading to the environment stress increment alone.

However, several $\Delta\sigma$ parameters can be defined, depending upon which stress on reloading is chosen. The yield stress can be chosen, but is in general close to the peak stress σ_p. Since the latter is easier to measure, a peak stress increment $\Delta\sigma_p = \sigma_p - \sigma_u$ can be defined. The parameter $\Delta\sigma_p$ does not give, however, any information about the stress σ_f near the lower yield point at which the flow becomes smooth. The stress σ_f is defined by extrapolating the smooth curve obtained beyond the peak towards zero strain and taking the point at which it intersects the loading curve. The stress increment $\Delta\sigma_f = \sigma_f - \sigma_u$ obtained in this way is plotted in Figure 6.4 together with $\Delta\sigma_p$. The insert in Figure 6.4 recalls the significance of the stresses used to calculate the $\Delta\sigma$ values.

Another stress increment $\Delta\sigma_s$ of interest has been plotted in Figure 6.4. It is defined as $\Delta\sigma_s = \sigma_i - \sigma_s$ where σ_s is the flow stress

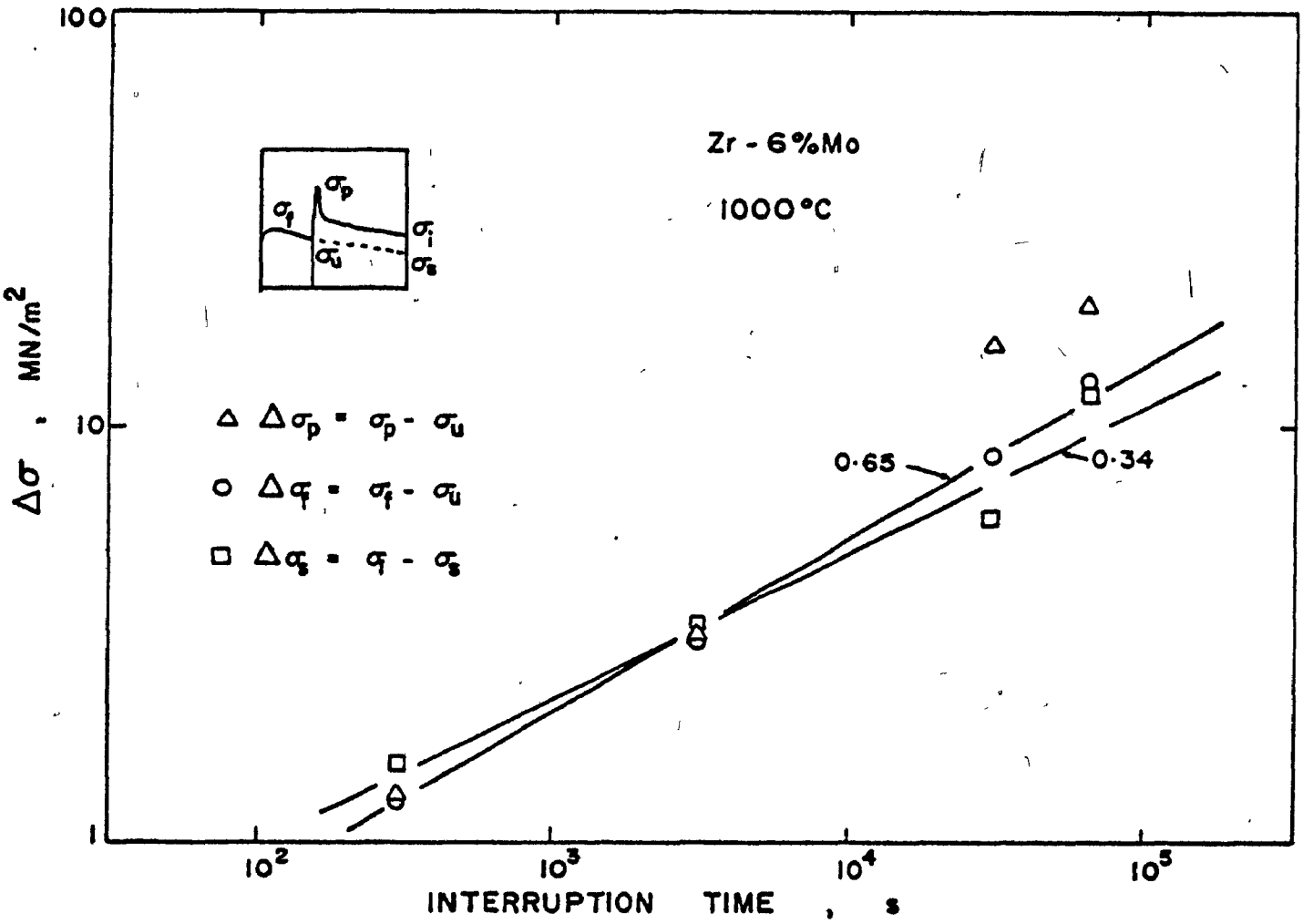

FIGURE 6.4 Variation of the stress increment during interrupted tests as a function of interruption time, from the data of Figure 5.11.

at 0.7 strain in a continuous stress-strain curve, and σ_i the flow stress at a similar strain in the interrupted curve. On Figure 6.4, the values of $\Delta\sigma_p$ appear the most scattered. For short delays, there is no yield drop and the values of $\Delta\sigma_p$ are similar to those of $\Delta\sigma_f$. The points representative of $\Delta\sigma_f$ follow approximately a straight line of slope 0.65. Thus the strengthening at the lower yield point follows an equation of the type

$$\Delta\sigma_f = k\, t^{0.65} \qquad (6.9)$$

Similarly, the values of $\Delta\sigma_s$, which give an indication of how much of the strengthening caused by the delay is maintained at a strain of 0.7, can be fitted by a straight line of slope 0.34 so that:

$$\Delta\sigma_s = k\, t^{0.34} \qquad (6.10)$$

There is a fairly large scatter in the values of $\Delta\sigma$ when a straight line fit is achieved. It is not, however, surprising since the oxygen pressure in the testing atmosphere could not be carefully controlled, and therefore probably varied significantly from one test to the next.

The presence of a large yield drop after long interruption delays is probably caused by the collapse of the oxide layer. It is of interest to note that in pure zirconium, after a 60,000s delay, no yield drop is observed. This is consistent with the conclusions of the discussion of the oxidation behaviour of Zr and Zr-Mo alloys, in which it was predicted that Zr-Mo alloys should have a thicker oxide scale than pure zirconium. A thick oxide is likely to affect the mechanical properties

more than a thin one. In the stress-strain curves of Zr-Mo alloys in Figures 5.3 to 5.5, the yield drop is observed only in a few cases. A very slight deformation inhomogeneity in the early straining region can easily result in the disappearance of the peak if the oxide cracks progressively from one part of the sample to the other, and it is felt that this could have very easily happened in some cases.

6.1.3 Strain Softening Behaviour

6.1.3.1 Alternative approaches

The simplest way to approach the mechanical behaviour is to consider the sample as a composite consisting of two separate parts, the β-core and the α-layer, each one bearing part of the load. This assumption is not unrealistic in that the α-layer appears to be ductile at 1000°C, and under some testing conditions achieves a thickness capable of making it contribute significantly to the overall strength. This approach assumes that maintaining the coherency between the α and β does not impose plastic constraints which result in an appreciable effect on the flow stress.

The alternative approach is to view the load bearing capacity of the α-phase as being negligible, which is probably true when its thickness is very small. The strengthening effect of the α-phase in this case can be considered as arising entirely from the plastic constraint exerted by the α-film on dislocations in the β-material. The calculation of the effect of this surface film on the flow curve of the β-material is in this case extremely complex, and we shall only discuss a few elements of the film model.

The actual situation can be expected to lie somewhere between these two approaches, and the simple load bearing model will now be examined

more closely to permit an estimate to be made of the real behaviour.

It should be noted that the effect of the oxide layer itself will not be considered in these models. As has been shown earlier, it appears that the effect of the oxide layer is essentially to cause a sharp yield drop to occur, after which it does not influence the behaviour with further strain.

6.1.3.2 Load bearing model

Here the sample is considered as a composite, and to be constituted of a β-core with a flow stress σ_β and an outer α-layer. The composition, and thus the strength of the α-layer varies across it but we shall assume an average flow stress σ_α.

The calculation of the flow stress assumes that the strength of the composite is the appropriate sum of the strengths of the α and β phases. At a given strain ε, the flow stress σ of the composite will therefore be

$$\sigma \simeq \frac{\pi R^2 \sigma_\beta + 2\pi R e \sigma_\alpha}{\pi R^2} \qquad (6.11)$$

$$\sigma \simeq \sigma_\beta + \frac{2e}{R}\sigma_\alpha \qquad (6.12)$$

where e is the thickness of the α-layer and R the radius of the sample at a strain ε. It is also implicit in this approach that R >> e.

The flow curves of the α- and β-phases are represented schematically in Figure 6.5, and are typical of metals undergoing dynamic recovery. The α-phase, being saturated with oxygen, will be several times stronger than the β-phase. Beyond a strain ε_s the flow curves of both phases show a steady state regime in which the flow stresses do not vary with strain

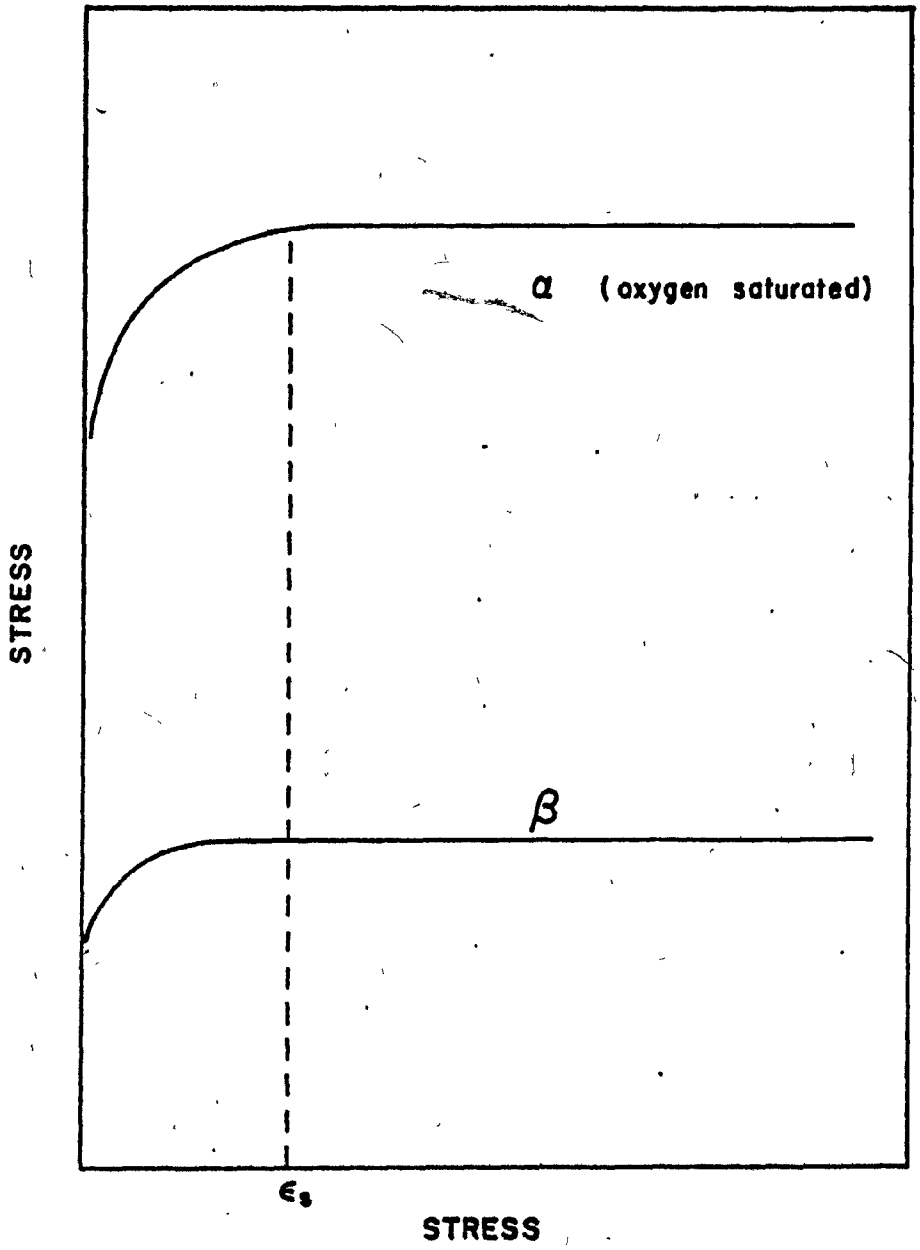

FIGURE 6.5 Schematic representation of the flow curves of the oxygen-stabilized α-phase and of the β-phase in Zr-Mo alloys.

and take the values $\sigma_{s\alpha}$ and $\sigma_{s\beta}$. Below the strain ε_s, σ_β and σ_α both increase with strain. Recalling that the sample radius R varies with strain according to $R = R_o \exp(\varepsilon/2)$, Equation 6.12 then becomes:

$$\sigma = \sigma_\beta(\varepsilon) \quad \frac{2e}{R_o} \sigma_\alpha(\varepsilon) \exp(-\varepsilon/2) \qquad \text{if } \varepsilon < \varepsilon_s \qquad (6.13)$$

$$\sigma = \sigma_{s\beta} \quad \frac{2e}{R_o} \sigma_{s\alpha} \exp(-\varepsilon/2) \qquad \text{if } \varepsilon > \varepsilon_s \qquad (6.14)$$

These equations represent the expected stress-strain curve of the composite. However, no information has yet been given about the variation of e with strain. Several hypotheses may now be considered:

i. The volume of α-phase remains constant with deformation. In this case $e = e_o \exp(+\varepsilon/2)$ where e_o is the thickness of the α-phase at zero strain. The ratio e/R is then independent of strain and equal to e_o/R_o. Inserting this value into Equations 6.13 and 6.14 we observe that for $\varepsilon < \varepsilon_s$, σ will increase with strain, as a result of the strain dependences of σ_β and σ_α, and for $\varepsilon > \varepsilon_s$, σ will be independent of strain. According to this assumption, the experimental softening cannot be explained.

ii. The experimental observations of undeformed and deformed samples suggest that the thickness of the α-phase does not increase with strain, but appears to remain approximately constant. Under these conditions, the flow curves will be described by Equations 6.13 and 6.14 with e constant and equal to e_o. A physical explanation of this behaviour will be suggested in Section 6.1.3.5 below. A strain softening component is then introduced by the exponential term, and this model is in fact able to predict or describe flow softening. As the present experiments were

all carried out to strains of less than 0,8, the exponential can be approximated by the first terms of its Taylor expansion. Equations 6.13 and 6.14 can therefore be rewritten in the form:

$$\sigma = \sigma_\beta(\varepsilon) \quad \frac{2e_o}{R_o}\sigma_\alpha(\varepsilon)(1 - \varepsilon/2) \qquad \text{if } \varepsilon < \varepsilon_s \qquad (6.15)$$

$$\sigma = \sigma_{s\beta} \quad \frac{2e_o}{R_o}\sigma_{s\alpha}(1 - \varepsilon/2) \qquad \text{if } \varepsilon > \varepsilon_s \qquad (6.16)$$

In Equation 6.15, the overall flow stress results from a balance between the term that increases with strain and the decreasing term $(1 - \varepsilon/2)$, and will in general increase with strain. On the other hand, Equation 6.16 predicts that, beyond ε_s the stress will decrease linearly with strain, with a slope equal to $-\frac{2e_o}{R_o}\sigma_{s\alpha}$.

6.1.3.3 Predictions of the load bearing model and the stress-strain curves

The model will now be applied to the strain softening observed in the Zr-Mo alloys. Let us consider first the case where the strengthening of the α-phase was maximum, i.e. for interrupted tests carried out on the Zr-6% Mo alloy at 1000°C at a strain rate of $1.5\times10^{-3}s^{-1}$. The flow stress of the β-core can be taken as $\sigma_\beta = 20$ MN/m^2 from the steady state value of the uninterrupted curve, the radius R_o is 4 mm, and the thickness of the α-layer was measured to be about 0.5, 0.25, 0.1 mm for delays of 60,000, 30,000 and 3,000 seconds, respectively. The value $\sigma_{s\alpha}$ is not known, but it can be derived from Equations 6.15 and 6.16. Figure 6.6 gives the stress-strain curves observed versus those calculated, assuming ε_s to be small enough to neglect the work-hardening region, which represents an oversimplification as some is observed on the experimental curves.

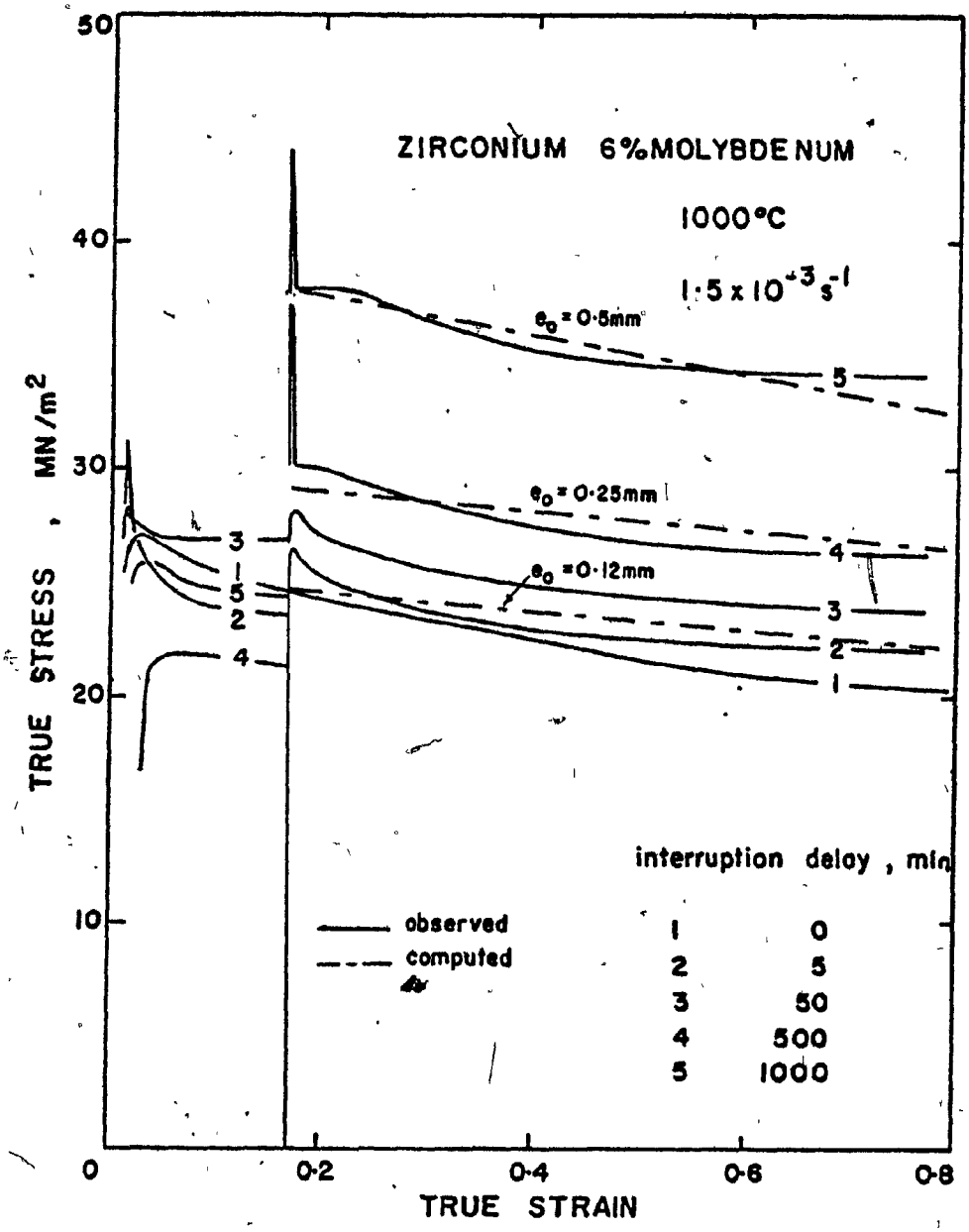

FIGURE 6.6 Flow curves of Figure 5.11 showing the effects of interruption delays on the flow stress of the Zr-6% Mo alloy at 1000°C, plotted together with the flow curves computed from the proposed model.

Considering the simplicity of the model, the agreement between the predicted and the observed curve is very good using $\sigma_{s\alpha}$ = 70 MPa for the curve obtained after a 60,000s delay. For a 30,000s delay, the same stress $\sigma_{s\alpha}$ again correctly predicts the flow stress using e_o = 0.25 mm. Further, for the 3,000s delay curve, the stress is again correctly predicted using e_o = 0.12 mm.

The match between the predicted and the observed curves is considered so far to be very satisfactory, in spite of the model not predicting the observed slope decrease with strain. The most encouraging finding from the fit of the model to the experimental data is that the stress $\sigma_{s\alpha}$ = 70 MN/m^2 is not unrealistic and in fact close to what could be expected from such an oxygen saturated phase. This value together with a roughly correct prediction of the slope, lend support to the load bearing model. Figure 6.7 shows the curve predicted by the model compared with the experimental one in pure zirconium subjected to a 60,000s delay. The calculated curve was obtained using σ_β = 4 MN/m^2, e_o = 0.25 mm, R_o = 4 mm and $\sigma_{s\alpha}$ = 70 MN/m^2. Although the relative error appears much larger, the absolute difference between predicted and observed value remains of the same order, i.e. $\sim$ 2 MN/m^2. The comparison between the predicted curve and the observed one for Zr-6% Mo at 1000°C, uninterrupted is shown in Figure 6.8. Here again the agreement is satisfactory using e_o = 0.15 mm; the other variables having their usual value.

6.1.3.4 The load bearing model and the experimental variables

i. strain rate

This model will enable us to understand the effects of strain rate on the mechanical properties of the alloys. The flow stresses σ_β

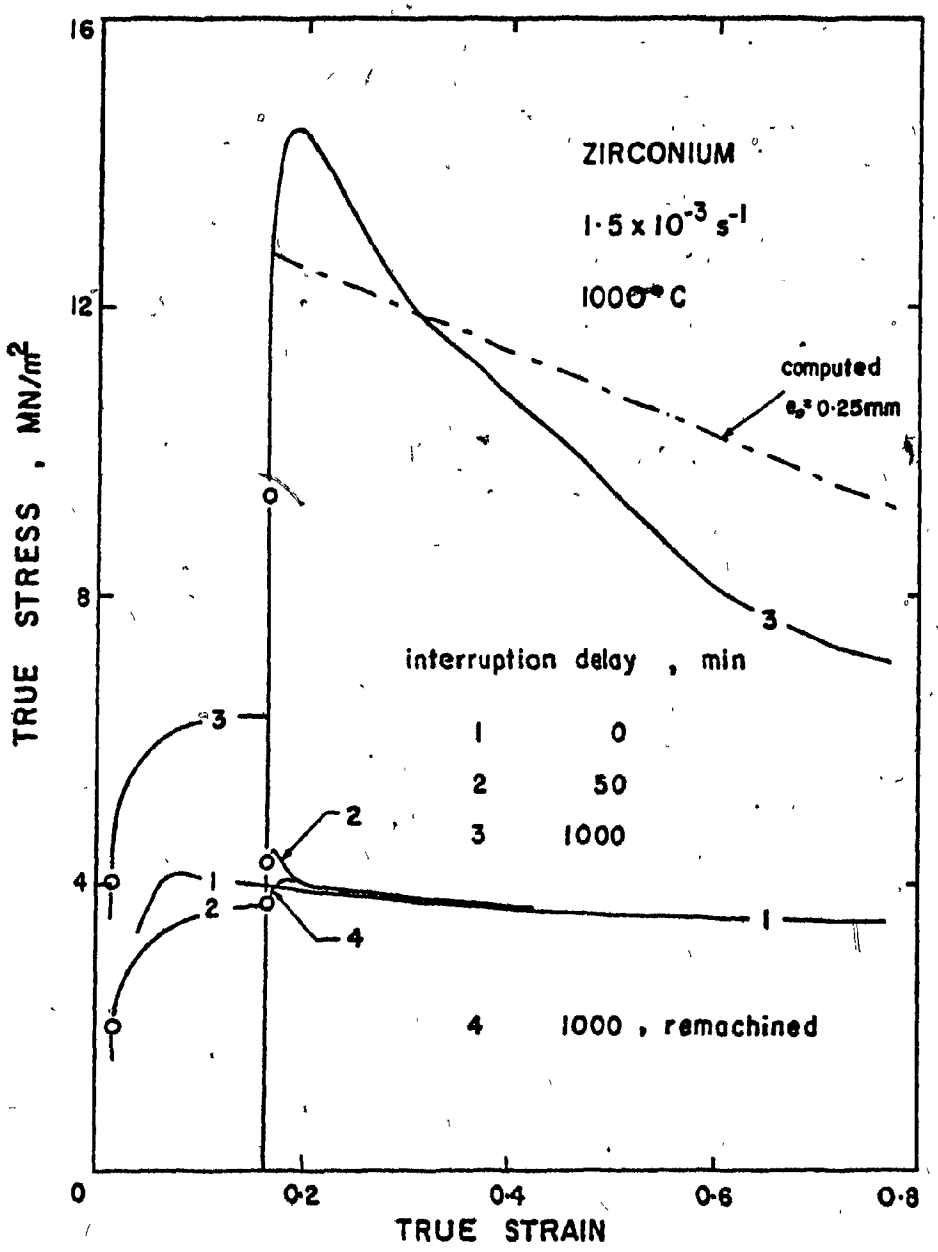

FIGURE 6.7 Flow curves of Figure 5.12 showing the effects of interruption delays on the flow stress of crystal bar zirconium at 1000°C, plotted together with the flow curves computed from the proposed model.

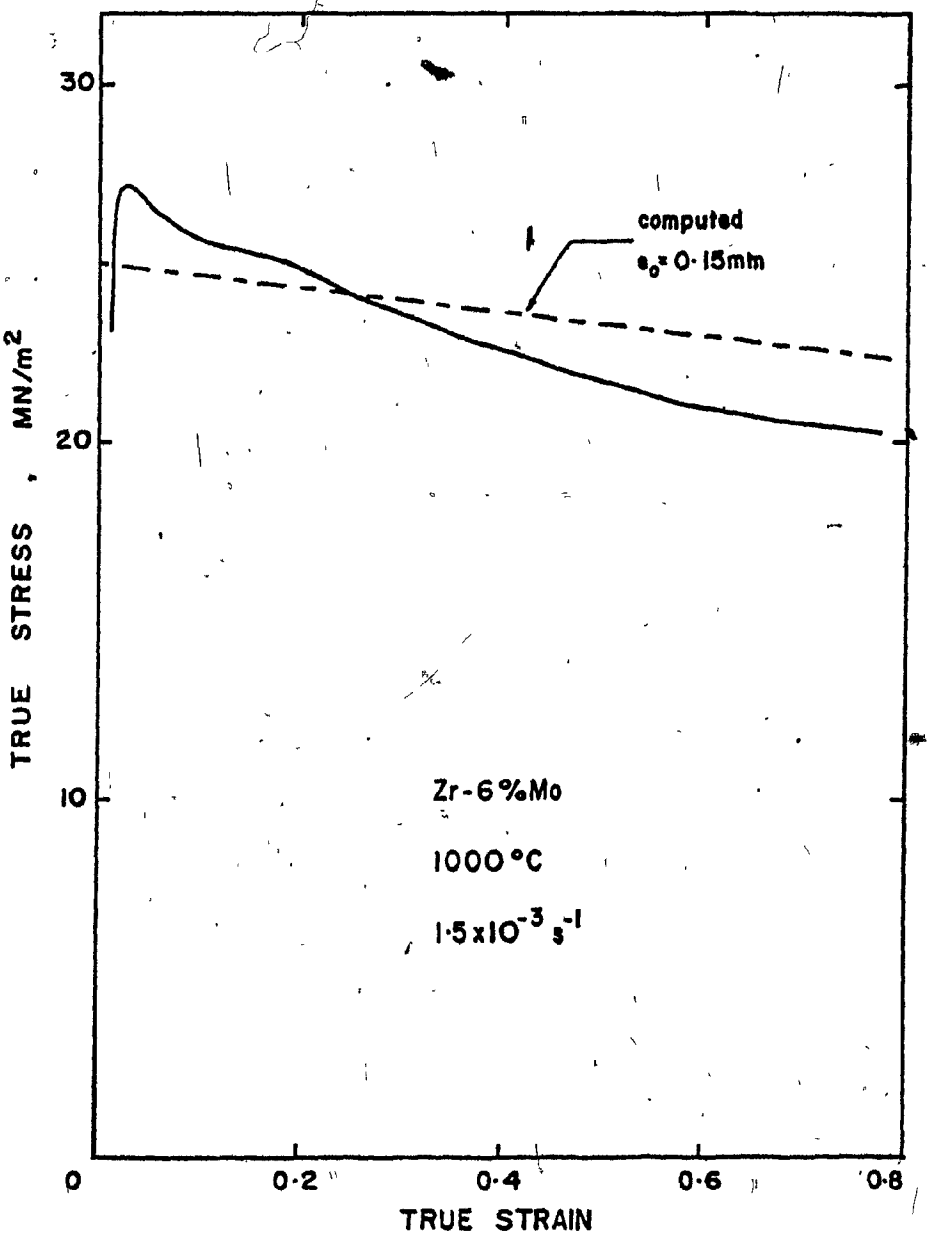

FIGURE 6.8 Comparison between the continuous stress-strain curve obtained from Zr-6% Mo at 1000°C and $1.5 \times 10^{-3} s^{-1}$, and the computed curve obtained from the model.

and σ_α are strain rate and temperature dependent since the deformation is thermally activated, and their variation will follow the empirical rate equations with different stress exponents. (This is to say that the deformation mechanisms are different in the α and the β phases.) Moreover, ε_s will increase with $\dot{\varepsilon}$ and decrease with T. In a first approximation, $\sigma_{s\beta}$ and $\sigma_{s\alpha}$ will follow about the same $\dot{\varepsilon}$ dependence. As a result, from Equation 6.16, we see that σ will be temperature and strain rate dependent. The slope $-\frac{e_o}{R_o}\sigma_{s\alpha}$ will increase with $\dot{\varepsilon}$ in absolute value, as does $\sigma_{s\alpha}$, but the relative softening $\frac{e_o}{R_o}\frac{\sigma_{s\alpha}}{\sigma_{s\beta}}$ will be approximately constant with $\dot{\varepsilon}$. Qualitatively these predictions agree with the experimental results. The increase in ε_s with strain rate should result in an increase in the extent of the work-hardening region with $\dot{\varepsilon}$. The oxide break-up taking place at the yield strain in every instance, the yield drop should be followed by a work-hardening region at high strain rates. Both predictions are observed in Figure 5.5. At the highest $\dot{\varepsilon}$, the work-hardening rate may be high enough to mask the stress drop caused by the oxide break-up, as was observed at $\dot{\varepsilon} = 0.15s^{-1}$.

ii. The effect of temperature is more complex. Not only are $\sigma_{s\alpha}$, $\sigma_{s\beta}$ and ε_s expected to vary with temperature, but e_o should decrease when the testing temperature is decreased from 1000°C to 900°C. As a result, the stresses should increase with temperature decrease, but the relative softening $\frac{e_o}{R_o}\frac{\sigma_{s\alpha}}{\sigma_{s\beta}}$ should decrease as well. This is not observed, which indicates that in this matter the load bearing model is not entirely adequate.

The present model does not explain the origin of the work-hardening observed in Figures 5.3 to 5.5, which is considerably larger

in amount than those of each component alone. In the interrupted curves, work-hardening is not observed upon reloading, in contradiction with the curve of Figure 6.5, where ε_s is typically > 0.1 at $\dot{\varepsilon} = 1.5\text{x}10^{-3}s^{-1}$.

iii. Effect of solute concentration

Solute concentration affects σ_β as shown in Figure 5.10 and also determines the α-phase thickness e_o through its effects on the oxidation rate. Experimentally, however, it is found that e_o does not increase appreciably with Mo content from 2 to 6%. The stress $\sigma_{s\alpha}$ will not be very sensitive to molybdenum content since oxygen is by far the most important solute. As a result, the absolute softening in the lower alloys is similar to that in the 6% Mo alloy.

iv. Effect of oxygen partial pressure

The effect of oxygen partial pressure arises only through its effect on the thickness e_o of the oxide layer. For the purest atmospheres (Figure 5.14), e_o is close to zero and as a result no appreciable softening is observed. The existence of a yield drop at $\dot{\varepsilon} = 1.5\text{x}10^{-2}s^{-1}$ and $\dot{\varepsilon} = 1.5\text{x}10^{-4}s^{-1}$ indicates that there is some oxide formation and break-up during the onset of straining.

v. The effect of delay time has been described earlier. For the present discussion, it is of interest to relate the oxide thickness e_o to the delay time. If we assume that the thickness of the α-phase is controlled by diffusion through the α-layer, then

$$e_o = k\, t^{1/2} \qquad (6.17)$$

where t is the time and k a constant. Inserting this value into Equation 6.14 we find

$$\sigma = \sigma_\beta \quad k \frac{\sigma_{s\beta}}{R_o}(1 - \varepsilon/2)t^{1/2} \qquad (6.18)$$

$\sigma - \sigma_\beta$ is the parameter that was defined as $\Delta\sigma$ in Section 6.1.2, and thus

$$\Delta\sigma_f = k\, t^{1/2} \qquad \text{at zero strain} \qquad (6.19)$$

and

$$\Delta\sigma_s = k' t^{1/2} \qquad \text{at } \varepsilon = 0.7 \qquad (6.20)$$

This is in reasonable agreement with the experimental results, which yielded $\Delta\sigma_f = k\, t^{0.65}$ and $\Delta\sigma_s = k' t^{0.33}$.

6.1.3.5 Interpretation of the observed constancy of e

The model described in the previous paragraphs explains in a satisfactory manner most of the deformation characteristics of the Zr-Mo alloys. One of the bases on which it rests is the experimental observation that e, the thickness of the α-phase layer, remains independent of strain. This has not yet been interpreted. The hardness curve, Figure 5.17, seems to indicate that no appreciable inwards oxygen diffusion takes place during deformation, since it would affect the hardness, hardness being very sensitive to oxygen content in Zr alloys. Thus, during deformation it seems unlikely that the $\alpha \rightleftharpoons \beta$ interface moves towards the surface of the sample as a result of accelerated diffusion. The other possible way by which the thickness decreases so as to match the increase that would result by deformation is through a displacement of the oxide-α-

interface. During yielding, the oxide cracks, thereby no longer protecting the α-phase. The increased oxygen flux will proceed to form oxide at the expense of the oxygen rich α, a process which may not need high fluxes. The oxide is continuously broken by deformation which renders the process nearly linear with time, and thus with strain since the strain rate is constant.

A more detailed investigation of the causes of constancy of the α-layer thickness with strain is still needed, however, to lend support to this hypothesis. If e , for example, actually decreases with ε, as a result of the crack-up of oxide, then the higher rates of flow softening observed would be fully accounted for.

6.1.3.6 Surface film model

The load bearing model has been shown to be capable of explaining, at least qualitatively, most of the features of the high temperature deformation of the Zr-Mo alloys. However, there are still a few minor points that are left unexplained by the load bearing model. For example, the work-hardening region in the Zr-Mo alloys was found to be less extensive at intermediate and low strain rates than it ought to have been if the flow stress had been a linear function of the stresses of the α and β phases.

The surface film model considers that the α layer affects the flow stress by preventing the egress of dislocations at the surface, thereby restricting slip. When a load is applied to the sample, shear stresses are generated on the slip planes and, in the microstrain region, free dislocations glide over short distances until they are arrested by obstacles such as grain boundaries. If the stress applied to the sample is increased to the yield point σ_β of the β-core, slip begins to take place, but is soon

stopped as the slip dislocations cannot egress at the sample surface. Dislocation pile-ups are thus generated near the α-β interface. The sample will yield only when the applied stress is sufficient to generate slip in the β-phase, thereby forming a slip step on the surface of the β-phase. Near the yield point, the Frank-Read sources will generate more dislocations than they would have done at a stress σ_β and thus a higher dislocation density is obtained at the macroscopic yield stress σ. This, in turn, causes higher rates of work-hardening, and eventually the steady-state flow stress of the material settles to a higher level than that of an unoxidized sample.

The quantitative description of the effect of a plastic constraint on the mechanical properties is extremely complex, and so only an abbreviated treatment will be attempted. The shear stress τ_h at the head of a pile-up is (220)

$$\tau_h = n\,\tau_a \qquad (6.21)$$

$$\tau_h = \frac{2L}{\mu b}\,\tau^2_a \qquad (6.22)$$

where τ_a is the applied shear stress in the slip plane, n the number of dislocations in the pile-up, L the length of the pile-up, μ the shear modulus and b the Burgers vector.

The stress generated at the head of the pile-up can generate slip in the α-phase in two ways. The most common one is by acting on a neighbouring Frank-Read source in the α-grain. The stress generated by the pile-up which is required to activate the Frank-Read source will generally depend upon the distance from the source to the pile-up through

a stress concentration factor, the distance between the anchoring points of the source and the geometric orientation of the slip plane. The second mechanism comes into play if no Frank-Read sources can be activated; in this case the local stress can reach the theoretical shear strength of the α-phase, and punch a dislocation into it, i.e. nucleate a dislocation homogeneously.

When glide has been initiated in the α-phase, if the α-film is monocrystalline, the dislocations can emerge onto the surface. The stress at the head of the pile-up will have to be greater than a critical value τ_c to generate slip in the α-phase but the effect of the thickness of the α-phase will not be likely to be important. On the other hand, if the α-layer is polycrystalline, the propagation of slip to the other grains may or may not introduce a strengthening component of the Hall-Petch type.

As can be seen, this approach does not lend itself easily to a calculation of the effects of the α-phase on that of the β. Qualitatively, however, it can predict higher work-hardening rates than could be expected in unconstrained phases, in agreement with experimental observations.

One method of determining the extent to which plastic constraint contributes to the overall strengthening would be the comparison of the subgrain size (and sub-surface dislocation density) of deformed samples having an α-layer with reference ones which have undergone a similar deformation in an ultra-high purity atmosphere. Since the flow stress is directly related to the subgrain size (Equation 2.1) the difference in subgrain sizes would be a measure of the dislocation strengthening mechanism.

6.1.4 Deformation Mechanisms in Zr-Mo Alloys

This section will comment briefly on the mechanisms controlling deformation in the Zr-Mo alloys. The values obtained for Q were about 155 and 105 kJ/mol for yield and steady state flow respectively, for the 1.9 and 6% Mo alloys. The data were not detailed enough to give any indication of the variation of Q with stress, which is pronounced in α-iron, silicon steel (47) and α-zirconium (17). The higher value obtained at yield cannot be directly attributed to the effect of the α-layer because the strengthening imparted to the alloy by the latter does not vary sufficiently with temperature and does not contribute more than 20% of the flow stress. It is of interest that the value of Q is rather low and compares with those for self-diffusion in bcc metals. The activation energies for self-diffusion range from 125 to 205 kJ/mol in β-titanium (221,222), 113 to 121 kJ/mol in γ-uranium (221,222,223), 92 to 280 kJ/mol in α-zirconium (224) and 88 to 272 kJ/mol in β-zirconium (225,226,227). The activation energy for molybdenum diffusion in β-zirconium is not known, but that of niobium, a neighbour on the periodic table ranges from 108 kJ/mol at low temperatures (< 1000°C) to 197 kJ/mol at high temperatures (> 1300°C).

The climb theory of dynamic recovery predicts $Q \simeq Q_{\text{self-diffusion}}$, which is approximately observed in the present work. For creep, the activation energies for β-Zr range from 134 to 188 kJ/mol (228,229), which again is close to self-diffusion. On the other hand, the climb theories do not predict the steady strengthening that arises from the addition of solute. It is not therefore possible to come to a definite conclusion about the precise mechanism which is rate-controlling, and much more detailed knowledge of the activation parameters will be required before such an insight can be obtained.

6.2 ZIRCONIUM NIOBIUM ALLOYS

In this section an attempt will be made to throw some light on the causes of the flow softening behaviour observed in the Zr-Nb alloys containing more than 2.5% Nb. In addition, the cause of the variation in strength with annealing time at 1000°C will be discussed in detail.

6.2.1 Position of the $\alpha + \beta \rightleftharpoons \beta$ Transus

Optical microscopy has shown, as have the X-ray investigations, that, in the presence of oxygen, the α-phase can be retained up to 825°C in the 15% Nb alloy. The amount of the α-phase appears to decrease with temperature but not very rapidly. These results agree with those of Richter et al (214) with regard to both the phase proportions and their morphology. The above authors attributed the enhanced stability of the α-phase to the oxygen present in the alloy, which gives the alloy a pronounced ternary character. The results of these workers can be used to construct isotherms of the Zr-rich corner of the ternary diagram Zr-Nb-O shown in Figure 6.9. It can be seen that, at about 800°C, the extent of the β-phase field appears severely restricted by the presence of oxygen. This gives a further indication of the strong effect of oxygen on $\alpha + \beta \rightleftharpoons \beta$ transus of the Zr-Nb system.

As far as the mechanical properties are concerned, the small amount of α-phase present at 825°C and the apparent absence of morphology change during deformation indicates that it does not participate in a central way in the deformation and softening process. Moreover, as softening is still present at 925°C and above, temperatures at which the α-phase is absent, mechanisms involving the α-phase can be ruled out as candidates responsible for the flow softening.

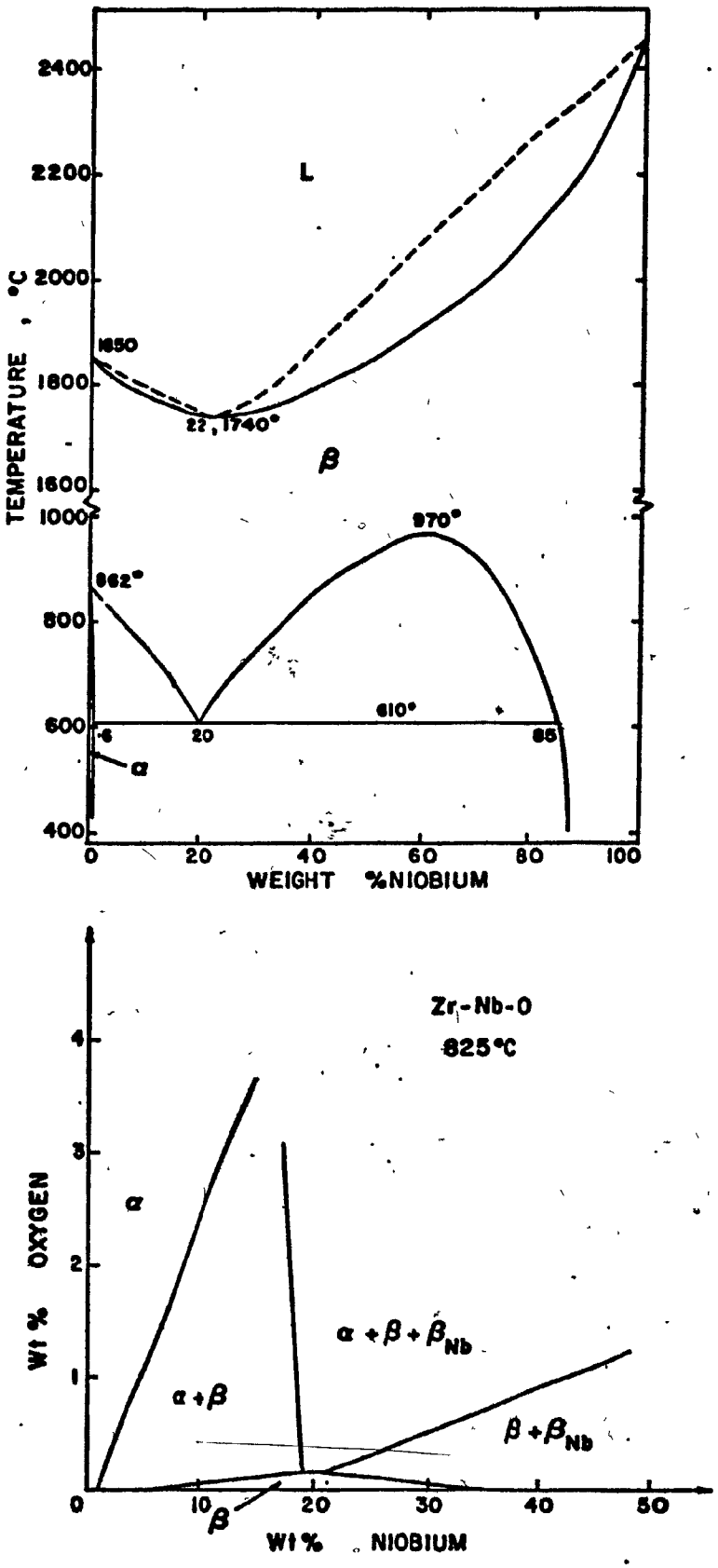

FIGURE 6.9 Estimated appearance of the Zr-rich corner of the Zr-Nb-O isothermal section at 825°C, from the data of Richter et al (214).

6.2.2 Flow Softening Mechanisms and the Observed Behaviour

The experimental results pertaining to the high Nb alloys presented in the preceding chapter have shown that the observed anneal hardening and flow softening do not have a simple explanation. However, before proceeding any further, it will be useful to review some of the flow softening mechanisms, and to consider whether any of the conventional ones can be responsible for the effect. In this way, the need for a further mechanism, hitherto undescribed can be established. Such a mechanism will, in fact, be proposed later.

6.2.2.1 Dynamic recrystallization

This is a mechanism which produces nearly equiaxed grains; its operation is preceded by a region of work-hardening, the extent of which increases very markedly with strain rate as well as with solute concentration. None of these features are apparent in the present observations. Furthermore, one could expect this mechanism to be operative in the 2.5% Nb alloy as well as in unalloyed zirconium, since alloying usually makes dynamic recrystallization more difficult (70). For these reasons it cannot be considered as a possible mechanism in the Zr-Nb system.

6.2.2.2 Texture effects

The texture determination that has been carried out on the 10% Nb alloy has shown that the texture does not change drastically with strain and furthermore its evolution should lead to a strengthening rather than to flow softening. It is perhaps redundant to note that the various strengthening and softening effects observed upon annealing cannot at all be predicted by texture changes.

6.2.2.3 Ostwald ripening

The curves of Figures 5.37 and 5.38 are similar to those which are obtained when precipitation and overaging take place. The increase in flow stress at short times can be attributed to the formation of precipitate, while the flow stress decrease at longer times can arise from Ostwald ripening of the second phase particles. According to this view, precipitation should take place at 1000°C, in the present alloys, and the flow softening would be attributed to particle coarsening. This hypothesis, however, is not supported by the results of the X-ray analyses which do not indicate the presence of any phase other than β at 1000°C. The microscopic observations agree with the X-ray results, since no precipitates were observed, even for the overaged and deformed conditions, for which the precipitates ought to have been visible optically. Furthermore, the chemical analyses of these alloys indicate an impurity level which is too low to allow the possibility of any massive precipitation. For these reasons, it can be concluded that the softening behaviour cannot be attributed to precipitation and ageing effects.

6.2.2.4 Grain boundary sliding

The extent of grain boundary sliding in Zr-15% Nb has been determined from grain size measurements in Section 5.3.8. It is relevant to the present discussion to point out that no grain size refinement has been detected during deformation, under the conditions which caused an appreciable grain boundary sliding effect. In consequence, flow softening cannot be attributed to this mechanism, except for a small decrease in stress at low strains that could be caused by the "smoothing out" of the boundaries. The flow curve of the as-received bar D tested at 825°C

(Figure 5.33) brings support to this conclusion. This material maintained a nearly equiaxed grain size during deformation, and deformed under a flow stress well below that of coarser-grained material. However, flow softening is nearly absent in this case, which indicates that flow softening essentially arises from deformation processes that take place within the bulk of the grains themselves.

The increase in strength of the alloy with corresponding grain growth during annealing experiments may be due to a significant extent to the progressive disappearance of grain boundary sliding, but the decrease in strength that takes place after very long anneal times must be attributed to another mechanism.

6.2.2.5 Other mechanisms

The other possible mechanisms are clearly not applicable to the present case. Any substructure present can be expected to have been reduced to a low density as a result of prolonged annealing at 1000°C. The strain rates are too low for any adiabatic heating effect to occur and spheroidization of a second phase is excluded in these single phase alloys. Furthermore, below 925°C, the softening cannot be attributed to environmental reactions, as was the case for Zr-Mo alloys.

It thus appears that, as far as anneal hardening is concerned, grain coarsening can be considered to be at least partly responsible. As regards flow softening, of the classical mechanisms, only the "smoothing of the grain boundaries" preceding superplastic flow is likely to have any influence on the flow curve, and this is likely to be a minor effect. We must therefore search elsewhere for a full rationalization of this effect.

6.2.3 Abnormal Features in the Zr-Nb Alloys

In the previous section, it was suggested that none of the classical flow softening mechanisms can be invoked to explain the present results. That is, no single mechanism appears to account for both anneal hardening and anneal flow softening. As a consequence, there may be an additional mechanism which is peculiar to the Zr-Nb alloys, and whose operation gives rise to the observed behaviour. The identification of this mechanism is rather difficult, although some help is available, because such special mechanisms can be expected to lead to an unusual behaviour in other respects besides the strength and flow characteristics. For this reason a careful examination of the other abnormal properties observed in these alloys will now be undertaken.

The microstructures of the Zr-15% Nb alloy annealed at 1000°C and cooled at the same rate from the β-phase present an unusual evolution with annealing time which has been described in detail in Section 5.3.5. The α-phase morphology was observed to vary markedly with anneal time. The α-particles formed during cooling subsequent to a short anneal were round and small. An increase in anneal time changed the morphology into plates of larger dimensions; which, with longer anneal times, turned into more massive and equiaxed particles. This indicates that the solution time significantly affects the transformation kinetics and morphology, independently of grain size.

These results, puzzling as they may seem, have been observed before in Zr and Ti alloys. Higgins and Banks (230) found that, in a Zr 2.5% Nb alloy, the isothermal transformation rate in the 725-800°C temperature range was faster for a β solution temperature of 1040°C than for a 1080°C anneal temperature. They attributed this effect to a clustering

process in the β-phase which could have accelerated the nucleation rate. Hunt and Niessen (231) on the other hand, determined continuous cooling curves for some Zr-Nb alloys, but did not find any effect of solution temperature on the transformation kinetics. They varied the solution time from a fraction of a second up to one hour without observing any changes in the transformation rate. However, they found that the temperature at which the transformation began on cooling increased with cooling rate, and they interpreted this in terms of a clustering mechanism in the following manner. A slow rate of cooling should maintain equilibrium clustering at all temperatures, thereby leaving the alloy in its lowest free energy state. A fast cooling rate, on the other hand, by not allowing equilibrium clustering to be attained should increase the free energy of the β-phase and therefore increase the temperature at which the α-phase nucleates. This requires a very substantial variation of free energy in order to offset the decrease in the transformation temperature that is caused by an increase in cooling rate.

Rizkalla (232), studying the mechanical behaviour of Zr-2.5% Nb in the α + β phase region observed some effects of the β solution time on the flow stress and microstructure. The alloy was heated up to 1000°C, maintained for 10 minutes at that temperature, cooled down to 725°C at a cooling rate of 62°C/min and quenched. He found that a decrease in heating rate results in a coarser Widmanstatten structure after treatment. After very slow heating rates, a continuous network of α-phase is present on the former β-boundaries. The α-plates then nucleate preferentially from the β-boundaries (side-plates). When these structures are tested at 725°C, Rizkalla found that the coarsest structure leads to the lowest strength. He was not able, however, to give a satisfactory explanation

of the effect of heating rate, but it may be speculated that an oxygen segregation effect could lead to a similar result.

In Ti-Cr alloys, McQuillan (233) observed that β-decomposition was markedly affected by the time and temperature of the β-treatment. She suggested that prolonged heating at temperatures towards the lower limits of the β-field could give rise to the formation of chromium-rich clusters which would in turn promote the faster precipitation of $TiCr_2$ upon cooling. The validity of McQuillan's results has been tested by Margolin et al (234) on a Ti-8% Cr alloy. They heat treated the alloy so as to minimize or to maximize clustering in the following manner. The alloy was given a β-anneal and then subsequently given one of the following three treatments:

i. quench down to 700°C (just above the $\alpha + \beta \rightleftharpoons \beta$ transus for this alloy), hold at 700°C there for from two hours to one week, water quench;

ii. transform isothermally at 500°C for from 30 seconds to six days, quench;

iii. treatment (i) followed by a quench to 500°C followed by treatment (ii).

The microstructures showed that treatment (i) did not produce any appreciable change in the structure with time. Heat treatment (ii) showed that the precipitation of α was insignificant up to one hour and appeared very fine after six days. The treatment (iii), gave rise to massive α-precipitation even after only 30 seconds at 500°C, the amount of α increasing with hold time at 700°C and with hold time at 500°C. Margolin et al also concluded that clustering was responsible for the acceleration of β decomposition. The interpretation given by McQuillan and Margolin of the effects of the formation of Cr-rich domains on the

decomposition is exactly the opposite of that proposed by Hunt and Niessen since in the former case it is hypothesized that clustering accelerates the transformation whereas in the latter it is assumed that it opposes the process. There is thus apparently some confusion about the subject of clustering and for this reason we shall devote the section that follows to a more careful discussion of its occurrence and its possible effects on the mechanical properties.

The metallographic examination of the present Zr-Nb alloys (Section 5.3.5) slowly cooled from the β-phase also revealed the presence of bands similar to those observed in low-carbon steels (235) and of grain boundary segregation. There is a marked difference in these two processes with respect to annealing time. The deformation bands tended to disappear with annealing time, although a few were still present after a 64-hour anneal. By contrast, precipitation at grain boundaries, which was absent after short holding times, became evident after four hours and was massive after 64 hours, leaving a wide precipitate-free zone on each side of the boundary. The microprobe results did not support the hypothesis of massive segregation, but the evolution of the microstructures suggests that a segregation effect is present in the Zr-Nb alloys. We shall therefore discuss in a further section the occurrence of solute segregation and consider its possible influence on the mechanical properties.

6.2.4 Clustering

Although the occurrence of clustering has been postulated in both the Zr-Nb and Ti-Cr systems, no direct experimental evidence of this phenomenon is as yet available in these systems. Worse still, there is no evidence of the nature, size, stability or properties of the proposed clusters. Any knowledge of the possible effects of the clusters on the

mechanical properties is limited to extrapolations based on the low temperature properties. These in turn are based on observations in Al-4% Cu alloys in which many investigations on the properties of solute clusters have been made. In consequence, the present discussion will only be qualitative, and will attempt to answer the question of how clustering might explain the observed flow behaviour in Zr-Nb alloys.

6.2.4.1 Thermodynamic basis

In an A-B binary system, if the like atoms have a larger binding energy than unlike atoms, there will be a tendency for a solute atom A to surround itself with A atoms. This tendency will be counterbalanced by the decrease in the entropy of mixing caused by such a process, particularly at high temperatures where clusters usually do not form. Another requirement for cluster formation is that the solute atoms have nearly equal radii, so that the distortion created by the cluster formation is small. The atomic radius of Nb (3.30 Å) is only about 8% smaller than the β-Zr radius (3.54 Å), indicating the feasibility of clustering. The distortion caused by the aggregation of like atoms creates elastic strains which prevent the formation of large zones; e.g. the diameters of these zones are usually 100 Å or less.

The presence in the Zr-Nb diagram of a region in which the β-phase decomposes into two β-phases, one Nb-rich and the other Zr-rich does support the contention that the Zr-Zr and Nb-Nb bonds are stronger than the Zr-Nb bonds. Were the thermodynamic properties of the β-phase known, it would be possible, by comparing the excess entropy and enthalpy of mixing with those of the ideal case, to have better insight into the stability of the clusters. The property that can be determined in an approximate manner

from the phase diagram of the Zr-Nb binary system is the excess free energy of mixing. The excess free energy ΔG^E of the alloy can be written in the form:

$$\Delta G^E = X_{Nb}X_{Zr}(p_o + p_1X_{Nb}) \qquad (6.23)$$

where X_{Nb} and X_{Zr} are the atomic fractions of Nb and Zr, respectively, and p_o and p_1 constants. For certain values of p_o and p_1, the free energy curve of the alloy will be such as to give rise to a miscibility gap. If the maximum temperature T_c at which the miscibility gap persists is known, as well as the composition at this point (the consolute point), that is X_{Nb} and X_{Zr}, the constants p_o and p_1 may be calculated through the relations (236)

$$\frac{RT_c}{X_{Zr}X_{Nb}} = 6p_1X_{Nb} - 2(p_1-p_o) \qquad (6.24)$$

$$\frac{RT_c}{X_{Nb}2X_{Zr}^2} = \frac{6p_1}{2X_{Nb} - 1} \qquad (6.25)$$

The Zr-Nb phase diagram exhibits such a miscibility gap, and the consolute point lies at $X_{Zr} = 0.4$, $X_{Nb} = 0.6$ and $T_c = 1243$ K. Substitution of the required values in the above equations, leads to

$$p_1 = 1430 \quad \text{and} \quad p_o = 4002$$

from which ΔG^E can be calculated. This has been carried out in Figure 6.10, which gives ΔG^E as a function of niobium concentration. In this diagram the ideal free energies of mixing ΔG^I for two temperatures, 1000°C and 825°C,

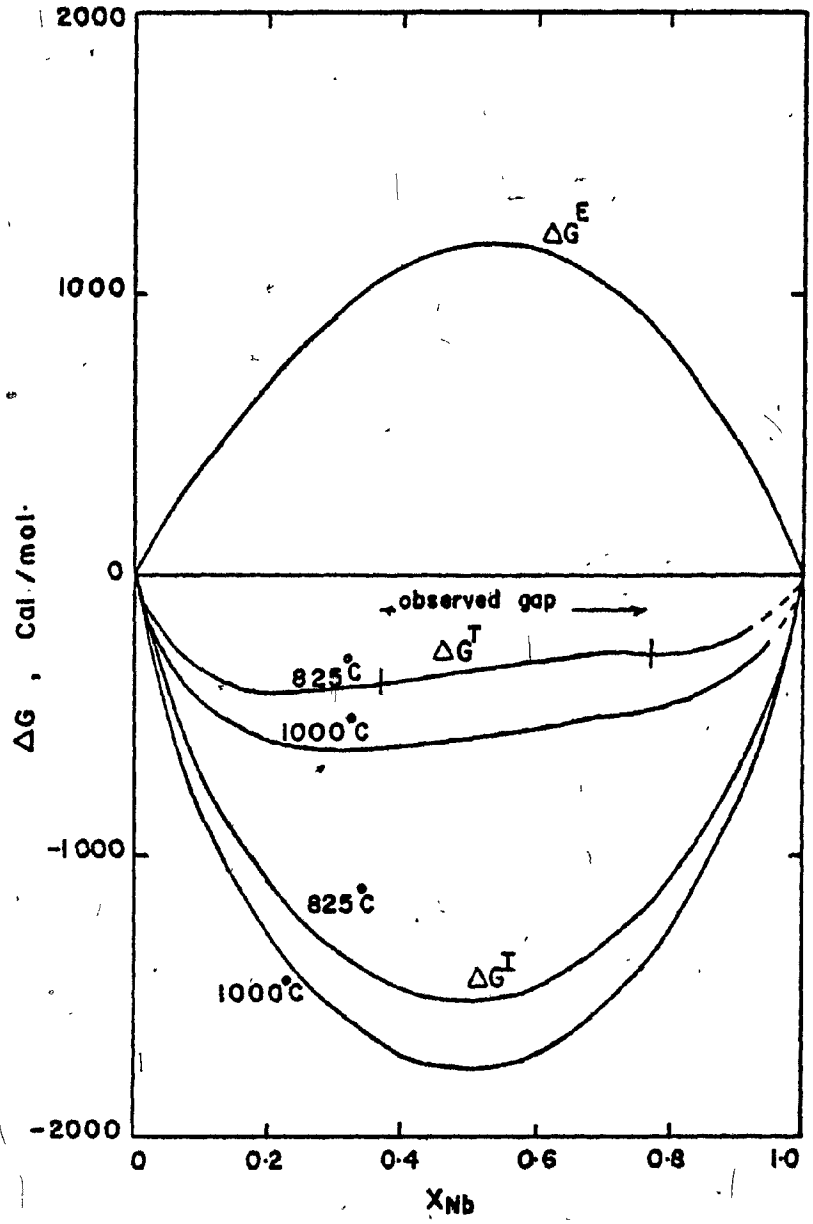

FIGURE 6.10 Estimation of the variation of the free energy of mixing of the Zr-Nb alloy with niobium atomic fraction.

are also represented. The values at these two temperatures represent the practical limits of the range of our investigation. The sum of ΔG^I and ΔG^E represents the total free energy ΔG^T of the alloy. We remark that the calculated miscibility gap at 825°C compares reasonably well with the observed one, assuming that ΔG^E is temperature independent.

This provides an indication that the excess free enthalpy of mixing ΔG^E arises essentially from the excess enthalpy of mixing ΔH as the latter would be expected to be little sensitive to temperature. Thus, for $X_{Nb} = 0.15$, ΔH will be about 600 cal/mol. This value is comparable to the values obtained in the α-phase of the Al-Zn system at 400°C. The Al-Zn system also exhibits a miscibility gap (237); the degree of clustering has been experimentally determined at 400°C. The clustering parameter α_1, defined as $\alpha_1 = 1 - \frac{p_1}{X_A}$, where X_A is the atomic fraction of the solute and p_1 the observed probability that an A atom be surrounded by like atoms is found to increase with zinc content from zero in pure Al (corresponding to random) to 0.16 for $X_{Zn} = 0.5$. It seems reasonable, in view of these results to conclude that clustering is likely to occur in the β-phase of Zr-Nb systems, even though the increase in the entropy term with temperature may adversely affect the process.

The case of Ti-Cr is of interest since abnormal transformation kinetics have been reported. The formation of Cr-rich regions which coexist with Ti-rich ones is <u>not due to clustering</u> (defined as the result of like-atom bonds being stronger than unlike-atom bonds) but to <u>short range order</u> corresponding to the $TiCr_2$ structure, because of the presence of the $TiCr_2$ intermetallic. It appears therefore by comparing the results obtained on Zr-Nb and Al-Zn systems on the one hand and TiCr on the other, that both clusters and short range order will affect the properties of the

alloys, as long as the positive or negative deviations from ideality are large.

6.2.4.3 Cluster formation kinetics

The knowledge of the rate at which clusters form is based on low temperature data, and the author is not aware of direct evidence regarding clusters of the present types at elevated temperatures. For the intermediate temperature case, Christian (238) has discussed in some detail the kinetics of cluster formation. Assuming that the driving force for cluster growth is the decrease in bulk energy of the zone, and that the driving force varies as 1/r, r being the zone radius, he was able to derive the following relation:

$$f = 1 - 1/(1 + Ct)^{1/3} \qquad (6.26)$$

where f is the fraction clustered, C a positive constant and t the time. The validity of this equation has been confirmed by calorimetric and resistivity measurements (239). According to this relation the clustering rate decreases with time due to a decrease in driving force and to an increase in the distance over which the atoms must diffuse. The clustering process does not require any incubation time, a feature which can distinguish it easily from precipitation. The constant C in Equation 6.26 cannot be estimated, however, which renders the equation of somewhat limited use in the present case. At room temperature, the formation of GP zones has been recognized to be faster by a factor of about 10^7 than is expected from the diffusion coefficient. Although a vacancy mechanism has been postulated, the discrepancy between the observed and predicted rates is

still not resolved. At elevated temperatures, however, the role of short circuit diffusion paths is likely to be negligible.

It is of interest to apply the diffusion data of chromium in titanium obtained by Gibbs et al (240) to the results of Margolin concerning the effect of hold time at 700°C on the transformation kinetics of the alloy at 500°C, which were summarized earlier.

The microstructures were influenced by the hold time at 700°C and equilibrium was not reached even after a day since further evolution occurred for a full week at 700°C. The diffusion coefficient of Cr in Ti is about 8×10^{-11} cm^2/s at 700°C, and the average distance over which an atom will diffuse in 24 hours is 26 μm, a distance at least three orders of magnitude larger than the short range domain size. The average distance travelled by a Cr atom is about 900 Å in one second, a distance again greater than the postulated domain size (∿ 100 Å). In this case there is a conflict between the calculated rate and that experimentally observed. It is difficult to conceive how this conflict can be resolved, as the theoretical rate is so much faster than the observed rate.

A similar computation of the diffusion distances of Nb in Zr-Nb alloys leads to a mean diffusion distance of 2000 Å in one second at 1000°C, and 26 μm in 4 hours, based on a diffusion coefficient of 4.5×10^{-10} cm^2/s due to Lundy et al. (225). These values are similar to those for Cr in Ti and they predict that the clustering process would take less than one second. If, indeed, clustering is responsible for the abnormal transformation microstructures and kinetics upon cooling and for the mechanical behaviour, then the clustering process is not as simple as hypothesized and may involve much more complex interactions.

6.2.4.3 The effect of oxygen on clustering

The principal impurity in both the Ti-Cr alloys already considered as well as in the present Zr-Nb alloys is oxygen. Internal friction studies of niobium containing zirconium and nitrogen (241) have revealed the presence at intermediate temperatures of two interaction peaks other than the Snoek peak. These were attributed to Zr-N and N-Zr-N bonds, therefore indicating a strong tendency for the nitrogen atoms to be trapped by zirconium atoms. It has been hypothesized (241), on the basis of the temperature dependence of the intensity of the relaxation peaks, that the N-Zr-N peak should disappear at 1000°C, whereas the N-Zr peak should still remain marked. Similar results (242) were found in Nb rich Nb-Zr-O alloys and led to similar conclusions regarding the properties and existence of O-Zr and O-Zr-O clusters.

In the Zr rich part of the Zr-Nb binary system, however, there are many more Zr atoms than O atoms. Oxygen atoms are thus not bound to any particular zirconium atoms, and they may shift the bond from one Zr to a neighbouring Zr atom. This is confirmed by the high value of the oxygen diffusion coefficient in β-Zr, which is about 8×10^{-9} cm^2/s at 1000°C (243) in the absence of a ternary element. When the like-like clustering of zirconium and niobium takes place, the 'de facto' segregation of oxygen to the zirconium-rich clusters can be expected to follow. This will, of course, complicate the oxygen diffusion process, thereby leading to an insight into the slowness of the clustering process in a ternary system compared to the rates of solute diffusion in the respective binary systems.

6.2.4.4 Effect of clustering on the mechanical properties

To the author's knowledge there is no information regarding the effects of clustering on the mechanical properties at high temperatures. At low temperatures, the formation of GP1 zones in supersaturated solutions results in a very marked increase in strength. The degree of strengthening increases with the number of clusters, until they begin to grow further and lose coherency (thus forming GP2 zones), at which stage the strength decreases again.

By analogy, the formation of clusters at elevated temperatures should also lead to an increase in strength because of the additional shear stress that is required to move a dislocation through the clusters.* It may also be inferred that, if the material is strained, the dislocations will destroy the clusters, since the passage of a single dislocation through the clusters will produce a displacement of one Burgers vector. In this way, continued deformation should lead to a randomization of the structure (i.e. to de-clustering). This should, in turn, produce flow softening, if no other process, such as work-hardening, comes into play to offset the strength decrease.

As mentioned above, a large part of the anneal hardening effect can be attributed to grain growth in the fine-grained (nearly superplastic) starting material, the remainder of the hardening is thought to arise from clustering during annealing. The clusters cannot be destroyed by annealing alone as they are thermodynamically stable but can be suppressed by deformation, leading to flow softening. This is indicated by the increase in the

---

* In Nb-rich clusters the line tension of the dislocation increases corresponding to a free energy peak, whereas in Zr-rich regions the line tension will be below the average value and correspond to a well in the free energy.

difference between the yield and the steady state stresses with annealing time. For annealing time up to four hours, the flow softening increases, which is consistent with the formation of clusters. The observation that the softening is more marked at the low temperatres as compared with the higher ones is also in qualitative agreement with the expected decrease in the driving force for clustering with increasing temperature. If the occurrence of some or all of the flow softening in the high niobium alloys in the β-phase is due to de-clustering, it would be expected that a similar effect would arise in the Zr-2.5% Nb alloy. This, however, is not the case. This conflict can be resolved if clustering is particularly effective in strengthening the alloys in the lower portion of the β field, i.e. below 900°C, a domain which is not attainable in Zr-2.5% Nb alloy. Moreover, the amount of grain boundary sliding is not likely to be of importance in the Zr-2.5% Nb alloy as the grain size of the alloy was always between 0.1 and 0.3 mm.

The strengthening caused by annealing at 1000°C decreases sharply with increasing testing temperature; that is, it is most marked at 825°C and is almost insignificant at 1000°C. This can be explained qualitatively by the variation in the magnitude of the grain boundary sliding component of strain as compared with the effect of clustering with temperature. At 1000°C, grain boundary sliding will be of relatively little importance, as small grain sizes (∿ 20 μm) are not stable at this temperature. After 20 minutes preheat, the average grain size reached is about 70 μm, so that the extent of grain boundary sliding and its influence upon the flow stress is reduced. On the other hand, the clusters present at 1000°C would not be expected to be as well defined and effective in opposing the dislocation movement as they are at 825°C. It seems, therefore, that

clusters exert a strong influence on the mechanical properties at 825°C only after annealing at 1000°C has been carried out. A hypothesis is that the clusters formed at 1000°C are ill-defined but gain strength during cooling to 825°C, possibly because oxygen then acts as a strong cluster stabilizer.

6.2.5 Segregation

The microstructure of Zr-15% Nb slowly cooled from 1000°C reveals the existence of a banded structure, which appears to fade as the anneal time at 1000°C is increased. By contrast, the grain boundary precipitates which are also evident become more massive with time. This variation in microstructure indicates that another type of reaction occurs during annealing, i.e. the redistribution of solutes. In discussing these effects, we shall attempt to relate them to the observed mechanical behaviour.

6.2.5.1 Banded structures

Figures 5.40 to 5.42 show that after a short anneal, there is in the material a marked banding of the α-phase. The structure changes from adjacent broad bands to a few narrow bands after four hours of annealing. The bands then broaden again but do not disappear after 64 hours of annealing. This effect is not unlike the segregation of pearlite and ferrite into bands in forged and rolled manganese steels (215,235,244). Their origin has been explained in the following way:

a. Manganese segregates in dendrite interstices during ingot freezing.

b. These high manganese regions subsequently become elongated during hot-working.

c. The low diffusion coefficient of manganese in austenite at the heat treating temperature renders homogenization difficult.

d. The heterogeneous distribution of manganese leads in turn to a banded distribution of carbon as a result of the Mn-C binding energy.

e. Thus, pearlite banding is due to Mn banding, which does not itself show up metallographically.

Similar results have been obtained with P, Ti, Cr and Mo as alloying elements (215,245).

The mechanical properties of Mn-bearing steels are not particularly affected in the band direction. However, transverse tensile strength has been found to be lower in banded steels than in the same steel, once homogenized. A typical such steel, containing 0.21% C and 1.47% Mn shows a transverse strength 10% smaller in the segregated condition. Homogenization of these structures is usually difficult, and for the above steel took six hours at 1250°C. The microprobe investigation carried out on the Zr-15% Nb alloy indicated composition variations not exceeding a few per cent. These results are in agreement with the phase diagram, which shows a freezing range of less than 50°C and a 10% variation in solute concentration for this particular composition. However, the extent of the banding effect is more pronounced than could be expected from such small composition fluctuations. A puzzling observation is that after 4 or 64 hours of annealing, the few bands present after cooling are rich in α precipitates, suggesting that Nb is depleted in these regions. The diffusion distance over which a Nb atom travels on the average is about 4, 25 and 100 μm in 5 minutes, 4 hours and 64 hours, at 1000°C, respectively. These distances are large enough to cause the disappearance of segregated zones after 4 hours, let alone 64 hours, in conflict with the experimental observations.

The mechanical properties in the present tests ought not to be affected by the bands since the latter are parallel to the compression axis. Moreover, there seems to be very little Nb segregation. In view of the above inconsistencies between the observed and predicted microstructures, compression samples were taken from adjacent positions in the same bar, one in the transverse, the other in the longitudinal direction. These were tested at 925°C after a 30-minute preheat, at a strain rate of $1.5 \times 10^{-3} s^{-1}$, without a prior anneal. The temperature was chosen so as to be away from the $\alpha + \beta$ boundary and the annealing time was reduced so that all the α present would dissolve without homogenizing the banded structure.

The stress-strain curves obtained under these conditions are shown in Figure 6.11. We note that the transverse flow stress is consistently lower than the longitudinal flow stress, from which the following remarks can be deduced:

i. The amount of softening is about the same in the two conditions, which shows that the banding of the solute is not responsible for the softening effect. This was already inferred from the mechanical properties of the longitudinal samples. Moreover, the structure homogenization rate did not match the rate of change in the mechanical properties, suggesting that two distinct phenomena are involved.

ii. The flow stress in the transverse direction is over 10% lower than in the longitudinal direction, a result that suggests the presence of significant banding.

iii. The two flow curves are similar and do not merge at high strains, indicating that solute banding leads to a fairly stable microstructure that cannot easily be destroyed by straining. This result was

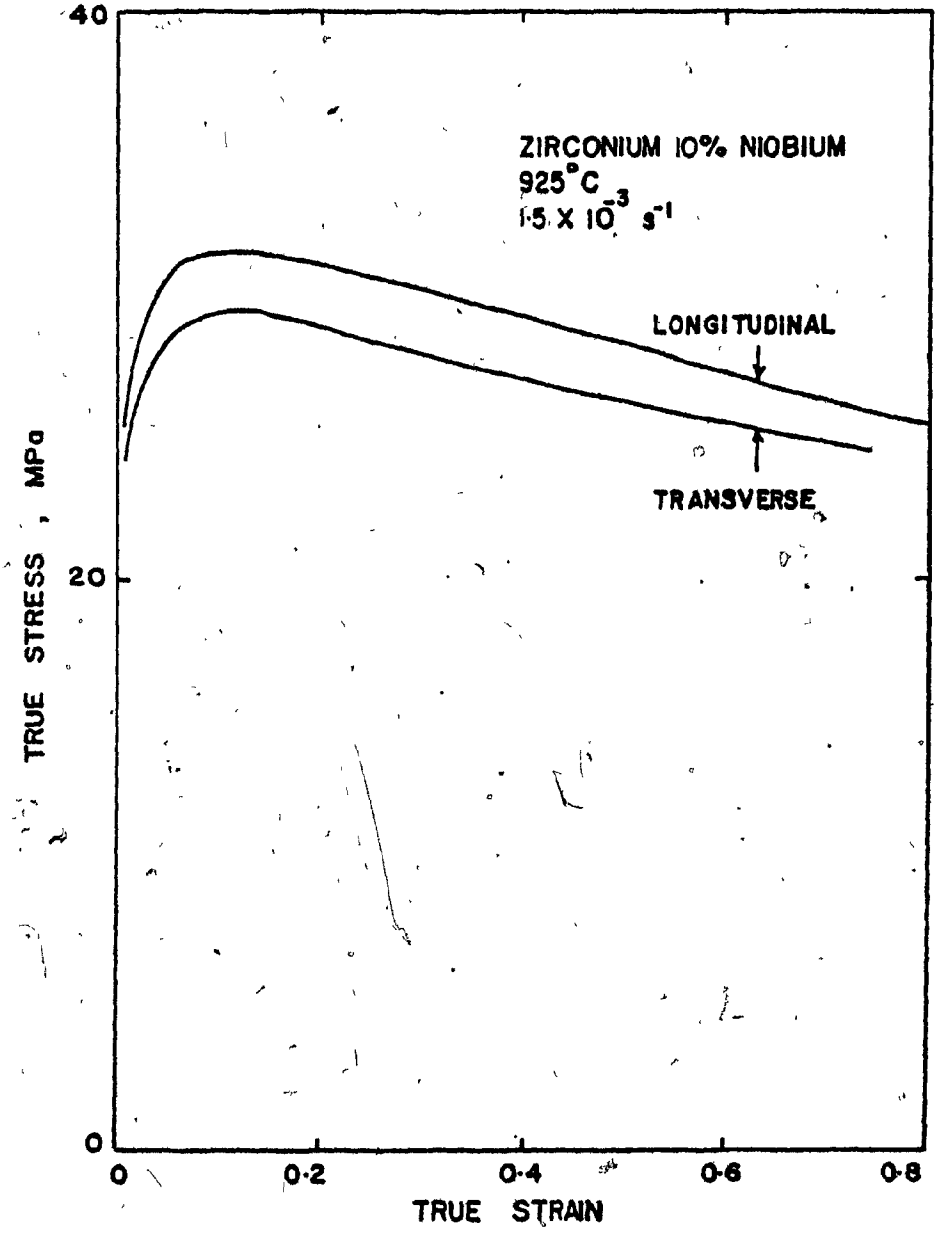

FIGURE 6.11 Flow curves obtained from the Zr-10% Nb alloy at 925°C on samples taken along the longitudinal and the transverse directions of the extruded bars

confirmed by microstructural observations that were made on most deformed samples, which showed that the bands began to expand and to bend as the sample became somewhat barrelled.

From these results, we can therefore conclude that there is some banding of solute in the Zr-Nb alloys. This can affect the transverse flow stress, but does not appear to affect the softening kinetics. The homogenization rate is slower than predicted, and the Nb concentration variations determined by microprobe analysis are smaller than the values required to cause the marked effect that is effectively observed.

6.2.5.2 Grain boundary precipitates

An increase in annealing time causes very marked grain boundary precipitation to occur. This is normally associated with the migration of solute atoms towards the lower energy positions at the boundaries. However, we meet an inconsistency if we assume a high Nb concentration at the grain boundaries because niobium should retard α-plate nucleation, and thus oppose any precipitation effect. The microprobe results indicate a slight decrease in Nb at the grain boundaries, supporting the hypothesis that Nb does not segregate to the boundaries in a massive way.

Another difficulty arises with the width of the precipitate-free zone as a function of time. If some niobium diffusion to or from the boundary occurs, the distance travelled by an atom is on the average much larger than the PFZ. Thus, here again, we meet some inconsistencies regarding diffusion rates.

The only α-stabilizer present in significant quantities in the alloy is oxygen. Oxygen diffusion towards the boundaries would certainly lead to more massive precipitation with annealing time, in qualitative

agreement with the results. The oxygen diffusion coefficient in β-Zr is higher than that of Nb and, as a consequence, the width of the precipitate-free zone is again in disagreement with the one predicted by the diffusion coefficients.

The conclusion that may be drawn at this point is that the simple Nb or O diffusion rates are too fast to account for the observed evolution of either the precipitate morphology at the grain boundaries or the streaks with annealing time. The simplest explanation perhaps lies in the effective diffusion rates being much lower in practice due to the coupled diffusion of solutes.

CHAPTER 7

CONCLUSIONS

The present investigation concerned the high temperature flow behaviour of two alloy families of zirconium. The first series contained .0, 1.9, 4 and 6% molybdenum, and the second contained 2.5, 10, 15 and 20% niobium. Mechanical tests were carried out in the β-phase using constant true strain rate compression, and under a nominally pure argon atmosphere. The imposed strain rates were in the range 1.5×10^{-5} to $1.5 \times 10^{-1} s^{-1}$. The following conclusions can be drawn from the results obtained in this work.

1. The flow curves of zirconium-molybdenum alloys exhibit marked flow softening, which is in strong contrast to the "normal" flow curves obtained with unalloyed zirconium or with zirconium-tin alloys. At low strain rates, the onset of flow softening occurs after little or no work-hardening while at high strain rates it is delayed until a significant amount of work-hardening has taken place. At the beginning of plastic flow, yield drops are frequently observed, but this is not the case for all of the tests.

2. When intermediate unloading tests are carried out on zirconium-molybdenum alloys, the flow stress on reloading increases with delay time t, approximately as $t^{\frac{1}{2}}$. During the delay period, a hard metallic layer is formed beneath an oxide film. This layer consists essentially of oxygen-stabilized α-zirconium as well as the intermetallic $ZrMo_2$. No such hard region is found when tests are conducted in a zircaloy gettered argon atmosphere. In addition, when tests are conducted, whereby samples are strained and allowed to dwell in the furnace and then have

their outer surface removed, no increase in flow stress is observed on reloading. The hardening that arises during the delay interval of normal intermediate unloading tests is therefore attributable to the formation of the oxygen-enriched α-zirconium layer.

3. The processes of formation and rapid growth of the hard α-phase layer that occur in zirconium-molybdenum alloys are much less marked in crystal bar zirconium. This result is attributable to the deleterious effect of molybdenum on the oxidation resistance of the alloys. The presence of molybdenum in the surface scale leads to the formation of oxides of molybdenum that are in the liquid phase at the test temperatures. The presence of a liquid component in the scale is expected to aid in the rapid transport of oxygen through the surface oxide.

4. The occurrence of flow softening in the zirconium-molybdenum alloys can be explained in terms of a model proposed in this work. The model assumes that the developed load originates partly from the α-phase skin and partly from the β-phase core. It is further assumed that the oxygen-saturated α-layer deforms plastically and thereby retains its load bearing capacity to large strains. The thickness of the α-phase layer is assumed to be independent of strain, which is in agreement with direct experimental observations. The model based on these assumptions is shown to be in satisfactory agreement with the observed flow softening behaviour.

5. The high temperature flow curves of the zirconium-molybdenum alloys are temperature, strain rate and concentration dependent. The stress sensitivity of the strain rate decreases from 4.0 to 3.4 as the molybdenum content increases from 0 to 6.0 weight per cent. These observations apply to the stresses at the onset of plastic flow and at a strain of 0.7. In the alloy containing 1.9% molybdenum, at a stress level of 30 MN/m^2, acti-

vation energies of 160 and 105 kJ/mol are associated with the onset of plastic flow and with the deformation of a strain of 0.8, respectively. Similarly, in the alloy containing 6% molybdenum, the values of the activation energies, at a stress of 55 MN/m^2, are 150 and 105 kJ/mol, respectively, for the same regimes. These values are close to the self and solute diffusion activation energies for these alloys; however, it is not possible with the present data to draw any further conclusions as to the nature of the rate controlling obstacles to dislocation glide.

6. The high temperature flow curves obtained on the zirconium-2.5% niobium alloy exhibit a normal work-hardening region, followed by a steady-state regime of flow. This type of behaviour is attributable to the occurrence of dynamic recovery during straining. Flow softening is not observed at all in this alloy under the present testing conditions. The stress sensitivity of the strain rate decreases from about 5.5 at the onset of plastic flow to about 4.5 in the steady-state regime. These values are typical of materials that behave in a likewise manner.

7. Zirconium-niobium alloys containing 10, 15 and 20% niobium, unlike the one containing 2.5% niobium, exhibit significant flow softening, which is most apparent at the lower temperatures in the β-phase. In addition, the stress at 825°C increases with annealing time at 1000°C and reaches a maximum after about 4 hours. With longer annealing treatments at 1000°C, the flow stress decreases once more. The occurrence of anneal hardening cannot be attributed to environmental effects, as it was in the zirconium-molybdenum alloys. Neither can the environmental effects explain the flow softening behaviour. The determination of the texture changes that take place during hot compression show that a (111) fiber texture is developed, which cannot explain the flow softening. Similarly, investigations by

means of X-ray techniques indicate that precipitate coarsening effects are not responsible for the flow softening, indeed no precipitates are present in these alloys. Furthermore, it is shown that dynamic recrystallization does not take place during the plastic flow.

8. It is established that appreciable grain growth occurs in these alloys during annealing at 1000°C, but significant changes in grain size do not take place during deformation of the annealed material. The alloy containing 15% Nb alloy, in the as-received condition, has a fine-grain structure which deforms at low stresses and maintains an equiaxed grain shape during deformation. In the fine grain condition, appreciable grain boundary sliding takes place during hot deformation, and progressively disappears as the grain size increases as a result of annealing. Thus, the grain coarsening that accompanies annealing at 1000°C can be seen to be responsible for a significant part of the anneal hardening phenomenon. Flow softening, on the other hand, is not associated with changes in grain size but may result for a part from grain boundary sliding contributions to the strain when deformation is initiated in the fine-grained material.

9. The miscibility gap in the Zr-Nb binary phase diagram suggests strong like-atom interactions are present in the β-zirconium-niobium alloys. Thermodynamic estimations further indicate that clustering probably takes place in the β-phase. The formation of clusters during annealing at 1000°C could give rise to part of the observed strengthening; conversely, the destruction of clusters during deformation would lead to flow softening. The presence of 1500 ppm oxygen in these alloys has been shown to move the $\alpha + \beta/\beta$ boundary upwards to about 800°C for the alloy containing 15% niobium and is expected to contribute to the stability of clusters.

SUGGESTIONS FOR FURTHER WORK

1. To verify and complete the analysis of the interruption hardening and flow softening behaviour of the Zr-Mo alloys presented here, studies should be carried out regarding the oxidation rate of the Zr-Mo in the β-phase. They should also deal with the structure of the oxide scale and with the rate of growth of both the oxide and the α-layer. The determination of the flow stresses of both the β-phase alone and of the oxygen-saturated α skin would also be useful.

2. The role of the α-layer with regard to the plastic constraint of the β-core should be determined, perhaps from a comparison of the subgrain sizes and dislocation densities produced when the β-phase is tested under an ultra-high vacuum with those produced in the presence of an α-phase outer layer. If a plastic constraint exists, the dislocation density in the latter case should be higher and the subgrain size smaller. It would also be of interest to apply the model proposed here to other systems in which oxygen (or nitrogen) promotes the formation of either a harder, or a softer, ductile phase at elevated temperatures.

3. A much more complete study of the effect of molybdenum addition on the high temperature flow curves of zirconium alloys should be carried out. Such an investigation would require that the dynamic oxygen pressure be reduced to less than 10^{-4} torr, and a temperature capability of 1100°C or better.

4. The unusual behaviour of the Zr-10,15 and 20% Nb alloys involved both anneal hardening and flow softening effects. These were attributed to a combination of grain growth and solute clustering effects,

although the explanations advanced were considered more tentative than in the case of Zr-Mo alloys. Clearly, more work is required in this field, and several different techniques could prove to be valuable. The occurrence of clustering can perhaps best be confirmed by detailed internal friction studies at high temperatures. These should lead to a reasonably good estimate of the kinetics of the process, which could then be compared with the kinetics of hardening and of grain growth. Supporting evidence for the softening effect could also be obtained from an electron micrographic study of the evolution of the dislocation structure, and particularly of the subgrain size, during straining.

5. The clustering and declustering which was suggested as being involved in anneal hardening and flow softening, respectively, is intimately associated with the thermodynamic properties of the Zr-Nb-O system. Much more information is required regarding the various thermodynamic functions of this system and evidence must be sought for the presence or absence of like-like clusters.

6. In the zirconium-2.5% niobium alloy, a wider range of temperatures should be covered in order to permit the accurate determination of the activation parameters and so as to lead to a more reliable assessment of the rate controlling mechanism and of the role of Nb as a solute strengthener.

STATEMENT OF ORIGINALITY AND CONTRIBUTION TO KNOWLEDGE

1. The flow curves for crystal bar zirconium and for zirconium-molybdenum alloys were determined at high temperatures, in the β-phase, under a nominally high purity argon atmosphere. This was carried out by means of constant true strain rate hot compression, leading to the determination over a range of strain rates of both yield and high strain flow stresses. Such measurements had not previously been made in this alloy system. The flow curves of these alloys exhibited two types of unusual behaviour. The first concerns the occurrence of flow softening, which persists up to the largest strain applied in this work (i.e. around 0.8). The onset of flow softening was observed to take place, after a significant amount of work-hardening at high strain rates; whereas, little or no work-hardening was encountered at intermediate and low strain rates. In the latter case, the onset of plastic deformation was usually associated with a yield drop. The characteristics of the type of flow softening observed in these alloys have not been reported previously. By contrast, crystal bar zirconium did not exhibit such flow softening and displayed, except at the very lowest strain rates, a marked work-hardening region followed by a steady-state regime of flow.

2. The second unusual characteristic of the flow behaviour was the interruption hardening observed when a compression specimen is unloaded during a test and then reloaded after a delay interval. These interrupted tests showed that the stress upon reloading increases with delay time t approximately as $t^{\frac{1}{2}}$. This strengthening was attributable to the presence of an oxygen-stabilized α-layer below the surface oxide film, the composition of which was determined by X-ray analysis. Tests

carried out under a higher purity argon than the one normally used led to flow curves in which interruption hardening was less marked. Furthermore, experiments involving the removal of the hard α-layer confirmed that the strengthening imparted to the alloy during the interruption delay was associated with the presence of this oxygen-stabilized α-layer. The formation of the layer was attributed to the deleterious effect of molybdenum on the oxidation resistance of the alloys that arises from the presence within the scale of liquid molybdenum oxides. This effect is absent in unalloyed zirconium, where interruption hardening was observed to be much less marked.

3. The occurrence of flow softening in zirconium-molybdenum alloys was also attributed to the presence of the oxygen-stabilized α-layer. Whereas the α-phase layer increases in volume during annealing, it decreases in volume during deformation. This results from a change in the balance between the rate of oxygen pick-up at the surface, and the rate of oxygen diffusion through the oxide film and metallic phases that is brought about by concurrent deformation. This picture of the build-up of a hard outer shell during annealing which tends to be destroyed during deformation, the former leading to interruption hardening and the latter to flow softening, has not been reported previously.

4. A simple model was developed to explain the interruption hardening and flow softening behaviour of the zirconium-molybdenum alloys in a quantitative manner. This model assumes that the developed load is shared between the hard layer of α-phase and the soft β-phase core. In the model, the α-phase is assumed to deform plastically, thereby retaining some load bearing capacity to large strains. The predictions of this model agree in a satisfactory manner with the experimental observations.

This result is in marked contrast to the lack of agreement found when similar models have been used to attempt to explain the deformation behaviour of oxidized or plated metals at low temperatures. The ability of the model to rationalize the observed characteristics of the zirconium-molybdenum alloys constitutes a step forward in the understanding of the effect of the environment on the mechanical properties of these materials.

5. By means of the tests described, the stress sensitivity of the strain rate of the zirconium-molybdenum alloys was found to decrease from 4.0 to 3.4 as the molybdenum concentration was increased from 0 to 6% weight. Experimental activation energies of 160 and 105 kJ/mol were determined at a stress level of 30 MN/m^2 for the onset of plastic flow and in the steady-state regime for the zirconium-1.9% molybdenum alloy. Similarly, values of 150 and 105 kJ/mol were found, at a stress level of 55 MN/m^2, for the onset of plastic flow and steady-state regime for the zirconium-6% molybdenum alloy. At a fixed temperature and strain rate, the flow stresses of the alloys increased with molybdenum concentration c approximately as $c^{0.7}$. However, the molybdenum atoms cannot be considered to act as individual obstacles to dislocation glide, but rather lead to strengthening indirectly, through their influence on a rate-controlling mechanism which was not identified.

6. By means of constant strain rate hot compression, the initial and steady state flow stresses of zirconium-2.5% niobium alloy were also determined in the β-phase field. The stress-strain curves obtained exhibit a work-hardening region, followed by a steady-state regime of flow characteristic of metals that recover dynamically. The stress sensitivity of the strain rate decreased from about 5.5 for yielding to about 4.5 for steady state flow. No flow softening was observed in this material.

7. The flow curves of zirconium alloys containing 10, 15 and 20% niobium were also characterized; in the β-phase field. These three alloys always exhibit both anneal hardening and flow softening, which distinguishes them from the 2.5% niobium alloy, and from other "normal" materials. This effect appears most marked at the lower experimental temperatures. It was shown that oxidation-induced hardening and softening, similar to that observed in the zirconium-molybdenum alloys, is unlikely to play a role in these alloys (at least below 900°C). Measurements of preferred orientation revealed that a (111) fiber texture is produced by straining. This type of texture development during deformation is not capable of inducing a flow stress decrease.

8. The mechanical properties at 825°C, as well as at the microstructures obtained after cooling to room temperature, were observed to be dependent upon the time of holding at 1000°C. This occurred in a manner that could not be attributed to grain size variations alone (see below). The effect of the duration of the 1000°C anneal treatment on the microstructure is in agreement with results previously reported in zirconium-niobium and titanium-chromium alloys, which were attributed to clustering and short range order, respectively. The results are also consistent with the modifications to the zirconium-niobium binary phase diagram called for by the presence of about 1500 ppm of oxygen. A significant proportion of the anneal hardening may be associated with solute clustering, while flow softening may be attributable to solute "de-clustering". This aspect of the current investigation requires corroboration by means of further work, both on the flow behaviour, as well as on the Zr-Nb-O phase diagram.

9. It was shown that the annealing of the soft, fine-grained as-received zirconium-15% niobium alloy led to a considerable increase

in grain size. In all conditions of the alloy the grain size did not change appreciably during deformation, although the grains did undergo shape changes. These were generally somewhat less than that expected in view of the imposed strain. By contrast, the fine grains of the material in the as-received condition remained equiaxed during straining. From these observations, it was inferred that the grain coarsening during annealing is responsible for a sizeable proportion of the hardening produced by annealing. The proposed roles of grain growth and cluster formation in anneal hardening, and of cluster destruction during flow softening are original to this author.

LIST OF REFERENCES

1. J.J. Jonas, C.M. Sellars and W.G. McG. Tegart: Metall. Reviews, 14, (1969), 1.
2. O.D. Sherby and P.M. Burke: Progr. Mater. Sci., 13, (1967), 325.
3. D. McLean: Rep. Progr. Physics, 29, (1966), 1.
4. M.J. Luton: PhD Thesis, McGill University, Montreal, (1971).
5. R. Lagneborg: Int. Metall. Reviews, 17, (1972), 130.
6. H.J. McQueen and J.J. Jonas: Plastic Deformation of Metals, R. Arsenault, editor, Academic Press, New York, (1975), p.393.
7. D. Hardwick and W.G. McG. Tegart: J. Inst. Metals, 90, (1961), 17.
8. J.E. Dorn: Creep and Recovery, ASM, Cleveland, (1957), p.255.
9. H. Laks, C.D. Wiseman, O.D. Sherby and J.E. Dorn: J. Appl. Mech., ASME, 24, (1957), 207.
10. J.L. Uvira: PhD Thesis, McGill University, Montreal, (1967).
11. J.L. Uvira and J.J. Jonas: Trans. Met. Soc. AIME, 242, (1968), 1619.
12. J.P.A. Immarigeon: M. Eng. Thesis, McGill University, Montreal, (1970).
13. S. Karashima, H. Oikawa and T. Watanabe: Trans. Met. Soc. AIME, 242, (1968), 1703.
14. D. McLean and K.F. Hale: Structural Processes in Creep, Iron Steel Inst., London, (1961), p.19.
15. J.P.A. Immarigeon and J.J. Jonas: Acta Met., 19, (1971), 1053.
16. H. Bühler and H.W. Wagener: Bänder, Blecher, Rohre, 7, (1966), 648.
17. M.J. Luton and J.J. Jonas: Can. Met. Quart., 11, (1972), 79.
18. G. Gagnon; PhD Thesis, McGill University, Montreal, (1968).
19. G.P. Lewis and W.J. McG. Tegart: J. Inst. Metals, 92, (1963-64), 249.
20. D. Hardwick and W.J. McG. Tegart: Mém. Sci. Rev. Mét., 58, (1962), 869.
21. H. Ormerod and W.J. McG. Tegart: J. Inst. Metals, 92, (1963-64), 297.

22. M.J. Luton and C.M. Sellars: Acta. Met., 17, (1969), 1033.

23. J.P. Sah, G.J. Richardson and C.M. Sellars: J. Australian Inst. Metals, 14, (1969), 292.

24. E. Shapiro and G.E. Dieter: Met. Trans., 2, (1971), 1386.

25. E. Shapiro and G.E. Dieter: Met. Trans., 1, (1970), 1711.

26. H.P. Stüwe: Deformation under Hot Working Conditions, Iron Steel Inst., (1968), London, p.1.

27. F. Garofalo: Fundamentals of Creep and Creep Rupture in Metals; McMillan, New York, (1965).

28. C. Rossard and P. Blain: Mem. Sci. Rev. Mét., 56, (1959), 286.

29. C. Rossard: D. Sc. Thesis, Paris, (1960).

30. R. Tamhankar, J. Plateau and C. Crussard: Rev. Mét., 55, (1958), 383.

31. Ye. N. Sokolkov, Y.P. Surkov and D.I. Gurfel: Physics of Metals and Metallog., 20, (1965), 83.

32. F.E. White and C. Rossard: Deformation under Hot Working Conditions, Iron Steel Inst., London, (1968), p.14.

33. A. Nicholson: Deformation under Hot Working Conditions, Iron Steel Inst., London, (1968), p.42.

34. H.P. Stüwe: Acta. Met., 13, (1965), 1337.

35. H.J. McQueen, W.A. Wong and J.J. Jonas: Can. J. Phys., 45, (1967), 1225.

36. H.J. McQueen and J.E. Hockett: Met. Trans., 1, (1970), 2997.

37. A.K. Mukherjee, J.E. Bird and J.E. Dorn: Trans. ASM, 62, (1969), 155.

38. J.J. Jonas, H.J. McQueen and W.A. Wong: Deformation under Hot Working Conditions, Iron Steel Inst., London, (1968), 49.

39. B. Modeer and R. Lagneborg: JernKontorets Ann., 155, (1971), 363.

40. J.E. Dorn: Creep and Fracture of Metals at High Temperatures, N.P.L. Symposium, H.M.S.O., London, (1956), p.89.

41. O.D. Sherby: Acta.Met., 10, (1962), 135.

42. C.R. Barrett, A.J. Ardell and O.D. Sherby: Trans. Met. Soc. AIME, 230, (1964), 200.

43. C.R. Barrett and O.D. Sherby: Trans. Met. Soc. AIME, 233, (1965), 2069.

44. D.H. Sastry, M.J. Luton and J.J. Jonas: Phil. Mag., 30, (1974), 115.

45. R.M. Bonesteel and O.D. Sherby: Acta. Met., 14, (1966), 385.

46. R. Jackson, H.J. Carvalhinhos and B.B. Argent: J. Iron Steel. Inst., 96, (1968), 210.

47. J.P.A. Immarigeon and J.J. Jonas: Acta. Met., 22, (1974), 235.

48. J. Weertman: J. Appl. Phys., 28, (1957), 362.

49. J. Weertman: J. Appl. Phys., 26, (1955), 1213.

50. H. Conrad: J. Metals, 16, (1964), 582.

51. J. Weertman: Trans. Met. Soc. AIME, 61, (1968), 680.

52. J.P. Poirier : Plasticité à haute température des solides cristallins, Editions Eyrolles, Paris, (1976), pp.51-54.

53. N.F. Mott: Creep and Fracture of Metals at High Temperatures, N.P.L. Symposium, H.M.S.O., London, (1956), p.21.

54. P. Hirsch and D. Warrington: Phil. Mag., 6, (1961), 735.

55. J. Friedel: Les Dislocations, Gauthier Villars, Paris, (1956), p.72.

56. L. Raymond and J. Dorn: Trans. Met. Soc. AIME, 230, (1964), 560.

57. J.E. Dorn: Energetics in Metallurgical Phenomena, Vol.1, Gordon and Breach, New York, (1965), p.241.

58. C.R. Barrett and W.D. Nix: Acta. Met., 13, (1965), 1247.

59. W.D. Nix: Acta. Met., 15, (1967), 1079.

60. J.J. Holmes: Acta. Met., 15, (1967), 570.

61. W.J. Duffin and F.A. Nichols: Acta. Met., 18, (1970), 1121.

62. A.H. Cottrell and V. Ayetkin: J. Inst. Metals, 77, (1950), 389.

63. N.F. Mott: Phil. Mag., 44, (1953), 742.

64. J.H. Gittus: Phil. Mag., 23, (1971), 1281.

65. R. Lagneborg: Metal Sci. J., 3, (1969), 161.

66. R. Lagneborg and B.H. Forsen: Acta. Met., 21, (1973), 781.

67. R.A. Petkovic-Luton: M. Eng. Thesis, McGill University, Montreal, (1971).

68. C. Rossard: Métaux, 35, (1960), 140 and 153.

69. C. Rossard: Third Int. Conf. on the Strength of Metals and Alloys, Vol. II, Iron and Steel Inst., London, (1973), p.175.

70. R.A. Petkovic-Luton: PhD Thesis, McGill University, Montreal, (1975).

71. B.J. Sunter and N.M. Burman: J. Australian Inst. Metals, 17, (1972), 91.

72. F.N. Rhines and P.J. Wray: ASM Trans. Quart., 54, (1961), 117.

73. S. Fulop and H.J. McQueen: Superalloys: Processing, Metals and Ceramics Information Center, Colombus, Ohio.

74. C. Rossard: Métaux Corros. Ind., 35, (1960), p.102, 140 and 190.

75. B.A. Wilcox and A.H. Clauer: Trans. Met. Soc. AIME, 215, (1959), 838.

76. B.A. Wilcox and A.H. Clauer: Trans. Met. Soc. AIME, 239, (1967), 1791.

77. C.L. Meyers, J.C. Shyne and O.D. Sherby: J. Australian Inst. Metals, 8, (1963), 171.

78. G.S. Ansell and F.V. Lenel: Trans. Met. Soc. AIME, 221, (1961), 452.

79. A.G. Evans and R.D. Rawlings: Phys. Stat. Solidi, 34, (1969), 9.

80. J.C.M. Li: Dislocation Dynamics, Rosenfield, Hahn, Bement and Jaffee, Editors, McGraw-Hill, New York, (1968), p.701.

81. G.B. Gibbs: Mater. Sci. Eng., 4, (1969), 313.

82. T. Surek, M.J. Luton and J.J. Jonas: Phys. Stat. Solidi, 57, (1973), 647.

83. T. Surek, M.J. Luton and J.J. Jonas: Phil. Mag., 27, (1973), 425.

84. T. Surek, L.G. Kuon, M.J. Luton and J.J. Jonas: J.E. Dorn Symposium on Rate Processes in Plastic Deformation, ASM, Cleveland, (1972).

85. U.F. Kocks, A.S. Argon and M.F. Ashby: Thermodynamics and Kinetics of Slip, Progress in Materials Science Series Vol.19, Pergamon Press, New York, (1975).

86. ibid., p.121-125.

87. G. Schoek: Phys. Stat. Solidi, 8, (1965), 499.

88. W.R. Tyson: Can. Met. Quart., 6, (1967), 301.

89. K.C. Cadien: M. Eng. Thesis, McGill University, Montreal, (1976).

90. M.A.W. Lowden and W.B. Hutchinson: Met. Trans., 6A, (1975), 441.

91. M.J. Luton and R. Holt: unpublished work; McGill University, (1974).

92. J.E. Hockett: Trans Met. Soc. AIME, 239, (1967), 969.

93. J.L. Robbins, O.G. Shepard and O.D. Sherby: J. Iron Steel Inst., 202, (1964), 804.

94. H. Paqueton and A. Pineau: J. Iron Steel Inst., 9, (1971), 991.

95. E.A. Chojnowski and W.J. McG. Tegart: Met. Sci. J., 2, (1968), 14.

96. A.S. Rizkalla: private communication.

97. D. Lee and W.A. Backofen: Trans. Met. Soc. AIME, 239, (1967), 1034.

98. M. Suery and B. Baudelet: J. Materials Sci., 8, (1973), 369.

99. W. Ostwald: Z. für Phys. Chem., 37, (1900), 495.

100. C. Wagner: Z. für Electrochem., 65, (1961), 581.

101. I.M. Lifshitz and V.V. Slezov: Soviet Physics J.E.T.P., 35, (1959), 331.

102. A.J. Ardell and R.B. Nicholson: Acta. Met., 14, (1966), 1295.

103. A.J. Ardell and R.B. Nicholson: J. Phys. Chem. Solids, 27, (1966), 1793.

104. G.R. Speich and R.A. Oriani: Trans. Met. Soc. AIME, 233 (1965), 625.

105. H.A. Moreen: Metallography, 1, (1968), 349.

106. A. LeBon, J. Rofes-Vernis and C. Rossard: Mém. Sci. Rev. Mét., 70, (1973), 577.

107. R.A. Petkovic, M.J. Luton and J.J. Jonas: to be published.

108. J. Schneibel: Diploma Thesis, Erlangen, (1974).

109. R. Lagneborg: Metal Sci. J., 3, (1969), 18.

110. K.E. Amin and J.E. Dorn: Acta. Met., 17, (1969), 1429.

111. J.P. Dennison and R. Stevens: Scripta Met., 5, (1970), 1063.

112. K.R. Williams and J.R. McLauchlin: J. Mat. Sci., 5, (1970), 1063.

113. B. Bergman and R. Lagneborg: Jernkontorets Ann., 155, (1971), 368.

114. E.E. Underwood: J. of Metals, 14, (1962), 914.

115. R.H. Johnson: Metall. Reviews, 4, (1970), 115.

116. H.W. Hayden, R.C. Gibson, H.F. Merrick and J.H. Brophy: Trans. Quart. ASM, 60, (1967), 3.

117. A. Ball and M.M. Hutchinson: Metal Sci. J., 3, (1969), 1.

118. H.E. Evans: Scripta Met., 2, (1968), 157.

119. T. Chandra: PhD Thesis, University of Waterloo, Waterloo, (1975).

120. D.H. Avery and W.A. Backofen: Trans. Quart. ASM, 58, (1965), 556.

121. R.B. Bones: Nature, 207, (1965), 70.

122. T.H. Alden: Trans. Quart. ASM, 61, (1968), 559.

123. C.E. Pearson: J. Inst. Metals, 54, (1934), 111.

124. H.E. Cline and T.H. Alden: Trans. Met. Soc. AIME, 239, (1967), 710.

125. S.W. Zehr and W.A. Backofen: Trans. Quart. ASM, 71, (1968), 300.

126. T.H. Alden: Acta. Met., 15, (1967), 469.

127. D.L. Holt and W.A. Backofen: Trans. Quart. ASM, 59, (1969), 755.

128. D. Lee: Acta. Met., 17, (1969), 1057.

129. T.H. Alden: J. Australian Inst. Metals, 14, (1969), 207.

130. M.F. Ashby and R.A. Verrall: Acta Met., 21, (1973), 149.

131. R.C. Gifkins: J. Inst. Metals, 95, (1967), 373.

132. P. Chaudhari: Acta. Met., 15, (1967), 1777.

133. A.K. Mukherjee: Mater. Sci. Eng., 8, (1971), 83.

134. J. Belle and M.W. Mallett: J. Electrochem. Soc., 101, (1954), 339.

135. R.G. Charles, S. Barnartt and E.A. Gulbransen: Trans. AIME, 212, (1958), 101.

136. E.A. Gulbransen and K.F. Andrew: J. of Metals, 9, (1957), 394.

137. H.A. Porte, J.G. Schnizlein, R.C. Vogel and D.F. Fischer: J. Electrochem. Soc., 107, (1960), 506.

138. K. Osthagen and P, Kofstad: J. Electrochem. Soc., 109, (1962), 204.

139. K.A. Sense: J. Electrochem. Soc., 109, (1962), 377.

140. W.W. Smeltzer, R.R. Haering and J.S. Kirkaldy: Acta. Met., 9, (1961), 880.

141. R.J. Hussey and W.W. Smeltzer: J. Electrochem. Soc., 111, (1964), 565.

142. K.H. Akram and W.W. Smeltzer: Can. Met. Quart., 1, (1962), 41.

143. G.R. Wallwork, W.W. Smeltzer and C.J. Rosa: Acta. Met., 12, (1964), 409.

144. E.A. Gulbransen and K.F. Andrew: Trans. Met. Soc. AIME, 185, (1949), 515.

145. M. Deschamps, J. Debuigne and P. Lehr: Mém. Sci. Rev. Mét., 68, (1971), 267.

146. M. Deschamps and P. Lehr: Compt. Rend. Acad. Sci., 270C, (1970), 169.

147. M. Deschamps and P. Lehr: ibid., p.1933.

148. J. Niederlich and J. Paidassi: Compt. Rend, Acad. Sci., 267C, (1968), 1429.

149. G. Hörz and M. Hammel: J. Nucl. Mat., 55, (1975), 284.

150. D. Cubiciotti: J. Am. Chem. Soc., 72, (1950), 4138.

151. R.J. Hussey and W.W. Smeltzer: J. Electrochem. Soc., 111, (1964), 1221.

152. D.L. Douglass: The Metallurgy of Zirconium, Atomic Energy Review, Supplement 1, Vienna, (1971), p.289.

153. D.E. Thomas: Metallurgy of Zirconium, Lustman and Kerge, Editors, McGraw-Hill, New York, (1955), p.635.

154. J.P. Pemsler: J. Electrochem. Soc., 112, (1965), 477.

155. C.J. Rosa and W.W. Smeltzer: Acta. Met., 13, (1965), 55.

156. C.J. Rosa: J. Less Common Met., 15, (1968), 35.

157. R.E. Westerman: J. Electrochem. Soc., 111, (1964), 140.

158. D.H. Bradhurst, J.E. Draley and C. Van Drunen: J. Electrochem. Soc., 112, (1965), 1171.

159. J. Levitan, J.E. Draley and C.J. Van Drunen: J. Electrochem. Soc., 114, (1967), 1086.

160. O. Kubachewski and B.E. Hopkins: Oxidation of Metals and Alloys, Butterworths Scientific Publications, London, (1953).

161. B. De Gelas, G. Beranger and P. Lacombe: J. Nucl. Mat., 29, (1969), 1.

162. O. Zmeskal and M.L. Brey: Trans. ASM, 53, (1961), 415.

163. I.R. Kramer and L.J. Demer: Progr. Met. Physics, 9, (1961), 131.

164. E.S. Machlin: Strengthening Mechanisms in Solids, ASM, (1960), 375.

165. R.H. Cook and R.P. Skelton: Int. Met. Reviews, 19, (1974), 199.

166. P. Shahinian and M.R. Achter: Trans. Met. Soc. AIME, 215, (1959), 37.

167. P. Shahinian and M.R. Achter: High Temperature Materials, Hehemann and Ault, Editors, John Wiley, New York, (1959), p.448.

168. D.A. Douglas: ibid., p.429.

169. Q.C. Shepard and W. Schalliol: Amer. Soc. Testing Mat. Spec. Tech. Publ., 108, (1951), 34.

170. P. Shahinian: Trans. ASM, 49, (1957), 862.

171. P. Shahinian: Trans. Amer. Soc. Mech. Eng.,D, 87, (1965), 344.

172. R. Widmer and N.J. Grant: Trans. Amer. Soc. Mech. Eng., D, 82, (1960), 882.

173. I. Lemay, K.J. Truss and P.S. Sethi: Trans. Amer. Soc. Mech. Eng., D, 91, (1969), 575.

174. K.U. Snowden: Acta. Met., 12, (1964), 295.

175. G.J. Danek, H.H. Smith and M.R. Achter: Proc. Amer. Soc. Test. Mat., 61, (1961), 775.

176. B.R. Livesay and E.A. Starke: Acta. Met., 21, (1973), 247.

177. F.D. Rosi: Acta. Met., 5, (1957), 348.

178. R.M. Johnson and R.J. Block: Acta. Met., 16, (1968), 831.

179. C.C. Law and W.A. Jemian: Acta. Met., 15, (1967), 1125.

180. R. Roscoe: Nature, 133, (1934), 912.

181. A.H. Cottrell and D.F. Gibbons: Nature, 162, (1948), 488.

182. D.R. Brame and T. Evans: Phil. Mag., 31, (1958), 971.

183. C. Barrett: Acta. Met., 1, (1953), 2.

184. J. Pridans and J.C. Bilello: Acta. Met., 20, (1972), 1339.

185. M.A. Adams: Acta. Met., 6, (1958), 327.

186. C. Wagner: Z. Electrochem., 63, (1959), 772.

187. F. Rhines: Trans. Met. Soc. AIME, 137, (1940), 246.

188. L.J. Bonis and N.J. Grant: Trans. Met. Soc. AIME, 224, (1962), 308.

189. G. Böhm and M. Kahlweit: Acta. Met., 12, (1964), 641.

190. D.M. Williams and G.C. Smith: Oxide Dispersion Strengthening, Ansell, Cooper and Lenel, ed., Gordon and Breach, New York, (1968), p.509.

191. M.F. Ashby and J.C. Smith: J. Inst. Metals, 91, (1963), 182.

192. D.J. Iden and L. Himmel: Acta. Met., 17, (1969), 1483.

193. J.L. Meijering: Z. Electrochem., 63, (1959), 824.

194. R.A. Rapp: Acta. Met., 9, (1959), 824.

195. R. Ebeling and M.F. Ashby: Phil. Mag., 13, (1966), 805.

196. D.J. Rowcliffe, R.M. Bonesteel and T.E. Tiez: Metallurgical Society Conference: "Oxide Dispersion Strengthening", Vol.47, Gordon and Breach, (1966), p.741.

197. H. Conrad: Mechanical Behaviour of Materials at Elevated Temperatures, J.E. Dorn, Editor, McGraw-Hill, New York, (1961), p.149.

198. H.J. McQueen: Materials Technology - An Inter-American Approach, ASME, New York, (1968), p.379.

199. H.J. McQueen and J.J. Jonas: Metal Forming: Interrelation Between Theory and Practice, A.L. Hoffmanner, Editor, Plenum Publ., New York, (1970), p.393.

200. P. Moore: Deformation under Hot Working Conditions, Special Rep. No.108, Iron and Steel Inst., London, (1968), p.103.

201. M.J. Luton, J.P. Immarigeon and J.J. Jonas: J. Phys. E: Sci. Instr., 7, (1974), 862.

202. J.P.A. Immarigeon: PhD Thesis, McGill University, Montreal, (1974).

203. J.F. Adler and V.A. Phillips: J. Inst. Metals, 83, (1954-55), 80.

204. R.L. Fleischer: Strengthening of Metals, D. Peckner, Editor, Reinhold, Publishing Co., New York, (1964), p.93.

205. U.F. Kocks: Seminar on "Solute Interactions in Metals", McGill University, (1974).

206. R.F. Domalaga, D.W. Levinson and D.J. McPherson: Trans. Met. Soc. AIME, 209, (1957), 1191.

207. B.A. Cheadle and S.A. Aldridge: J. Nucl. Mat., 47, (1973), 255.

208. P. Van Effenterre: D. Sc. Thesis, Université Paris Sud, (1972).

209. D.J. Abson and J.J. Jonas: J. Nucl. Mat., 42, (1972), 73.

210. B. Holmberg and T. Dagerhamn: Acta. Chem. Scand., 15, (1961), 919.

211. R.F. Hehemann: Can. Met. Quart., 11, (1972), 201.

212. I.L. Dillamore and W.T. Roberts: Met. Reviews, 10, (1965), 271.

213. C.E. Lundin and R.H. Cox: USAEC Report No.1/AT (11-1)-752, (1960).

214. H. Richter, P. Wincierz, K. Anderko and U. Zwicker: J. Less Common Metals, 4, (1962), 252.

215. H. Schwartzbart: Trans. ASM, 44, (1952), 845.

216. G.V. Samsonov: The Oxide Handbook, Plenum Publ., New York, (1973).

217. S.S. Brenner: J. Electrochem. Soc., 102, (1955), 16.

218. G.W. Rathenau and J.L. Meijering: Metallurgia, Manchr., 42, (1950), 167.

219. C. Ilschner-Gensch: J. Electrochem. Soc., 105, (1958), 635.

220. J. Friedel: Dislocations, Addison-Wesley Publ., (1964), pp.260-69.

221. G.B. Gibbs: Mém. Sci. Rev. Mét., 62, (1965), 841.

222. D. Lazarus: Diffusion in Body-Centered Cubic Metals, ASM, Cleveland, (1965), p.155.

223. S.J. Rothman and N.L. Peterson: Diffusion in Body-Centered Cubic Metals, ASM, Cleveland, (1965), p.183.

224. M.G. Naik and R.P. Ragarwala: Acta. Met., 15, (1967), 1521.

225. T.S. Lundy, J.I. Federer, R.E. Pawel and F.R. Winslow: Diffusion in Body-Centered Cubic Metals, ASM, Cleveland, (1965), p.35.

226. G.V. Kidson: Diffusion in Body-Centered Cubic Metals, ASM, Cleveland, (1965), p.329.

227. B.D. Sharma and G.P. Tiwari: Acta. Met., 15, (1967), 1552.

228. L.I. Ivanov and Y.A. Yanushkevich: Fiz. Metallov i Metalloved., 17, (1964), 112.

229. A.J. Ardell: PhD Thesis, Stanford University, (1964).

230. G.T. Higgins and E.E. Banks: Brit. J. Appl. Phys., 17, (1966), 283.

231. C.E.L. Hunt and P. Niessen: J. Nucl. Mat., 38, (1971), 17.

232. A.S. Rizkalla: M. Eng. Thesis, McGill University, Montreal, (1976).

233. M.K. McQuillan: J. Inst. Metals, 82, (1953-54), 433.

234. H. Margolin, P. Farrar and W. Kirk: Report to the Bureau of Aeronautics on Contract No.54-655-C, May 1955, (New York University PB 119528).

235. M.C. Flemings, D.R. Poirier, R.V. Barone and H.D. Brody: J. Iron Steel Inst., 208, (1970), 371.

236. W.T. Thompson and A.D. Pelton: Progr. in Solid State Chem., 10, (1975).

237. P.S. Rudman and B.L. Averbach: Acta. Met., 2, (1954), 576.

238. J.W. Christian: The Theory of Transformations in Metals and Alloys, Pergamon Press, London, (1965).

239. W. De Sorbo, H.N. Treaftis and D. Turnbull: Acta. Met., 6, (1958), 401.

240. G.B. Gibbs, D. Graham and D.H. Tomlin: Phil. Mag., 8, (1963), 1269.

241. D. Mosher, C. Dollins and C. Wert: Acta. Met., 18, (1970), 797.

242. P.M. Bunn, D.G. Cummings and H.W. Leavenworth: J. Appl. Physics, 33, (1962), 3009.

243. J.J. Kearns and J.N. Chirigos: Westinghouse Report WAPD-TM-306, (1962).

244. G.R. Purdy and J.S. Kirkaldy: Met. Trans., 2, (1971), 371.

245. P.H.S. Cox, B.G. Reisdorf and G.E. Pelissier: Trans. Met. Soc. AIME, 239, (1967), 1809.

246. O. Lindquist and F. Wengelin: Arkiv för Kemi, 28, (1967), 179.

APPENDIX 1

DETERMINATION OF THE LATTICE PARAMETERS

During the past ten years, several methods have been devised to accurately determine the lattice parameters of known substances. These techniques are also capable of identifying the crystal structure of unknown substances. Although these schemes are laborious, the use of computer programs can lead to efficient lattice parameter, or crystal structure, determinations.

The procedure used in the present work was that of Lindquist and Wengelin (246). This method begins with fundamental property of reciprocal lattice, which is that a vector r^*_{hkl} in the reciprocal lattice, joining the origin to the point of coordinates hkl is perpendicular to a plane in the direct lattice whose indices are (hkl). The length of the reciprocal lattice vector r^*_{hkl} is equal to $1/d_{hkl}$ where d_{hkl} is the spacing of the (hkl) planes in direct space. The vector r^*_{hkl} can be expressed in tests of the basic lattice vectors a*, b*, c* by:

$$r^*_{hkl} = ha^* + kb^* + lc^* \qquad (A1.1)$$

It follows that the dot product $r^*_{hkl} \cdot r^*_{hkl}$ gives:

$$(r^*_{hkl})^2 = \frac{1}{d^2} = h^2(a^*.a^*) + k^2(b^*.b^*) + l^2(c^*.c^*)$$

$$+ 2hk(a^*.b^*) + 2kl(b^*.c^*) + 2lk(c^*.a^*) \qquad (A1.2)$$

In the most general case of a triclinic lattice characterized by the lattice vectors a, b, c and the angles α, β and γ, these dot products can be written:

$$a^*.a^* = (b^2c^2 \sin^2\alpha)/v^2 \qquad \text{(A1.3)}$$

$$b^*.b^* = (a^2c^2 \sin^2\beta)/v^2 \qquad \text{(A1.4)}$$

$$c^*.c^* = (a^2b^2 \sin^2\gamma)/v^2 \qquad \text{(A1.5)}$$

$$a^*.b^* = abc^2(\cos\alpha \cos\beta - \cos\gamma)/v^2 \qquad \text{(A1.6)}$$

$$b^*.c^* = a^2bc(\cos\beta \cos\gamma - \cos\alpha)/v^2 \qquad \text{(A1.7)}$$

$$c^*.a^* = ab^2c(\cos\alpha \cos\gamma - \cos\beta)/v^2 \qquad \text{(A1.8)}$$

where v^2 is the volume of the unit cell.

Recalling that Bragg's law can be expressed as:

$$\sin^2\theta = \frac{\lambda^2}{4} \cdot \frac{1}{d^2} \qquad \text{(A1.9)}$$

and, replacing $\frac{1}{d^2}$ by the expression in Equation A1.2, one obtains

$$\sin^2\theta = k_1h^2 + k_2k^2 + k_3l^2 + k_4hk + k_5kl + k_6lh \qquad \text{(A1.10)}$$

in which:

$$k_1 = \lambda^2 b^2 c^2 \sin^2\alpha / 4v^2 \qquad \text{(A1.11)}$$

$$k_2 = \lambda^2 a^2 c^2 \sin^2\beta / 4v^2 \qquad \text{(A1.12)}$$

$$k_3 = \lambda^2 a^2 b^2 \sin^2\gamma / 4v^2 \qquad \text{(A1.13)}$$

$$k_4 = \lambda^2 abc^2 (\cos\alpha \cos\beta - \cos\gamma) / 2v^2 \qquad \text{(A1.14)}$$

$$k_5 = \lambda^2 a^2 bc (\cos\beta \cos\gamma - \cos\alpha) / 2v^2 \qquad \text{(A1.15)}$$

$$k_6 = \lambda^2 ab^2 c (\cos\alpha \cos\gamma - \cos\beta) / 2v^2 \qquad \text{(A1.16)}$$

Therefore, by taking a set of indexed $\sin^2\theta$ values, a set of linear equations is obtained from which the k constants can be determined, using statistical methods of linear regression. The cell parameters a, b, c, α, β, γ can then be determined by the solution of Equations A1.10 to A1.16. The problem is, of course, much more simple in higher symmetry structures for which only a few parameters have to be found, such as in the present case where only a and c need to be determined.

The listing of the Fortran version of the program written by Lindquist and Wengelin is given below.

```
FORTRAN IV G1  RELEASE 2.0            MAIN                DATE = 76037

0001                  DIMENSION WORDS(18)
0002                  COMMON IA,IOUT,NRP,IQ
0003                  IA=5
0004                  IOUT=6
0005                10 READ(5,1)WORDS
0006                 1 FORMAT(18A4)
0007                   WRITE(6,2)WORDS
0008                 2 FORMAT(1H1 18A4///)
0009                   CALL CARD
0010                   IQ=0
0011                   IF(IQ.EQ.0) CALL SETSYM(64,63)
0012                 4 IF(NRP.EQ.1) CALL GENERA
0013                   IF(NRP.EQ.2.OR.NRP.EC.3) CALL PCNDER(610,63)
0014                   GO TO 10
0015                 3 STOP
0016                   END

 *OPTIONS IN EFFECT*   NOTERM,ID,EBCDIC,SOURCE,NOLIST,NODECK,LOAD,NOMAP,NOTEST
 *OPTIONS IN EFFECT*   NAME = MAIN      , LINECNT =      56
 *STATISTICS*     SOURCE STATEMENTS =      16,PROGRAM SIZE =     736
 *STATISTICS*  NO DIAGNOSTICS GENERATED
```

```
FORTRAN IV G1  RELEASE 2.0            SETSYM              DATE = 76037        01/12/30

0001                  SUBROUTINE SETSYM(*,*)
0002                  COMMON IA,IOUT,NRP,DUP(17),IEXT,ISYM,NSPGR,ENC(6),IFIC(5)
0003                  INTEGER NCLL2/'0'/,ICLB/'CUB'/,ITET/'TET'/,IHEX/'HEX'/,IORT/'ORT'/
                     *,IMCN/'MCN'/,ITRI/'TRI'/
0004                  INTEGER NCLL/'0'/,IP/'P'/,IC/'C'/,II/'I'/,IF/'F'/,IA/'A'/,IR/'R'/
0005                  READ(IN,1)ISYM,NSPGR
0006                1 FORMAT(2X,A3,4X,A1)
0007                  IF(ISYM.EQ.ICLB) GO TO 21
0008                  IF(ISYM.EQ.ITET) GO TO 22
0009                  IF(ISYM.EQ.IHEX) GO TO 23
0010                  IF(ISYM.EQ.IORT) GO TO 24
0011                  IF(ISYM.EQ.IMCN) GO TO 25
0012                  IF(ISYM.EQ.ITRI) GO TO 26
0013                  WRITE(IOUT,14)ISYM
0014               14 FORMAT(1HO,A3,22H IS NO CRYSTAL LATTICE)
0015                  RETURN 2
0016               21 ISYM=1
0017                  WRITE(IOUT,2)
0018                2 FORMAT('0 THE CRYSTAL IS CUBIC')
0019                  GO TO 30
0020               22 ISYM=2
0021                  WRITE(IOUT,3)
0022                3 FORMAT('0 THE CRYSTAL IS TETRAGONAL')
0023                  GO TO 30
0024               23 ISYM=3
0025                  WRITE(IOUT,4)
0026                4 FORMAT('0 THE CRYSTAL IS HEXAGONAL')
0027                  GO TO 30
0028               24 ISYM=4
0029                  WRITE(IOUT,5)
0030                5 FORMAT('0 THE CRYSTAL IS ORTHORHOMBIC')
0031                  GO TO 30
0032               25 ISYM=5
0033                  WRITE(IOUT,6)
0034                6 FORMAT('0 THE CRYSTAL IS MONOCLINIC')
0035                  GO TO 30
0036               26 ISYM=6
0037                  WRITE(ICLT,7)
0038                7 FORMAT('0 THE CRYSTAL IS TRICLINIC')
0039               30 IFIG(5)=2
0040                  IF(NSPGR.EQ.IP) GO TO 31
0041                  IF(NSPGR.EQ.IC) GO TO 32
0042                  IF(NSPGR.EQ.II) GO TO 33
0043                  IF(NSPGR.EQ.IF) GO TO 34
0044                  IF(NSPGR.EQ.IA) GO TO 35
0045                  IF(NSPGR.EQ.IR) GO TO 36
0046                  WRITE(IOUT,15)NSPGR
0047               15 FORMAT(1HO,A1,16H IS NO CENTERING)
0048               31 WRITE(IOUT,8)
0049                8 FORMAT('0 THE LATTICE IS PRIMITIVE'///)
0050                  DO 101 I=1,4
0051              101 IFIG(I)=0
0052                  NSPGR=1
0053                  GO TO 40
```

```
FORTRAN IV G1  RELEASE 2.0            SETSYM          DATE = 76037

0094                32 WRITE(IOUT,9)
0095                 9 FORMAT(27HO THE LATTICE IS C-CENTERED///)
0096                   IFIG(1)=0
0097                   IFIG(4)=0
0098                   IFIG(2)=1
0099                   IFIG(3)=1
00E0                   NSPGR=2
00E1                   GO TO 40
00E2                23 WRITE(IOUT,10)
00E3                10 FORMAT(27HO THE LATTICE IS I-CENTERED///)
00E4                   IFIG(1)=0
00E5                   IFIG(2)=1
00E6                   IFIG(3)=1
00E7                   IFIG(4)=1
00E8                   NSPGR=3
00E9                   GO TO 40
00F0                34 WRITE(IOUT,11)
00F1                11 FORMAT(27HO THE LATTICE IS F-CENTERED///)
00F2                   IFIG(1)=1
00F3                   IFIG(2)=1
00F4                   IFIG(3)=1
00F5                   IFIG(4)=0
00F6                   NSPGR=4
00F7                   GO TO 40
00F8                35 WRITE(IOUT,12)
00F9                12 FORMAT(27HO THE LATTICE IS A-CENTERED///)
00FA                   IFIG(1)=0
00FB                   IFIG(2)=0
00FC                   IFIG(3)=1
00FD                   IFIG(4)=1
00FE                   NSPGR=5
00FF                   GO TO 40
0100                36 WRITE(IOUT,13)
0101                13 FORMAT(27HO THE LATTICE IS R-CENTERED///)
0102                   IFIG(1)=0
0103                   IFIG(2)=-1
0104                   IFIG(3)=1
0105                   IFIG(4)=1
0106                   IFIG(5)=3
0107                   NSPGR=6
0108                40 RETURN 1
0109                   END

 *OPTIONS IN EFFECT*   NOTERM,ID,EBCDIC,SOURCE,NOLIST,NODECK,LOAD,NOMAP,NOTEST
 *OPTIONS IN EFFECT*   NAME = SETSYM   , LINECNT =      56
 *STATISTICS*     SOURCE STATEMENTS =      55,PROGRAM SIZE =     1942
 *STATISTICS*   NO DIAGNOSTICS GENERATED
```

```
FORTRAN IV G1  RELEASE 2.0            CARD            DATE = 76037        01/12/30

0001                   SUBROUTINE CARD
0002                   COMMON IA,IOUT,NRP
0003                   INTEGER*4NCLL/'0'/,IGEN/'GEN'/,IIND/'IND'/,IREF/'REF'/,IFIN/'FEN'/
0004                   READ(IN,1)NRP
0005                 1 FORMAT(2X,A3)
0006                   IF(NRP.EQ.IGEN)GO TO 11
0007                   IF(NRP.EQ.IIND)GO TO 12
0008                   IF(NRP.EQ.IREF)GO TO 13
0009                11 NRP=1
0010                   WRITE(IOUT,2)
0011                 2 FORMAT(34HO SIN$Q-THETA VALUES ARE GENERATED)
0012                   RETURN
0013                12 NRP=2
0014                   WRITE(IOUT,3)
0015                 3 FORMAT(58HO INDICES ARE SEARCHED AND THE CELL DIMENSIONS ARE REFIN
                     *ED)
0016                   RETURN
0017                13 NRP=3
0018                   WRITE(IOUT,4)
0019                 4 FORMAT(33HO THE CELL DIMENSIONS ARE REFINED)
0020                   RETURN
0021                   END

 *OPTIONS IN EFFECT*   NOTERM,ID,EBCDIC,SOURCE,NOLIST,NODECK,LOAD,NOMAP,NOTEST
 *OPTIONS IN EFFECT*   NAME = CARD     , LINECNT =      56
 *STATISTICS*     SOURCE STATEMENTS =      21,PROGRAM SIZE =      656
 *STATISTICS*   NO DIAGNOSTICS GENERATED
```

```
FORTRAN IV G1  RELEASE 2.0          GENERA          DATE = 76037          01/12/30

CC01                  SUBROUTINE GENERA
CC02                  LOGICAL FILLEC
CC03                  DIMENSION ISIN(4000),IIND(4000),IFIG(3)
CC04                  COMMON IA,IOUT,NRP,IQ,ED(6),ELAM,IHMIN,IHMAX,IKMIN,IKMAX,ILMIN,
                     1ILMAX,SMIN,SMAX,ITCL,IEXT,ISYM,NSPGR,EKO(6)
CC05                  IF(IQ.EQ.1) GO TO 19
CC06                  READ(IN,1)ED(1),ED(2),ED(3),ED(4),ED(5),ED(6),ELAM
CC07                1 FORMAT(3F10.4,4F10.6)
CC08                  WRITE(IOUT,2)
CC09                2 FORMAT(23HO INPUT CELL DIMENSIONS)
CC10                  WRITE(IOUT,3)ED(1),ED(4),ED(2),ED(5),ED(3),ED(6),ELAM
CC11                3 FORMAT('0 A =',F9.5,11X,'ALFA  =',F9.4,/,' B =',F9.5,10X,'BETA ='
                     1,F9.4,/'   C =',F9.5,10X,'GAMMA =',F9.4,/'0 LAMBDA =',F9.6,/)
CC12                  DO 359 I=        4,6
CC13              359 ED(I)=ED(I)/180.*3.1415926536
CC14                  CALL COAST
CC15               19 READ(IN,4)IHMIN,IHMAX,IKMIN,IKMAX,ILMIN,ILMAX,SMIN,SMAX,ITOL
CC16                4 FORMAT(6I5, 2F5.5, I5)
CC17                  WRITE(IOUT,5)IHMIN,IHMAX,IKMIN,IKMAX,ILMIN,ILMAX,SMIN,SMAX
CC18                5 FORMAT('C GENERATION RANGES'/' HMIN=',I5,5X,'HMAX=',I5,/'  KMIN ='
                     2,I5,5X,'KMAX=',I5,/'  LMIN=',I5,5X,'LMAX=',I5,//'0 SINSQ-THETA MIN
                     3=',F5.3,5X,'SINSQ-THETA MAX=',F5.3)
CC19                  WRITE(IOUT,6)
CC20                6 FORMAT(38H1 GENERATED LIST OF SINSQ-THETA VALUES)
CC21                  FILLEC=.FALSE.
CC22                  NSC=0
CC23                  IHMIN=IHMIN+1CO
CC24                  IHMAX=IHMAX+1CO
CC25                  IKMIN=IKMIN+1CO
CC26                  IKMAX=IKMAX+1CO
CC27                  ILMIN=ILMIN+1CO
CC28                  ILMAX=ILMAX+1CO
CC29                  DO 2C JIH=IHMIN,IHMAX
CC30                  DO 20 JIK=IKMIN,IKMAX
CC31                  DO 20 JIL=ILMIN,ILMAX
CC32                  IIH=JIH-1CO
CC33                  IIK=JIK-1CO
CC34                  IIL=JIL-100.
CC35                  CALL EXT(IIH,IIK,IIL)
CC36                  IF(IEXT.EC.0) GO TC 25
CC37                  SINSQ=EKO(1)*IIH**2+EKO(2)*IIK**2+EKO(3)*IIL**2+EKO(4)*IIK*IIL
                     3+EKO(5)*IIH*IIL+EKO(6)*IIH*IIK
CC38                  IF(SINSQ.GT.SMAX.OR.SINSQ.LT.SMIN) GO TC 25
CC39                  NSC=NSC+1
CC40                  IF(NSC.LE.4000) GO TC 24
CC41                  WRITE(ICLT,7)IIH,IIK,IIL
CC42                7 FORMAT(26HO ARRAY FILLED WHEN    H= I4, 5H  K= I4, 5H  L= I4)
CC43                  FILLEC=.TRUE.
CC44               24 ISIN(NSC)=SINSQ*1000000.+0.5
CC45                  IIND(NSC)=IIH*1CCCCC+IIK*1000+IIL*10
CC46               25 IF(FILLEC) GO TO 100
CC47               2C CCNTINUE
CC48                  WRITE(IOUT,8)NSC
CC49                8 FORMAT(43HO NUMBER OF GENERATED SINSQ-THETA VALUES=  I4)

FORTRAN IV G1  RELEASE 2.0          GENERA          DATE = 76037          01/12/30

CC50              1CO NSCSL=NSC-1
CC51                  DO 110 I=1,NSCSL
CC52                  MU=NSC-I
CC53                  MQ=MU+1
CC54                  DO 110 J=1,MU
CC55                  IDIFF=ISIN(J)-ISIN(MQ)
CC56                  IF(IDIFF.LE.0) GO TO 110
CC57                  IDUM=ISIN(MQ)
CC58                  ICAM=IIND(MQ)
CC59                  ISIN(MQ)=ISIN(J)
CC60                  ISIN(J)=IDUM
CC61                  IIND(MQ)=IIND(J)
CC62                  IIND(J)=ICAM
CC63              110 CONTINUE
CC64                  NRAD=3
CC65                  WRITE(IOUT,9)
CC66                9 FORMAT(4HO        H      K      L      SINSQ-C      C//)
CC67                  DO 120 I=1,NSC
CC68                  CX=ISIN(I)/10C0000.
CC69                  DX=ELAM/2./SQRT(CX)
CC70                  SLASK1=IIND(I)/1CCCCO.
CC71                  IF(SLASK1)222,111,111
CC72              111 IFIG(1)=SLASK1+0.5
CC73                  GOTO 223
CC74              222 IFIG(1)=SLASK1-0.5
CC75              223 SLASK2=(IIND(I)-IFIG(1)*100C000)/10C0.
CC76                  IF(SLASK2)333,444,444
CC77              444 IFIG(2)=SLASK2+0.5
CC78                  GOTO 445
CC79              333 IFIG(2)=SLASK2-0.5
CC80              445 SLASK3=(IIND(I)-IFIG(1)*100C00-IFIG(2)*1000)/10.
CC81                  IF(SLASK3)555,556,556
CC82              555 IFIG(3)=SLASK3-0.5
CC83                  GOTO 121
CC84              556 IFIG(3)=SLASK3+0.5
CC85              121 NRAD=NRAD+1
CC86                  IF(NRAD-60)120,666,666
CC87              666 NRAD=C
CC88                  IF(I.EQ.NSC) GO TO 12C
CC89                  WRITE(3,11)
CC90               11 FORMAT('1')
CC91                  WRITE(3,9)
CC92              120 WRITE(IOUT,10)(IFIG(J),J=1,3),ISIN(I),DX
CC93               10 FORMAT(I10,21X, I13,F10.5)
CC94                  IQ=1
CC95                  RETURN
CC96                  END

*OPTIONS IN EFFECT*   NOTERM,ID,EBCDIC,SOURCE,NOLIST,NODECK,LOAD,NOMAP,NOTEST
*OPTIONS IN EFFECT*   NAME = GENERA   , LINECNT =      56
*STATISTICS*     SOURCE STATEMENTS =      96,PROGRAM SIZE =    35504
*STATISTICS*  NO DIAGNOSTICS GENERATED
```

```
FCRTRAN IV G1  RELEASE 2.0            CCNST          DATE = 76037        01/12/30

CCC1                  SUBROUTINE CONST
CCC2                  COMMON DUM(4),ED(6),ELAM,CDUM(12),EKC(6)
CCC3                  VSC=EC(1)**2*EC(2)**2*ED(3)**2*(1-COS(ED(4))**2-COS(ED(5))**2
                     1-COS(EC(6))**2+2*CCS(ED(4))*COS(EC(5))*COS(ED(6)))
CCC4                  EKC(1)=ELAM**2*ED(2)**2*ED(3)**2*SIN(ED(4))**2/4/VSC
CCC5                  EKC(2)=ELAM**2*EC(1)**2*ED(3)**2*SIN(ED(5))**2/4/VSC
CCC6                  EKC(3)=ELAM**2*ED(1)**2*EC(2)**2*SIN(EC(6))**2/4/VSC
CCC7                  EKC(4)=ELAM**2*ED(1)**2*EC(2)*ED(3)*(CCS(ED(5))*CCS(ED(6))-
                     1CCS(EC(4)))/2/VSC
CCC8                  EKC(5)=ELAM**2*ED(1)*EC(2)**2*ED(3)*(COS(ED(4))*COS(ED(6))-
                     1COS(EC(5)))/2/VSC
CCC9                  EKC(6)=ELAM**2*ED(1)*ED(2)*ED(3)**2*(COS(ED(4))*COS(ED(5))-
                     1CCS(EC(6)))/2/VSC
CC10                  RETURN
CC11                  END

 *CPTIONS IN EFFECT*  NOTERM,ID,EBCDIC,SOURCE,NOLIST,NODECK,LOAD,NOMAP,NOTEST
 *CPTIONS IN EFFECT*  NAME = CONST   , LINECNT =      56
 *STATISTICS*     SOURCE STATEMENTS =      11,PROGRAM SIZE =     1242
 *STATISTICS*  NO DIAGNOSTICS GENERATED
```

```
FCRTRAN IV G1  RELEASE 2.0            EXT            DATE = 76037        01/12/30

CC01                  SUBROUTINE EXT(IN,IK,IL)
CC02                  LOGICAL ENKEL
CC03                  COMMON DUM(20),IEXT,ISYM,NSPGR,EKD(6),IFIG(5)
CC04                  I=1
CCC5                  IF(IFIG(2).NE.0.OR.IFIG(3).NE.0.OR.IFIG(4).NE.0) GO TO 10
0CC6                  IEXT=1
CC07                  GO TO 20
CCC8                10 II=IN*IFIG(2)+IK*IFIG(3)+IL*IFIG(4)
0009                  IF(IFIG(1).LE.0) GO TO 15
CC10                  I=IK+IL
CC11                  ENKEL=.FALSE.
0012                  GO TO 16
CC13                15 ENKEL=.TRUE.
CC14                16 IF(II/IFIG(5)*IFIG(5).EQ.II.AND.(I/2*2.EQ.I.OR.ENKEL)) GO TO 19
CC15                  IEXT=0
CC16                  RETURN
CC17                19 IEXT=1
CC18                20 IF(ISYM.NE.1) GO TO 21
0019                   IF(IN.LT.IK.OR.IK.LT.IL.OR.IN.LT.IL) IEXT=0
CC20                   RETURN
CC21                21 IF(ISYM.NE.2.AND.ISYM.NE.3) GO TO 22
0022                   IF(IN.LT.IABS(IK)) IEXT=0
CC23                22 RETURN
CC24                   END

 *CPTIONS IN EFFECT*  NOTERM,ID,EBCDIC,SOURCE,NOLIST,NODECK,LOAD,NOMAP,NOTEST
 *CPTIONS IN EFFECT*  NAME = EXT     , LINECNT =      56
 *STATISTICS*     SOURCE STATEMENTS =      24,PROGRAM SIZE =      916
 *STATISTICS*  NO DIAGNOSTICS GENERATED
```

```
FORTRAN IV G1  RELEASE 2.0            DET                    DATE = 76037

CC01                  FUNCTION DET(YA,N,IBYT)
CC02                  DIMENSION YA(6,7),A(6,7)
CC03                  M=N+1
CC04                  DO 1 I=1,N
CC05                  DO 1 IK=1,M
CC06                1 A(I,IK)=YA(I,IK)
CC07                  IF(IBYT.EQ.0) GO TO 10
CC08                  DO 2 I=1,N
CC09                2 A(I,IBYT)=A(I,M)
CC10               10 DO 20 I=1,N
CC11                  IR=0
CC12                  IF(A(I,I).NE.0.0) GO TO 20
CC13               13 IR=IR+1
CC14                  IF(A(IR,I).EQ.0.0) GO TO 13
CC15                  DO 14 IK=1,N
CC16               14 A(I,IK)=A(I,IK)+A(IR,IK)
CC17               20 CONTINUE
CC18                  MM=N-1
CC19                  DO 30 IR=1,MM
CC20                  MMM=IR+1
CC21                  DO 30 IK=MMM,N
CC22                  FACT=A(IR,IK)/A(IR,IR)
CC23                  DO 30 I=1,N
CC24               30 A(I,IK)=A(I,IK)-FACT*A(I,IR)
CC25                  DETA=1
CC26                  DO 40 I=1,N
CC27               40 DETA=DETA*A(I,I)
CC28                  DET=DETA
CC29                  RETURN
CC30                  END

 *OPTIONS IN EFFECT*   NOTERM,IC,EBCDIC,SOURCE,NOLIST,NODECK,LOAD,NOMAP,NOTEST
 *OPTIONS IN EFFECT*   NAME = DET      , LINECNT =      56
 *STATISTICS*     SOURCE STATEMENTS =       30,PROGRAM SIZE =     1306
 *STATISTICS*   NO DIAGNOSTICS GENERATED
```

```
FORTRAN IV G1  RELEASE 2.0            POWDER                 DATE = 76037          01/12/30

CC01                  SUBROUTINE POWDER(*,*)
CC02                  DIMENSION IH(300),IK(300),IL(300),ISIN(300),ICSIN(300),CO(6),
                     >D1A(6),EAVK(6),REC(6),SIG(6),AI(7),APEC(7),ISUM(8),CER(6,6),
                     XSL(6,7),VC(6,6),CI,C(6,7),ISOOS(300),DI(6),FVALUE(4,6)
CC03                  COMMON IA,IOUT,NRP,IQ,ED(6),ELAM,IHMIN,IHMAX,IKMIN,IKMAX,
                     XILMIN,ILMAX,SMIN,SMAX,ITOL,IEXT,ISYM,NSPCE,EKO(6),IFIG(5)
CC04                  REAL*4 CLIVER/184./,OVALUE/2.095,0.,0.,C.,1.047,C.,C.786,0.,0.524,
                     *0.393,0.393,0.393,0.15,0.681,0.,0.113,0.214,0.786,C.,0.16,1CC0.,10
                     *C0.,1C0C.,100C./
CC05                  DO 2000 I=1,6
CC06               2000 SL(I,7)=0
CC07                  JQ=0
CC08                  IRA=C
CC09                  IF(NRP.EQ.2) GO TO 100
CC10                  READ(IN,1)ELAM
CC11                1 FORMAT(F10.6)
CC12                  WRITE(IOUT,2)ELAM
CC13                2 FORMAT(17HO WAVE LENGHT IS F10.6)
CC14                  I=1
CC15               40 READ(IN,3)IH(I),IK(I),IL(I),ISIN(I)
CC16                3 FORMAT(3I5,I10)
CC17                  IF(IH(I)-999)52,50,50
CC18               52 I=I+1
CC19                  GO TO 40
CC20               50 NPNT=I-1
CC21                  WRITE(IOUT,4)
CC22                4 FORMAT('1 THE REFINEMENT IS BASED ON INCEXEC REFLEXIONS')
CC23                  DO 60 I=1,6
CC24               60 EKO(I)=0
CC25                  GO TO 200
CC26              100 IF(IQ.EC.1) GO TO 110
CC27                  READ(IN,5)ED(1),ED(2),ED(3),ED(4),ED(5),ED(6),ELAM
CC28                5 FORMAT(3F10.4,4F10.6)
CC29                  WRITE(IOUT,6)
CC30                6 FORMAT(23HO INPUT CELL DIMENSIONS)
CC31                  WRITE(IOUT,7)ED(1),ED(4),ED(2),ED(5),ED(3),ED(6),ELAM
CC32                7 FORMAT('0A =',F9.5,10X,' ALFA =',F9.4,/' B =',F9.5,10X,'BETA  =',
                     2F9.4,/' C =',F9.5,10X,'GAMMA =',F9.4,/'0 LAMBDA =',F9.6,/)
CC33                  DO 498 I= 4,6
CC34              498 ED(I)=ED(I)*3.1415926536/180.
CC35                  CALL COAST
CC36              110 WRITE(IOUT,8)
CC37                8 FORMAT(46HO THE REFINEMENT IS BASED ON GENERATED INDICES)
CC38                  READ(IN,9)IHMIN,IHMAX,IKMIN,IKMAX,ILMIN,ILMAX,SMIN,SMAX,ITOL
CC39                9 FORMAT(6I5,2F5.5,I5)
CC40                  WRITE(IOUT,10)IHMIN,IHMAX,IKMIN,IKMAX,ILMIN,ILMAX,SMIN,SMAX,
                     XITOL
CC41               10 FORMAT('0GENERATION RANGES',/' HMIN =',I5,5X,'HMAX =',I5,/' KMIN =
                     *',I5,5X,'KMAX =',I5,/' LMIN =',I5,5X,'LMAX= ',I5,///'0SINSQ-THETA M
                     4IN=',F5.3,5X,'SINSQ-THETA MAX =',F5.3,///'0 INDEXING TOLERANCE=',I5
                     *,///)
CC42                  I=1
CC43              120 READ(IN,11)ISOBS(I)
CC44               11 FORMAT(I10)
```

```
FORTRAN IV G1  RELEASE 2.0            POWDER            DATE = 76037          01/12/3
C0045                 IF(ISOBS(I).GE.999999) GO TO 130
C0046                 I=I+1
C0047                 GO TO 120
C0048           130 NSC=I-1
C0049                 WRITE(IOUT,12)
C0050            12 FORMAT('0 IMPLT SINSC-THETA VALUES'//)
C0051                 WRITE(IOUT,13)(ISOBS(I),I=1,NSC)
C0052            13 FORMAT(8I10)
C0053           142 JC=JC+1
C0054                 WRITE(IOUT,14)JC
C0055            14 FORMAT('1 CYCLE',I2)
C0056                 NHIT=0
C0057                 DO 150 I=1,ASC
C0058           150 ICSIN(I)=0
C0059                 JHMIN=IHMIN+ICO
C0060                 JHMAX=IHMAX+ICO
C0061                 JKMIN=IKMIN+ICO
C0062                 JKMAX=IKMAX+ICO
C0063                 JLMIN=ILMIN+ICO
C0064                 JLMAX=ILMAX+ICO
C0065                 DO 160 IJH=JHMIN,JHMAX
C0066                 DO 161 IJK=JKMIN,JKMAX
C0067                 DO 162 IJL=JLMIN,JLMAX
C0068                 IIH=IJH-ICO
C0069                 IIK=IJK-ICO
C0070                 IIL=IJL-ICO
C0071                 CALL EXT(IIH,IIK,IIL)
C0072                 IF(IEXT.EQ.0) GO TO 162
C0073                 SINSC=EKO(1)*IIH**2+EKO(2)*IIK**2+EKO(3)*IIL**2+EKO(4)*IIK*IIL
                     2+EKO(5)*IIH*IIL+EKO(6)*IIH*IIK
C0074                 IF(SINSC.GT.SMAX.OR.SINSQ.LT.SMIN) GO TO 162
C0075                 ISA=SINSC*100C000.+0.5+IRA
C0076                 DO 163 I=1,ASC
C0077                 IDEL=IABS(ISOBS(I)-ISA)
C0078                 IF(IDEL.GT.ITOL.OR.IDEL.GE.IABS(ISOBS(I)-ICSIN(I))) GO TO 163
C0079                 IF(ICSIN(I).EQ.0) NHIT=NHIT+1
C0080                 ICSIN(I)=ISA
C0081                 IH(I)=IIH
C0082                 IK(I)=IIK
C0083                 IL(I)=IIL
C0084           163 CONTINUE
C0085           162 CONTINUE
C0086           161 CONTINUE
C0087           160 CONTINUE
C0088                 J=0
C0089                 DO 170 I=1,NSC
C0090                 IF(ICSIN(I).EQ.0) GO TO 170
C0091                 J=J+1
C0092                 IH(J)=IH(I)
C0093                 IK(J)=IK(I)
C0094                 IL(J)=IL(I)
C0095                 ISIA(J)=ISOBS(I)
C0096                 ICSIN(J)=ICSIA(I)
C0097           170 CONTINUE

FORTRAN IV G1  RELEASE 2.0            POWDER            DATE = 76037          01/12/30
C0098           200 IF(ISYM.EQ.1) N=1
C0099                 IF(ISYM.EQ.2.OR.ISYM.EQ.3) N=2
C0100                 IF(ISYM.EQ.4) N=3
C0101                 IF(ISYM.EQ.5) N=4
C0102                 IF(ISYM.EQ.6) N=6
0103                  M=N+1
C0104                 IF(NHIT.GT.N+2) GO TO 210
C0105                 WRITE(IOUT,15)
0106             15 FORMAT(55H0 NUMBER OF TOLERATED SINSC-THETA VALUES NOT SUFFICIENT)
C0107                 RETURN 2
C0108           210 IF(JQ.EQ.0) JHIT=NHIT
0109            211 IF(JQ.EQ.1) JHIT=N+2
C0110                 IF(JQ.EQ.2) JHIT=N+1+(NHIT-N-1)/2
C0111                 IF(JQ.EC.3) JHIT=NHIT
C0112                 IF(JQ.LE.3) GO TO 212
0113                  WRITE(IOUT,1175)
C0114           1175 FORMAT(40H0 THERE IS SOMETHING RUTTEN IN YOUR DATA)
C0115                 RETURN 2
C0116           212 ISUMH=0
C0117                 ISUMK=0
C0118                 ISUML=0
C0119                 DO 220 I=1,JHIT
C0120                 ISUMH=IABS(IH(I))+ISUMH
C0121                 ISUMK=IABS(IK(I))+ISUMK
C0122           220 ISUML=IABS(IL(I))+ISUML
0123                  ISUMA=ISUMH+ISUMK
C0124                 IF(ISYM-3)226,226,227
C0125           226 IF(ISUMA.EQ.0.OR.ISUML.EQ.0) GO TO 221
C0126                 GO TO 222
C0127           227 IF(ISUMH.NE.0.AND.ISUMK.NE.0.AND.ISUML.NE.0) GO TO 222
C0128           221 JC=JQ+1
C0129                 WRITE(IOUT,16)
C0130            16 FORMAT(75H0 FOR ALL REFLEXIONS ONE CERTAIN INDEX IS NEVER ASSIGNED
                    X ANY NON-ZERO VALUE)
                      GO TO 211
C0131           222 DO 223 I=1,7
C0132           223 ISUM(I)=0
C0133                 ASUM=0
C0134                 DO 224 I=1,JHIT
0135                  ASUM=ASUM+ISIA(I)/1C0CC00.
C0136                 ISUM(1)=ISUM(1)+IH(I)**2
C0137                 ISUM(2)=ISUM(2)+IK(I)**2
C0138                 ISUM(3)=ISUM(3)+IL(I)**2
C0139                 ISUM(4)=ISUM(4)+IK(I)*IL(I)
C0140                 ISUM(5)=ISUM(5)+IH(I)*IL(I)
0141            224 ISUM(6)=ISUM(6)+IH(I)*IK(I)
C0142                 FIT=JHIT
C0143                 DO 225 I=1,6
C0144           225 AMED(I)=ISUM(I)/FIT
0145                  AMED(7)=ASUM/JHIT
C0146                 IF(N.EQ.1) AMED(1)=AMED(1)+AMED(2)+AMED(3)
C0147                 IF(N.NE.2) GO TO 230
C0148                 AMED(1)=AMED(1)+AMED(2)
C0149                 AMED(2)=AMED(3)
C0150
```

```
FORTRAN IV G1  RELEASE 2.0            POWDER                  DATE = 76037

0151.                 IF(ISYP.EQ.3) AMEC(1)=AMEC(1)+AMED(6)
0152              230 IF(N.EQ.4) AMEC(4)=AMED(5)
0153                  DO 231 I=1,6
0154                  ENYK(I)=EKC(I)
0155              231 SIG(I)=0 .
0156                  DO 232 IR=1,N
0157                  DO 232 J=1,M
0158              232 C(IR,J)=0.
0159                  DO 842 IR=1,N
0160                  DO 841 J=1,M
0161                  DO 240 I=1,JHIT
0162                  A(7)=ISIN(I)/1000000.
0163                  A(1)=IH(I)**2
0164                  A(2)=IK(I)**2
0165                  A(3)=IL(I)**2
0166                  A(4)=IK(I)*IL(I)
0167                  A(5)=IH(I)*IL(I)
0168                  A(6)=IH(I)*IK(I)
0169                  IF(N.EQ.1) A(1)=A(1)+A(2)+A(3)
0170                  IF(N.NE.2) GO TO 233
0171                  A(1)=A(1)+A(2)
0172                  A(2)=A(3)
0173                  IF(ISYP.EQ.3) A(1)=A(1)+A(6)
0174              233 IF(N.EC.4) A(4)=A(5)
0175                  A(M)=A(7)
0176                  AMED(M)=AMED(7)
0177              240 C(IR,J)=C(IR,J)+(A(IR)-AMED(IR))*(A(J)-AMED(J))
0178              841 CCATINUE
0179              842 CONTINUE
0180                  DENOM=DET(C,N,0)
0181                  IF(CEACP.GT.0.02)GCTO 248
0182                  WRITE(ICLT,668)
0183              668 FORMAT('C LEAST SCLARES METHOD FAILED IN THIS CYCLE')
0184                  GO TC 142
0185              248 DC 241 I=1,N
0186                  ENYK(I)=DET(C,N,I)/DENOM
0187                  IF(ENYK(I).GT.0.COOCOI) GC TO 241
0188                  WRITE(ICUT,1176)
0189             1176 FCRMAT(' C ONE INCEX HAS ALWAYS THE SAME VALUE')
0190                  JO=JO+1
0191                  GC TC 211
0192              241 CONTINUE
0193                  IF(N.NE.1) GO TO 242
0194                  EKO(1)=ENYK(1)
0195                  EKC(2)=ENYK(1)
0196                  EKO(3)=ENYK(1)
0197              242 IF(N.NE.2) GO TO 243
0198                  EKC(1)=ENYK(1)
0199                  EKO(2)=ENYK(1)
C2C0                  EKO(3)=ENYK(2)
C2C1                  IF(ISYP.EC.3) EKO(6)=ENYK(1)
C2C2              243 IF(N.NE.3.AND.N.NE.4) GO TO 245
C2C3                  DO 244 I=1,3
C204              244 EKO(I)=ENYK(I)

FORTRAN IV G1  RELEASE 2.0            POWDER                  DATE = 76037          01/12/30

C205                  IF(N.EQ.4) EKC(5)=ENYK(4)
0206              245 IF(N.NE.6) GO TO 247
C2C7                  DO 246 I=1,6
C2C8              246 EKO(I)=ENYK(I)
C209              247 WRITE(IOUT,17) JHIT
C210               17 FCRMAT('0 AUMBER CF REFLEXIONS=',I4,//' SIN2TH CALC ARE BASED ON
                     AREFINED CONSTANTS'///)
C211                  WRITE(IOUT,18)
C212               18 FCRMAT( '0    H     K     L     SIN2TH    SIN2TH      DIFF
                     X       O-CBS      C-CAL'/'                                    CBS      CALC')
C213                  NRAD=11
0214                  DO 250 I=1,3
C215              250 REC(I)=2*SCRT(EKO(I)/ELAM
C216                  REC(4)=2*EKO(4)/(ELAM**2*REC(2)*REC(3))
C217                  REC(5)=2*EKO(5)/(ELAM**2*REC(1)*REC(3))
C218                  REC(6)=2*EKO(6)/(ELAM**2*REC(1)*REC(2))
C219                  VREC=REC(1)*REC(2)*REC(3)*SCRT(1+2*REC(4)*REC(5)*REC(6)
                     X-REC(4)**2-REC(5)**2-REC(6)**2)
C220                  DC 255 I=1,4
C221              255 D(I)=DVALUE(I,ISYP)
C222                  IF(NSPGR.NE.2.AND.NSPGR.NE.3) GO TC 257
C223                  DO 256 I=1,4
C224              256 D(I)=0.5*D(I)
C225              257 IF(NSPGR.NE.4) GC TC 259
C226                  DO 258 I=1,4
C227              258 C(I)=0.25*C(I)
C228              259 DO 260 I=1,JHIT
C229                  ICSIN(I)=(EKO(1)*IH(I)**2+EKO(2)*IK(I)**2+EKC(3)*IL(I)**2+
                     XEKC(4)*IK(I)*IL(I)+EKC(5)*IH(I)*IL(I)+EKO(6)*IH(I)*IK(I))*1.E6
C230                  IDEL=ISIN(I)-ICSIN(I)
C231                  GLUFS=ISINCI)
C232                  IEPS=0.5*VREC/(1.5*C(1)*SQRT(GLUFS/100.C)*D(2)*REC(1)+D(3)*REC(2)
                     X+D(4)*REC(3))*1000000.
C233                  DAB=ISIN(I)/1COCOCO.
0234                  DCA=ICSIN(I)/1000000.
C235                  DAB=ELAM/2./SCRT(DAB)
C236                  DCA=ELAM/2./SCRT(DCA)
C237                  WRITE(IOUT,19) IH(I),IK(I),IL(I),ISIN(I),ICSIN(I),IDEL,DAB,DCA
C238               19 FCRMAT(3I6,I12,219,10X,2F10.5)
C239                  NRAD=NRAD+1
C240                  IF(NRAD-60)26C,888,888
C241              888 NRAD=0
C242                  IF(I.EQ.JHIT) GO TO 260
C243                  WRITE(3,778)
C244              778 FORMAT('1')
C245                  WRITE(3,18)
C246              26C IRA=IRA+IDEL
C247                  IRA=IRA/JHIT
C248                  IF(NRP-2)678,679,678
C249              679 IF(JO-3)142,678,678
C250              678 ED(1)=REC(2)*REC(3)*SCRT(1-REC(4)**2)/VREC
C251                  FC(2)=REC(1)*REC(3)*SCRT(1-REC(5)**2)/VREC
C252                  ED(3)=REC(1)*REC(2)*SCRT(1-REC(6)**2)/VREC
C253                  CO(4)=(REC(5)*REC(6)-REC(4))/SCRT((1-REC(5)**2)*(1-REC(6)**2))

                                                                                292.
```

```
C254                  CO(5)=(REC(4)*REC(6)-REC(5))/SQRT((1-REC(4)**2)*(1-REC(6)**2))
C255                  CC(6)=(REC(4)*REC(5)-REC(6))/SQRT((1-REC(4)**2)*(1-REC(5)**2))
C256                  PI=3.141592653
0257                  CO 271 I=4,6
C258                  IF(ABS(CC(I)).GT.0.0001) GO TO 270
C259                  ED(I)=PI/2
C260                  GO TO 271
C261              270 EC(I)=ARCCS(CC(I))
C262              271 CONTINUE
C263                  ASLM=C
C264                  DO 275 I=1,JMIT
C265              275 ASLP=ASLP+((ISIN(I)-ICSIN(I))/1.E6)**2
C266                  SLPN=ASLP/(JMIT-N)
C267                  DO 280 I=1,6
C268                  DO 280 J=1,6
C269              280 VD(I,J)=0
C270                  DO 290 I=1,N
C271                  DO 290 J=1,N
C272                  DO 285 IR=1,N
C273                  DO 285 M=1,N
C274              285 SL(IR,M)=C(IR,M)
C275                  DO 286 JP=1,N
C276              286 SL(JP,J)=C
C277                  SL(I,J)=1
C278              290 VC(J,I)=SUMA/CENOM=DET(SL,N,0)
C279                  IF(ISYM.EQ.6) GO TO 300
0280                  IF(ISYM.NE.5) GO TO 293
C281                  VC(5,5)=VC(4,4)
C282                  DO 291 I=1,3
C283                  VD(5,I)=VD(4,I)
C284              291 VC(I,5)=VC(I,4)
C285                  DO 292 I=1,6
C286                  VD(4,I)=C
C287              292 VC(I,4)=0
C288                  GO TO 300
C289              293 IF(ISYM.EQ.1.OR.ISYM.EQ.4) GO TO 300
C290                  VD(3,3)=VC(2,2)
C291                  VC(1,3)=VC(1,2)
C292                  VD(3,1)=VD(2,1)
C293                  DO 294 I=1,3
C294                  VC(2,I)=0
C295              294 VC(I,2)=0
C296              300 VREC=SQRT(64*EKO(1)*EKO(2)*EKO(3)+16*EKC(4)*EKC(5)*EKO(6)
                   * -16*EKO(1)*EKC(4)**2-16*EKO(2)*EKC(5)**2-16*EKO(3)*EKO(6)**2)/
                    ELAM**3
C297                  DA=1./2./VREC*(64*EKC(2)*EKC(3)-16*EKC(4)**2)/ELAM**6
C298                  DB=1./2./VREC*(64*EKO(1)*EKC(3)-16*EKC(5)**2)/ELAM**6
C299                  DC=1./2./VREC*(64*EKC(1)*EKO(2)-16*EKO(6)**2)/ELAM**6
C300                  CC=1./2./VREC*(16*EKO(5)*EKO(6)-32*EKO(1)*EKO(4))/ELAM**6
C301                  DE=1./2./VREC*(16*EKC(4)*EKO(6)-32*EKO(2)*EKO(5))/ELAM**6
C302                  DF=1./2./VREC*(16*EKC(4)*EKC(5)-32*EKC(3)*EKO(6))/ELAM**6
C303                  UA=2/(ELAM**2*SQRT(4*EKO(2)*EKO(3)-EKO(4)**2))
C304                  DER(1,1)=-EC(1)*CA/VREC
C305                  DER(1,2)=(UA*2*EKC(3)-ED(1)*DB)/VREC
C306                  DER(1,3)=(UA*2*EKC(2)-EC(1)*CC)/VREC
C307                  DER(1,4)=-(UA*EKC(4)+EC(1)*DD)/VREC
C308                  DER(1,5)=-EC(1)*DE/VREC
C309                  DER(1,6)=-EC(1)*DF/VREC
C310                  UA=2/(ELAM**2*SQRT(4*EKO(1)*EKC(3)-EKC(5)**2))
0311                  DER(2,1)=(UA*2*EKO(3)-ED(2)*DA)
0312                  DER(2,2)=-ED(2)*DB/VREC
C313                  DER(2,3)=(UA*2*EKC(1)-EC(2)*CC)/VREC
C314                  DER(2,4)=-ED(2)*DD/VREC
C315                  DER(2,5)=-(EKC(5)*UA+ED(2)*DE)/VREC
C316                  DER(2,6)=-ED(2)*DF/VREC
C317                  UA=2/(ELAM**2*SQRT(4*EKC(1)*EKC(2)-EKC(6)**2))
0318                  DER(3,1)=(UA*2*EKC(2)-ED(3)*DA)/VREC
C319                  DER(3,2)=(UA*2*EKO(1)-ED(3)*DB)/VREC
C320                  DER(3,3)=-ED(3)*DC/VREC
C321                  DER(3,4)=-ED(3)*DD/VREC
C322                  DER(3,5)=-ED(3)*DE/VREC
C323                  DER(3,6)=-(UA*EKC(6)+EC(3)*CF)/VREC
C324                  UA=-SQRT(1/(1-CO(4)**2))
C325                  UB=SQRT(16*EKC(1)**2*EKO(2)*EKO(3)-4*EKO(1)*EKC(3)*EKC(6)**2
                   -4*EKO(1)*EKO(2)*EKC(5)**2*EKO(5)**2*EKO(6)**2)
C326                  DER(4,1)=UA/UB*(-2*EKC(4)-1./2.*CC(4)*(32*EKO(1)*EKC(2)*EKO(3)
                   -4*EKO(3)*EKO(6)**2-4*EKO(2)*EKO(5)**2)/UB)
C327                  DER(4,2)=-LA/LB**2*CC(4)*(8*EKO(1)**2*EKO(3)-2*EKO(1)*
                   EKO(5)**2)
C328                  DER(4,3)=-UA/LB**2*CO(4)*(8*EKO(1)**2*EKC(2)-2*EKC(1)*EKO(6)**2)
C329                  DER(4,4)=-2*UA*EKO(1)/UB
C330                  DER(4,5)=UA/UB*(EKO(6)-(EKO(5)*EKO(6)**2-4*EKC(1)*EKC(2)*EKC(5))
                   *CO(4)/UB)
C331                  DER(4,6)=UA/UB*(EKO(5)-(EKO(5)**2*EKO(6)-4*EKO(1)*EKC(3)*EKC(6))
                   *CO(4)/UB)
C332                  UA=-SQRT(1/(1.-CO(5)**2))
C333                  UB=SQRT(16*EKC(1)*EKO(2)**2*EKO(3)-4*EKO(2)*EKO(3)*EKC(6)**2
                   -4*EKO(1)*EKO(2)*EKC(4)**2*EKO(4)**2*EKO(6)**2)
C334                  DER(5,1)=-UA/LB**2*(8*EKO(2)**2*EKC(3)-2*EKC(2)*EKC(4)**2)*CO(5)
C335                  DER(5,2)=-UA/LB*(2*EKC(5)+(16*EKC(1)*EKC(2)*EKO(3)-2*EKC(3)*
                   EKC(6)**2-2*EKO(1)*EKC(4)**2)*CO(5)/UB)
C336                  DER(5,3)=-LA/LB**2*(8*EKO(1)*EKC(2)**2-2*EKO(2)*EKC(6)**2)*CO(5)
C337                  DER(5,4)=UA/UB*(EKO(6)-(EKO(4)*EKC(6)**2-4*EKO(1)*EKC(2)*EKC(4))
                   4*CC(5)/UB)
C338                  DER(5,5)=-UA/LB*2*EKC(2)
C339                  DER(5,6)=UA/UB*(EKO(4)-(EKO(4)**2*EKC(6)-4*EKO(2)*EKC(3)*EKC(6))
                   *CO(5)/UB)
C340                  UA=-SQRT(1/(1.-CO(6)**2))
C341                  UB=SQRT(16*EKC(1)*EKC(3)**2*EKC(2)-4*EKC(2)*EKO(3)*EKC(5)**2
                   -4*EKO(1)*EKO(3)*EKO(4)**2*EKO(4)**2*EKC(5)**2)
C342                  DER(6,1)=-UA/LB**2*(8*EKO(2)*EKO(3)**2-2*EKO(3)*EKO(4)**2)*CO(6)
C343                  DER(6,2)=-LA/LB**2*(8*EKO(1)*EKC(3)**2-2*EKC(3)*EKC(5)**2)*CO(6)
0344                  DER(6,3)=-UA/LB*(2*EKC(6)+(16*EKC(1)*EKC(2)*EKC(3)-4*EKC(2)*
                   EKC(5)**2-4*EKO(1)*EKC(4)**2)*CO(6)/UB)
C345                  DER(6,4)=UA/UB*(EKO(5)-(EKO(4)*EKC(5)**2-4*EKO(1)*EKO(3)*EKO(4)
                   )*CO(6)/LB)
0346                  DER(6,5)=UA/UB*(EKO(4)-(EKO(5)*EKO(4)**2-4*EKO(2)*EKC(3)*EKC(5))
                   *CO(6)/UB)
```

```
FORTRAN IV G1  RELEASE 2.0            POWDFR            DATE = 76037        01/12/30

C347                  DER(6,6)=-UA/LB**2*EKO(3)
C348                  DO 310 IR=4,6
C349                  DO 310 IP=1,6
C350              310 DER(IR,IP)=DER(IR,IP)*180/PI
C351                  DO 320 IR=1,6
C352                  DO 320 M=1,6
C353              320 SL(IR,M)=0
C354                  DO 330 IR=1,6
C355                  DO 330 M=1,6
C356                  DO 330 I=1,6
C357              330 SL(IR,M)=SL(IR,M)+DER(IR,I)*VO(I,M)
C358                  DO 335 IR=1,6
C359              335 DIA(IR)=0
C360                  DO 340 IR=1,6
C361                  DO 340 I=1,6
C362              340 DIA(IR)=DIA(IR)+SL(IR,I)*DER(IR,I)
C363                  DO 345 I=1,6
C364                  SIG(I)=SQRT(VC(I,I))
C365              345 DIA(I)=SQRT(DIA(I))
C366                  WRITE(IOUT,20)
C367               20 FORMAT(1HO///65H1 REFINED CELL DIMENSIONS AND CONSTANTS WITH STAND
                     ARD DEVIATIONS /)
C368                  IF(N.NE.1) GO TO 346
C369                  SIG(2)=SIG(1)
C370                  SIG(3)=SIG(1)
C371                  DIA(2)=DIA(1)
C372                  DIA(3)=DIA(1)
C373              346 IF(N.NE.2) GO TO 347
C374                  SIG(2)=SIG(1)
C375                  DIA(2)=DIA(1)
C376                  IF(ISYM.NE.3) GO TO 347
C377                  SIG(6)=SIG(1)
C378                  DIA(6)=0
C379              347 WRITE(IOUT,21)ED(1),DIA(1),EKO(1),SIG(1),ED(2),DIA(2),EKO(2),
                     XSIG(2),ED(3),DIA(3),EKO(3),SIG(3)
C380               21 FORMAT(4HO A=F10.7,2H+-F9.7,9H       K1=F10.8,2H+-F10.8//
                     X4H  B=F10.7,2H+-F9.7,9H       K2=F10.8,2H+-F10.8//
                     X4H  C=F10.7,2H+-F9.7,9H       K3=F10.8,2H+-F10.8 //)
C381                  DO 350 I=4,6
C382                  D(I)=ED(I)/PI*180
C383                  IF(D(I).LT.0)D(I)=D(I)+180
C384              350 CONTINUE
C385                  WRITE(IOUT,22)D(4),DIA(4),EKO(4),SIG(4),D(5),DIA(5),EKO(5),
                     XSIG(5),D(6),DIA(6),EKO(6),SIG(6)
C386               22 FORMAT(8HO ALFA =F10.6,2H+-F8.6,6H   K4=F 9.7,2H+-F 9.7//
                     X8H  BETA =F10.6,2H+-F8.6,6H   K5=F 9.7,2H+-F 9.7//
                     X8H  GAMMA=F10.6,2H+-F8.6,6H   K6=F 9.7,2H+-F 9.7)
C387                  C(1)=ED(1)*ED(2)*ED(3)*SQRT(1+2*CO(4)*CO(5)*CO(6)-CC(4)**2
                     X-CO(5)**2-CO(6)**2)
C388                  WRITE(IOUT,23) D(1)
C389               23 FORMAT('0 CELL VOLUME ',F10.5)
C390                  IQ=1
C391                  RETURN
C392                  END
```

APPENDIX 2

TEXTURE DETERMINATION METHOD

A.2.1 Sample Preparation

The Zr-10% Nb alloy was chosen as typifying the softening behaviour of the high niobium alloys. The samples were annealed in the same manner as the standard compression samples, that is, they were held for 30 minutes at 1000°C and subsequently cooled to room temperature at a rate of 1°C/sec. The samples were then preheated for 20 minutes at 825°C, and deformed to strains of 0.0, 0.1, 0.4 and 0.8, respectively. The undeformed sample permitted the determination of the texture prior to testing, and the other strains were chosen so as to exemplify the development of texture with strain.

The tested samples were spark cut into slices about 0.75 mm thick along planes parallel to the bar axis; the slices obtained on each sample were mounted in bakelite, care being taken to keep their relative orientation constant. The mounts were first polished on silicon carbide paper, and then finished on a wheel using diamond paste. In order to eliminate the surface cold work introduced during polishing, the samples were etched using a solution of 46 parts H_2O, 46 parts HNO_3 and 8 parts lactic acid.

A.2.2 Experimental Procedure for Texture Determination

The texture goniometer was a Philips PW 1078/24 model. The counter arm was positioned so as to receive the (110) diffracted beam only ($2\theta \simeq 35.2^\circ$), fine adjustments being made so as to maximize the diffracted intensity.

The sample holder was able to perform one translation and two rotations. The translation movement was parallel to the plane of the sample and was designed to average the diffracted intensity over a large number of grains. The first rotation (angle α) took place about an axis normal to the sample surface. The axis of the second rotation (of angle ϕ) was contained in the plane defined by the incident and the (110) reflected beam and perpendicular to the bisector of the angle defined by the incident and the reflected beams. The sample was initially positioned so that, for $\alpha = 0$ and $\phi = 0$, the direction corresponding to the compression axis was perpendicular to the above defined plane.

The α and ϕ rotations are combined in such a way that when ϕ increases by 360°, ϕ increases by 5° (5° pitch). The locus on a stereographic projection of the directions taken when α varies in this way is given in Figure A.2.1. The stereogram must be considered as fixed with respect to the sample, and oriented so that the normal of the sample surface is at the center of the stereogram. The combined movement of α and ϕ makes the normal to the reflecting (110) plane describe a spiral of pitch 5°. The center of the stereogram thus corresponds to reflecting planes <u>parallel</u> to the bar axis.

A.2.3 <u>Absorption Correction Curve</u>

The surface area of the sample subject to diffraction varies with the degree to which the sample is tilted with respect to the X-ray beam, that is with ϕ. This causes the diffracted intensity to vary with ϕ, independently of variations in the pole density. A correction curve was therefore constructed in order to eliminate this spurious effect. A random sample was produced by compacting a powder produced by filing the

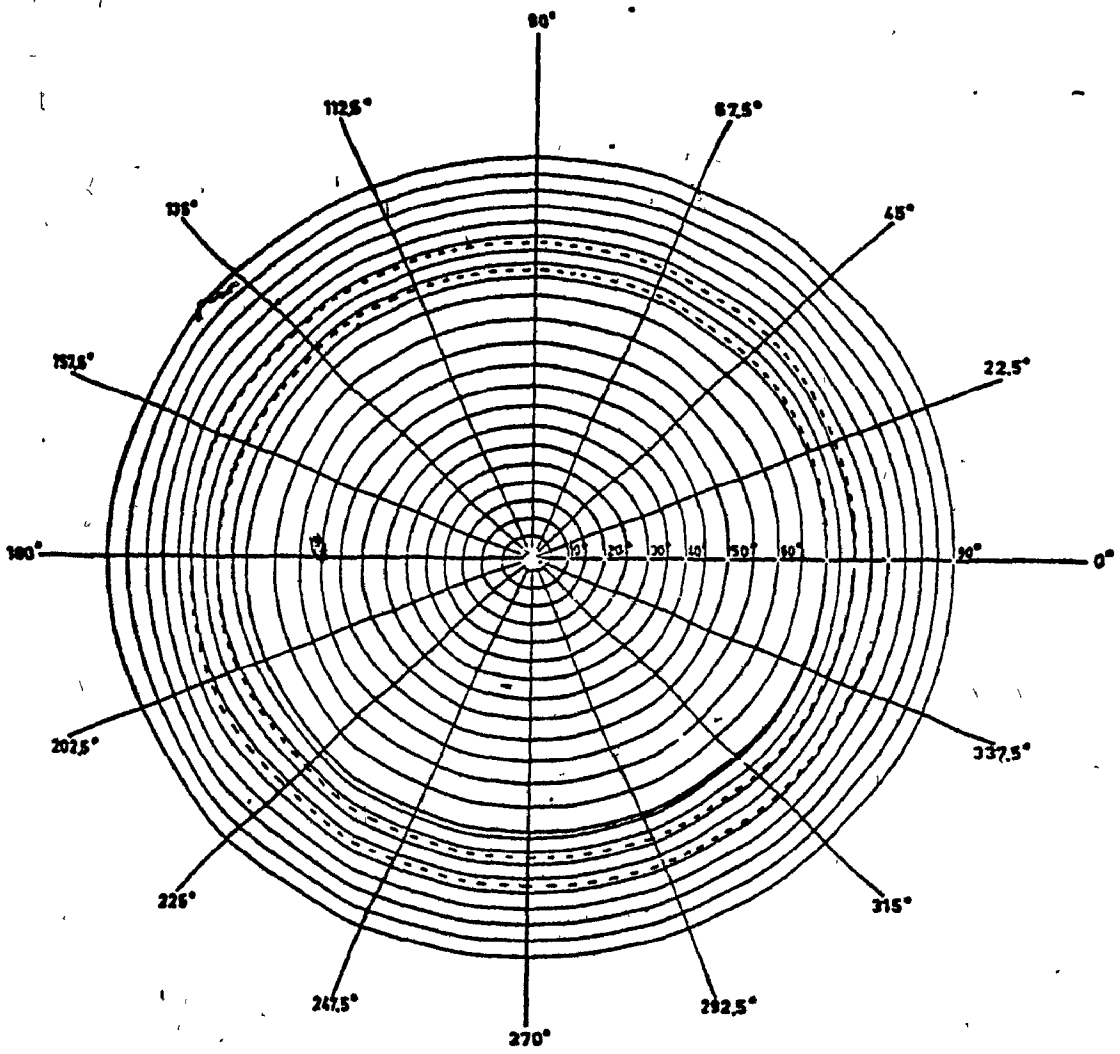

FIGURE A2.1 Locus on the stereographic projection of the reflecting plane normals, for the coupled variation of α and ϕ.

alloy. The α angle was kept equal to zero and ϕ values were increased in 10^{o} steps from 0 to 70^{o}. For each ϕ value, the intensity was integrated over 40 seconds each measurement being repeated 10 times and thus a grand average $\overline{I}(\phi)$ was obtained. A second grand average $\overline{I}_b(\phi)$ was then determined in the same way for the background by changing the 2θ value to 30^{o}. The true peak intensity was then taken as proportional to $(\overline{I}(\phi) - \overline{I}_b(\phi))$, so that the intensities could be normalized through the factor F defined as

$$F(\phi) = \frac{\overline{I}(\phi) - \overline{I}_b(\phi)}{\overline{I}(0) - \overline{I}_b(0)} \qquad (A.2.1)$$

Here $\overline{I}(0)$ and $\overline{I}_b(0)$ represent the values of $\overline{I}(\phi)$ and $\overline{I}_b(\phi)$ respectively for $\phi = 0$. The variation of F with ϕ is shown in Figure A.2.2. The decrease of F is linear with ϕ up to 50^{o}, and then becomes sharper until the intensities are too low to be measured with a reasonable accuracy at $\phi > 75^{o}$.

A.2.4 Absorption in Transmission

The absorption curve of Figure A.2.2 shows that the full stereogram cannot be obtained by reflection of the X-ray beam only. Usually, a transmission method is used through a thinned portion of the sample to cover the remaining part of the stereogram. The overlapping regions permit the intensities to be normalized.

In our samples, a thickness of 0.2 mm was the minimum that could be obtained with the spark machine, leading without a great deal of difficulty to 0.1 mm after polishing. The ratio of transmitted intensity I_t over incident intensity I_i is

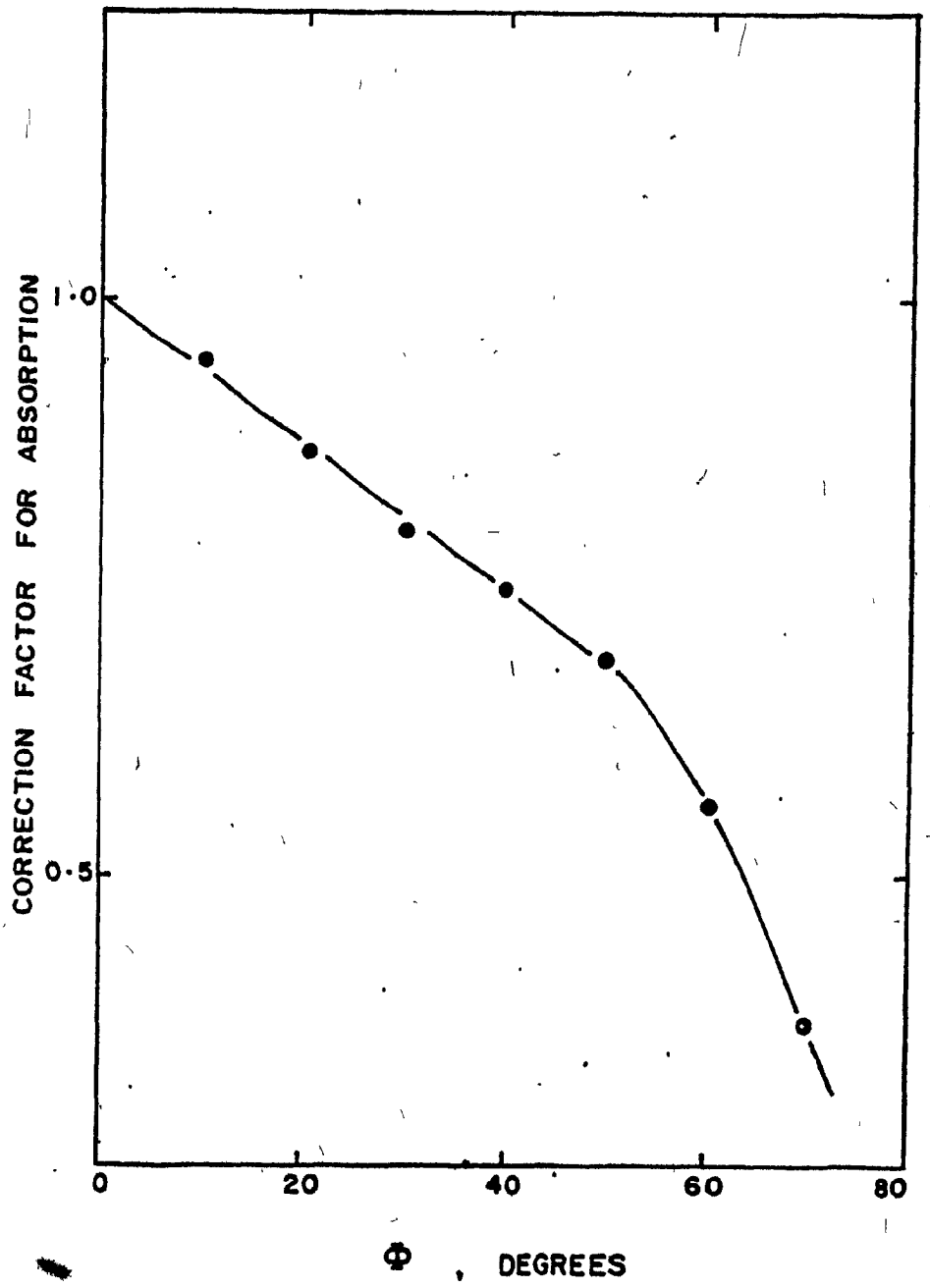

FIGURE A2.2 Correction curve used to compensate for the variation in diffracted intensity with ϕ.

$$\frac{I_t}{I_i} = \exp(-(\frac{\mu}{\rho})\rho\ x)$$

where ρ is the density ($\rho = 6.5\ g/cm^3$), x the thickness of the sample, $\frac{\mu}{\rho}$ the absorption factor. The latter is, for various wavelengths:

	$\mu/\rho\ (cm^2/g)$
$Mo_{k\alpha}$	17.2
$Cu_{k\alpha}$	143
$Co_{k\alpha}$	211
$Cr_{k\alpha}$	391

The ratio $\frac{I_t}{I_i}$ for $x = 0.1$ mm is 0.33 for Mo radiation and 10^{-6} for the Cu radiation. As a result, a Mo tube had to be used for transmission in order to give an appreciable intensity.

A.2.5 Alternative Method

The standard method, which uses the transmitted beam is relatively difficult to apply. An alternative method that was followed is based on the assumption that the texture has a rotational symmetry around the bar (or compression) axis. This assumption is reasonable since all the deformations applied to the metal (swaging, compression) had the above symmetry. The pole density for a fiber texture is thus dependent only on the angle ψ from the compression axis. The reflection method covers ψ angles in the range $25^\circ < \psi \leq 90^\circ$. The only missing reflections required to complete the pole figure were those for low ψ values, near the bar axis. In order to obtain them, samples were prepared in the manner described above, excepted that the compression samples were sectioned along planes perpendi-

cular to the bar axis.

A new stereogram, similar to the one in Figure A.2.1 was obtained, save that since the central point of the stereogram now represents reflecting planes perpendicular to the compression axis. The two stereograms, corresponding to sections parallel and perpendicular to the compression axis, can however be rotated and combined in a single stereogram in which there are overlapping regions. This is shown schematically in Figure A.2.3.

A.2.6 Data Analysis

The intensities were recorded on chart paper, with tick marks each time α increased by 90°. The samples were run first with a 2θ setting corresponding to the peak, then repeated for a Bragg angle corresponding to background reflections only. About two hundred point pairs were read off each chart, giving the true intensity ($I_{peak} - I_{background}$) in arbitrary units versus the angular position of the reflecting planes (determined from the linear displacement of the chart).

A computer program was prepared, by means of which the data were analyzed, the points were plotted on the stereograms, and the pole densities were calculated. The listing is given in Appendix 3. The computer first calculates α and ϕ values from the data, and then derives a corrected normalized intensity n through the relation

$$n(\alpha,\phi) = \frac{(I_p(\alpha,\phi) - I_b(\alpha,\phi)) \times F(\phi)}{IF_{max}}$$

IF_{max} being the maximum of the numerator values obtained from the data points. This calculation was applied successively to both sets of data.

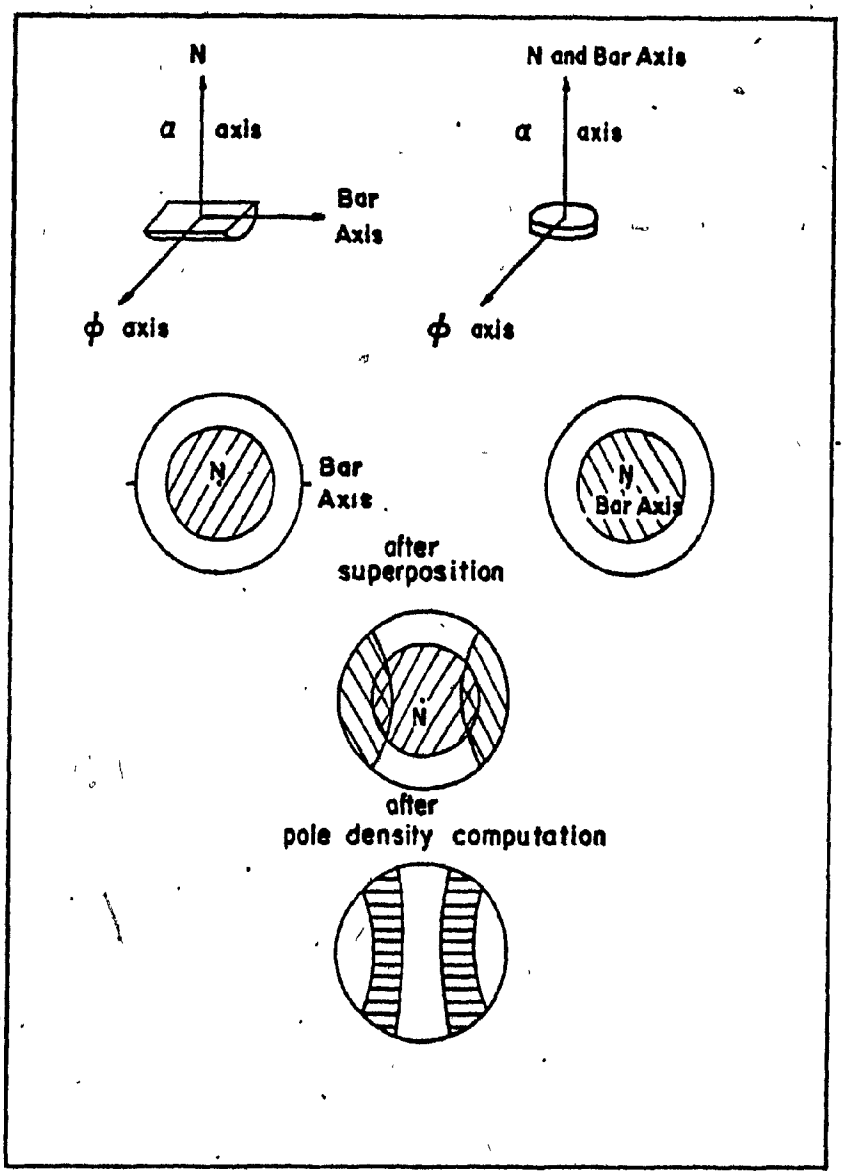

FIGURE A2.3 Schematic diagram illustrating the method used to obtain the full pole figure.

A rotation was then applied to the second set of results in order to place it properly on the first stereographic projection. The points were then plotted on a stereogram (by means of an off-line Calcomp digital plotter), each point being represented by a symbol related to the normalized intensity. Such a plot is shown in Figure A.2.4 and permits a visual check of the data.

The computer then proceeded to a normalization of the two sets of data, using the overlapping regions. In order to do so, the stereogram was divided into regions defined by 5° increase in ψ. The first zone was thus defined as $0 \leq \psi < 5^{\circ}$, the second one $5^{\circ} \leq \psi < 10^{\circ}$ up to $85^{\circ} \leq \psi \leq 90^{\circ}$. In each zone the average of the normalized intensities was obtained, together with the standard deviation. In overlapping zones, two normalized intensities were obtained, one for each set. Their ratio, or compounded ratio when the overlapping region extended to several zones was computed and applied to the averages of one set of data, giving normalized average intensities over the full stereogram.

The calculation of the pole density p(j) for each zone j was then simply obtained from

$$p(j) = \frac{\cos(5j) - \cos(5(j-1))}{\sum_{j=1}^{18} (\cos(5j) - \cos(5(j+1)))} \frac{\bar{n}(j)}{\bar{n}(j)}$$

The decision to divide the stereogram into 5° zones was arbitrary, but it was felt to be a good compromise between the need on the one hand for numerous zones to give an accurate picture and the requirement of a minimum number of points per zone on the other.

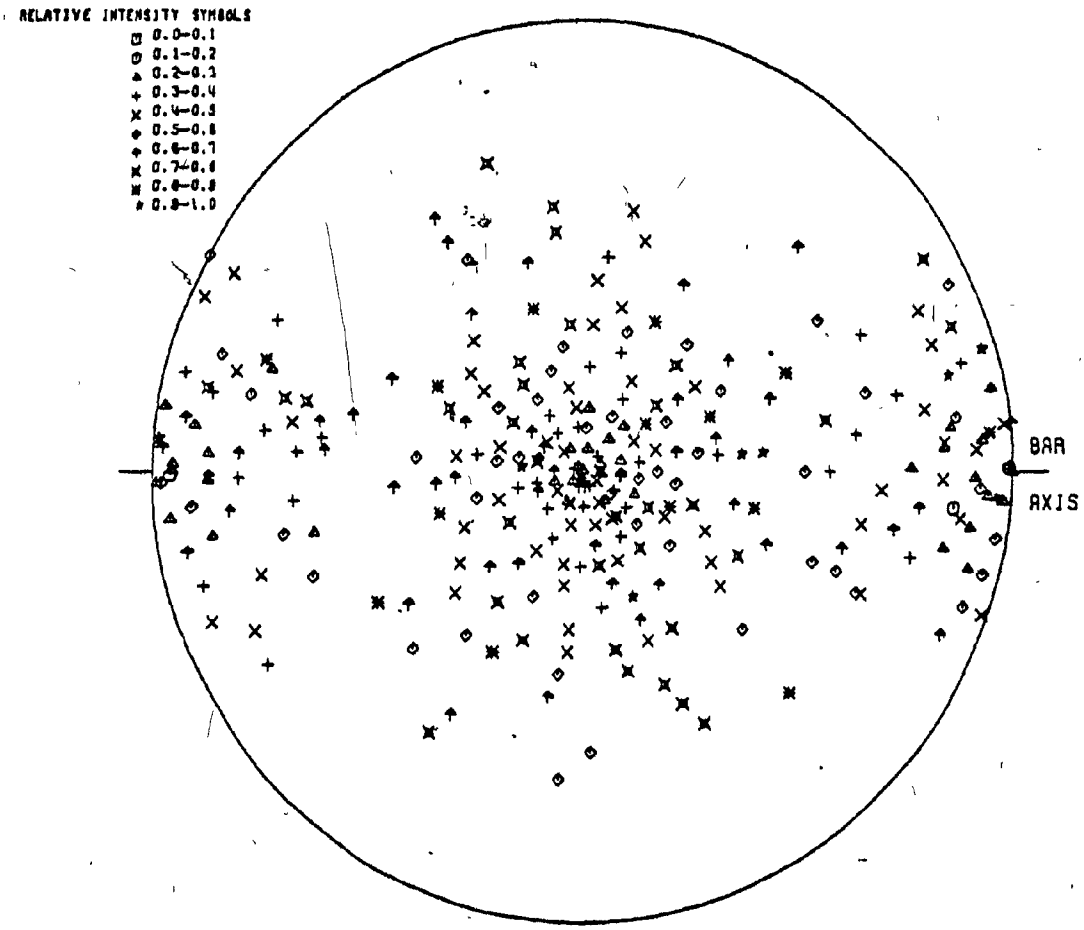

FIGURE A2.4 Specimen of the computer drawn stereographic projections of the corrected and normalized intensities.

APPENDIX 3

LISTING OF THE COMPUTER PROGRAM USED FOR THE DETERMINATION OF THE DEFORMATION TEXTURES

```
      DIMENSION X(500),Y(500),Z(500),PHI(500),F(500),ALPHA(500),T(500)
      DIMENSION XT(500),YT(500),ZT(500),PHIT(500),FT(500),ALPHAT(500)
      DIMENSION TT(500),NS(1000),NST(500),ALFT(500),PHT(500),XX(1000)
      DIMENSION YY(500),AVG(20),AVGT(20),SD(20),SDT(20),NSTP(20)
      DIMENSION NSTPT(20),P(20),TTO(500),TO(500),PHIR(500),ALPHAR(500)
      DATA RD/1.745E-2/
      DATA PITCH,PHPP/5.0,1A.0/
C
C
C
C     READS  N FIRST DATA SET  (LONGITUDINAL SAMPLE SECTION)
C
      DO 10 I=1,500
      READ(5,100,END=900) X(I),Y(I)
      M=I
      IF(X(I),EQ.-100.0) GO TO 13
   10 CONTINUE
C
C     READS IN SECOND DATA SET IF ANY (TRANSVERSE SAMPLE SECTION)
C
   13 M=M-1
      DO 14 I=1,500
      READ(5,100,END=900) XT(I),YT(I)
      MM=I
   14 CONTINUE
C
C     INDEX DETERMINES HOW MANY DATA SETS  WERE READ IN
C
  900 INDEX=2
      GO TO 902
  900 INDEX=1
C
C     DATANY CALCULATES ABSORPTION FACTOR (F),PHI,ALPHA,,CORRECTED
C     INTENSITIES(T),AND RELATIVE INTENSITIES (TT)
C
C     PERFORMS CALCULATION FOR THE FIRST DATA SET
C
  902 CALL DATANY(X,Y,M,ALPHA,PHI,F,Z,T,PHPP,PITCH)
C
C     SYM ASSOCIATES WITH EACH INTENSITY CLASS A PLOTTING SYMBOL
C
      CALL SYM(T,NS,M)
C
C     RESULTS ARE PRINTED OUT
C
      WRITE(6,150)
      WRITE(6,200)
      WRITE(6,300)
      WRITE(6,200)
      DO 30 I=1,M
      IF(Y00(I),EQ.0) WRITE(6,500)
      WRITE(6,400)X(I),Y(I),PHI(I),ALPHA(I),F(I),Z(I),T(I)
   30 CONTINUE
      WRITE(6,200)
C
C     REPEATS CALCULATION FOR 2ND DATA SET , IF ANY
C
      IF(INDEX.EQ.2) GO TO 53
      CALL DATANY(XT,YT,MM,ALPHAT,PHIT,FT,ZT,TT,PHPP,PITCH)
      CALL SYM(TT,NST,MM)
C
C     ROT EFFECTS A 90 DEGREES ROTATION AROUND AN AXIS PERPENDICULAR
C     TO THE PLANE DEFINED BY THE NORMALS TO THE SAMPLES IN THE DATA SETS
C
      PSI=-90.0
      CALL ROT(ALPHAT,PHIT,ALFT,PHT,MM,PSI,RD)
C
C     RESULTS ARE PRINTED OUT
C
      WRITE(6,600)
      WRITE(6,610)
      WRITE(6,620)
      WRITE(6,610)
      DO 61 I=1,MM
      PPHT=PHT(I)/RD
      AALFT=ALFT(I)/RD
      IF(MOD(I,5).EQ.0) WRITE(6,500)
      WRITE(6,630)XT(I),YT(I),PHIT(I),ALPHAT(I),FT(I),ZT(I),TT(I),PPHT,A
     1ALFT
   61 CONTINUE
      WRITE(6,610)
   53 CONTINUE
C
C     IF PLOTTING IS NOT REQUIRED REMOVE THIS SECTION
C
C     POINTS COORDINATES ARE CHANGED FROM ANGULAR TO CARTESIAN
C
C     FIRST SET
C
      DO 62 I=1,M
      TETA=ALPHA(I)*RD
      RO=TAN(PHI(I))*RD/2.0)
      XX(I)=12.0*RO*COS(TETA)
      YY(I)=12.0*RO*SIN(TETA)
   62 CONTINUE
C
C     SECOND DATA SET ,IF ANY, IN SAME ARRAY
C
      IF(END-X.NE.2) GO TO 66
      NINT=M+1
      NMAX=M+MM
      DO 63 I=NINT,NMAX
      TETA=ALFT(I-M)
      RO=TAN(PHT(I-M)/2.0)
      XX(I)=12.0*RO*COS(TETA)
      YY(I)=12.0*RO*SIN(TETA)
      NS(I)=NST(I-M)
   63 CONTINUE
      GO TO 65
   66 NMAX=M
   65 CONTINUE
C
C     PLOT PROCESS STARTS
C
      CALL PLOTON
      CALL FACTOR(0.333)
```

```
      CALL PLOTS(40,0,30,0)
      CALL SYMBOL(2,0,W,0,0,5,'STEREOGRAPHIC PROJECTION',90,0,24)
      CALL PLOT(18,0,15,0,-3)
      CALL CIRCLE(0,0,0,0,12,0)
      CALL DASHL(-12,0,0,0,-13,0,0,0,0,0)
      CALL DASHL(12,0,0,0,13,0,0,0,0,0)
      CALL SYMBOL(12,5,0,5,0,375,'MAX',0,0,3)
      CALL SYMBOL(12,5,-1,0,0,375,'AXIS',0,0,4)
      DO 42 I=1,NMAX
      A=XX(I)
      B=YY(I)
      N=S(I)
      CALL SYMBOL(A,B,0,33,N,0,0,-1)
   42 CONTINUE
      CALL SYMBOL(-15,75,12,0,0,25,'RELATIVE INTENSITY SYMBOLS',0,0,26)
      CALL SYMBOL(-12,0,11,5,0,25,'0.0 0.1',0,0,7)
      CALL SYMBOL(-12,0,11,0,0,25,'0.1 0.2',0,0,7)
      CALL SYMBOL(-12,0,10,5,0,25,'0.2 0.3',0,0,7)
      CALL SYMBOL(-12,0,10,0,0,25,'0.3 0.4',0,0,7)
      CALL SYMBOL(-12,0,09,5,0,25,'0.4 0.5',0,0,7)
      CALL SYMBOL(-12,0,09,0,0,25,'0.5 0.6',0,0,7)
      CALL SYMBOL(-12,0,08,5,0,25,'0.6 0.7',0,0,7)
      CALL SYMBOL(-12,0,08,0,0,25,'0.7 0.8',0,0,7)
      CALL SYMBOL(-12,0,07,5,0,25,'0.8 0.9',0,0,7)
      CALL SYMBOL(-12,0,07,0,0,25,'0.9 1.0',0,0,7)
      CALL SYMBOL(-12,5,11,5,0,25,0,0,-1)
      CALL SYMBOL(-12,5,11,0,0,25,1,0,-1)
      CALL SYMBOL(-12,5,10,5,0,25,2,0,-1)
      CALL SYMBOL(-12,5,10,0,0,25,3,0,-1)
      CALL SYMBOL(-12,5,9,5,0,25,4,0,0,-1)
      CALL SYMBOL(-12,5,9,0,0,25,5,0,0,-1)
      CALL SYMBOL(-12,5,8,5,0,25,6,0,0,-1)
      CALL SYMBOL(-12,5,8,0,0,25,10,0,0,-1)
      CALL SYMBOL(-12,5,7,5,0,25,11,0,0,-1)
      CALL SYMBOL(-12,5,7,0,0,25,14,0,0,-1)
      CALL ENDPLT
C
C     END OF PLOTTING SECTION
C
C      POLE DENSITY CALCULATION
C
C     STEP 1   BRINGS BAR AXES IN CENTER OF STEREOGRAM
C
      PSI=0.0
      CALL ROT(ALPHA,PHI,ALPHAR,PHIR,N,PSI,RD)
C
C     PRINTS RESULT
C
      WRITE(6,650)
      WRITE(6,660)
      WRITE(6,730)
      WRITE(6,740)
      DO 311 I=1,N
      PHIR(I)=PHIR(I)/RD
      ALPHAR(I)=ALPHAR(I)/RD
  311 CONTINUE
      DO 348 I=1,N,5
      IF(MOD(I,20),EQ,0) WRITE(6,500)
```



```
      WRITE(6,740) PHI(I),ALPHA(I),PHIR(I),ALPHAR(I)
  348 CONTINUE
      WRITE(6,750)
C
C     STEP 2  ARRANGES 1ST DATA SET IN INCREASING PHI VALUES
C
C
C     PRINTS RESULT
      WRITE(6,150)
      WRITE(6,660)
      WRITE(6,650)
      WRITE(6,660)
      DO 312 I=1,N
      IF(MOD(I,5),EQ,0) WRITE(6,500)
  312 WRITE(6,660) PHI(I),ALPHA(I),TTO(I)
      WRITE(6,660)
C
C     ARRANG-S 2ND DATA SET IN SAME WAY , IF ANY
C
      IF(INDEX,NE,2) GO TO 313
      CALL ORDER(PHI,ALFT,TTO,PHIT,ALPHAT,IT,MM)
C
C     PRINTS RESULT
C
      WRITE(6,600)
      WRITE(6,660)
      WRITE(6,650)
      WRITE(6,660)
      DO 314 I=1,MM
      IF(MOD(I,5),EQ,0) WRITE(6,500)
  314 WRITE(6,660) PHT(I),ALFT(I),TTO(I)
C
C     STEP 3, CALCULATES AVERAGE AND STANDARD DEVIATION IN EACH 5 DEG. S
C
C     STARTS WITH 1ST DATA SET
C
  313 CALL SECTN(PHI,TO,AVG,SD,NSTP,M)
C
C     PRINTS RESULT
C
      WRITE(6,660)
      WRITE(6,670)
      WRITE(6,660)
      DO 317 J=1,18
      IF(MOD(J,5),EQ,0) WRITE(6,500)
  317 WRITE(6,680)J,AVG(J),SD(J),NSTP(J)
      WRITE(6,660)
C
C     REPEATS CALCULATION FOR SECOND SET IF ANY
C
      IF(INDEX,NE,2) GO TO 316
      CALL SECTN(PHT,TTO,AVGT,SDT,NSTPT,MM)
C
C     PRINTS RESULT
C
      WRITE(6,600)
      WRITE(6,660)
      WRITE(6,670)
```

```
      WRITE(A,440)
      DO 340 J=1,18
      IF(NOBS(I,5),EQ,0) WRITE(6,500)
  340 WRITE(A,450)J,AVGT(J),SDT(J),NSTPT(J)
      WRITE(A,460)
C
C     STEP 4  NORMALIZES BOTH DATA SETSINTENSITIES , IF POSSIBLE
C
      CALL NORM(AVG,AVGT,NSTP,NSTPT,FC)
C
C     PRINTS RESULT
C
      WRITE(A,470)FC
C
C     STEP 5  CALCULATES POLE DENSITY FROM FC JUST OBTAINED
C
      CALL POLE(AVG,P,BD)
C
C     PRINTS RESULT
C
      WRITE(A,700)
      WRITE(A,710)
      WRITE(A,700)
      DO 320 J=1,18
      JK=5*(I-1)
      JL=5+J
      IF(NOBS(I,5),EQ,0) WRITE(A,500)
  320 WRITE(A,720) JK,JL,P(J)
      WRITE(A,700)
  100 FORMAT(1H,1,65,1)
  150 FORMAT('1',5X,'LONGITUDINAL SECTION'///)
  200 FORMAT(I3),1(A1,'*'))
  300 FORMAT(I1),'*   DISTANCE   *  INTENSITY   *     PHI      *     '
     1'ALPHA      * CORR. FACTOR * CORR. INTENS.* REL. INTENS.*')
  400 FORMAT(10,3F15.2,F15.0,F15.3,F15.2,F15.3)
  500 FORMAT(1H0)
  600 FORMAT('1',5X,'TRANSVERSE SECTION'///)
  610 FORMAT(I3:12(1A1,'*'))
  620 FORMAT(1H,'*  DISTANCE  *  INTENSITY  *  PHI(DEG.)  * ALPHA(DEG.)'
     1,' * CORR. FACTOR* CORR. INTENS* REL. INTENS.*  PSI(DEG.)  *',
     2'  BETA(DEG.) *')
  630 FORMAT(1H,3F14.2,F14.0,F14.3,F14.2,F14.3,2F14.2)
  640 FORMAT('1',30('*'))
  650 FORMAT(1H,'*  PHID  * ALPHAD *    T    *')
  660 FORMAT('1',3F10.3)
  670 FORMAT(1H1,'*  I  *  AVG  *  SD  *  NSTEP *')
  680 FORMAT('1',I5,2F7.3,I9)
  690 FORMAT(1H,'ADJUSTMENT FACTOR FOR SET 2 WITH RESPECT TO SET 1 IS:',F
     1'0.3///)
  700 FORMAT(30X,30('*'))
  710 FORMAT(30X,'*  PSI RANGE *  POLE  DENS.  *')
  720 FORMAT(30X,'*',2I5,2X,'*',F15.2,'*')
  730 FORMAT(1H,10X,'*  PHI   * ALPHA *   PHIR   *ALPHAR *')
  740 FORMAT(1H,10X,2(F10.3,F10.0))
  750 FORMAT('1',10X,60('*'))
      STOP
      END
      SUBROUTINE ANSE(FI,FACT)
      DATA ANS0,ANS1,ANS2,ANS3/-6.9E-3,-4.4E-4,3.97E-2,-0.154/
      IF(FI-50.0) 20,20,21
   20 FACT=ANS0*FI+1.0
      GO TO 22
   21 FACT=ANS1*FI**2+ANS2*FI+ANS3
   22 RETURN
      END
C
C
      SUBROUTINE ALPH(XX,N,PMPP)
      DO 50 I=1,100
      N=I
      IF(XX.LT.(PMPP*I)) GO TO 51
   50 CONTINUE
   51 RETURN
      END
C
C
      SUBROUTINE DATANY(X,Y,M,ALPHA,PHI,F,Z,T,PMPP,PI,CM)
      DIMENSION X(1),Y(1),PHI(1),ALPHA(1),F(1),Z(1),T(1)
      ZMAX=-1.0
      DO 11 I=1,M
      PHI(I)=X(I)*PITCH/PMPP
      XAA=X(I)
      CALL ALPH(XAA,N,PMPP)
      ALPHA(I)=(X(I)-(N-1)*PMPP)*360.0/PMPP
      FI=PHI(I)
      CALL ANSE(FI,FACT)
      F(I)=FACT
      Z(I)=Y(I)/F(I)
      IF(Z(I).GT.ZMAX) ZMAX=Z(I)
   11 CONTINUE
      DO 12 I=1,M
   12 T(I)=Z(I)/ZMAX
      RETURN
      END
      SUBROUTINE SYMIT(MS,M)
      DIMENSION T(1),MS(1)
      DO 31 I=1,M
      IF(T(I)-0.5) 21,22,22
   21 IF(T(I)-0.3) 23,24,24
   23 IF(T(I).LT.0.1) GO TO 25
      IF(T(I).LT.0.2) GO TO 26
      GO TO 27
   24 IF(T(I).LT.0.4) GO TO 28
      GO TO 29
   22 IF(T(I)-0.8) 32,33,33
   32 IF(T(I).LT.0.6) GO TO 34
      IF(T(I).LT.0.7) GO TO 35
      GO TO 36
   33 IF(T(I).LT.0.9) GO TO 37
      GO TO 38
   25 MS(I)=0
      GO TO 31
   26 MS(I)=1
      GO TO 31
   27 MS(I)=2
      GO TO 31
```

```
      34    NS(I)=3
            GO TO 31
      35    NS(I)=6
            GO TO 31
      36    NS(I)=8
            GO TO 31
      37    NS(I)=10
            GO TO 31
      38    NS(I)=11
            GO TO 31
      39    NS(I)=16
      31    CONTINUE
            RETURN
            END
            SUBROUTINE ROT(ALPHAT,PHIT,ALFT,PHT,MM,PSI,RD)
            DIMENSION ALPHAT(1),PHIT(1),ALFT(1),PHT(1)
            DATA PI/3.1415927/
C
C     ROTATION RELATIONS
C
            PSI=PSI*RD
            DO 35 I=1,MM
            X0=SIN(PHIT(I)*RD)*COS(ALPHAT(I)*RD)
            Y0=SIN(PHIT(I)*RD)*SIN(ALPHAT(I)*RD)
            Z0=0.5*COS(PHIT(I)*RD)
            XT=X0*COS(PSI)+Z0*SIN(PSI)
            YT=Y0
            ZT=-X0*SIN(PSI)+Z0*COS(PSI)
            PHT(I)=ARCOS(ZT)
            IF(PHT(I).EQ.0.0) GO TO 56
            SH=YT/SIN(PHT(I))
            CH=XT/SIN(PHT(I))
            IF(CH).2,3
    3       IF(SH)4,5,6
    4       ALFT(I)=2.0*PI-ARCOS(CH)
            GO TO 59
    5       ALFT(I)=PI
            GO TO 59
    6       ALFT(I)=ARCOS(CH)
            GO TO 59
    2       IF(SH)7,7,8
    7       ALFT(I)=(3.0*PI)/2.0
            GO TO 59
    8       ALFT(I)=PI/2.0
            GO TO 59
    9       IF(SH)55,56,57
   55       ALFT(I)=2.0*PI-ARCOS(CH)
            GO TO 59
   56       ALFT(I)=0.0
            GO TO 59
   57       ALFT(I)=ARCOS(CH)
   59       IF(PHT(I)-PI/2.0) 15,15,60
   60       PHI(I)=PI-PHT(I)
            ALFT(I)=ALFT(I)+PI
   15       IF(ALFT(I).GT.(2.0*PI)) ALFT(I)=ALFT(I)-2.0*PI
            GO TO 15
   54       ALFT(I)=0.0
   16       CONTINUE
            RETURN
            END
            SUBROUTINE ORDER(PHI0,ALPHA0,T0,PHI,ALPHA,T,M)
            DIMENSION PHI(1),PHI0(1),ALPHA(1),ALPHA0(1),T(1),T0(1)
            MM=M-1
            DO 101 J=1,MM
            INDT=1
            ND=M-J+1
            ALO=PHI(1)
            DO 102 I=2,ND
            IF(PHI(I).LT.ALO) GO TO 103
            GO TO 102
  103       ALO=PHI(I)
            INDT=I
  102       CONTINUE
            T0(J)=T(INDT)
            ALPHA0(J)=ALPHA(INDT)
            PHI0(J)=PHI(INDT)
            IF(INDT.EQ.ND) GO TO 101
            NP=ND-1
            DO 104 I=INDT,NP
            ALPHA(I)=ALPHA(I+1)
            T(I)=T(I+1)
  104       PHI(I)=PHI(I+1)
  101       CONTINUE
            PHI0(M)=PHI(1)
            ALPHA0(M)=ALPHA(1)
            T0(M)=T(1)
            RETURN
            END
            SUBROUTINE SECTN(PHI,T,AVG,SD,NSTP,M)
            DIMENSION PHI(1),T(1),AVG(1),SD(1),NSTP(1)
            DO 111 I=1,M
            AVG(I)=0.0
            SD(I)=0.0
  111       NSTP(I)=0
C
            IMIN=1
            DO 112 J=1,M
            IF(PHI(IMIN).GT.5.0*I) GO TO 112
            DO 113 I=IMIN,M
            IF(PHI(I).GE.5.0*J) GO TO 114
  113       CONTINUE
            NSTP(J)=M-IMIN+1
            IMAX=M
            GO TO 115
C   CALCULATES AVERAGE AND STANDARD DEVIATION
  114       IMAX=I-1
  115       SUM=0.0
            NSTP(J)=IMAX-IMIN+1
            IF(NSTP(J).EQ.0) GO TO 112
            DO 116 I=IMIN,IMAX
  116       SUM=SUM+T(I)
            AVG(J)=SUM/NSTP(J)
            IF(NSTP(J).EQ.1) GO TO 117
            DV=0.0
```

```
      DO 118 I=IMIN,IMAX
  118 DV=DV+(T(I)-AVG(J))**2
      SD(J)=SQRT(DV)/(NSTP(J)-1)
  117 IF(IMAX.EQ.M) GO TO 119
      IMIN=IMAX+1
  112 CONTINUE
  119 CONTINUE
      RETURN
      END
      SUBROUTINE NORM(AVG1,AVG2,NSTP1,NSTP2,FC)
      DIMENSION AVG1(1),AVG2(1),NSTP1(1),NSTP2(1)
      NF=0
      NG=0
      IF(NSTP1(6).EQ.0) NF=10
      IF(NSTP2(6).EQ.0) NF=10
      IF(NSTP1(7).EQ.0) NG=1
      IF(NSTP2(7).EQ.0) NG=1
      NF=NF+NG
      IF(NF.EQ.11)FC=1.0
      IF(NF.EQ.1)  FC=AVG1(6)/AVG2(6)
      IF(NF.EQ.10)FC=AVG1(7)/AVG2(7)
      IF(NF.EQ.0)  FC=(AVG1(6)/AVG2(6)+AVG1(7)/AVG2(7))/2.0
      DO 201 J=1,6
  201 AVG1(J)=AVG2(J)*FC
      RETURN
      END
      SUBROUTINE POLE(AVG,P,RD)
      DIMENSION AVG(1),P(1)
C       CALCULATES FACTOR
      PSUM=0.0
      DO 401 J=1,18
      PSUM=PSUM+AVG(J)*(COS(5.0*RD*(J-1))-COS(5.0*RD*J))
  401 CONTINUE
      PFACT=1.0/PSUM
C        NORMALIZES
      DO 402 J=1,18
  402 P(J)=AVG(J)*PFACT
      RETURN
      END
```

APPENDIX 4

X-RAY DIFFRACTION PATTERNS

The standard conditions used were:

Cu tube, Ni filter

40 kV, 24 mA

1^{o} divergence slit

0.2 mm receiving slit

1^{o} scatter slit

2 seconds time constant

40 mm/min chart paper speed

1^{o}/min scanning rate

Zirconium - 15% Niobium (Bar D), As-Received

2θ	I	Indexation	
		α-phase	β-phase
31.88	VW	$(10\bar{1}0)_\alpha$	-
34.85	VS	$(0002)_\alpha$	-
36.16	VS	$(10\bar{1}1)_\alpha$	$(110)_\beta$
47.86	VW	$(10\bar{1}2)_\alpha$	-
51.08	W	-	$(200)_\beta$
52.11	W	-	-
56.79	M	$(11\bar{2}0)_\alpha$	-
63.58	W	$(10\bar{1}3)_\alpha$	-
65.13	W	-	$(211)_\beta$
68.29	-	-	-

The peaks are extremely broad, and at large angles ($2\theta > 70^\circ$) the diffraction peaks can barely be distinguished from the background.

Zirconium 15% Niobium (Bar D), Held for 15 Minutes at 825°C, and Water Quenched

2θ	I	Indexation
34.72	VW	$(0002)_\alpha$
35.85	VS	$(110)_\beta$
51.47	S	$(200)_\beta$
64.37	VS	$(211)_\beta$
75.91	VW	$(220)_\beta$
86.71	VW	$(310)_\beta$

Zirconium 15% Niobium (Bar D) Held 15 Minutes at 925°C, and Water Quenched

2θ	I	Indexation
35.80	VS	$(110)_\beta$
51.26	M	$(200)_\beta$
64.26	S	$(211)_\beta$
~ 75.84	VW	$(220)_\beta$
~ 86.55	VW	$(310)_\beta$
~108.80	VW	$(321)_\beta$

Zirconium -15% Niobium (Bar D), Held 15 Minutes at 1025°C, and Water Quenched

2θ	I	Indexation
35.74	VS	$(110)_\beta$
51.41	VS	$(200)_\beta$
64.19	VS	$(211)_\beta$
~75.65	VW	$(220)_\beta$
86.69	W	$(310)_\beta$

Zirconium -15% Niobium (Bar 15A), Held for 15 Minutes at 1000°C, then Deformed at 1025°C to a Strain of 0.6 at a Strain Rate of $1.5 \times 10^{-3} s^{-1}$, and Water Quenched

2θ	I	Indexation
35.79	VS	$(110)_\beta$
51.28	M	$(200)_\beta$
64.22	S	$(220)_\beta$
~75.75	VW	$(220)_\beta$
~86.50	W	$(310)_\beta$
~97.5	VW	$(222)_\beta$

Zirconium -15% Niobium (Bar 15A),
Annealed 64 Hours at 1000°C, and Air Cooled

2θ	I	Indexation
28.8	VW	$(0001)_{\omega}$
32.0	VW	$(10\bar{1}0)_{\alpha}$
34.08	M	$(0002)_{\alpha}$
36.46	S	$(110)_{\beta}$
		$(10\bar{1}1)_{\alpha}$
47.1	W	$(111)_{\omega}$
		$(10\bar{1}2)_{\alpha}$
50.79	W	$(200)_{\beta}$
56.7	VW	$(11\bar{2}0)_{\alpha}$
63.44	W	$(10\bar{1}3)_{\alpha}$
64.86	VS	$(211)_{\beta}$
68.34	VW	$(11\bar{2}2)_{\alpha}$

Zirconium 15% Niobium (Bar 15A), Annealed 64 Hours at 1000°C. Air Cooled, Reheated to 825°C then Deformed at 825°C at a Strain Rate of $1.5 \times 10^{-3} s^{-1}$ to a Strain of 0.6

2θ	I	Indexation
34.85	VW	$(0002)_\alpha$
35.73	VS	$(\bar{1}10)_\beta$
51.53	VS	$(220)_\beta$
64.39	S	$(211)_\beta$
75.92	M	$(220)_\beta$
86.87	M	$(310)_\beta$
∿108.93	W	$(222)_\beta$

APPENDIX 5

MICROPROBE RESULTS ON Zr-15% Nb (15A) AND Zr-20% Nb (20B)

Sample designations

#1 Zr-15% Nb alloy (bar 15A) annealed 5 minutes at 1000°C, air cooled. Reheated 1 hour at 1000°C, water quenched.

#2 As #1, except 4 hours at 1000°C prior to air cooling.

#3 As #1, except 64 hours at 1000°C prior to air cooling.

#4 Zr-20% Nb alloy (bar 20B), annealed 64 hours at 1000°C, air cooled. Reheated 1 hour at 1000°C, water quenched.

Each average represents the mean of 5 or more values, each of which involves integrating the intensity over 10 seconds.

Element	Count	Standard Deviation	Niobium Content (Atomic Percent)
Pure Nb standard			
Nb	25763	775	-
Zr	25	6	-
Pure Zr standard			
Nb	1236	51	-
Zr	3118	49	-
#1 Clear area			
Nb	5111	77	15.8
Zr	2528	69	80.9
#1 β" plate-like feature, adjacent to above area			
Nb	5199	32	16.2
Zr	2594	67	83.1
#1 At triple point			
Nb	5502	86	17.4
Zr	2793	118	89.5
#1 In the center of an adjacent grain			
Nb	5855	39	18.8
Zr	3270	67	105
#1 At other triple point			
Nb	5468	75	17.3
Zr	2793	73	89.5
#2 At triple point			
Nb	6096	82	19.8
Zr	3439	84	110.4
#2 In an adjacent grain			
Nb	6024	106	19.5
Zr	3340	74	107.2
#1 Middle of longitudinal streak			
Nb	5691	73	18.2
Zr	2819	65	90.3

.....(cont'd.)

APPENDIX 5 (cont'd.)

Element	Count	Standard Deviation	Niobium Content (Atomic Percent)
#1 Edge of streak			
Nb	5593	25	17.8
Zr	2772	44	88.8
#1 Further from streak			
Nb	5307	77	16.6
Zr	2550	65	81.6
#1 Still further from streak			
Nb	5522	92	17.5
Zr	2666	54	85.4
#1 Furthest from streak			
Nb	5376	107	16.9
Zr	2601	91	83.3
#1 On a particle-like feature			
Nb	5551	-	17.6
Zr	2676	-	85.7
#3 Grain boundary			
Nb	5021	72	15.4
Zr	2355	45	75.3
#3 Next to grain boundary			
Nb	5116	168	15.8
Zr	2317	76	74.1
#3 Middle of grain			
Nb	5305	125	16.6
Zr	2475	66	79.2
#3 Middle of grain			
Nb	5831	134	18.7
Zr	2946	117	94.4

.....(cont'd.)

APPENDIX 5 (cont'd.)

Element	Count	Standard Deviation	Niobium Content (Atomic Percent)
#3 Grain boundary			
Nb	4968	553	15.2
Zr	2199	414	70.3

Note here that both the Nb and Zr readings decrease together, suggesting either an unclean surface or an inclusion is involved.

#1 Grain boundary particle-like feature			
Nb	6050	98	19.6
Zr	3213	62	103
#1 Longitudinal streak			
Nb	5870	132	18.9
Zr	2907	58	93.2
Nb standard			
Nb	26614	618	-
Zr	20	2	-
Zr standard			
Nb	1296	51	-
Zr	2638	59	-
#4 Dark area			
Nb	4069	90	10.9
Zr	1502	65	56.7

Both the Nb and Zr values are low, suggesting that segregation is not involved.

#4 White area			
Nb	4858	93	14.1
Zr	1953	36	73.8
#4 Dark patch			
Nb	5493	137	16.6
Zr	2469	73	93.5